Technische Universität München

Ingenieurfakultät Bau Geo Umwelt

Lehrstuhl für Statik

CAD-INTEGRATED ISOGEOMETRIC ANALYSIS AND DESIGN OF LIGHTWEIGHT STRUCTURES

Anna Maria Bauer

Vollständiger Abdruck der von der Ingenieurfakultät Bau Geo Umwelt der Technischen Universität München zur Erlangung des akademischen Grades eines

Doktor-Ingenieurs

genehmigten Dissertation.

Vorsitzender:

    Prof. Dr.-Ing. habil. Fabian Duddeck

Prüfer der Dissertation:

1. Prof. Dr.-Ing. Kai-Uwe Bletzinger
2. Prof. Dr.-Ing. Josef Kiendl
3. Prof. Dr. Carlos Lázaro Fernández

Die Dissertation wurde am 07.04.2020 bei der Technischen Universität München eingereicht und durch die Ingenieurfakultät Bau Geo Umwelt am 20.07.2020 angenommen.

Anna Maria Bauer

CAD-integrated Isogeometric Analysis and Design of Lightweight Structures

Abstract

The design of lightweight structures is a challenging task. Shape and stress are strongly dependent on each other and cannot be separated. Tensile and bending-active structures are examples of this. Isogeometric analysis provides the possibility to unify the design and analysis model. The model conversion to a polygonal mesh is avoided and the parametrization by Non-uniform Rational B-Splines (NURBS) is maintained while generating the simulation model from the geometric design in Computer-Aided-Design (CAD). This is a major advantage in the digital design of lightweight structures because structural feedback can be provided during the shape generation.

This research extends the existing isogeometric methods in order to obtain design through analysis. Missing links in the design chain were found in the coupling of the individual structural members. Therefore, three novel coupling formulations are proposed. The first one deals with the rotational coupling of displacement-based element formulations, e.g. Bernoulli beams. The second one provides an embedding technique using implicit geometry description through the parameter space. The last one uses the large parameter space of NURBS to inherently describe a frictionless sliding contact between objects in an innovative manner. Furthermore, a form finding technique for bending-active structures for fast design exploration is proposed.

Lightweight structures are often assembled in several steps. This makes the construction process important, which is very challenging in the simulation. Therefore, the linking of several analysis steps is investigated and incorporated into CAD. The necessary components in order to enable a smooth workflow, from the geometric design to the analysis and results, are developed and the potentials of parametrics in the design process, including multi-stage, nonlinear structural analysis, are revealed. The gained knowledge is consolidated in the plug-in Kiwi!3d for Rhino/Grasshopper, which allows for a smooth parametric design chain. The benefits and applicability of the extended isogeometric concept for real structures are demonstrated with several examples.

iii

Zusammenfassung

Der Entwurf leichter Tragwerke ist aufgrund des Wechselspiels zwischen Form und Kraft besonders anspruchsvoll. Formgebung und Mechanik können z. B. für Membranbauten und biegeaktive Strukturen nicht getrennt voneinander betrachtet werden. Die isogeometrische Analyse bietet die Möglichkeit das Entwurfs- und Analysemodel zu vereinen. Die Erstellung eines Polygonnetzes für die Strukturanalyse kann vermieden werden, indem die Parametrisierung mit Non-uniform Rational B-Splines (NURBS), welche für Computer-Aided-Design (CAD) üblich ist, auch im Analysemodell genutzt wird. Dies bietet einen immensen Vorteil im digitalen Entwurfsprozess von Leichtbaubaustrukturen, da mechanisches Feedback schon während der Geometrieerstellung möglich ist.

Diese Arbeit erweitert die bestehenden isogeometrischen Ansätze um eine durchgängige Entwurfskette zu gewährleisten. Hierfür werden zusätzliche, noch fehlende Kopplungsmethoden für individuelle Strukturelemente benötigt. Deswegen werden drei unterschiedliche Kopplungsmethoden vorgeschlagen. Die erste beschäftigt sich mit der Rotationskopplung von verschiebungsbasierten Elementformulierungen, wie z. B. Bernoullibalken. Die zweite Methodik integriert die Kopplung zweier Elemente durch eine implizite Geometriebeschreibung im Parameterraum. Das letzte Verfahren ermöglicht durch die Ausnutzung des NURBS-Parameterraumes die Einbeziehung von reibungslosen Gleitkontakt ohne die explizite Bestimmung der Kontaktflächen. Darüber hinaus wird eine Methode zur schnellen Formfindung von biegeaktiven Strukturen im Vorentwurf vorgestellt.

Leichte Tragwerke bestehen oftmals aus mehreren Bestandteilen, die in mehreren Schritten zusammengefügt werden, was wiederum die Einbeziehung des Bauablaufes in die Analyse erfordert. Dies kann eine große Herausforderung in der Simulation darstellen. Deswegen wird die Verkettung verschiedener Analysen untersucht und in CAD integriert. Die für einen von der Formgebung bis hin zur Simulation reibungslosen Arbeitsablauf notwendigen Bestandteile im Entwurf von nichtlinearen, mehrstufigen Prozessen werden beleuchtet und die Potentiale des parametrischen Modells aufgedeckt. Das gewonnene Wissen ist die Basis für das Plug-In Kiwi!3d für Rhino/Grasshopper, welches eine nahtlose Entwurfskette ermöglicht. Die Vorteile und die Anwendbarkeit der erweiterten isogeometrischen Methoden in der Praxis werden anhand mehrerer Beispiele gezeigt.

Acknowledgments

CONTENTS

Contents

LIST OF SYMBOLS

Greek letters

$\boldsymbol{\epsilon}$	Normal strain derived from Green-Lagrange strain tensor
$\boldsymbol{\kappa}$	Change in curvature derived from Green-Lagrange strain tensor
$\boldsymbol{\Lambda}$	Smallest-rotation mapping matrix
$\boldsymbol{\sigma}$	Cauchy stress tensor
$\alpha^{\text{disp}}, \alpha^{\text{rot}}$	Penalty factor for the displacement and the rotation, respectively
α, β	Indices that are either 1 or 2 for surfaces or 2 or 3 for curves
Γ	Boundary of the physical domain
$\delta \square$	Virtual entity of $\square$ in the Principle of Virtual Work
ϵ	Unspecified strain or axial strain of a beam derived from Green-Lagrange strain tensor
H	Knot vector in η-direction
η	Parameter for B-Splines or NURBS geometries
θ_i, θ^i	Co- and contravariant coordinates, respectively
κ	Curvature or strain w.r.t. bending or torsion of a beam derived from Green-Lagrange strain tensor
ν	Poisson's ratio
Ξ	Knot vector in ξ-direction
ξ	Parameter for B-Splines or NURBS geometries
$\bar{\xi}$	Parameter for B-Splines or NURBS curves within parameter space
σ	Unspecified stress
Ω	Physical domain

1

List of Symbols

Mathematical symbols and operators

$(\bullet) \otimes (\bullet)$	Dyadic product
$(\bullet) \cdot (\bullet)$	Inner product
$(\bullet) \times (\bullet)$	Cross product
$(\bullet) : (\bullet)$	Tensor product
$(\bullet)_{,i}$	Partial derivative w.r.t. a contravariant coordinate θ^i
$(\bullet)_r$	Partial derivative w.r.t. a discretization parameter u_r
$\det(\bullet)$	Determinant of $(\bullet)$
$(\bullet)^T$	Transpose of $(\bullet)$

Latin letters

$\varDelta\mathbf{u}$	Displacement increment
δW	Virtual work
$\mathbf{A}$	Metric tensor on a surface or curve
$\mathbf{A}_i, \mathbf{A}^i$	Co- and contravariant basis on a geometry, respectively
$\mathbf{B}, \mathbf{b}$	Body force in the reference or current configuration, respectively
$\mathbf{C}$	B-Spline or NURBS curve
$\overline{\mathbf{C}}$	B-Spline or NURBS curve in the parameter space
$\mathbf{E}$	Green-Lagrange strain tensor
$\mathbf{e}$	Euler-Almansi strain tensor
$\mathbf{e}_i$	Global or local orthonormal coordinate system
$\mathbf{F}$	Deformation gradient
$\mathbf{G}_i, \mathbf{G}^i$	Co- and contravariant basis in space, respectively
$\mathbf{I}$	Identity matrix/tensor
$\mathbf{K}$	Tangential stiffness matrix or curvature tensor
$\mathbf{P}$	Control point or 1st Piola-Kirchhoff stress tensor
$\overline{\mathbf{P}}$	Control point in the parameter space
$\mathbf{p}$	External force
$\mathbf{R}$	Residual force vector or rotation matrix
$\mathbf{S}$	B-Spline or NURBS surface or 2nd Piola Kirchhoff stress tensor
$\mathbf{S}_0$	Prestress as 2nd Piola Kirchhoff stress tensor

2

$\mathbf{T}, \mathbf{t}$	Normalized base vector or external force on the boundary in the reference or current configuration, respectively
$\mathbf{u}$	Displacement field
$\mathbf{u}_0$	Initial displacement
$\mathbf{X}, \mathbf{x}$	Geometry in the reference or current configuration, respectively
$\mathbf{X}_c$	Spatial point on a curve in the reference configuration
$\mathbf{X}_s$	Spatial point on a surface in the reference configuration
A	Area of a surface or cross section
A_{ij}, A^{ij}	Co- and contravariant metric coefficients, respectively
$B_{\alpha\beta}$	Covariant coefficients of the curvature tensor
E	Young's modulus
E_{ij}	Coefficients of the Green-Lagrange strain tensor
$\widetilde{E}_{ij}$	Coefficients of the Green-Lagrange strain tensor refering to a local Cartesian coordinate system
F	Force
h	Height
i, j	Indices that span from 1 to 3 if not otherwise defined
J	Jacobian used for different mapping operations
K_{rs}	$(r, s)^{\text{th}}$ component of the stiffness matrix
L, l	Length (of a curve element) in the reference or current configuration, respectively
M	(B-Spline) basis function in η-direction or moment
N	(B-Spline) basis function in ξ-direction or normal force in curve element
$n_\square$	Quantity of an entity $\square$
p, q	Polynomial degree in ξ- and η-direction, respectively
R	NURBS basis function or radius
R_r	r^{th} component of the residual force vector
$\widetilde{S}^{ij}$	Coefficients of the 2nd Piola Kirchhoff stress tensor refering to a local Cartesian coordinate system
t	Thickness
w	Control point weight or quadrature weight or deflection or width

List of Symbols

Abbreviations

B-Rep	Boundary Representation
BB	Bernoulli beam
CAD	Computer-Aided Design
CAE	Computer-Aided Engineering
DOF	Degree of Freedom
FEM	Finite Element Method
GL	Green-Lagrange strain measure
IGA	Isogeometric Analysis
KL	Kirchhoff-Love
NURBS	Non-Uniform Rational B-Splines
PK2	2nd Piola-Kirchhoff stress measure
TUM	Technische Universität München

INTRODUCTION AND MOTIVATION

Isogeometric analysis (IGA) as introduced by Hughes et al. [70] in 2005 has the aim of seamlessly linking the analysis, i.e. computer-aided engineering (CAE), into the design environment, i.e. computer-aided design (CAD). The main idea is to use the basis functions of the geometry also for the analysis. These basis functions are usually non-uniform rational B-Splines (NURBS), which are common in CAD. The choice of these basis functions removes the step of meshing, i.e. reparametrizing the geometry with classical analysis-inherent basis functions, from the design process of structural systems.

The potential of isogeometric analysis with finite element methods (FEM) and boundary element methods (BEM) were explored extensively and many element formulations for volumes, surfaces and curves, modeling a huge variety of structural aspects, emerged. Most of the researchers refer to problems in mechanical or biomedical engineering if an application case is shown. The potential of the method in construction engineering is often disregarded. Nonetheless, isogeometric analysis is in fact very suitable for this field. Every construction is unique. Consequently, the design process

Figure 1.1: *INSIDE/OUT* pavilion at the inner court of the
Technical University of Munich by Eike Schling.

becomes more important, since the structural system has to be conceptu-
alized, constructed, evaluated and verified for every single produced entity.
These complex systems, as for example shown in Figure 1.1, consist of
many structural members, which makes the assembly process particularly
important. Existing research on IGA in this context mainly focuses on the
coupling of surfaces. Construction engineering, on the contrary, requires
also curve-like elements, such as beams and cables, and therefore, also
coupling techniques for these elements are crucial.

Furthermore, smooth shapes, which are perfect for the simulation with IGA,
appear particularly often in lightweight design. Lightweight structures are
characterized by their substantial form and force interaction accompanied
by large deflections. The shape and the stress state are inseparable. These
delicate structures gain their stiffness by implying some initial internal
stresses. Deforming and connecting the structural members usually intro-
duce those stresses. Consequently, it is necessary to design and model the
structure including these stresses. Here, the direct possibility of integrating
structural analysis into CAD is a huge benefit, since direct structural feed-
back can be provided to the designer. It is usually not possible to directly
constitute the shape in lightweight design. Since the shape is a primary cri-
terion in the initial design phases, a parametric setup that allows testing of

several configurations in an automated manner is highly beneficial. Many modern CAD system already provide a parametric design environment for the conception of the geometry. However, generating the classical FEM model for the necessary structural feedback interrupts the tool chain. The results are provided in the CAE environment. The parametric geometry model is then manually adapted in order to meet the design criteria. IGA can remove the interruptions of this highly iterative process by including the structural analysis of the system into the parametric CAD environment using the same parametric description. Providing an enclosed, smooth design chain can speed up the process and enrich the design space.

This thesis will present several aspects of isogeometric analysis, which enable an efficient CAD-integrated design of lightweight structures. It has been organized in the following way.

CHAPTER 2 outlines typical sources of nonlinearity in structural systems. The essential components of structural analysis are reviewed. These are necessary for the implementation of an isogeometric design workflow including construction stages.

CHAPTER 3 presents the fundamentals of isogeometric analysis. This comprises the geometric description of NURBS as well as the geometry representation of common CAD programs, i.e. Boundary-Representation and Trimming. The chapter is completed with some special aspects of NURBS, which have to be taken into account while setting up a simulation.

CHAPTER 4 gives a brief overview of the isogeometric element formulations, which are implemented in the research FE code Carat++[1] and applied in the CAD-integrated analysis of the application examples.

CHAPTER 5 presents the findings of this doctoral research related to the coupling of structural elements with isogeometric analysis. After a short introduction to the topic, three different novel techniques and fields of application are proposed. The first one addresses the coupling of rotations focusing on the application with beams. The second one explains the approach of embedding entities inside the parameter domain of another NURBS patch, which corresponds to an implicit description of the coupling. Lastly, the two methods are combined in an innovative approach for sliding interfaces by explicitly describing the coupling condition and implicitly describing the geometry.

---

[1]   https://www.bgu.tum.de/st/software2/forschung/carat/

CHAPTER 6 investigates several important features of a fully CAD-integrated isogeometric workflow for the design of structures. This includes some aspects of pre- and post-processing as well as the potential of parametrics in CAD. Furthermore, it shows the possibilities of applying IGA in the design of lightweight structures. The design cycle of membrane structures is presented and an approach for fast design explorations of bending-active structures is proposed.

CHAPTER 7 demonstrates the applicability of isogeometric analysis for a holistic design process. The gathered showcases consist of academic examples, which are oriented towards real structural systems, and a built gridshell pavilion, where isogeometric analysis has already been involved in the design process.

CHAPTER 8 contains some conclusions of this thesis and suggests interesting future investigations and potential applications.

2

FUNDAMENTALS OF STRUCTURAL ANALYSIS

Lightweight structures are very delicate in their conception. Structural feedback needs to be generated in order to obtain a feasible design. In the past, physical mock-ups and trial-and-error were the main possibilities to generate the required information. Nowadays, it is much more common to digitally design the shape and compute the structural response. The ability to conduct a numerical structural analysis significantly sped up the design loops and enabled the study of a larger range of structural systems.

This chapter resumes the fundamentals of structural analysis. Because of the high form-force-interaction of lightweight structures, which are a main field of application of the proposed methods in this thesis, differential geometry plays a crucial part. Furthermore, large displacements and nonlinear behavior have to be considered.

2.1 Structural Mechanics

The following conventions hold for the whole thesis if not indicated differently. Capital letters denote entities in the undeformed configuration whereas lower-case characters are linked to the current configuration. Latin indices are typically in the set of $i \in \{1,2,3\}$ whereas for Greek indices it holds $\alpha \in \{1,2\}$ for surfaces and $\alpha \in \{2,3\}$ for curves. The partial derivative w.r.t. a variable x_i with index i is abbreviated by $\frac{\partial(\bullet)}{\partial x_i} = (\bullet)_{,i}$. This is typically used for the partial derivatives w.r.t. a convective coordinate θ^i or w.r.t. the degrees of freedom (DOFs) of an element u_r.

2.1.1 Nonlinearities

Nonlinearity in structural analysis means that the response of a system to an impact is not linearly correlated with the impact (see Figure 2.1). This behavior may originate from different sources which are described in the following sections.

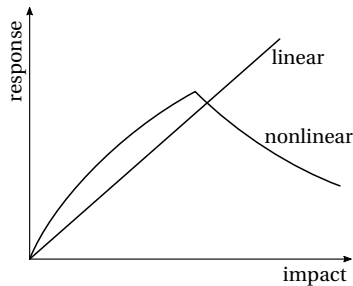**Figure 2.1:** Impact-response-diagram for linear and nonlinear behavior of a structural system.

Material Nonlinearity

Material nonlinearity means that the stress-strain relation is not constant. In simplified computations, linear elastic materials are often used (see Figure 2.2(a)). A double strain implies a double stress response in the structure. The relation can be described by the Young's modulus E, which

is the slope in the stress-strain diagram. Nonlinear elastic material (see Figure 2.2(b)) removes the linear dependency between stress σ and strain ϵ. However, one strain value is related to one stress value. Plasticity is an additional source of nonlinearity. The material behaves like an elastic material in the beginning. If a certain stress level σ_y is reached, the stresses do not correlate linearly to the strains anymore. An ideal elasto-plastic material (see Figure 2.2(c)) does not increase the stresses after the yielding level is reached, i.e. the structure deforms further without increasing the load. Elastic behavior is observed while unloading and reloading up to the yield strength. Therefore, a strain value is not directly linked to one stress value. The loading history has to be incorporated into the model. Figure 2.2(d) shows the stress-strain relation for an elasto-plastic material without idealizing the yielding zone. Further loading is needed in order to increase the strains also after reaching the yield stress. Un- and reloading also induces elastic behavior which in return implies that the loading history is needed for the correct modeling of the material.

These are only a few of many existing material models. Other factors like temperature, strain-rate, damage or time could also be considered in the constitutive law.

Geometric Nonlinearity

For a geometrically linear system, the equilibrium equation is set up only once and all stiffnesses and forces can be computed with the initial local coordinate systems. In consequence, strains and stresses are linearly dependent on the nodal displacement since the stiffness matrix does not change. This solution strategy is typically valid and applied if the displacements are small. Geometric nonlinearity by contrast requires an update of the equilibrium equations during the analysis because stresses and forces may change their direction and amplitude.

The difference between linear and geometrically nonlinear analysis is illustrated in Figure 2.3. It shows the undeformed and deformed configuration of a truss system with length L and l, respectively. The elongation ΔL of the trusses is measured in the direction of the initial truss for a linear approach. A doubled deformation u results in a doubled elongation. The nonlinear approach compares the total lengths of the trusses in both configurations. The different elongation measures are also reflected in the
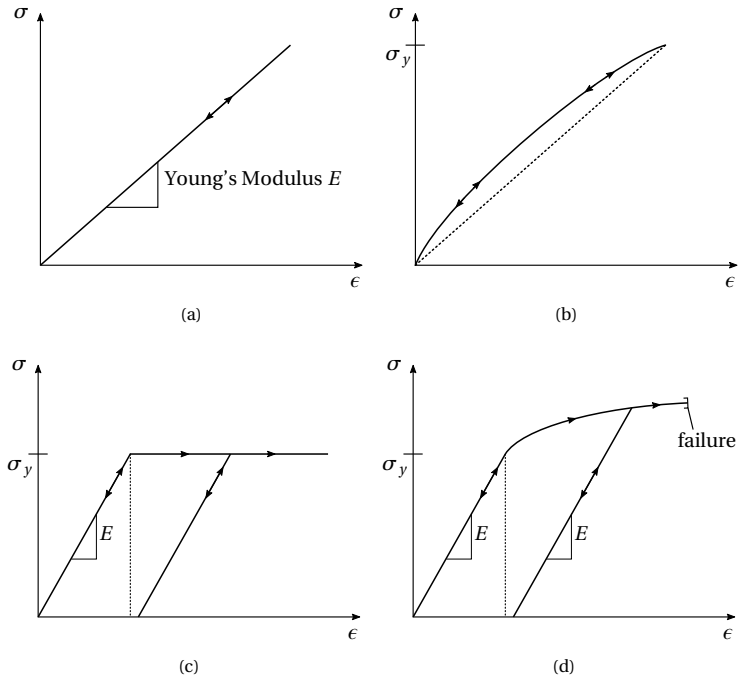
Figure 2.2: Stress-strain-diagram for: (a) linear elastic material, (b) nonlinear elastic material, (c) ideal elasto-plastic material and (d) elasto-plastic material.

emerging stresses and forces N in Figure 2.3. Lastly, the location and the orientation of the equilibrium computation differ. For the given system in Figure 2.3, the linear and the geometrically nonlinear approach result in different loads, which are required to obtain the displacement u.

Constraint and Contact Nonlinearity

Nonlinearity in a system can also occur as a result of changing boundary conditions. Contact problems are a common example. The structural behavior of the system changes when two bodies collide. The contact areas of the bodies with each other or the boundaries have to be detected and

Figure 2.3: Equilibrium determination for the geometrically (a) linear and (b) nonlinear case.

resolved by adding additional constraints. Note that the structural element formulation does not change. Penalty methods or Lagrange methods are often used to enforce the constraint.

In this thesis, nonlinearities related to changing contact constraints, which are directly detected during the simulation, are not considered. However, controlled contact scenarios or changes of the boundary conditions, occurring for e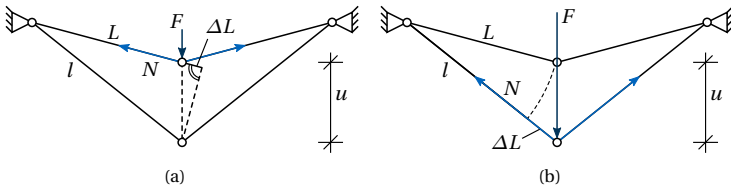xample in an assembly process, can be represented by several stages of analysis and a correct linking of those (see Section 2.2). Figure 2.4 shows such an assembly process. A beam is bent into a loop using two cables in order to align the ends. The system can only bend in one direction. Once the beam ends are connected and aligned, the cables are removed and a clamped support is applied to the beam ends. Furthermore, another cable is added to the middle of the beam, which pulls the top out-of-plane towards another support.

In addition to the modeling of assembly processes, an approach for sliding contact using the beneficial properties of NURBS will be elaborated in Section 5.5.

2.1.2 Structural Modeling

Real structures are always volumes. However, common procedure is to perform a reduction of dimensions for surface- and curve-like elements, such as shells and beams, in order to reduce the degrees of freedom and computational costs. Geometric assumptions are made for the reduced dimensions, which are usually much smaller than the remaining dimensions, i.e. $t \ll L_1, L_2$ or $h, w \ll L$ (see Figure 2.5). The dimensional reduction is, if
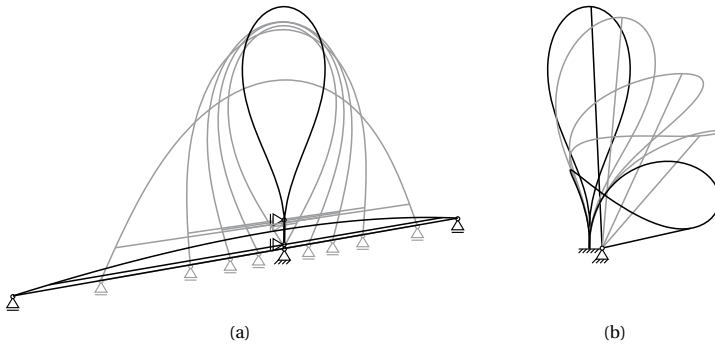
(a)   (b)

Figure 2.4:   Constraint nonlinearity of an assembly process: (a)
in-plane-bending of a beam to a loop with aligned ends with
contracting cables and (b) out-of-plane-bending with different
boundary conditions and structural elements towards another
support by another contracting cable.

necessary, preceded by a homogenization of the material. Furthermore, it
is common to use the mid surface or center line for the reduction. The re-
duced entities are then described by the parametric geometry description
and the missing dimensions for the volume are derived from the reduced
geometry. This means e.g. that a surface-like structural element will be
described by its mid surface and a vector that is dependent on the paramet-
ric description of the mid surface, e.g. the surface normal, represents the
thickness. In the case of a curve, a frame that represents the cross section
of the line-like element describes the reduced dimensions.

2.1.3   Differential Geometry

A large portion of this thesis is strongly related to geometry. Therefore,
this section gives a brief overview of differential geometry in its different
dimensions. The reader is referred to Başar et al. [6], Klingbeil [77], and
Pottmann [108] for more details.

Geometry can be described in an explicit, implicit or parametric way. The
parametric description will be pursued in more depth since it is the most
general and flexible approach. A set of curvilinear coordinates θ^i describes
the geometrical entity. The number of those parameter lines is equal to the

(a)

(b)
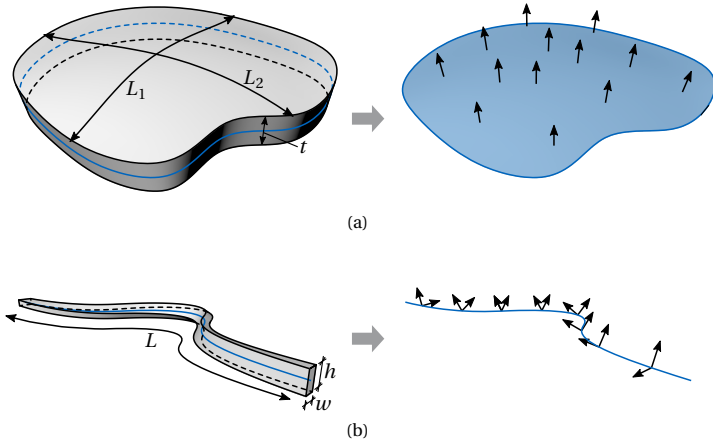
Figure 2.5: Dimensional reduction with base vectors of a (a) surface-like and (b) curve-like volume.

dimension of the geometric object. A curve has one parameter whereas a surface has two and a volume three. Functions that generate the coordinates x^j in a given coordinate system map these parameters into space (see Figure 2.6). In Euclidean space, the Cartesian coordinate system is defined by the static orthonormal base vectors $\mathbf{e}_j$.

$$\left(\theta^1, \theta^2, \theta^3\right) \mapsto \mathbf{X}\left(\theta^1, \theta^2, \theta^3\right) = X^j\left(\theta^1, \theta^2, \theta^3\right)\mathbf{e}_j \tag{2.1}$$

A curvilinear local coordinate system is beneficial for describing local properties of a geometry. The covariant base vectors $\mathbf{G}_i$ are derived by partial differentiation of the position vector w.r.t. geometry parameters, i.e. the curvilinear coordinates:

$$\mathbf{G}_i = \frac{\partial \mathbf{X}}{\partial \theta^i} = \mathbf{X}_{,i} \tag{2.2}$$
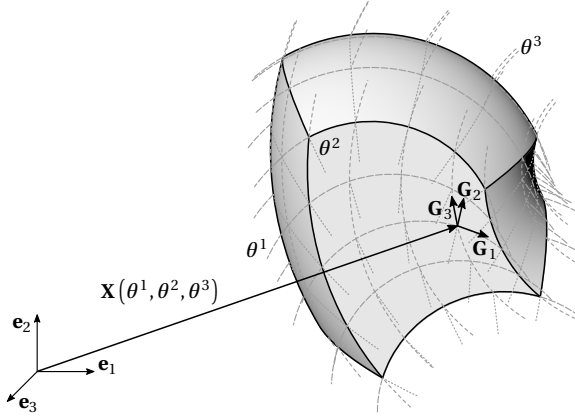
Figure 2.6: Volume with curvilinear coordinate system and base vectors.

The corresponding contravariant basis $\mathbf{G}^i$ is defined by the following condition.

$$\mathbf{G}^i \cdot \mathbf{G}_j = \delta^i_j = \begin{cases} 1 & \text{for } i = j \\ 0 & \text{for } i \neq j \end{cases} \tag{2.3}$$

The metric coefficients are computed by a scalar product.

$$G_{ij} = \mathbf{G}_i \cdot \mathbf{G}_j \qquad \text{and} \qquad G^{ij} = \mathbf{G}^i \cdot \mathbf{G}^j \tag{2.4}$$

The metric is used to transform the base vectors into the other coordinate system

$$\mathbf{G}^i = G^{ij} \mathbf{G}_j \qquad \text{and} \qquad \mathbf{G}_i = G_{ij} \mathbf{G}^j \tag{2.5}$$

The metric tensor $\mathbf{G}$ is defined as

$$\mathbf{G} = G_{ij} \mathbf{G}^i \otimes \mathbf{G}^j = G^{ij} \mathbf{G}_i \otimes \mathbf{G}_j \tag{2.6}$$

The relation between the metric coefficients is given by

$$\left[G^{ij} \right] = \left[G_{ij} \right]^{-1} \tag{2.7}$$
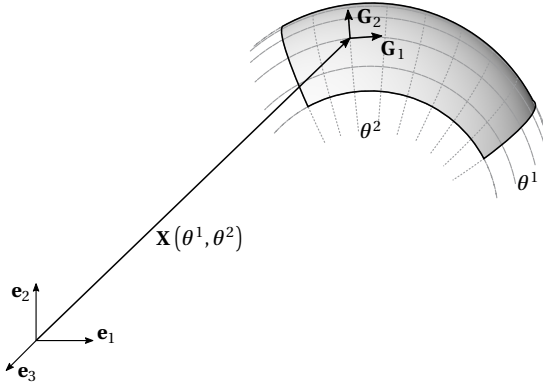
Figure 2.7: Surface with curvilinear coordinate system and base vectors.

Differential Geometry of Surfaces

A surface can be described as a volume for which one curvilinear coordinate is constant, e.g. $\theta^3 = 0$ (see Figure 2.7). The position vector is then only depending on two parameters.

$$\mathbf{X} = \mathbf{X}\left(\theta^1, \theta^2\right) = X^j\left(\theta^1, \theta^2\right)\mathbf{e}_j \tag{2.8}$$

In the following chapters of the thesis, base vectors w.r.t. the continuum will be denoted with $\mathbf{G}_i$, whereas base vectors w.r.t. the dimensionally reduced entity will be denoted with $\mathbf{A}_i$. The Equations (2.2) - (2.7) also hold for the differential geometry of surfaces. However, some additional geometric properties can be evaluated. In order to do so, the surface normal is needed. The vectors $\mathbf{A}_1$ and $\mathbf{A}_2$ are the tangent vectors of the surface and can be used to compute the normal. The normalized surface normal also defines the third base vector.

$$\mathbf{A}_3 = \frac{\mathbf{A}_1 \times \mathbf{A}_2}{\|\mathbf{A}_1 \times \mathbf{A}_2\|_2} \tag{2.9}$$

In this case, the covariant and contravariant third base vector coincide.

$$\mathbf{A}^3 = \mathbf{A}_3 \tag{2.10}$$
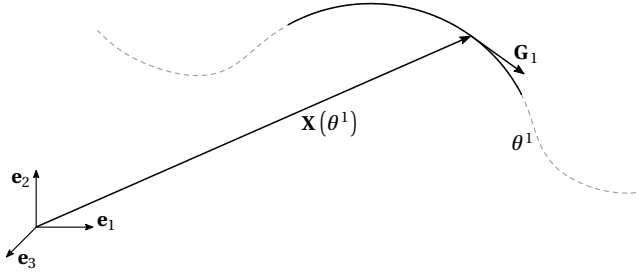
Figure 2.8: Curve with curvilinear coordinate and base vector.

The curvature of a surface is an important property and is defined by the curvature tensor

$$\mathbf{K} = B_{\alpha\beta}\mathbf{A}^{\alpha} \otimes \mathbf{A}^{\beta} = B^{\alpha\beta}\mathbf{A}_{\alpha} \otimes \mathbf{A}_{\beta} \tag{2.11}$$

where $B_{\alpha\beta}$ is the second fundamental form of the surface defined as:

$$B_{\alpha\beta} = B_{\beta\alpha} = -\mathbf{A}_{\alpha} \cdot \mathbf{A}_{3,\beta} = \mathbf{A}_{\alpha,\beta} \cdot \mathbf{A}_{3} \tag{2.12}$$

More details can be found in Başar et al. [6] and Klingbeil [77].

Differential Geometry of Curves

Fixating another coordinate in Equation (2.8) to a constant value further reduces the geometry. A parametric curve is resulting (see Figure 2.8).

$$\mathbf{X} = \mathbf{X}(\theta^{1}) = X^{j}(\theta^{1})\mathbf{e}_{j} \tag{2.13}$$

Similar to the surface, additional geometric properties might be of interest. Therefore, a so-called frame is needed. Many ways are possible to define a frame for a curve. One of the most common is the orthonormal Frenet-Serret base. It is defined by the tangent **T**, the binormal **B** and the normal
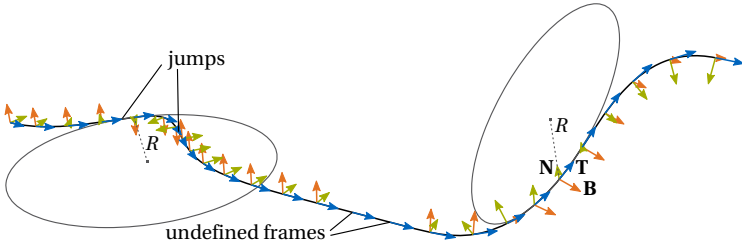
Figure 2.9: Curve with Frenet-Serret frames including jumps and undefined behavior at straight segments.

N (see Figure 2.9).

$$\mathbf{T} = \frac{\mathbf{A}_1}{\|\mathbf{A}_1\|_2} \tag{2.14}$$

$$\mathbf{B} = \frac{\mathbf{A}_1 \times \mathbf{A}_{1,1}}{\|\mathbf{A}_1 \times \mathbf{A}_{1,1}\|_2} \tag{2.15}$$

$$\mathbf{N} = \mathbf{B} \times \mathbf{T} \tag{2.16}$$

The corresponding circle of the maximum curvature lies in the plane, which has the binormal **B** as its normal. The normal **N** is pointing towards the center of the circle.

Important features like the curvature κ and torsion τ can be evaluated.

$$\kappa = \frac{\|\mathbf{A}_1 \times \mathbf{A}_{1,1}\|_2}{\|\mathbf{A}_1\|_2^{\,3}} \tag{2.17}$$

$$\tau = \frac{\left(\mathbf{A}_1 \times \mathbf{A}_{1,1}\right) \cdot \mathbf{A}_{1,1,1}}{\|\mathbf{A}_1 \times \mathbf{A}_{1,1}\|_2^{\,2}} \tag{2.18}$$

Although very common, this basis has two problems (cf. Figure 2.9). First of, **B** and **N** are undefined for a straight curve. Furthermore, sudden jumps in the frame are possible, which might be problematic for the description of the continuum.

Hence, another frame, namely the Bishop Frame (see Bishop [22]), is often used. It requires an initial frame at the beginning of the curve. This frame

Figure 2.10: Curve with Bishop frames.

is then moved along the curve such that the torsion τ of the frame around the curve is minimal (see Figure 2.10).
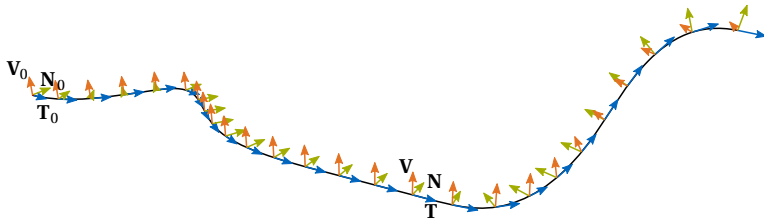
$$\min \int_L \tau(\theta^1) \mathrm{d}\theta^1 \tag{2.19}$$

The smallest-rotation-mapping is another possibility for the definition of curve frames. It maps an initial frame from one point to all other points of a curve. The starting point is often used for the initial frame, but it is not restricted to it. In contrast to the Bishop frame, the orientation of the frame at an arbitrary point on the curve can be determined directly and it is not necessary to perform an integral over the arc length in-between the actual point and the initial frame. The mapping matrix Λ is defined using the Rodrigues' rotation formula. The rotation is defined by an axis $\hat{\mathbf{e}}$ and an angle ϕ.

$$\mathbf{R} = \hat{\mathbf{e}} \otimes \hat{\mathbf{e}} + \cos\phi\,(\mathbf{I} - \hat{\mathbf{e}} \otimes \hat{\mathbf{e}}) + \sin\phi\,(\hat{\mathbf{e}} \times \mathbf{I}) \tag{2.20}$$

The axis is defined by the cross product of the normalized tangents $\mathbf{T}_0$ and $\mathbf{T}$ of the curve at the point of the initial frame and the point, where the frame has to be computed. The corresponding angle is defined by the angle between those two tangents.

$$\hat{\mathbf{e}} = \frac{\mathbf{T}_0 \times \mathbf{T}}{\|\mathbf{T}_0 \times \mathbf{T}\|_2} \qquad \cos\phi = \mathbf{T}_0 \cdot \mathbf{T} \qquad \sin\phi = \|\mathbf{T}_0 \times \mathbf{T}\|_2 \tag{2.21}$$
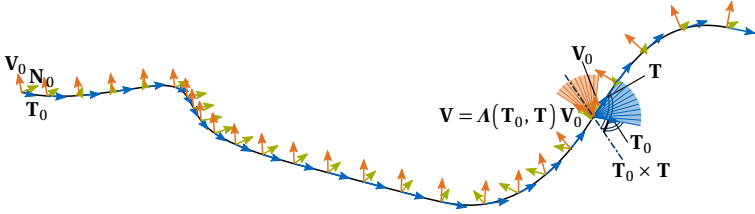
Figure 2.11: Curve with frames constructed by smallest-rotation-mapping.

Inserting those quantities into Equation (2.20) including some rearrangements results in the following mapping matrix $\boldsymbol{\Lambda}$ for the initial frame.

$$\boldsymbol{\Lambda}\big(\mathbf{T}_0, \mathbf{T}\big) = \big(\mathbf{T}_0 \cdot \mathbf{T}\big)\mathbf{I} + \big(\mathbf{T}_0 \times \mathbf{T}\big) \times \mathbf{I} + \frac{1}{1 + \mathbf{T}_0 \cdot \mathbf{T}}\big(\mathbf{T}_0 \times \mathbf{T}\big) \otimes \big(\mathbf{T}_0 \times \mathbf{T}\big)$$

$$(2.22)$$

Applying this rotation to the initial frame results in the frame at the actual point:

$$\mathbf{N} = \boldsymbol{\Lambda}\big(\mathbf{T}_0, \mathbf{T}\big)\mathbf{N}_0 \qquad \text{and} \qquad \mathbf{V} = \boldsymbol{\Lambda}\big(\mathbf{T}_0, \mathbf{T}\big)\mathbf{V}_0 \qquad (2.23)$$

A curve with frames constructed by this mapping operation is shown in Figure 2.11. The mapping is undefined for $\mathbf{T} = -\mathbf{T}_0$ since the denominator in Equation (2.22) becomes zero. An exception can be added for this case.

2.1.4 Kinematics

The deformation gradient $\mathbf{F}$ is used to described the relation between the current configuration $\mathbf{x}$ and the reference configuration $\mathbf{X}$ as shown in Figure 2.12.

$$\mathbf{F} = \frac{\partial \mathbf{x}}{\partial \mathbf{X}} = \mathbf{g}_i \otimes \mathbf{G}^i \qquad (2.24)$$

Figure 2.12: Reference and current configuration of a domain.
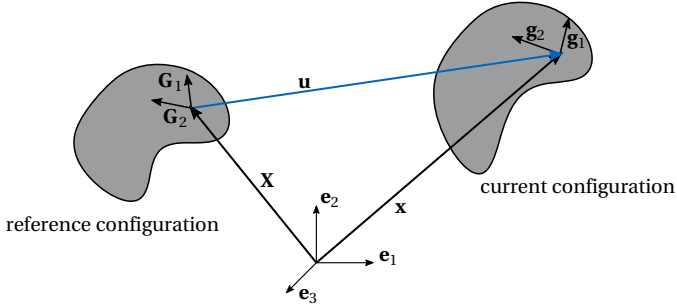
The Green-Lagrange (GL) strains $\mathbf{E}$ are used in this thesis to derive the element formulations and to set up the equilibrium.

$$\mathbf{E} = \frac{1}{2}\left(\mathbf{F}^T \cdot \mathbf{F} - \mathbf{I}\right) = E_{ij}\,\mathbf{G}^i \otimes \mathbf{G}^j = \frac{1}{2}\left(g_{ij} - G_{ij}\right)\mathbf{G}^i \otimes \mathbf{G}^j \qquad (2.25)$$

where $\mathbf{I}$ is the identity tensor. The GL strains express the distortion w.r.t. the reference configuration. The coefficients E_{ij} are determined by half the difference between the metrics g_{ij} and G_{ij}.

The counterpart of the GL strain in the current configuration is the Euler-Almansi strain tensor $\mathbf{e}$.

$$\mathbf{e} = \frac{1}{2}\left(\mathbf{I} - \mathbf{F}^{-T} \cdot \mathbf{F}^{-1}\right) = e_{ij}\mathbf{g}^i \otimes \mathbf{g}^j = \frac{1}{2}\left(g_{ij} - G_{ij}\right)\mathbf{g}^i \otimes \mathbf{g}^j \qquad (2.26)$$

The coefficients e_{ij} are equal to the ones from the GL strain tensor $e_{ij} = E_{ij}$.

2.1.5 Constitutive Law and Stresses

Every strain measure has its energetically conjugated stress measure. The second Piola-Kirchhoff (PK2) stresses $\mathbf{S}$ relate to the Green-Lagrange strains $\mathbf{E}$ as

$$\mathbf{S} = \mathbb{C} : \mathbf{E} \qquad (2.27)$$

The fourth order elasticity tensor $\mathbb{C}$, which is given in the curvilinear coordinate system, links strains and stresses (see Equation (2.28)). Throughout

this thesis linear St. Venant-Kirchhoff material will be used and thus a time and path independent linearization can be used.

$$\mathbb{C} = C^{ijkl}\, \mathbf{G}_i \otimes \mathbf{G}_j \otimes \mathbf{G}_k \otimes \mathbf{G}_l \tag{2.28}$$

The Cauchy stresses $\boldsymbol{\sigma}$ are related to the Euler-Almansi strains $\mathbf{e}$, which refer to the current configuration.

$$\boldsymbol{\sigma} = \sigma^{ij}\mathbf{g}_i \otimes \mathbf{g}_j \tag{2.29}$$

They can also be computed from the PK2 stresses due to the assumed linear relation between stress and strain.

$$\boldsymbol{\sigma} = \frac{1}{\det \mathbf{F}}\, \mathbf{F} \cdot \mathbf{S} \cdot \mathbf{F}^{T} \tag{2.30}$$

The first Piola-Kirchhoff stresses $\mathbf{P}$ are another stress measure. They refer to both the current and the reference configuration and can be computed from the other introduced stress tensors.

$$\mathbf{P} = \det\mathbf{F} \cdot \boldsymbol{\sigma} \cdot \mathbf{F}^{-T} = \mathbf{F} \cdot \mathbf{S} = P^{ij}\mathbf{g}_i \otimes \mathbf{G}_j \tag{2.31}$$

The constitutive law is often given in the local Cartesian coordinate system for standard materials. If this is the case, the strains have to be transferred from the curvilinear local coordinate system to a local Cartesian one.

2.1.6 Equilibrium

The strong form of the static equilibrium is defined in the deformed state. Internal stresses $\boldsymbol{\sigma}$ and external body forces $\mathbf{b}$ have to be in equilibrium inside the domain. On the boundary Γ_D, the Dirichlet boundary conditions have to be fulfilled, i.e. the displacement $\mathbf{u}$ has to be equivalent to the predefined displacements $\hat{\mathbf{u}}$. The Neumann boundary conditions are described on Γ_N by the balance of the internal forces with the external forces $\mathbf{t}$ on the boundary (cf. Figure 2.13).

$$\text{div}\boldsymbol{\sigma} + \mathbf{b} = 0 \tag{2.32}$$

$$\mathbf{u} = \hat{\mathbf{u}} \qquad \text{on } \Gamma_{\text{D}} \tag{2.33}$$

$$\mathbf{n}\boldsymbol{\sigma} = \mathbf{t} \qquad \text{on } \Gamma_{\text{N}} \tag{2.34}$$
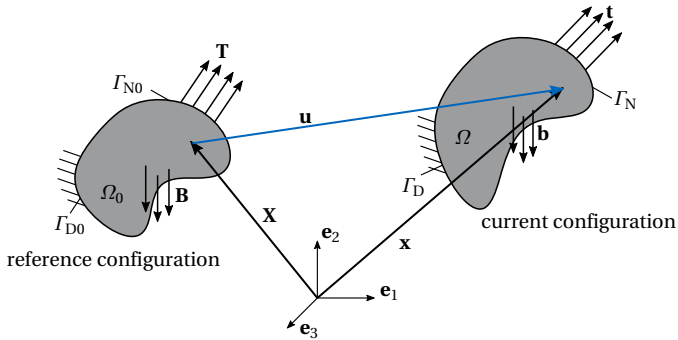
Figure 2.13: Structural domain in the undeformed and deformed configuration.

The Principle of Virtual Work is used in order to derive the weak form of the equilibrium. The equilibrium equations are then only fulfilled in an integral sense (see Wunderlich et al. [132]). The total virtual work δW is composed by the work of the internal and external forces.

$$\delta W = \delta W_{\text{int}} + \delta W_{\text{ext}} = 0 \tag{2.35}$$

$$\text{with } \delta W_{\text{int}} = -\int_{\Omega_0} \mathbf{S} : \delta \mathbf{E} \, \mathrm{d}\Omega \qquad \text{and} \tag{2.36}$$

$$\delta W_{\text{ext}} = \int_{\Gamma_{\text{N0}}} \mathbf{T} : \delta \mathbf{u} \, \mathrm{d}\Gamma + \int_{\Omega_0} \rho_0 \mathbf{B} : \delta \mathbf{u} \, \mathrm{d}\Omega \,, \tag{2.37}$$

where Ω_0 describes the domain and Γ_0 the boundary in the undeformed state. The external forces on the boundary Γ_{N0} are denoted as $\mathbf{T}$. Note that PK2 stresses are not physical. However, describing the potential fully within the reference configuration has some advantages as the domain, which has to be integrated, is known. Furthermore, every increment in an incremental analysis refers to the same configuration, which in return implies that the solving of the increment can be separated from the already known stress-strain state.

2.2   Sequenced Simulation Process

Complex erection processes often require to incorporate several analysis steps. The structural systems of the different stages may alternate w.r.t. structural members and boundary conditions. This design process makes it necessary to interrupt the analysis, add the required modifications and restart the analysis considering the previous analysis steps, i.e. stresses and strains.

Dieringer et al. [42] discussed two methods, namely the *InitDisp* and *Init-Stress* method, for transferring results from one simulation to another one in a Total Lagrangian framework.

The first analysis step is the same for both approaches. The Principle of Virtual Work is used to compute the equilibrium state:

$$\delta W_{\text{int}} = -\int_{\Omega_0} \mathbf{S}(\mathbf{u}) : \delta \mathbf{E}(\mathbf{u}) \, \mathrm{d}\Omega \,, \tag{2.38}$$

$$\delta W_{\text{ext}} = \int_{\Gamma_{\text{N0}}} \mathbf{T} : \delta \mathbf{u} \, \mathrm{d}\Gamma + \int_{\Omega_0} \rho_0 \mathbf{B} : \delta \mathbf{u} \, \mathrm{d}\Omega \,, \tag{2.39}$$

The difference appears in the consecutive analysis. The *InitDisp* approach uses basically the same expression as Equation (2.38) and (2.39) for the computation of the equilibrium, starting to look for the equilibrium with the solver at the previously computed displacement. These displacements can be seen as initial displacements $\mathbf{u}_0$. Stresses and strains still refer to the initial configuration and the integrals for the virtual work are performed on the same domain as in the previous steps.

$$\delta W_{\text{int}} = -\int_{\Omega_0} \mathbf{S} \overbrace{\left(\mathbf{u}_0 + \Delta\mathbf{u}\right)}^{\mathbf{u}} : \delta \mathbf{E}(\mathbf{u}) \, \mathrm{d}\Omega \,, \tag{2.40}$$

$$\delta W_{\text{ext}} = \int_{\Gamma_{\text{N0}}} \mathbf{T} : \delta \mathbf{u} \, \mathrm{d}\Gamma + \int_{\Omega_0} \rho_0 \mathbf{B} : \delta \mathbf{u} \, \mathrm{d}\Omega \tag{2.41}$$

New boundary conditions, which are defined in the deformed configuration of the first analysis, can easily be transferred to the reference configuration for the integration due to the parametric geometry description.

The *InitStress* method updates the geometry by the deformed geometry of the first analysis, i.e. a new reference configuration is established in the
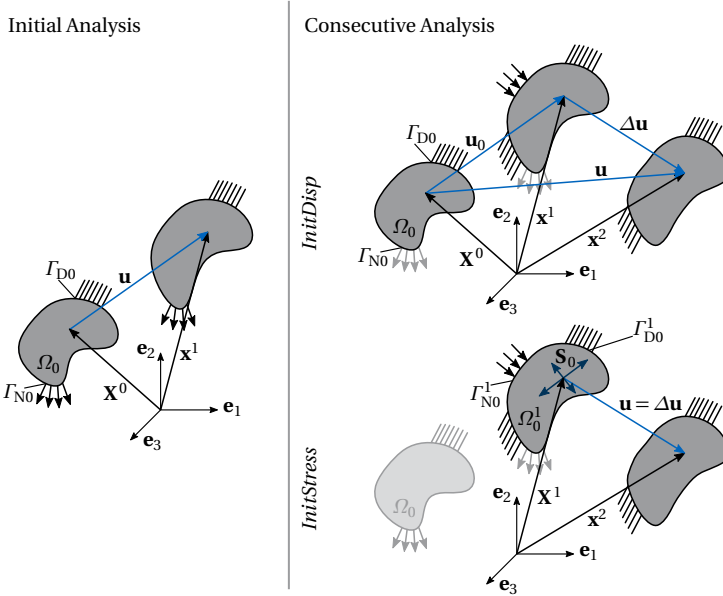
Figure 2.14: Definition of the displacement, the reference **X** and deformed **x** configuration for the *InitDisp* and *InitStress* approach.

consecutive analysis. The resulting stresses of the previous analysis are applied as initial stresses $\mathbf{S}_0$, i.e. prestresses.

$$\delta W_{\text{int}} = - \int_{\Omega_0^1} \Big(\mathbf{S}_0 \big(\mathbf{u}_0 \big) + \mathbf{S} \left(\Delta \mathbf{u} \right) \Big) : \delta \mathbf{E} \left(\Delta \mathbf{u} \right) \, \mathrm{d}\Omega \,, \tag{2.42}$$

$$\delta W_{\text{ext}} = \int_{\Gamma_{\text{N0}}^1} \mathbf{t} : \delta \left(\Delta \mathbf{u} \right) \, \mathrm{d}\Gamma + \int_{\Omega_0^1} \rho_1 \mathbf{b} : \delta \left(\Delta \mathbf{u} \right) \, \mathrm{d}\Omega \,, \tag{2.43}$$

The methods are visualized in Figure 2.14. The difference of the approaches can clearly be seen in how the displacement **u** is defined and which configuration is set as reference.

The *InitDisp* approach may be inconvenient since the nodes of the initial meshes sometimes do not coincide for coupled structures. This is for example the case if the first deformed part of the structure is used to derive

the second part. Then the initial meshes do not match. The *InitStress* approach only provides an approximation of the structural behavior in the consecutive analysis and is therefore examined for its general applicability.

The two methods are compared for a simple membrane strip, which is tensioned by a line load (see Figure 2.15). Each method provides the correct equilibrium in the second simulation as long as the load level stays the same. However, if the boundary conditions, here the load level λ, change, the equilibrium matches the reference solution only for the *InitDisp* method. The system computed with the *InitStress* method behaves softer for an increased load and unloading does not result in the initial unstressed patch but a much smaller one.
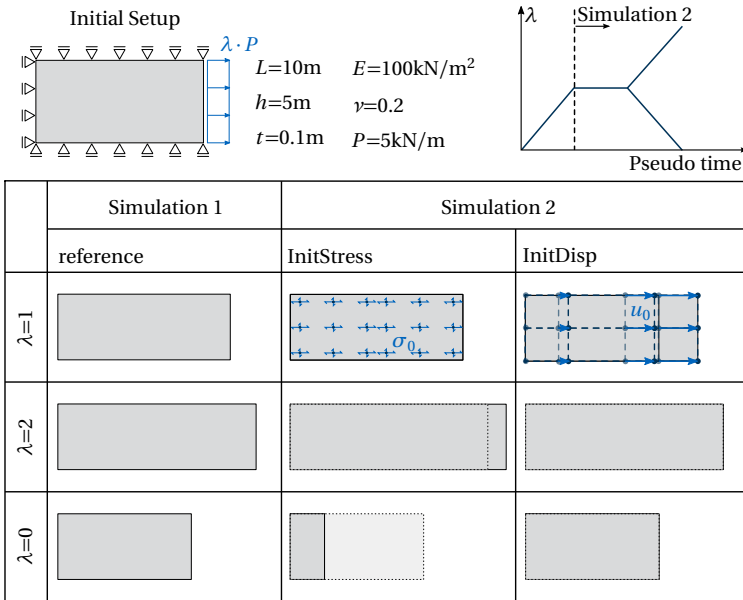

Figure 2.15: Comparison of the two methods *InitStress* and *InitDisp* for simulating staged construction. Note that the computation was carried out with better refinement, *i.e.* more Gauss points and control points, than illustrated. The reference solution is added for simulation 2 with dotted lines (adapted from Bauer et al. [14]).

The problem can also be illustrated analytically with a simple truss example, which is supported on one end and loaded by a single force $\lambda \cdot P$ on the other (see Figure 2.16). The equilibrium condition can be determined analytically for $\nu = 0.0$:

$$\lambda \cdot P = N = EA \cdot \epsilon_{GL} \cdot \frac{l}{L} = EA \cdot \frac{(l^2 - L^2) \cdot l}{2L^3}, \tag{2.44}$$

where the Green-Lagrange strain is denoted by ϵ_{GL} in derogation from **E**, which is used in the rest of the thesis, for the sake of readability. The mapping $\frac{l}{L}$ is needed in order to obtain a physical normal force N.

By splitting the loading into several load steps, the equilibrium condition for the i-th step can be rewritten using the *InitStress* method as follows:

$$\lambda^{(i)} \cdot P = N_0^{(i)} + \Delta N^{(i)} = \left(\lambda^{(i-1)} \cdot P + EA \cdot \frac{l^{(i)^2} - L^{(i)^2}}{2L^{(i)^2}} \right) \cdot \frac{l^{(i)}}{L^{(i)}} \tag{2.45}$$

with $L^{(i)} = l^{(i-1)}$

The geometry is updated to $L^{(i)} = l^{(i-1)}$ in every step i and the previous stress state $N^{(i-1)}$ is implied as prestress $N_0^{(i)}$ to the structure. The missing forces $\Delta N^{(i)}$ required to balance the external forces are generated by the deformation with respect to the equilibrium shape in the previous step. This equation can be solved for $l^{(i)}$ in order to get the necessary deformation. Or in the case of displacement control, the needed force in order to arrive at the given elongation is computed. This is reiterated until the necessary loading level is reached.

The introduced error for one step decreases if the deformation of the individual step is small. Whether splitting the deformation in many small steps results in a reduced total error is investigated in the following. The previously described truss should be elongated by a fixed value $\hat{u}$ and the corresponding load level is computed. The elongation is split in n equal load steps, where the load level $\lambda^{(i)}$ is determined in every step and applied as prestress in the following step.

Figure 2.16 shows the relative error of the final load level for different elongations $\frac{\hat{u}}{L}$ applied by one to a hundred steps. The analytic solution of applying the displacement in one step is taken as reference solution. Note that the equilibrium of all steps is computed exactly and is not numerically approximated. Hence, the emerging error is fully attributed to

the methodological setup of the *InitStress* approach. If the elongation is applied in more steps, the error of the final load level becomes larger even though the error in every single step is becoming smaller. Consequently, this method can only be applied for very small deformations where the error stays in a certain range. An elongation of 10% introduces an error of up to 13% which is usually not acceptable but cannot be avoided by using many updating steps. If only a small elongation, e.g. 0.1%, is applied, the error is around 0.15% which may be tolerable for certain applications.
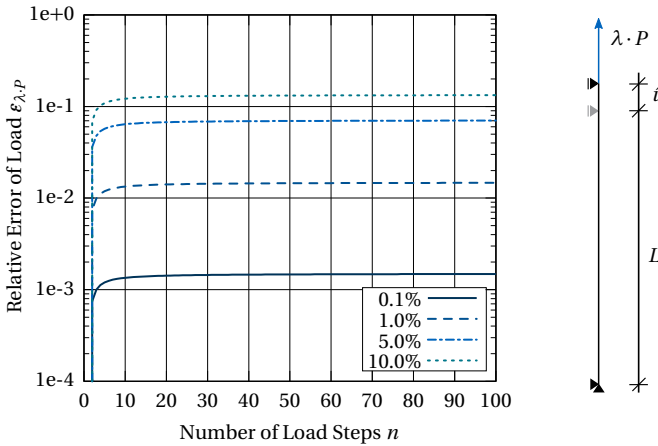

Figure 2.16: Relative error of the load, which is needed to elongate the truss within n steps for several final elongations $\frac{\hat{u}}{L}$.

Figure 2.16 shows also that the error accumulates and that fewer steps provide better accuracy. The error potential of two steps, i.e. only one update of the reference configuration, is investigated in the following since this is a typical application case. Figure 2.17 compares the relative error of the final load level of the truss when applying the final displacement in two steps, where the percentage k of the first displacement w.r.t. the total displacement $\hat{u}$ is varied. The error is maximal for equal load steps and minimal if one load steps is much larger than the other. If the coupling of non-matching nodes massively interrupts the workflow as described in Dieringer et al. [42] and Dieringer [43] or at least one deformation is very small, the *InitStress* method might be applicable despite the introduced

error. However, this thesis will only apply the *InitDisp* method for transferring analysis results to further simulations since it models the correct structural behavior. The effort of storing the initial displacements in the isogeometric workflow is less computationally expensive than tracking the stress history of each integration point. First of all, there are in general many more integration points than control points, i.e. FE nodes, and secondly, the coupling of patches is generally accomplished by weak coupling and not by directly imposing coupling conditions on the nodes.
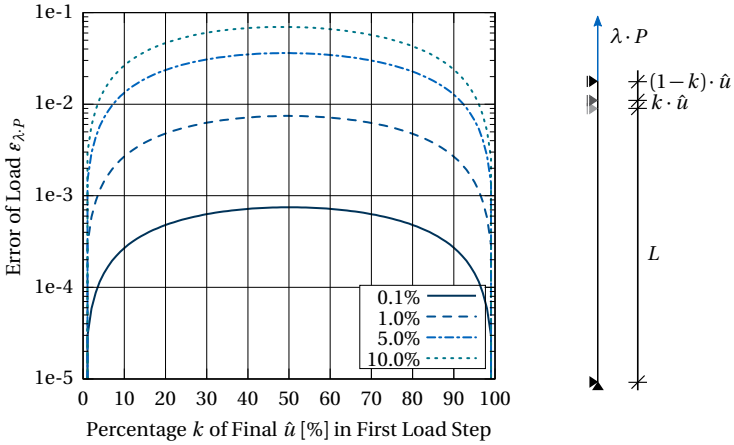

Figure 2.17: Relative error of the load needed to elongate the truss within two steps for several final elongations $\frac{\hat{u}}{L}$ plotted against the relative displacement in the first step.

3

FUNDAMENTALS OF ISOGEOMETRIC ANALYSIS (IGA)

Isogeometric Analysis distinguishes itself from classical finite element analysis by the applied basis functions. CAD-related splines and other description techniques are used instead of (linear) polynomials. The isogeometric concept is conform to the isoparametric one of FEM since the same basis functions are used for the geometry description and the solution field. Isogeometric analysis is often attributed with the usage of Non-Uniform Rational B-Splines (NURBS) as basis functions since most common CAD programs for free form surfaces use this geometry description. Nevertheless, literature on other forms of isogeometric analysis, such as subdivision surfaces (see Cirak et al. [35–37]), can also be found. From the idea of using B-Splines/NURBS, other branches of research emerged on spline technology, which focus more on using the advantages of splines in the analysis and further development of new spline types. T-Splines as investigated in e.g. Bazilevs et al. [16], Beirão da Veiga et al. [18], and Casquero et al. [31, 32] and Hierarchical splines as analyzed in e.g. Bracco

et al. [26], Buffa et al. [30], and Schillinger et al. [115] are two of the largest groups of alternatives to NURBS. They will not be treated in this thesis, since they are not part of currently established CAD programs and are therefore not applicable for a fully CAD-integrated design process.

3.1 Geometry Description

NURBS became popular for CAD programs since they simplify the description and modification of free forms. They are an integral part of the design process in many industries. Complex CAD models are often assembled from several NURBS geometries. This chapter will give a general overview. The reader is referred to Cohen et al. [39] and Piegl et al. [107] for more details on NURBS.

3.1.1 B-Splines

B-Splines represent the basis of NURBS. A set of B-Splines $N_{i,p}(\xi)$ is defined by a polynomial degree p and a knot vector Ξ. The knot vector bounds the parametric coordinate ξ of the parameter space. The sum over the product of the basis functions with a matching set of n control points $\mathbf{P}_i$ constitutes the curve $\mathbf{C}(\xi)$ in the geometry space.

$$\mathbf{C}(\xi) = \sum_{i=1}^{n} N_{i,p}(\xi)\mathbf{P}_i \tag{3.1}$$

The knot vector Ξ is defined by a set of non-decreasing numbers ξ_i. The basis functions are defined piece-wise between these knots. They are computed recursively by the Cox-deBoor formula (see Boor [25]) starting from $p = 0$:

$$N_{i,0}(\xi) = \begin{cases} 1, & \text{if } \xi \in [\xi_i, \xi_{i+1}[\\ 0, & \text{otherwise} \end{cases} \tag{3.2}$$

The computation continues for $p \geq 1$ and $\xi \in [\xi_i, \xi_{i+p+1}[$ with

$$N_{i,p}(\xi) = \frac{\xi - \xi_i}{\xi_{i+p} - \xi_i} N_{i,p-1}(\xi) + \frac{\xi_{i+p+1} - \xi}{\xi_{i+p+1} - \xi_{i+1}} N_{i+1,p-1}(\xi) \tag{3.3}$$
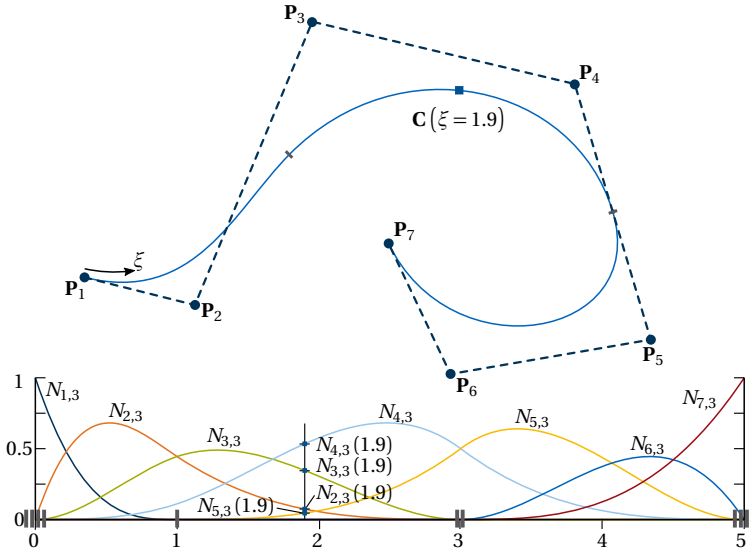
Figure 3.1: B-Spline curve $\mathbf{C}\left(\xi\right)$ and basis functions with polynomial degree $p=3$ and knot vector $\Xi=[0,0,0,0,1,3,3,5,5,5,5]$.

Inside each knot span, i.e. knot interval, the basis functions are C^{∞}-continuous and only $p+1$ basis functions are nonzero. At a single knot, the basis functions are C^{p-1}-continuous. If a knot appears k times, it has the multiplicity k. A multiplicity of p results in a C^0-continuity and the respective control point of the curve is interpolated. If a knot vector has a $p+1$ multiplicity at the start and end, it is called an open knot vector. The first and last control point coincide with the start and end of the curve. The tangents at both ends are defined by the line between the first and second or last and second-last control point, respectively. Figure 3.1 shows a B-Spline curve with its respective control points and basis functions in the parameter space.

3.1.2 Non-uniform Rational B-Splines (NURBS)

Non-uniform Rational B-Splines are weighted B-Splines functions. Every control point $\mathbf{P}_i$ with respective basis function $N_{i,p}$ has an attributed weight w_i. The weighted basis functions are denoted as $R_{i,p}$.

$$\mathbf{C}(\xi) = \sum_{i=1}^{n} R_{i,p}(\xi) \mathbf{P}_i \qquad \text{with} \qquad R_{i,p}(\xi) = \frac{N_{i,p}(\xi) w_i}{\sum_{j=1}^{n} N_{j,p}(\xi) w_j} \tag{3.4}$$

If all weights are equal, the NURBS curve is a regular B-Spline curve. Figure 3.2 shows the curve of Figure 3.1 with a weighted control point $\mathbf{P}_2$ and the respective resulting changes in the parameter and geometry space. The initial B-Spline curve and basis functions are indicated in gray. Note that the changes happen only in the knot spans, where the basis function $N_{2,3}$ is nonzero.

3.1.3 NURBS Surfaces

NURBS curves can be extended to NURBS surfaces by a tensor product of two independent sets of B-Splines defined by p and Ξ and q and H, which are then weighted. The rectangular parameter space is defined by the parametric coordinates ξ and η. The NURBS surface is then computed as a linear combination of the basis functions and the respective control points.

$$\begin{aligned}
\mathbf{S}(\xi, \eta) &= \sum_{i=1}^{n} \sum_{j=1}^{m} \frac{N_{i,p}(\xi) \cdot M_{j,q}(\eta) \cdot w_{ij}}{\sum_{k=1}^{n} \sum_{l=1}^{m} N_{k,p}(\xi) \cdot M_{l,q}(\eta) \cdot w_{kl}} \mathbf{P}_{ij} \\
&= \sum_{i=1}^{n} \sum_{j=1}^{m} R_{ij,pq}(\xi, \eta) \mathbf{P}_{ij}
\end{aligned} \tag{3.5}$$

Figure 3.3 shows the parameter space of a NURBS surface with polynomial degree $p = q = 2$, $\Xi = [0, 0, 0, 5, 10, 10, 10]$ and $H = [0, 0, 0, 7, 10, 10, 10]$ and its basis functions. The resulting NURBS surface for a given control point net is shown in Figure 3.4.
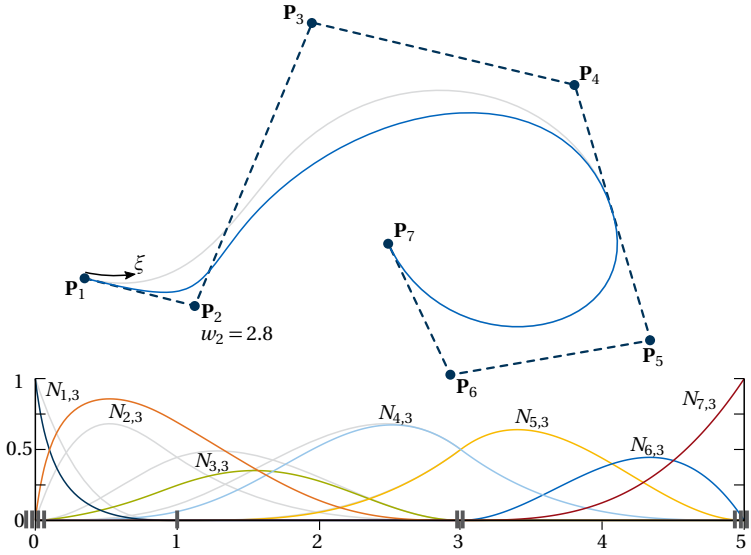
Figure 3.2: NURBS curve $\mathbf{C}\left(\xi\right)$ and basis functions with polynomial degree $p = 3$, knot vector $\Xi = [0, 0, 0, 0, 1, 3, 3, 5, 5, 5, 5]$ and $w_2 = 2.8$.

3.1.4 Boundary Representation (B-Rep)

Volume models in CAD are usually described using a boundary representation (B-Rep). This implies that volumes are defined by their outer surfaces as depicted in Figure 3.5. This model has a topological and a geometrical part. In order to describe the topology, the following entities are used:

- Faces F

- Edges E

- Vertices V

The connections between the independent geometrical entities are defined by the topology. An edge is for example attributed to several borders of
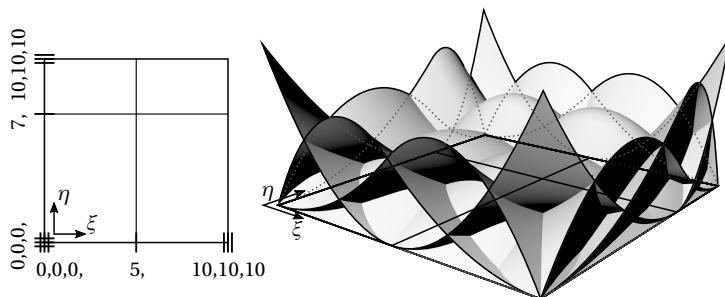
Figure 3.3: Parameter space and basis functions of a B-Spline surface with $p = q = 2$ and $\Xi = [0, 0, 0, 5, 10, 10, 10]$ and $H = [0, 0, 0, 7, 10, 10, 10]$.
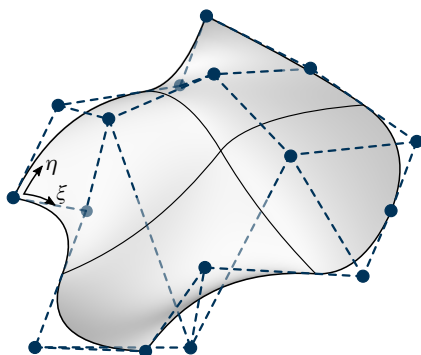

Figure 3.4: B-Spline surface in geometry space of the parametrization of Figure 3.3.
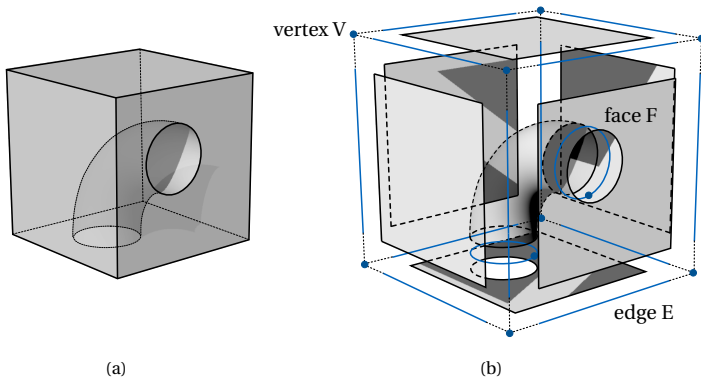
Figure 3.5: Boundary representation (B-Rep) of a volume: (a) spatial and (b) topological.

the surfaces and thereby connects them. Vertices are used analogously to connect the edges. This simple principle of creating objects is used in most CAD programs. An alternative is Constructive Solid Geometry (CSG), which stores the object as a sequence of Boolean operations, e.g. unions and intersections, of simpler shape. While this method is only used for solids, B-Reps are also used for large and complex surface models and the principle is also transferable to structural models that contain independent curves.

3.1.5 Trimming

NURBS surfaces are restrained to a topological rectangle due to their tensor-product structure. This restriction is not always suitable for geometry models, since splitting the geometry in topological rectangles may be unintuitive and requires a lot of effort. Therefore, the boundary representation is adapted for the NURBS surfaces. The NURBS surface describes the geometry, i.e. the shape, but the borders of the surface are defined by curves on the NURBS surface. These curves are typically described in the parameter space of the NURBS patch by $\overline{\mathbf{C}}\left(\bar{\xi}\right)$ as shown in Figure 3.6. Note that $\overline{\bullet}$ signifies entities which are related to the parameter space. The parts
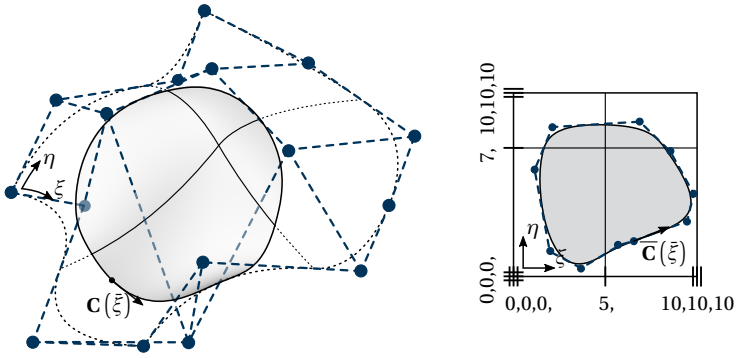
Figure 3.6: Trimmed surface in geometry and parameter space
with related boundary curves.

of the surface, which are inside these boundary curves, are considered as existing and are allocated with material. Those outside are ignored. The parametrization of the NURBS patch itself does not change. The boundary curve $\mathbf{C}\left(\bar{\xi}\right)$ in the geometry space belonging to the trimmed surface is then computed from the parameter curve. Both curve representations are attributed to the topological edge.

3.2 Analysis with NURBS

The following properties make B-Splines particularly suitable for finite element analysis:

- Partition of unity: $\sum_{i=1}^{n} N_{i,p}\left(\xi\right) = 1$

- Local support in the interval $\left[\xi_i, \xi_{i+p+1}\right]$

- Non-negativity: $N_{i,p}\left(\xi\right) \geq 0$

- Linear independence: $\sum_{i=1}^{n} \alpha_i N_{i,p}\left(\xi\right) = 0 \Leftrightarrow \alpha_i = 0$

The same properties hold for NURBS if all weights are positive, which is usually the case.

3.2.1 Finite Element Method

The finite element analysis is based on the Principle of Virtual Work as defined in Section 2.1.6. The NURBS basis functions describe the geometry and the respective solution field within the isogeometric approach. The problem is thus discretized by the discrete control point coordinates and the degrees of freedom u_r, which are also related to the control points. The discretization is a requirement for solving the problem numerically with the Finite Element Method (FEM).

Equation (2.35) is rewritten by the variational principle to

$$\delta W = \sum \frac{\partial W}{\partial u_r} \delta u_r = \sum -R_r \delta u_r = 0$$

$$\xrightarrow{\text{arbitrary } \delta u_r} R_r = -\frac{\partial W}{\partial u_r} = 0 \tag{3.6}$$

for the discretized system. It follows that for arbitrary virtual displacements δu_r, the components of the residual force vector $\mathbf{R}$ representing the unbalanced forces have to be zero. This expression is generally nonlinear and is thus linearized at the current displacement $\mathbf{u}^*$ in order to solve it with an iterative procedure.

$$LIN(R_r) = -\frac{\partial W}{\partial u_r} - \frac{\partial^2 W}{\partial u_r \partial u_s} \Delta u_s$$

$$= R_r|_{\mathbf{u}^*} + \sum_s \frac{\partial R_r}{\partial u_s} \Delta u_s = R_r|_{\mathbf{u}^*} + \sum_s K_{rs} \Delta u_s = 0 \tag{3.7}$$

The residual force vector $\mathbf{R}$ and the stiffness matrix $\mathbf{K}$ are then defined as:

$$R_r = -\frac{\partial W}{\partial u_r} = -\frac{\partial W_{\text{int}}}{\partial u_r} - \frac{\partial W_{\text{ext}}}{\partial u_r} = R_r^{\text{int}} + R_r^{\text{ext}} \tag{3.8}$$

$$K_{rs} = \frac{\partial R_r}{\partial u_s} = -\frac{\partial^2 W}{\partial u_r \partial u_s} = -\frac{\partial^2 W_{\text{int}}}{\partial u_r \partial u_s} - \frac{\partial^2 W_{\text{ext}}}{\partial u_r \partial u_s} = K_{rs}^{\text{int}} + K_{rs}^{\text{ext}} \tag{3.9}$$

3.2.2 Integration

A numerical integration has to be performed in order to obtain the integral of the virtual work over the whole domain. The domain of a curve is defined by its length L and the domain of a surface by its area A. A curve can also

be inscribed in the parameter space of another NURBS patch and has the domain $\bar{L}$ in the geometry space.

Typically, Gauss integration is used for the numerical integration. Therefore, the integral over the curve or surface has to be mapped from the geometry space into the parameter space by the Jacobian $J_{x,\xi}$. The mapping from the parametric to the Gaussian domain, which is defined by $u, v \in [-1, 1]$, is provided by the Jacobian $J_{\xi,u}$. Furthermore, the parameter domain is split into the nonzero knot spans. Each knot span is integrated separately, i.e. has its own Gauss domain for the integration since the basis function are defined continuously within. These integrals are then summed up to the total integral.

The integral of a nonzero knot span from ξ_s to ξ_e along a curve is given by:

$$\|L\| = \int_L \mathrm{d}L = \int_{\xi_s}^{\xi_e} J_{x,\xi}\,\mathrm{d}\xi = \int_G J_{x,\xi} J_{\xi,u}\,\mathrm{d}G \tag{3.10}$$

$$\text{with } J_{x,\xi} = \left\| \frac{\partial \mathbf{X}}{\partial \xi} \right\|_2 \text{ and } J_{\xi,u} = \frac{\partial \xi}{\partial u} = \frac{\xi_e - \xi_s}{2}$$

Analogously, a surface integral over a knot span defined in $\left[\xi_s, \xi_e\right] \times \left[\eta_s, \eta_e\right]$ is computed as follows

$$\|A\| = \int_A \mathrm{d}A = \int_{\xi_s}^{\xi_e} \int_{\eta_s}^{\eta_e} J_{x,\xi}\,\mathrm{d}\eta\,\mathrm{d}\xi = \int_G J_{x,\xi} J_{\xi,u}\,\mathrm{d}G \tag{3.11}$$

$$\text{with } J_{x,\xi} = \left\| \frac{\partial \mathbf{X}}{\partial \xi} \times \frac{\partial \mathbf{X}}{\partial \eta} \right\|_2 \text{ and}$$

$$J_{\xi,u} = \frac{\partial \xi}{\partial u} \cdot \frac{\partial \eta}{\partial v} = \frac{\xi_e - \xi_s}{2} \cdot \frac{\eta_e - \eta_s}{2}$$

Furthermore, it is possible that the integration along a trimmed boundary $\bar{L}$ is needed.

$$\|\overline{L}\| = \int_{\overline{L}} \mathrm{d}\overline{L} = \int_{\bar{\xi}_s}^{\bar{\xi}_e} J_{x,\bar{\xi}}\,\mathrm{d}\bar{\xi} = \int_G J_{x,\bar{\xi}} J_{\bar{\xi},u}\,\mathrm{d}G \tag{3.12}$$

$$\text{with } J_{x,\bar{\xi}} = \left\| \frac{\partial \mathbf{X}}{\partial \xi} \frac{\partial \xi}{\partial \bar{\xi}} \times \frac{d \mathbf{X}}{d\eta} \frac{\partial \eta}{\partial \bar{\xi}} \right\|_2 \text{ and}$$

$$J_{\bar{\xi},u} = \frac{\partial \bar{\xi}}{\partial u} = \frac{\bar{\xi}_e - \bar{\xi}_s}{2}$$
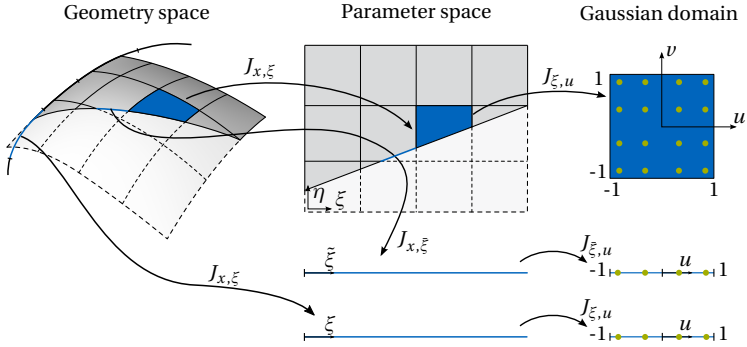
Figure 3.7: Mapping from the geometry space to the Gauss space for curve, surface and boundary curve (adapted from Teschemacher et al. [123]).

A common number of Gauss points within an untrimmed knot span is $p+1$ in the respective direction. This integration scheme, which is used throughout this thesis, was proposed by Hughes et al. [70]. More efficient algorithms can be found in e.g. Auricchio et al. [5], Dornisch et al. [46], and Hughes et al. [71].

Defining the position of the integration points inside a trimmed knot span is more complex. The Adaptive Gaussian Integration Procedure (AGIP) by Breitenberger [27], which is an established method for the integration of trimmed knot spans, is applied in this thesis. Other strategies were proposed by Guo et al. [64], Kang et al. [72], Kim et al. [75], Kudela et al. [80, 81], Nagy et al. [96], Parvizian et al. [102], Rank et al. [110], Ruess et al. [111, 112], Seo et al. [120], and Wang et al. [128]. A comprehensive review of integration approaches of trimmed patches can be found in Marussig et al. [92].

Figure 3.7 provides an overview of the different mappings for the integration of different geometric entities.

3.2.3 Refinement

Another important feature of NURBS is the refinement. It adds more design handles, i.e. control points, to the curve or surface. Hence, local disconti-

nuities can be created. It is important to state that the NURBS refinement does not modify the geometry but the parametrization. The same holds for the degrees of freedom, which can be exactly transferred to the refined parametrization. This is advantageous when dealing with several analysis steps. It is possible that the model, which already contains some results, needs to be refined e.g. for capturing some local effects of a newly added joint during a later stage.

Order elevation and knot insertion are the two basic refining procedures.

Order elevation, also called p-refinement, increases the polynomial degree of the NURBS basis function by Δp. The continuity at all knots is preserved. Consequently, the multiplicity k is also increased at every knot by Δp since $C^{p_{\text{new}}-k_{\text{new}}} = C^{p_{\text{old}}+\Delta p-(k_{\text{old}}+\Delta p)}$. Figure 3.8(a) shows the order elevated B-Spline curve and the corresponding parametrization and basis functions from Figure 3.1. The shape of the curve does not change whereas the parametrization does.

Knot insertion, also called h-refinement, adds additional elements to the parametrization by subdividing existing ones. An additional knot is inserted and hence a nonzero knot span is subdivided into two. This can also be used to increase the multiplicity of a knot, i.e. decrease the parametric continuity. Two additional knots are inserted into the knot vector of the B-Spline curve of Figure 3.1. The first one increases the multiplicity at $\xi = 1$ and therefore decreases the continuity to $C^{p-k} = C^{3-2} = C^1$ (see Figure 3.8(b)). The curve interpolates the control polygon at $\xi = 1$. The second inserted knot at $\xi = 2$ subdivides the second nonzero knot span $\xi \in [1,3[$. As for order elevation, the knot insertion only changes the parametrization, i.e. control points and basis functions, and not the geometry of the curve.

The combination of the procedures is possible, but the sequence is not commutative. A p-refinement followed by a h-refinement is called k-refinement.

More details on the refinement procedures can be found in Boehm [24], Cohen et al. [38], and Piegl et al. [107] and on refinement in the context of isogeometric analysis in Cottrell et al. [40] and Hughes et al. [70].

Especially with NURBS, it is often easy to describe the initial geometry with few control points. However, these control points with their basis functions also have to represent the solution. If only few control points
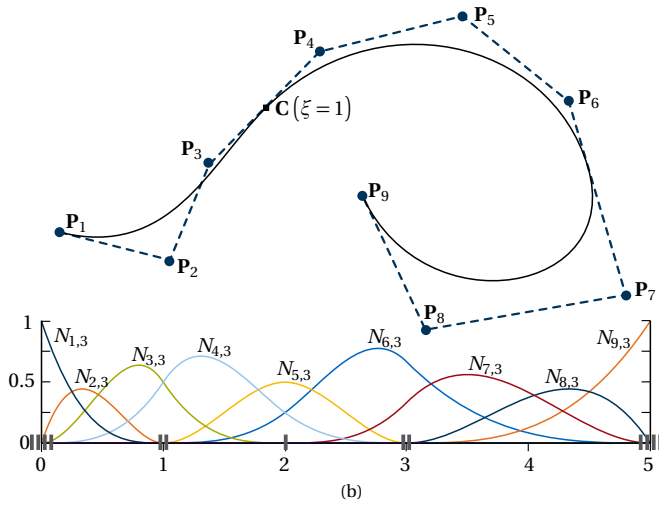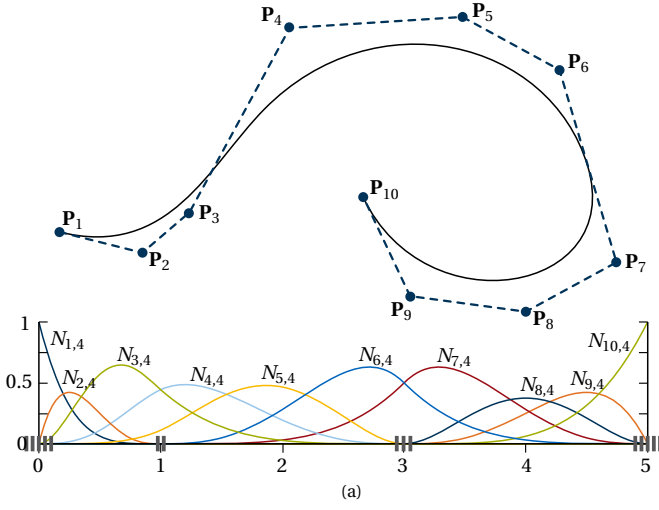
(a)

(b)

Figure 3.8: Refined B-Spline curve with control points and basis function: (a) order elevation and (b) knot insertion.

are used, the solution space is very restricted. This can be overcome by a sufficient refinement.

The effect of the refinement on the results can easily be visualized with the simple elastica. The ends of an initially straight beam are moved towards each other (see Figure 3.9). Depending on the refinement level, different deformations evolve. Note that due to the smooth geometry description, it is much more difficult to visually evaluate the quality of the result than for classical linear finite elements.

Furthermore, the choice of the refinement level, i.e. the number of control points, is not only dependent on the ability to represent the deformed state but on the ability to represent the undeformed and deformed state with the same parametrization.

The elastica from Figure 3.9 is taken as a short illustrative example of the problem. The final equilibrium shape of the highest refinement level, i.e. $p = 4$ and 17 control points (see Figure 3.10(a)), can also be represented with only small deviations by the parametrization of refinement level two, $p = 2$ and 11 control points, (see Figure 3.10(b)). The found parametrization, i.e. the knot vector, is transferred to the flat initial patch by refining a linear curve accordingly. When pulling the ends of this flat curve onto the supports, not the desired rebuilt shape of Figure 3.10(b) is evolving due to the respective normal strains. The energy minimum in equilibrium is shown in Figure 3.10(c), which clearly deviates from the correct solution.

Beyond the ability to represent the solution field, e.g. the displacements, one also has to consider a sufficient polynomial degree for the correct evaluation of the internal forces. The inner forces are related to derivatives of the displacements for some structural elements. If the initial polynomial degree is not high enough, the distribution of the inner forces is corrupted as illustrated for a straight Bernoulli beam under a line load in Figure 3.11.

The displacements match well for all polynomial degrees. However, the correct solution of the bending moments, i.e. a parabola, can only be approximated by $p = 2, 3$ since the bending moment is related to the second derivative of the displacement for a Bernoulli beam. The same holds for the shear force, where the solution of $p = 3$ can still approximate the analytic, linear distribution, but the solution of $p = 2$ is zero since the shear force is related the third derivative of the displacements.
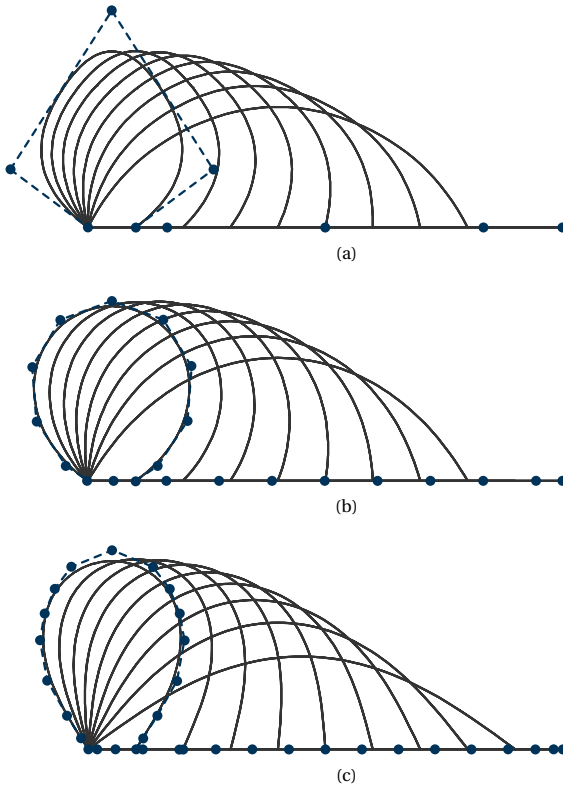
Figure 3.9: Bending of the elastica with control points in the initial and final state for: (a) 5 control points and $p = 2$, (b) 11 control points and $p = 2$ and (c) 17 control points and $p = 4$ (adapted from Bauer et al. [12]).
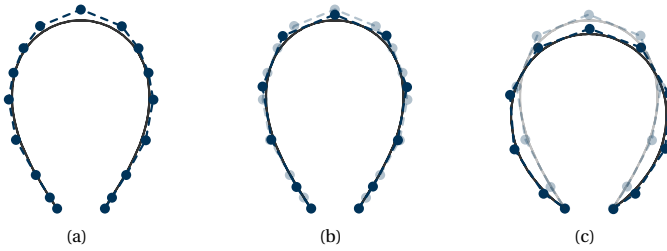
Figure 3.10: Elastically bent strip: (a) final equilibrium state for $p = 4$ and 17 control points, (b) geometrically approximating the equilibrium shape with $p = 2$ and 11 control points and (c) equilibrium shape of the rebuilt geometry.
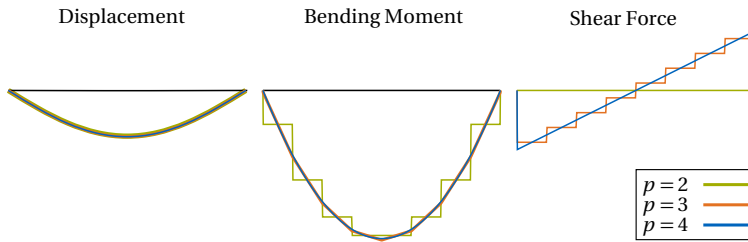

Figure 3.11: Displacement, bending moment, and shear force of a simply supported beam under line load for $p = 2$ (green), $p = 3$ (orange), and $p = 4$ (blue).

3.3   Special Aspects of NURBS-based Analysis

NURBS basis functions are beneficial for many types of analyses and structural systems due to their smoothness. Nevertheless, some drawbacks related to the parametrization exist. Some of the most important ones in the context of geometrically nonlinear structural design will be briefly presented in this section.
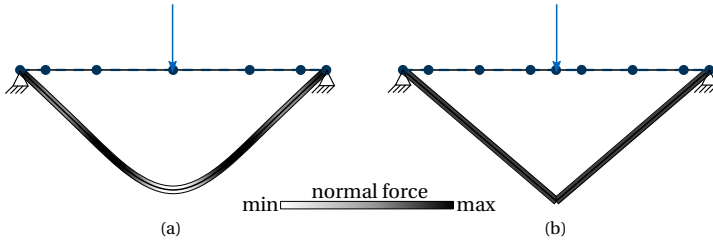
Figure 3.12: Cable under single load with deformation and normal forces for a B-Spline with (a) $\Xi = [0,0,0,0,1,2,3,4,4,4,4]$ and (b) $\Xi = [0,0,0,0,1,2,2,2,3,4,4,4,4]$.

3.3.1 Local Discontinuities

The representation of local discontinuities inside a knot span, e.g. related to concentrated load application, is one of the biggest issues within classical isogeometric analysis. The basis functions in combination with the structural element formulation are not able to represent a discontinuity as can be seen in Figure 3.12(a). A point load is set onto the middle of a cable, which is supported at both ends. The correct solution would be a triangulated displacement with the peak under the point load. It is not possible to represent this with a polynomial degree $p > 1$. A parametric discontinuity C^0 is needed in order to be able to represent a kink. Note that it is possible to create geometric discontinuities G^0 for higher degrees if p control point positions are coinciding. However, this also implies that the length of the tangent becomes zero at the discontinuity, which in return would result in very large inner forces. Consequently, this solution, which would represent the correct displacement shape, represents no equilibrium state, i.e. minimum potential. The problem behind that is the same as in Figure 3.10. Another interfering effect is the oscillation of the inner forces around a discontinuity. The correct solution for displacements and forces is obtained if the parametrization is suitable and provides a parametric discontinuity C^0 at the point of the force as can be seen in Figure 3.12(b).

The solution quality of an initially continuous curve can be improved by h-refinement. The discontinuity can either be directly generated by knot insertion at the location of the local feature until the required discontinuity is obtained or a knot insertion can be performed in order to generate more
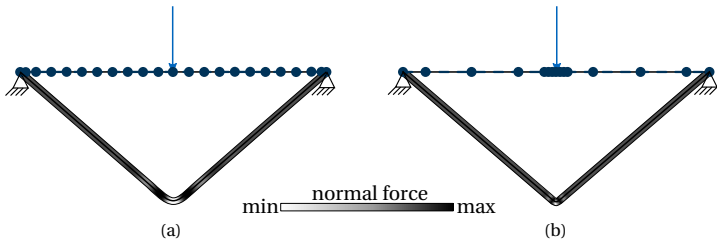
Figure 3.13: Cable under single load with deformation and normal forces for a B-Spline, which has no C^0-continuity in the discretization, with (a) 20 equally distributed nonzero knot spans and (b) 12 locally concentrated elements.

elements. Creating a C^0-discontinuity is only applicable for cables since this discontinuity acts as a hinge for beams as explained in the following section. Figure 3.13 presents two refinement strategies without directly creating the C^0-discontinuity. One system is refined equally over the whole knot vector, i.e. every nonzero knot span is subdivided into five elements. The other procedure inserts the knots around the local feature in order to locally generate many small elements keeping the error local. The oscillations and the error in the displacements are localizing and diminishing for both approaches. However, the locally concentrated refinement with only 12 elements achieves a better result than the equally distributed one with 20 elements.

The same effect arises for NURBS surfaces. Figure 3.14 shows the result of a form found four-point sail with a ridge cable between the low points. Figure 3.14(a) is modeled by one patch whereas Figure 3.14(b) is modeled by two coupled, trimmed triangular patches meeting at the ridge cable. The respective geometric discontinuity at the ridge cable emerges only for the model with two patches.

Local refinement of surfaces by inserting knots into the knot vectors is more problematic. It is not possible to locally insert knots around a feature, since the inserted knots are active over the whole domain due to the tensor product structure. Especially if the discontinuity is not aligned to a knot line, the whole patch has to be refined, which results in a large number of degrees of freedom. They might be unnecessary in other regions of the patch. Local refinement techniques such as T-Splines or Hierarchical B-
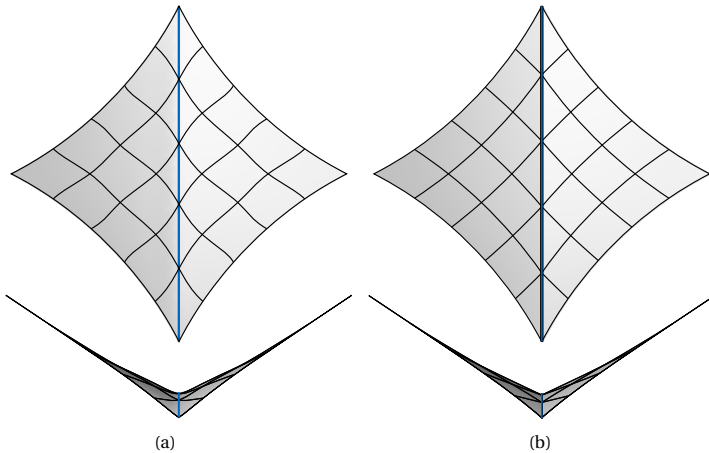
Figure 3.14: Four-point sail with ridge cable modeled by (a) one patch and (b) two patches joint at the ridge cable.

Splines provide a solution to this problem. However, since these advanced basis functions are not available in common CAD programs, this falls outside the scope of this thesis. Alternatively, the problem can be bypassed by trimming the discontinuity and its assumed region of influence out of the patch, refining only this part and coupling it to the remaining unrefined patch.

3.3.2 Hidden Discontinuities

Unintended discontinuities in the solution due to the discretization may also be a problem. The initial geometry might be geometrically continuous in the desired way while the parametrization is not. The discontinuity may appear after the analysis (see Figure 3.15). This is for example typically the case for a circular segment with an angle larger than $\frac{\pi}{2}$. The C^0-continuity is hidden in the initial geometry. When the structure is loaded, the C^0-continuity acts like a hinge.

Two solutions to avoid this problem in the analysis are feasible. Either one rebuilds and consequently approximates the geometry by a parametriza-
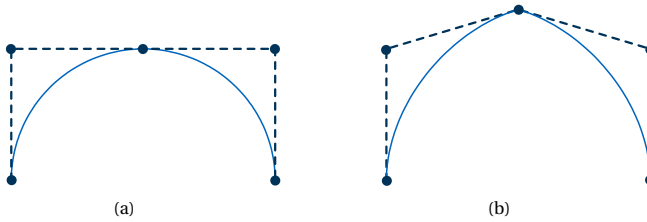
(a) (b)

Figure 3.15: Hidden discontinuity for a semicircle: (a) geometrically continuous in the undeformed configuration and (b) discontinuous in the deformed configuration (adapted from Bauer et al. [12]).

tion without this discontinuity or one adds a geometric boundary condition at the discontinuity in order to preserve the desired smoothness.

3.3.3 Trimming

The last presented drawback in using the geometry description directly provided by CAD may appear with trimmed geometries. The effect is the most distinct for narrow or small holes. Note that the definition of small is relative to the size of the affected knot spans. The problem is related to the local discontinuities. The smooth solution space is not able to represent this discontinuity of missing material. Figure 3.16 shows a trimmed plate, which is clamped on one side. A long slit is trimmed out with the result that two cantilevering stripes emerge. One of them is loaded at its tip. Additionally, the short edge of the hole is simply supported. If the trimmed patch is used as is in the calculation, the unloaded strip also deforms since the basis functions distribute the load to this side (cf. Figure 3.16(b)). Appropriate refinement can avoid this behavior (cf. Figure 3.16(c); note that only refinement around the hole would be sufficient) or by assembling several independent patches (cf. Figure 3.16(d)).
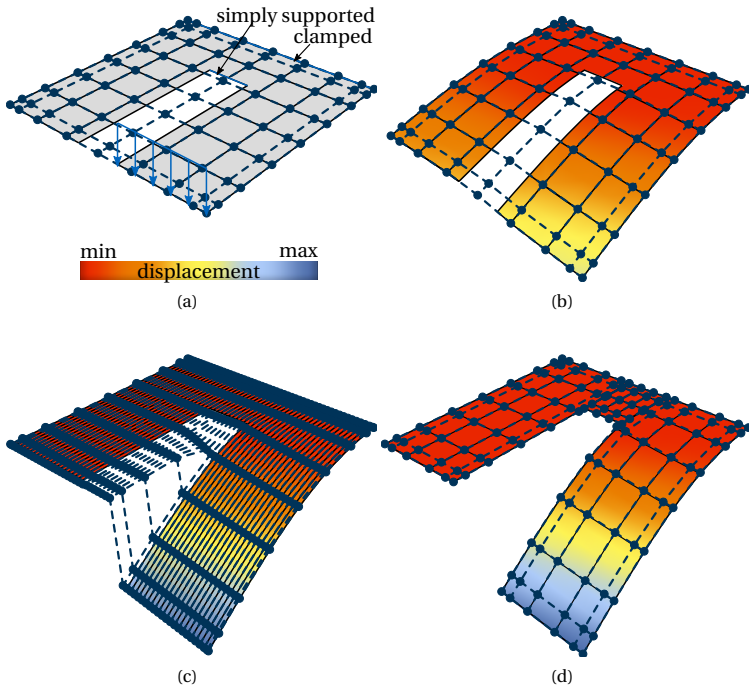
Figure 3.16: Trimmed patch with control points: (a) setup with boundary conditions, (b) deformation of the initial parametrization, (c) deformation of a refined parametrization and (d) deformation of a remodeled system consisting of several coupled patches.

4

ISOGEOMETRIC STRUCTURAL ELEMENTS

In order to model the assembly of complex systems, it is necessary to be able to simulate the behavior of different structural elements with different dimensions. This chapter's purpose is to present basic formulas and assumptions of the applied geometrically nonlinear structural element formulations. The solid formulation is step by step dimensionally reduced to a shell and a beam formulation.

4.1   Solid Elements

The element formulation of a solid can be derived from the geometry description. The position vector of the undeformed and deformed configuration is equal to the volumetric (NURBS) geometry description as illustrated in Figure 4.1.

$$\mathbf{X}\left(\theta^1,\theta^2,\theta^3\right) = \mathbf{X}_{\text{v}}\left(\theta^1,\theta^2,\theta^3\right) \tag{4.1}$$

$$\mathbf{x}\left(\theta^1,\theta^2,\theta^3\right) = \mathbf{x}_{\text{v}}\left(\theta^1,\theta^2,\theta^3\right) \tag{4.2}$$
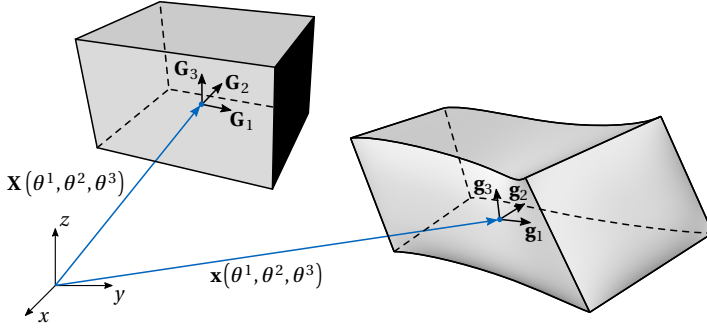
Figure 4.1: Geometry description of a solid with position and base vectors in the undeformed and deformed configuration.

The Green-Lagrange strains are computed by the metric of the deformed and undeformed configuration.

$$E_{ij} = \frac{1}{2}\left(g_{ij} - G_{ij}\right) \tag{4.3}$$

The energetically conjugated PK2 stresses are determined by the material law, which is typically described by a fourth order tensor.

$$S^{ij} = C^{ijkl} E_{kl} \tag{4.4}$$

If the material law is given in a locally orthonormal coordinate system, the strains have to be transformed into this coordinate system $\mathbf{e}_i$. Entities referring to a Cartesian coordinate system will be denoted by $\widetilde{\bullet}$.

$$\widetilde{E}_{ij} = E_{kl}\left(\mathbf{e}_i \cdot \mathbf{G}^k\right)\left(\mathbf{G}^l \cdot \mathbf{e}_j\right) \tag{4.5}$$

The internal work is defined as in Equation (2.36).

$$W_{\text{int}} = -\int_{\Omega_0} \mathbf{S} : \delta\,\mathbf{E}\,\mathrm{d}\Omega \tag{4.6}$$

4.2 Shell Elements

A shell is a volume which is reduced by one dimension. All points of the volume outside of the center surface are addressed by a third base vector.
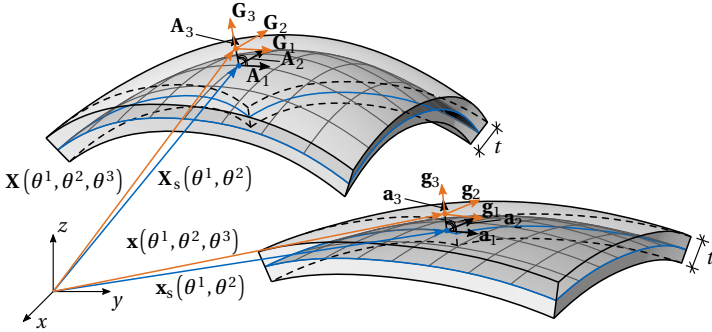
Figure 4.2: Geometry description of the Kirchhoff-Love shell with position and base vectors in the undeformed and deformed configuration.

The assumptions, which are made for this vector, are defined by the applied shell theory. Many shell models for isogeometric analysis exist in the literature. Isogeometric adaptions of the Reissner-Mindlin theory can be found in Beirão da Veiga et al. [17], Benson et al. [20, 21], and Dornisch et al. [45, 46] among others. Especially the Kirchhoff-Love theory found its revival with IGA since a C^1-continuity is required between the elements, which is directly the case for NURBS in contrast to classical polynomial approximations. The isogeometric Kirchhoff-Love shell formulation was proposed by Kiendl et al. [74]. The hierarchic shell by Echter et al. [50] and Oesterle et al. [99] provides the possibility of enabling and disabling higher order theories based on the Kirchhoff-Love shell.

Despite the available higher order shell theories, the Kirchhoff-Love shell by Kiendl et al. [74] is one of the most applied formulations, since it is simple and still effective, especially for thin shells. With the kinematics of Kirchhoff-Love, the cross section has to remain straight and perpendicular to the surface and a constant thickness t of the shell is assumed. Hence, the normalized surface normal can directly be applied for the definition of the cross section (see Figure 4.2).

This results in the following position vectors in the undeformed and deformed configuration. The curvilinear coordinate θ^3 is defined by the

thickness t in the interval $\left[-\frac{t}{2}, \frac{t}{2}\right]$.

$$\mathbf{X}\left(\theta^1, \theta^2, \theta^3\right) = \mathbf{X}_{\mathrm{s}}\left(\theta^1, \theta^2\right) + \theta^3 \mathbf{A}_3\left(\theta^1, \theta^2\right) \tag{4.7}$$

$$\mathbf{x}\left(\theta^1, \theta^2, \theta^3\right) = \mathbf{x}_{\mathrm{s}}\left(\theta^1, \theta^2\right) + \theta^3 \mathbf{a}_3\left(\theta^1, \theta^2\right) \tag{4.8}$$

The base vectors are derived by applying Equation (2.2) to Equation (4.7).

$$\mathbf{G}_1 = \frac{\partial \mathbf{X}_{\mathrm{s}}\left(\theta^1, \theta^2\right)}{\partial \theta^1} + \theta^3 \frac{\partial \mathbf{A}_3\left(\theta^1, \theta^2\right)}{\partial \theta^1} = \mathbf{A}_1 + \theta^3 \mathbf{A}_{3,1} \tag{4.9}$$

$$\mathbf{G}_2 = \frac{\partial \mathbf{X}_{\mathrm{s}}\left(\theta^1, \theta^2\right)}{\partial \theta^2} + \theta^3 \frac{\partial \mathbf{A}_3\left(\theta^1, \theta^2\right)}{\partial \theta^2} = \mathbf{A}_2 + \theta^3 \mathbf{A}_{3,2} \tag{4.10}$$

$$\mathbf{G}_3 = \mathbf{A}_3 \tag{4.11}$$

The metric is simplified by neglecting higher order terms $\mathcal{O}\left(\left(\theta^3\right)^2\right)$ because it is assumed that $t \ll L_1, L_2$.

$$\begin{aligned} G_{\alpha\beta} &= \left(\mathbf{A}_\alpha + \theta^3 \mathbf{A}_{3,\alpha}\right) \cdot \left(\mathbf{A}_\beta + \theta^3 \mathbf{A}_{3,\beta}\right) \\ &\approx A_{\alpha\beta} - 2\theta^3 B_{\alpha\beta} \end{aligned} \tag{4.12}$$

The same holds for the deformed configuration, analogously.

Applying Equation (2.25), the following strain components are all zero:

$$E_{33} = E_{13} = E_{23} = E_{31} = E_{32} = 0 \tag{4.13}$$

The remaining nonzero strain components are computed as follows:

$$E_{\alpha\beta} = \frac{1}{2}\left(g_{\alpha\beta} - G_{\alpha\beta}\right) = \frac{1}{2}\left(a_{\alpha\beta} - A_{\alpha\beta}\right) + \theta^3\left(B_{\alpha\beta} - b_{\alpha\beta}\right) = \epsilon_{\alpha\beta} + \theta^3 \kappa_{\alpha\beta} \tag{4.14}$$

The strain can be split into parts related to extension or compression $\epsilon_{\alpha\beta}$, and change of curvature $\kappa_{\alpha\beta}$, i.e. normal forces and bending moments.

The stress-strain relation can also be written in Voigt notation since both tensors are symmetric. The material matrix $\mathbf{D}$ is defined in a local Cartesian coordinate system. Thus, locally orthogonal strains and stresses are used. Analogously to the strain, the stresses can be split into parts of normal

forces $\tilde{\mathbf{n}}$ and bending moments $\tilde{\mathbf{m}}$. This already includes a pre-integration over the thickness.

$$
\begin{bmatrix} \tilde{n}^{11} \\ \tilde{n}^{22} \\ \tilde{n}^{12} \end{bmatrix} = t \cdot \mathbf{D} \cdot \begin{bmatrix} \tilde{\epsilon}^{11} \\ \tilde{\epsilon}^{22} \\ 2\tilde{\epsilon}^{12} \end{bmatrix} \quad \text{and} \quad \begin{bmatrix} \tilde{m}^{11} \\ \tilde{m}^{22} \\ \tilde{m}^{12} \end{bmatrix} = \frac{t^3}{12} \cdot \mathbf{D} \cdot \begin{bmatrix} \tilde{\kappa}^{11} \\ \tilde{\kappa}^{22} \\ 2\tilde{\kappa}^{12} \end{bmatrix} \tag{4.15}
$$

The following term for the internal virtual work arises:

$$
W_{\text{int}} = - \int_{\Omega_0} \mathbf{S} : \delta \mathbf{E} \, \mathrm{d}\Omega = - \int_A (\tilde{\mathbf{n}} : \delta\tilde{\boldsymbol{\epsilon}} + \tilde{\mathbf{m}} : \delta\tilde{\boldsymbol{\kappa}}) \, \mathrm{d}A \tag{4.16}
$$

4.3 Membrane Elements

The membrane element is contained in the KL-shell element. It is assumed that membranes have no resistance to bending moments. The curvature of membranes can change without resulting stresses. In order to compensate this weakness, membranes are often prestressed. The prestress $\tilde{\mathbf{n}}_0$ can directly be considered in the virtual work.

$$
W_{\text{int}} = - \int_{\Omega_0} \left(\mathbf{S} + \mathbf{S}_0 \right) : \delta \mathbf{E} \, \mathrm{d}\Omega = - \int_A \left(\tilde{\mathbf{n}} + \tilde{\mathbf{n}}_0 \right) : \delta\tilde{\boldsymbol{\epsilon}} \, \mathrm{d}A \tag{4.17}
$$

More details on isogeometric membrane elements can be found in Philipp et al. [105].

4.4 Beam Elements

Beam elements are required for a full set of structural elements in civil engineering. They are modeled by a curve with additional properties. In the realm of lightweight structures including large deformations, spatial, geometrically nonlinear element formulations are crucial. The first isogeometric spatial, nonlinear beam was proposed by Raknes et al. [109], which is neglecting torsion and can therefore be seen as a bending-stabilized cable. An extended Timoshenko beam theory can be found in e.g. Marino et al. [91] and Weeger et al. [130]. Analogously to the Kirchhoff-Love shell theory, Euler Bernoulli kinematics can be adopted since a C^1-continuity
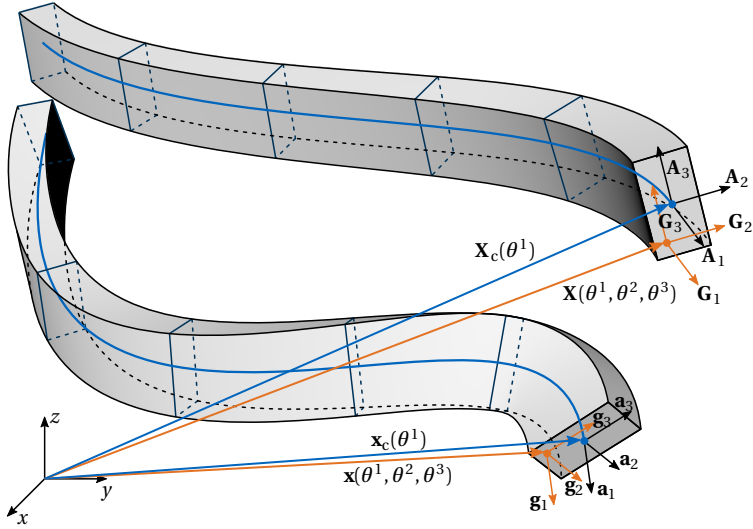
Figure 4.3: Geometry description of the Euler-Bernoulli beam with position and base vector in undeformed and deformed configuration (adapted from Bauer et al. [8]).

between the elements of the NURBS curve is naturally given. Greco et al. [60] applied this for a linear 3D application, which was extended to a geometrically nonlinear formulation in Bauer et al. [10].

The development of this structural element was already part of my Master's thesis (see Bauer [7]). The present summary of the beam formulation is a revised version of Section 2.1 of Bauer et al. [8].

The isogeometric geometrically nonlinear beam accounts for Bernoulli kinematics. The cross sections remain orthogonal to the center line after deformation and there are no changes of the cross sectional dimensions. Torsion according to St. Venant is considered whereas warping effects are neglected. Three translational degrees of freedom and one for a relative rotation around the beam axis are used for the spatial beam.

The continuum of the undeformed and deformed beam, $\mathbf{X}$ and $\mathbf{x}$, respectively, can be defined by the longitudinal beam axis, represented by a NURBS curve ($\mathbf{X}_c$ and $\mathbf{x}_c$, respectively) and two normalized base vectors

$\mathbf{A}_\alpha$, $\alpha \in \{2,3\}$, which are perpendicular to each other and to the beam axis $\mathbf{A}_1$ (see Figure 4.3). Under the Bernoulli assumption, every kinematic can be described by:

$$\mathbf{X}\left(\theta^1, \theta^2, \theta^3\right) = \mathbf{X}_c\left(\theta^1\right) + \theta^2 \mathbf{A}_2\left(\theta^1\right) + \theta^3 \mathbf{A}_3\left(\theta^1\right) \tag{4.18a}$$

$$\mathbf{x}\left(\theta^1, \theta^2, \theta^3\right) = \mathbf{x}_c\left(\theta^1\right) + \theta^2 \mathbf{a}_2\left(\theta^1\right) + \theta^3 \mathbf{a}_3\left(\theta^1\right) \tag{4.18b}$$

The peculiarity of this beam formulation is in the determination of the base vectors $\mathbf{A}_\alpha$. Two mapping matrices based on the Euler-Rodrigues formula are applied to define the undeformed configuration of the beam. Two initial base vectors at the beginning of the beam $\mathbf{A}_\alpha^0$ are mapped to every position of the center line by the mapping matrix $\Lambda(\mathbf{T}_0, \mathbf{T})$ in order to create a unique orientation. Subsequently, they are aligned to the real beam orientation by a rotation around the beam axis by the rotation matrix $\overline{\mathbf{R}}_\mathbf{T}(\Psi)$. This results in

$$\mathbf{A}_\alpha\left(\theta^1\right) = \overline{\mathbf{R}}_{\mathbf{T}(\theta^1)}\left(\Psi\left(\theta^1\right)\right) \Lambda\left(\mathbf{T}_0, \mathbf{T}\left(\theta^1\right)\right) \mathbf{A}_\alpha^0, \tag{4.19}$$

where $\mathbf{T}$ is the normalized tangent of the beam axis and $\mathbf{T}_0$ the tangent at the beginning of the beam. The vectors $\mathbf{T}_i$ are the normalized $\mathbf{A}_i$ vectors, i.e. represent the orthonormal local coordinate system.

We use the same mapping for the base vectors $\mathbf{a}_\alpha$ of the deformed beam. In contrast to the undeformed configuration, the mapping matrix $\Lambda(\mathbf{T}, \mathbf{t})$ maps not the initial base vectors at the beginning of the beam $\mathbf{A}_\alpha^0$, but the base vectors $\mathbf{A}_\alpha\left(\theta^1\right)$ of the undeformed configuration. The cross section is rotated around the axis of the deformed beam $\mathbf{t}$ by the rotation matrix $\overline{\mathbf{R}}_\mathbf{t}(\psi)$. The rotation angle ψ is also the fourth degree of freedom.

$$\mathbf{a}_\alpha\left(\theta^1\right) = \overline{\mathbf{R}}_{\mathbf{t}(\theta^1)}\left(\psi\left(\theta^1\right)\right) \Lambda\left(\mathbf{T}\left(\theta^1\right), \mathbf{t}\left(\theta^1\right)\right) \mathbf{A}_\alpha\left(\theta^1\right) \tag{4.20}$$

The Green-Lagrange strain tensor and the energetically conjugated second Piola-Kirchhoff stress tensor are used for the Principle of Virtual Work. Consequently, the covariant base vectors $\mathbf{G}_i$ of the continuum are required. They are computed by the differentiation of the position vector $\mathbf{X}$ by the respective contravariant coordinate θ^i. The same applies for the deformed configuration.

$$\mathbf{G}_1 = \mathbf{A}_1 + \theta^2 \mathbf{A}_{2,1} + \theta^3 \mathbf{A}_{3,1}, \qquad \mathbf{G}_2 = \mathbf{A}_2, \qquad \mathbf{G}_3 = \mathbf{A}_3 \tag{4.21}$$

Recall that the GL strain tensor in the curvilinear coordinate system is defined as

$$\mathbf{E} = \frac{1}{2}\left(g_{ij} - G_{ij}\right)\mathbf{G}^i \otimes \mathbf{G}^j, \quad E_{ij} = \frac{1}{2}\left(g_{ij} - G_{ij}\right) \tag{4.22}$$

In order to simplify the derivation of the element formulation for slender beams with $h, w \ll L$, the following is assumed: second order terms $\mathcal{O}\left(\left(\theta^2\right)^2\right), \mathcal{O}\left(\left(\theta^3\right)^2\right), \mathcal{O}\left(\theta^2 \cdot \theta^3\right)$ can be neglected and $\left\|\mathbf{G}_1\right\|_2 \approx \left\|\mathbf{A}_1\right\|_2$. Warping effects vanish with these assumptions.

Consequently, the remaining nonzero components of the strain tensor are

$$E_{11} = \frac{1}{2}\left(g_{11} - G_{11}\right) = \frac{1}{2}\left(a_{11} - A_{11}\right) + \theta^2 (\overbrace{\mathbf{a}_{2,1} \cdot \mathbf{a}_1}^{b_2} - \overbrace{\mathbf{A}_{2,1} \cdot \mathbf{A}_1}^{B_2})$$

$$+ \theta^3 (\overbrace{\mathbf{a}_{3,1} \cdot \mathbf{a}_1}^{b_3} - \overbrace{\mathbf{A}_{3,1} \cdot \mathbf{A}_1}^{B_3})$$

$$= \overbrace{\frac{1}{2}\left(a_{11} - A_{11}\right)}^{\epsilon} + \theta^2 \overbrace{\left(b_2 - B_2\right)}^{\kappa_{21}} + \theta^3 \overbrace{\left(b_3 - B_3\right)}^{\kappa_{31}} \tag{4.23}$$

$$E_{1\alpha} = \frac{1}{2}\left(g_{1\alpha} - G_{1\alpha}\right) = \frac{1}{2}\theta^\beta (\overbrace{\mathbf{a}_{\beta,1} \cdot \mathbf{a}_\alpha}^{t_\alpha} - \overbrace{\mathbf{A}_{\beta,1} \cdot \mathbf{A}_\alpha}^{T_\alpha}) = \frac{1}{2}\theta^\beta \overbrace{\left(t_\alpha - T_\alpha\right)}^{\kappa_{\beta\alpha}} \tag{4.24}$$

The corresponding strain in the Cartesian coordinate system is

$$\widetilde{E}_{11} = \frac{E_{11}}{\left\|\mathbf{G}_1\right\|_2^2} = \frac{\epsilon + \theta^2 \kappa_{21} + \theta^3 \kappa_{31}}{\|\mathbf{A}_1\|_2^2} \tag{4.25}$$

$$\widetilde{E}_{1\alpha} = \frac{E_{1\alpha}}{\left\|\mathbf{G}_1\right\|_2 \left\|\mathbf{G}_\alpha\right\|_2} = \frac{\theta^\beta \kappa_{\beta\alpha}}{2\|\mathbf{A}_1\|_2}, \tag{4.26}$$

where ϵ is the axial strain and $\kappa_{\alpha i}$ is the change in curvature in direction of the base vectors $\mathbf{a}_\alpha$. $\kappa_{\alpha i}$ consists either of b_α and B_α denoting the curvature of the respective configuration in the particular direction or t_α and T_α denoting the change of the torsion in the structural element formulation of the Euler-Bernoulli beam.

The second Piola-Kirchhoff stresses $\mathbf{S}$ are then computed using the elasticity tensor $\mathbb{C}$:

$$\mathbf{S} = \mathbb{C} : \mathbf{E} \tag{4.27}$$

The following term for the internal virtual work results from inserting the nonzero strain components in the equation of the weak form of the equilibrium as defined in Equation (2.36),

$$\delta W_{\text{int}} = -\int_{\Omega_0} \mathbf{S} : \delta \mathbf{E} \, d\Omega = -\int_{\Omega_0} \widetilde{S}^{11} \delta \widetilde{E}_{11} + \widetilde{S}^{12} \delta \widetilde{E}_{12} + \widetilde{S}^{13} \delta \widetilde{E}_{13} \, d\Omega \tag{4.28}$$

This term can be pre-integrated over the cross section assuming that the base vectors $\mathbf{A}_\alpha$ are the principal axes of the cross section:

$$\begin{aligned}
\delta W_{\text{int}} = -\int_{\Omega_0} & E \widetilde{E}^{11} \delta \widetilde{E}_{11} + G \widetilde{E}^{12} \delta \widetilde{E}_{12} + G \widetilde{E}^{13} \delta \widetilde{E}_{13} \, d\Omega \\
= -\int_L & \frac{E}{\|\mathbf{A}_1\|_2^4} \cdot \left(A\epsilon \, \delta\epsilon + I_{\mathbf{A}_3} \kappa_{21} \, \delta\kappa_{21} + I_{\mathbf{A}_2} \kappa_{31} \, \delta\kappa_{31} \right) \\
& + \frac{GI}{\|\mathbf{A}_1\|_2^2} \cdot \left(-\frac{1}{2} \kappa_{32} \, \delta\kappa_{32} + \frac{1}{2} \kappa_{23} \, \delta\kappa_{23} \right) dL
\end{aligned} \tag{4.29}$$

Young's modulus E and shear modulus G originate from the constitutive law of a linear elastic material.

4.5   Cable Elements

The same geometric description as for the beam can be used for the cable. In contrast to the beam, it is assumed that not only second order terms of the cross section can be neglected in the computation of the strains but also first order terms due to the high slenderness. This implies that the strain is constant over the cross section. The strain $\widetilde{E}_{11}$ is simplified and $\widetilde{E}_{1\alpha}$ vanishes.

$$\widetilde{E}_{11} = \frac{\frac{1}{2}\left(a_{11} - A_{11}\right)}{\|\mathbf{A}_1\|_2^2} = \frac{\epsilon}{\|\mathbf{A}_1\|_2^2} \tag{4.30}$$

Cables are typically prestressed. This can be considered in the analysis by adding a prestress value $\widetilde{S}^{11}_{\text{prestress}}$ to the stresses emerging from elastic deformation.

$$\widetilde{S}^{11} = \widetilde{S}^{11}_{\text{elastic}} + \widetilde{S}^{11}_{\text{prestress}} \tag{4.31}$$

The following term for the virtual work evolves:

$$\delta W_{\text{int}} = -\int_{\Omega_0} \widetilde{S}^{11} \delta \widetilde{E}_{11} \, \mathrm{d}\Omega = -\int_L \left(\frac{EA\epsilon}{\|\mathbf{A}_1\|_2^2} + \widetilde{S}^{11}_{\text{prestress}} \right) \frac{\delta\epsilon}{\|\mathbf{A}_1\|_2^2} \, \mathrm{d}L \tag{4.32}$$

Deriving the cable from the beam formulation in Equation (4.29) by removing the terms of bending and twisting leads to the same expression.

5

ISOGEOMETRIC COUPLING

This chapter elaborates on several novel coupling procedures for structural elements. Both implicit and explicit coupling are possible. The explicit coupling introduces additional conditions in order to enforce the coupling conditions. Two explicit coupling formulations will be presented. The first one implements rigid coupling between two beams (see Section 5.3) while the second one allows for slippage between a spatial point and a NURBS patch. This sliding condition will be presented for curves (see Section 5.5) but would be also applicable for surfaces. The proposed implicit coupling involves an approach of embedding structural elements inside another one. No additional coupling formulation is needed since it is already implied in the geometry description (see Section 5.4).

5.1 Fundamentals of Weak Coupling within Isogeometric Analysis

Coupling is an essential and well-researched component in the analysis of complex structures. The first approaches in IGA were restricted to

matching discretizations, i.e. coinciding control points. Later, the methods were extended to nonconforming patches. The penalty method (see e.g. Breitenberger et al. [28], Herrema et al. [67], and Lei et al. [84]), Lagrange multipliers (see e.g. Apostolatos et al. [2] and Teschemacher et al. [123]), Nitsche's (see e.g. Du et al. [49], Guo et al. [62, 63], Nguyen et al. [97], and Ruess et al. [112]) and mortar method (see e.g. Brivadis et al. [29], Dornisch et al. [47, 48], and Schuß et al. [118]) are established methodologies in IGA. An overview can be found in e.g. Apostolatos et al. [2] and Marussig et al. [92].

The coupling approaches suggested in this thesis base on the concept of Isogeometric B-Rep Analysis (IBRA) as proposed in Breitenberger [27] and Breitenberger et al. [28]. The principal steps for coupling multiple patches will be summarized in the following. These steps are essentially independent of the coupling formulation that will eventually be applied.

There are usually two patches to be coupled. One of them is referred to as master $(\bullet)^{\mathrm{m}}$ and the other one as slave $(\bullet)^{\mathrm{s}}$. An additional term is added to the virtual work in order to incorporate the coupling conditions by the penalty method. Equation (5.1) specifies this term for the coupling of the displacement $\mathbf{u}$ along a domain Γ with a penalty factor α.

$$\delta W_{\mathrm{int}}^{\mathrm{coup}} = -\int_{\Gamma_0} \alpha \cdot \left(\mathbf{u}^{\mathrm{m}} - \mathbf{u}^{\mathrm{s}}\right) \cdot \delta\left(\mathbf{u}^{\mathrm{m}} - \mathbf{u}^{\mathrm{s}}\right) \mathrm{d}\Gamma \qquad (5.1)$$

The integration over the weak coupling domain Γ is done on the master side. In general, the procedure is the same for curves and surfaces as indicated in Figure 5.1. The coupling domain has to be defined by a geometric entity. This description is an approximation, if the intersection of non-matching parametrized NURBS is not describable with NURBS or if CAD only provides a solution within the defined tolerances. This coupling domain is then typically either a point, a curve in the parameter space of a surface or an interval in the parameter space of a curve. The intersection points of all knot lines with the coupling domain have to be projected into the coupling domain in order to ensure continuous coupling (see Figure 5.1(a)). In the case of two curves, the knots of the master can be used directly and only the respective slave knots have to be projected onto the parameter space of the master curve. The coupling domain, which is described by a NURBS curve, is then refined by knot insertion at the respective knot lines. Note that this is only done for the coupling formu-

lation. The number of control points in the system and consequently the amount of DOFs is not changing. The Gauss points are set according to the refined knots. Computing the stiffness matrices and force vectors of the coupling formulation with both sides requires the projection of the integration points into the parameter space of the slave patch (see Figure 5.1(b)). The coupling domain is then integrated as described in Section 3.2.2. In the case of a point, the procedure reduces to determining the parametric coordinates of the point in both patches and evaluating the stiffness matrix and the force vector.

Alternatively, as described in Guo et al. [62], it is possible to describe the coupling domain in 3D space and use this entity as integration domain. Such an entity, named edge, is provided by CAD in B-Rep descriptions of surfaces only. It can compromise between the non-matching boundary descriptions and parametrizations of the coupled surface. Nevertheless, the parametrization, i.e. knot lines, have to be projected onto this entity.

The final outcome for FEM is always a set of integration points with integration weights and parameter coordinates on the master and the slave side.

5.2 Connecting NURBS Patches

The coupling conditions can also be used for connecting points in space and aligning cross sections (see Figure 5.2). This can be achieved by a simple change in the coupling condition which is added to the virtual work. Instead of penalizing different displacements, the difference in location between both sides can be penalized. This results in the following additional term for connecting point $\mathbf{x}^{\mathrm{m}}$ with point $\mathbf{x}^{\mathrm{s}}$.

$$\delta W_{\mathrm{int}}^{\mathrm{connect}} = -\alpha \cdot \left(\mathbf{x}^{\mathrm{m}} - \mathbf{x}^{\mathrm{s}} \right) \cdot \delta \left(\mathbf{x}^{\mathrm{m}} - \mathbf{x}^{\mathrm{s}} \right) \tag{5.2}$$

The tips of the base vectors $\mathbf{t}_i^{\mathrm{m}}$ and $\mathbf{t}_j^{\mathrm{s}}$ can be pulled together in order to align two elements by penalizing the difference of the tips.

$$\delta W_{\mathrm{int}}^{\mathrm{align}} = -\alpha \cdot \left(\mathbf{t}_i^{\mathrm{m}} - \mathbf{t}_j^{\mathrm{s}} \right) \cdot \delta \left(\mathbf{t}_i^{\mathrm{m}} - \mathbf{t}_j^{\mathrm{s}} \right) \tag{5.3}$$

Note that the indices of the base vectors do not have to match, since various right angles can be realized with this formulation. Furthermore, the

(a)

(b)
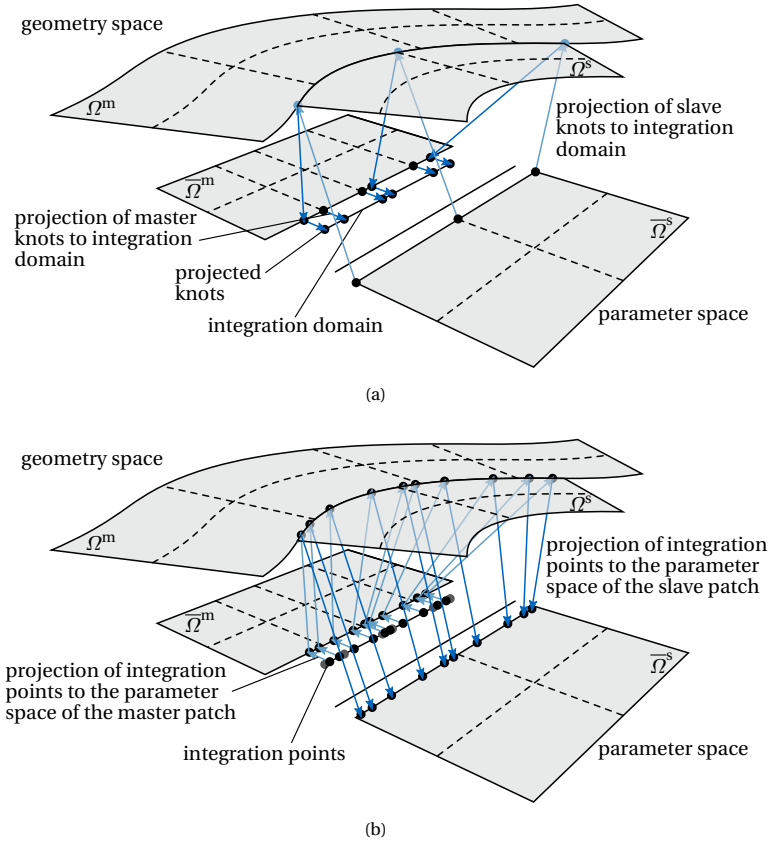
Figure 5.1: General steps of the coupling procedure of two
NURBS patches: (a) knot projection into the integration domain
and (b) projection of the integration points into the parameter
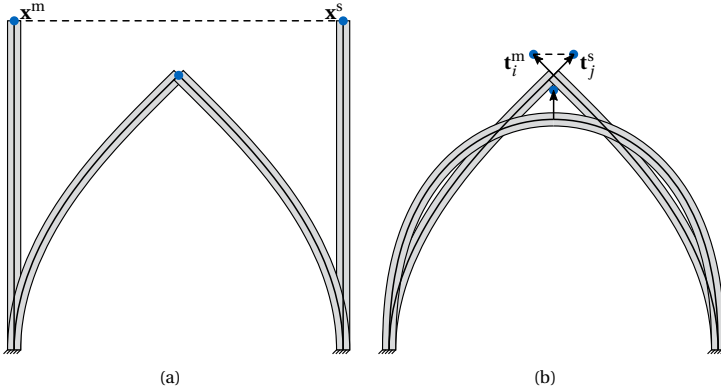domain of the NURBS patches.

Figure 5.2: (a) Connecting and (b) aligning of the cross sections of two beams.

negative value of a base vector could be used in order to get the intended alignment. Of course, the formulation can be used to align several base vectors or only one per side.

If the points are far apart or have a large angle in between, applying these conditions might result in an instable simulation in the case of geometrically nonlinear analysis. Therefore, it is proposed to apply the weak boundary condition step-wise, which is similar to increasing loads. Only a portion of the initial distance is penalized such that the points approach each other but do not have to coincide directly. This portion is then increased by $\lambda \in [0,1]$ in every step.

$$
\begin{aligned}
\delta W_{\text{int}}^{\text{connect}} = {} & -\alpha \cdot \left(\left(\mathbf{x}^{\text{m}} - \mathbf{x}^{\text{s}} \right) - (1-\lambda)\left(\mathbf{X}^{\text{m}} - \mathbf{X}^{\text{s}} \right) \right) \\
& \cdot \delta \left(\left(\mathbf{x}^{\text{m}} - \mathbf{x}^{\text{s}} \right) - (1-\lambda)\left(\mathbf{X}^{\text{m}} - \mathbf{X}^{\text{s}} \right) \right)
\end{aligned}
\tag{5.4}
$$

The simple version of this step-wise approaching has the disadvantage that the direction of the movement towards each other is predetermined. If large and potentially non-symmetric displacements are involved, this might result in large restraint stresses during the movement, which again might result in instability of the simulation. Therefore, contracting cables are recommended for complex connections. They are flexible concerning
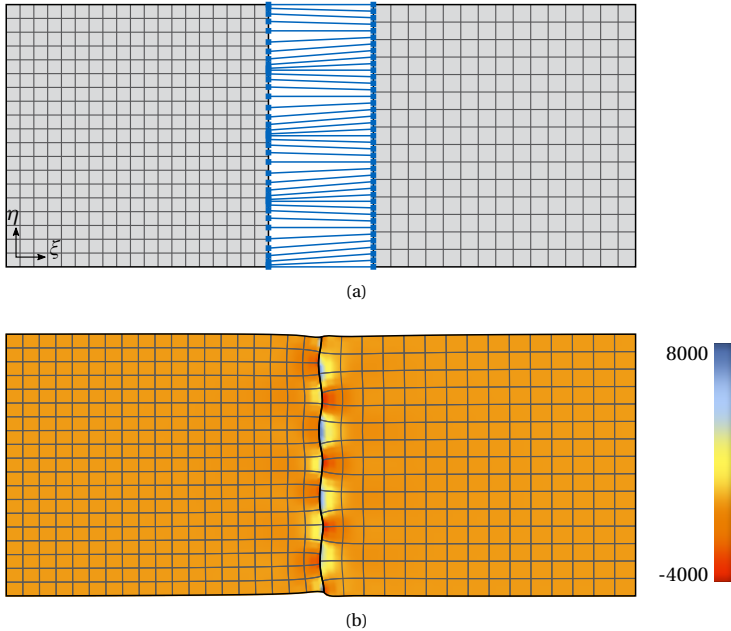
(a)

(b)
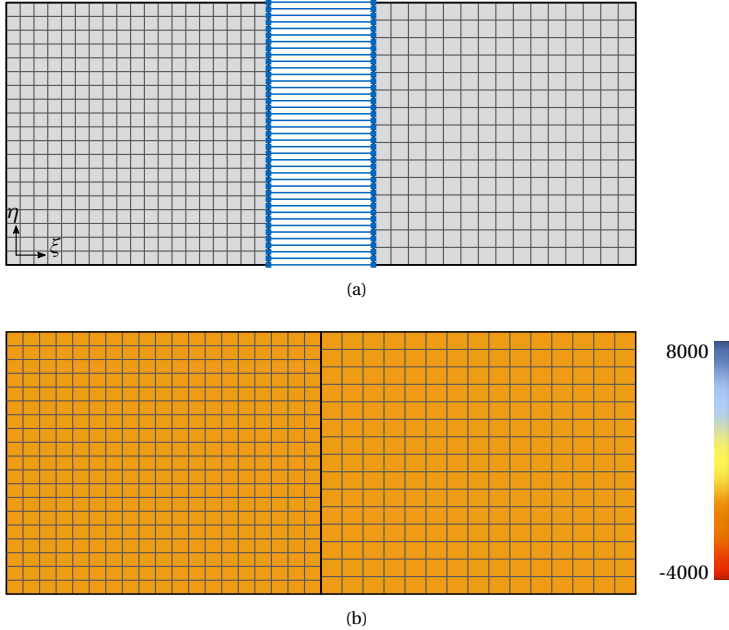
Figure 5.3: Connecting of edges with evenly distributed connectors illustrated in blue: (a) setup of shells and (b) normal force in η-direction of the connected patches.

the direction of the pulling and adapt the displacement of each step around critical points (see Lienhard [85] and Philipp [106]).

When applying this to a continuous connection, one has to take care of matching coupling points on each side. The main factor is the geometric distance between the neighboring coupling points. They should possess the same relation on both sides (see Figure 5.3). If this is not the case, stresses parallel to the coupling edge appear (see Figure 5.4).

Note that fulfilling this requirement might be non-trivial if the connecting sides have different lengths and shapes. In order to conform to the continuous coupling of edges as proposed by Breitenberger [27], one has to consider the knot spans of both sides and use $p + 1$ Gauss points per element. Nonetheless, it was observed that even fewer connection points may

(a)

(b)

Figure 5.4: Connecting of edges with not evenly distributed connectors illustrated in blue: (a) setup of shells and (b) normal force in η-direction of the connected patches.

provide good results. The number of connection points can be reduced to one for knot spans inside the domain.

5.3 Rotational Coupling of Beams

The coupling of the rotation of two adjacent beams is an essential component for the structural analysis in construction engineering. A general coupling technique for rotations is proposed in this section, which is a revised and shortened version of Bauer et al. [8]. Additional sections, which are only part of this thesis, are added as remarks and indented.

In general, there are different coupling scenarios in 2D and 3D space (see Figure 5.5 and Figure 5.6). The simplest case is a coupling at interpolated

control points with matching tangents and cross section. In 3D space, the cross sections can also be non-matching for parallel tangents (cf. Figure 5.6(b)). If the tangents remain parallel during the deformation, this case can be treated like the matching cross sections if the gap can be described by a local twisting angle around the tangent. The next step in complexity is integrating non-matching tangents. The bending strip method of Kiendl et al. [73] can be adopted in 2D space in order to enforce the kink during the deformation. However, the bending strip is not directly applicable in 3D space as it cannot enforce the torsional coupling. The most general case is a coupling inside the parametric domain, where no control points interpolate the curve with non-matching tangents and cross sections. Note that the 2D case is much simpler since the rotational axis is always defined by the normal of the plane. Hence, the rotation can be described by one angle around a fixed axis, whereas 3D space requires a more sophisticated method to uniquely describe the rotation of both sides, which is especially the case for a geometrically nonlinear application. Greco and Cuomo proposed a G^1-coupling for Euler-Bernoulli kinematics in Greco et al. [59] at interpolated control points. Coupling of Timoshenko beams in the strong form may inherently be given if the degrees of freedom for the cross section are defined globally, e.g. by quaternions in Weeger et al. [129]. In the present paper, an approach to directly deal with the last and the most general scenario for structural elements without these respective DOFs is proposed. Furthermore, the formulation will be valid for large displacements and rotations in 3D space in the context of a geometrically nonlinear analysis.

5.3.1   Element Formulation

A special coupling condition is needed in the context of isogeometric analysis since the isogeometric FE nodes with the degrees of freedom are in general not interpolating and since there are structural elements without global degrees of freedom for rotations.

Consequently, the strong form of the coupling condition is not possible, even for displacements, in the general case if the discretization and the parametric continuity should remain unchanged. By allowing a change in the parametrization, it is legitimate to insert as many knots as necessary for a C^0-continuity in order to generate an interpolating control point at
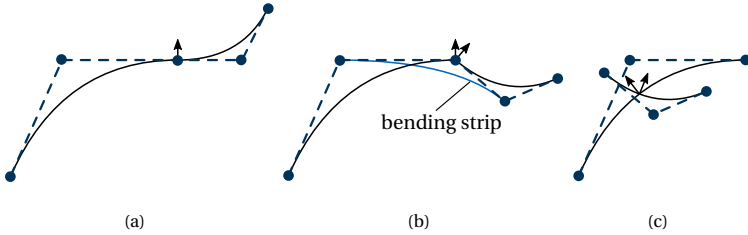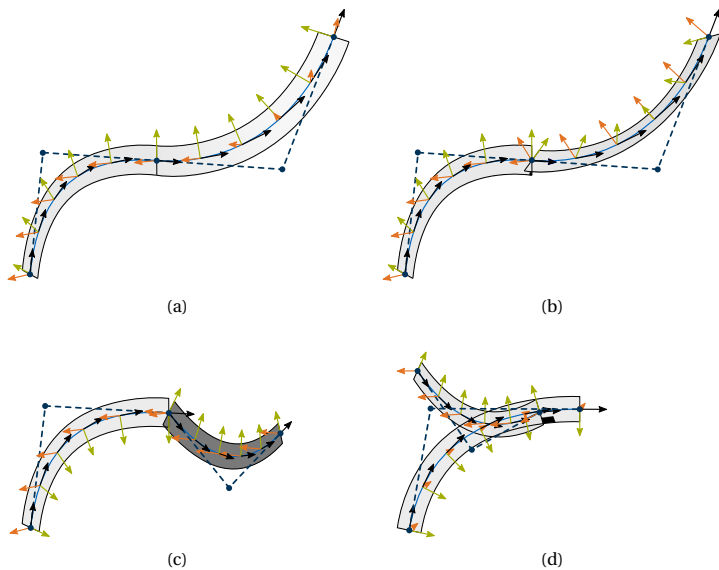
Figure 5.5: Coupling scenarios in 2D space with increasing complexity: (a) matching cross section and interpolated control points at patch boundaries, (b) non-matching cross section and interpolated control points and (c) non-matching cross section and non-interpolated control points (adapted from Bauer et al. [8]).

the coupling location (see Figure 5.7), which is e.g. used by Greco et al. [59]. The continuity is then maintained by deriving respective kinematic constraints for the DOFs on the nodes. This procedure can be bypassed by a weak formulation of the coupling problem as shown in the following. Generally, there are several methods to apply boundary conditions in a weak sense to a structural system, e.g. penalty approach, (augmented) Lagrange method or Nitsche method. The penalty approach is chosen since it provides sufficiently good results (Apostolatos et al. [2] and Breitenberger [27]) for isogeometric shell models and is a flexible and straight-forward to implement approach.

General Weak Form of the Coupling Formulation

There are basically two conditions which can be used for enforcing coupling. It can be assured that either both sides of the coupling condition follow the same translation and rotation (see Equation (5.5)) or that the relation between the both sides (see Equation (5.6)) is constant (see also Figure 5.8). Both approaches result in an additional term in the virtual work:

$$\delta W^{\text{coup}} = -\alpha^{\text{disp}} \cdot \left(\mathbf{u}^{\text{m}} - \mathbf{u}^{\text{s}}\right) \cdot \delta\left(\mathbf{u}^{\text{m}} - \mathbf{u}^{\text{s}}\right) + \alpha^{\text{rot}} \cdot \left(\mathbf{w}^{\text{m}} - \mathbf{w}^{\text{s}}\right) \cdot \delta\left(\mathbf{w}^{\text{m}} - \mathbf{w}^{\text{s}}\right)$$

$$(5.5)$$

Figure 5.6: Coupling scenarios in 3D space with increasing complexity: (a) matching cross section and interpolated control points at patch boundaries, (b) non-matching cross section, parallel tangents and interpolated control points, (c) non-matching cross section, non-parallel tangents and interpolated control points and (d) non-matching cross section and tangents and non-interpolated control points (adapted from Bauer et al. [8]).

$$\delta W^{\mathrm{coup}} = -\alpha^{\mathrm{disp}} \cdot \left(\left(\mathbf{x}^{\mathrm{m}} - \mathbf{x}^{\mathrm{s}} \right) - \left(\mathbf{X}^{\mathrm{m}} - \mathbf{X}^{\mathrm{s}} \right) \right) \cdot \delta \left(\left(\mathbf{x}^{\mathrm{m}} - \mathbf{x}^{\mathrm{s}} \right) - \left(\mathbf{X}^{\mathrm{m}} - \mathbf{X}^{\mathrm{s}} \right) \right)$$
$$- \alpha^{\mathrm{rot}} \cdot \left(r \left(\mathbf{t}^{\mathrm{m}}, \mathbf{t}^{\mathrm{s}} \right) - \delta r \left(\mathbf{T}^{\mathrm{m}}, \mathbf{T}^{\mathrm{s}} \right) \right) \tag{5.6}$$

with α^{disp} being the penalty factor for displacements and α^{rot} for rotations. $\mathbf{u}$ and $\mathbf{w}$ represent translation and rotation whereas $r\left(\mathbf{T}^{\mathrm{m}}, \mathbf{T}^{\mathrm{s}}\right)$ quantifies the relation between two vectors on the master and slave sides. A preliminary study on the choice of the penalty factor for the proposed coupling conditions was conducted and will be presented in Section 5.3.2.
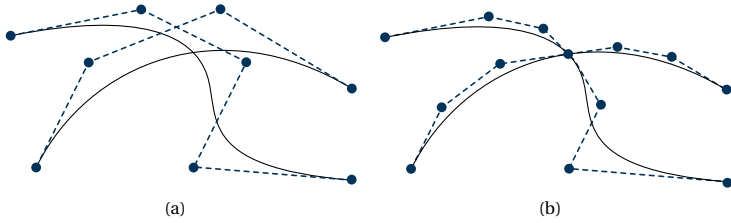
Figure 5.7: Two coupled curves with their control points: (a) no interpolation of the curve through a control point at the coupling point and (b) with respective C^0-continuity at the coupling point for interpolated control points (adapted from Bauer et al. [8]).
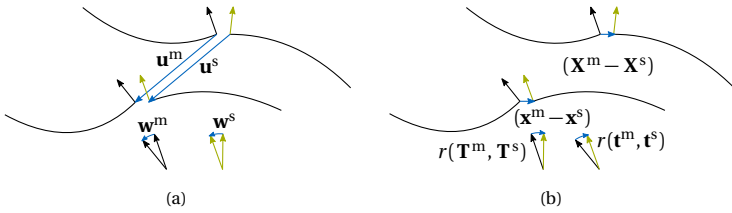
Figure 5.8: Coupling conditions: (a) same displacement and rotation and (b) same relation between position and base vectors in initial and actual configuration (adapted from Bauer et al. [8]).

The respective contributions to the right-hand-side R_r^{coup} and the stiffness matrix K_{rs}^{coup} are defined similarly to the structural element formulations by deriving the additional term with respect to the degrees of freedom $\hat{u}_r / \hat{u}_s$. This is shown for Equation (5.5) since this will eventually be chosen.

$$R_r^{\text{coup}} = \alpha^{\text{disp}} \cdot \left(\mathbf{u}^{\text{m}} - \mathbf{u}^{\text{s}}\right) \cdot \frac{\partial \left(\mathbf{u}^{\text{m}} - \mathbf{u}^{\text{s}}\right)}{\partial \hat{u}_r} + \alpha^{\text{rot}} \cdot \left(\mathbf{w}^{\text{m}} - \mathbf{w}^{\text{s}}\right) \cdot \frac{\partial \left(\mathbf{w}^{\text{m}} - \mathbf{w}^{\text{s}}\right)}{\partial \hat{u}_r}$$

(5.7)

$$K_{rs}^{\text{coup}} = \alpha^{\text{disp}} \cdot \frac{\partial \left(\mathbf{u}^{\text{m}} - \mathbf{u}^{\text{s}}\right)}{\partial \hat{u}_s} \cdot \frac{\partial \left(\mathbf{u}^{\text{m}} - \mathbf{u}^{\text{s}}\right)}{\partial \hat{u}_r} + \alpha^{\text{rot}} \cdot \frac{\left(\mathbf{w}^{\text{m}} - \mathbf{w}^{\text{s}}\right)}{\partial \hat{u}_s} \cdot \frac{\partial \left(\mathbf{w}^{\text{m}} - \mathbf{w}^{\text{s}}\right)}{\partial \hat{u}_r}$$

$$+ \alpha^{\text{rot}} \cdot \left(\mathbf{w}^{\text{m}} - \mathbf{w}^{\text{s}}\right) \cdot \frac{\partial^2 \left(\mathbf{w}^{\text{m}} - \mathbf{w}^{\text{s}}\right)}{\partial \hat{u}_r \, \partial \hat{u}_s}$$

(5.8)

73

The derivation of a coupling condition for large displacements and rotations is shown at the example of a beam since it is one of the most obvious application examples. However, it can be transferred to every other formulation, such as the Kirchhoff-Love shell, with respective properties. The coupling of different structural elements, e.g. shell and beam, is also possible.

Coupling Conditions

A general, nonlinear coupling condition is required to be unique without singularity for every configuration of connection and displacement. As already mentioned, there are in principle two ways of describing a coupling condition. Either the relation between the two triads of the beams is preserved or it has to be ensured that the points including the respective triads on each side deform in the same way. A coupling condition which enforces the same displacement and rotation on both sides is chosen since the formulation should be general and applicable to rotational supports. By choosing the relative condition, it would be necessary to define a reference triad at a support, which is less intuitive. However, the two conditions are convertible into each other. The respective changes will briefly be shown after the proposed, implemented and tested formulation.

Describing large displacements and rotations in a unique way in 3D space can be demanding for arbitrary initial configurations. Therefore, the approach of Lumpe et al. [90] for a nonlinear beam formulation was used and modified. There, the displacements of the tips of the base vectors were used to describe the rotation of the cross section of a nonlinear beam element from the reference configuration to the actual one. These displacements are computed by the difference of the reference and the actual base vector. The displacements of the three base vectors are then split into parts which are oriented along the reference base vectors. Consequently, nine projected displacements evolve for an arbitrary rotation in space. In contrast to Lumpe et al. [90], the amount of considered projected tip displacements was not reduced to three displacements describing the rotation in space for this coupling condition. This decision is based on the fact that the orthonormal base vectors do not have to be kept orthonormal as they are defined by the structural element and not the rotation components. Furthermore, a singularity can be avoided for large rotations by taking every tip displacement component into account. Figure 5.9 shows
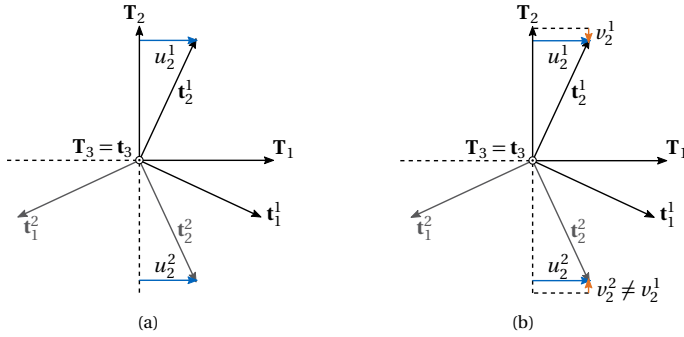
Figure 5.9: Description of the rotation of base vectors by their tip displacement: (a) one displacement value and respective valid configuration and (b) two displacement values (adapted from Bauer et al. [8]).

a simple rotation around $\mathbf{T}_3$. With the reduction, only the displacement of the tip of $\mathbf{T}_2$ in $\mathbf{T}_1$-direction would be taken into account and consequently there are two valid configurations $\mathbf{t}_i^{\alpha}$ (see Figure 5.9(a)) with the same displacement u_2. If the second displacement component of the tip is also included in the formulation, the rotation is uniquely defined since the component of the tip displacement in the direction of the base vector is not equal for the two possible configurations of Figure 5.9(a) (see Figure 5.9(b)).

Note that in our case of 3D rotations of an orthonormal triad, the tip displacements of only two of three base vectors would be sufficient to uniquely describe the rotation. However, all of them are considered in order to provide a general implementation.

Additionally, the rotations are expressed by a projection into the local coordinate system of the initial beam of the master side in this contribution, which is indicated by $w_{\bullet/\mathbf{T}_i^{\mathrm{m}}}$. This allows the coupling of selected directions. As the same displacement and rotation should be enforced on both sides, the following coupling conditions can be used, where u is the displacement of the spatial point of the center line and w is the difference of the base vectors in the actual and reference configuration:

$$u_x^{\mathrm{m}} = u_x^{\mathrm{s}} \qquad\qquad u_y^{\mathrm{m}} = u_y^{\mathrm{s}} \qquad\qquad u_z^{\mathrm{m}} = u_z^{\mathrm{s}} \qquad (5.9)$$
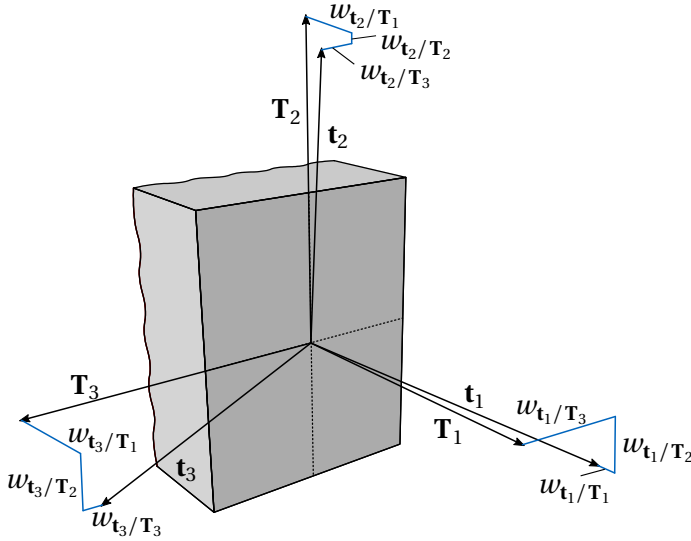
Figure 5.10: Rotation of the cross sectional triad and respective tip displacements of the base vectors separated into the components of the initial base vectors (adapted from Bauer et al. [8]).

$$w^{\mathrm{m}}_{\mathbf{t}^{\mathrm{m}}_1/\mathbf{T}^{\mathrm{m}}_1} = w^{\mathrm{s}}_{\mathbf{t}^{\mathrm{s,mod}}_1/\mathbf{T}^{\mathrm{m}}_1} \qquad w^{\mathrm{m}}_{\mathbf{t}^{\mathrm{m}}_1/\mathbf{T}^{\mathrm{m}}_2} = w^{\mathrm{s}}_{\mathbf{t}^{\mathrm{s,mod}}_1/\mathbf{T}^{\mathrm{m}}_2} \qquad w^{\mathrm{m}}_{\mathbf{t}^{\mathrm{m}}_1/\mathbf{T}^{\mathrm{m}}_3} = w^{\mathrm{s}}_{\mathbf{t}^{\mathrm{s,mod}}_1/\mathbf{T}^{\mathrm{m}}_3} \qquad (5.10)$$

$$w^{\mathrm{m}}_{\mathbf{t}^{\mathrm{m}}_2/\mathbf{T}^{\mathrm{m}}_1} = w^{\mathrm{s}}_{\mathbf{t}^{\mathrm{s,mod}}_2/\mathbf{T}^{\mathrm{m}}_1} \qquad w^{\mathrm{m}}_{\mathbf{t}^{\mathrm{m}}_2/\mathbf{T}^{\mathrm{m}}_2} = w^{\mathrm{s}}_{\mathbf{t}^{\mathrm{s,mod}}_2/\mathbf{T}^{\mathrm{m}}_2} \qquad w^{\mathrm{m}}_{\mathbf{t}^{\mathrm{m}}_2/\mathbf{T}^{\mathrm{m}}_3} = w^{\mathrm{s}}_{\mathbf{t}^{\mathrm{s,mod}}_2/\mathbf{T}^{\mathrm{m}}_3} \qquad (5.11)$$

$$w^{\mathrm{m}}_{\mathbf{t}^{\mathrm{m}}_3/\mathbf{T}^{\mathrm{m}}_1} = w^{\mathrm{s}}_{\mathbf{t}^{\mathrm{s,mod}}_3/\mathbf{T}^{\mathrm{m}}_1} \qquad w^{\mathrm{m}}_{\mathbf{t}^{\mathrm{m}}_3/\mathbf{T}^{\mathrm{m}}_2} = w^{\mathrm{s}}_{\mathbf{t}^{\mathrm{s,mod}}_3/\mathbf{T}^{\mathrm{m}}_2} \qquad w^{\mathrm{m}}_{\mathbf{t}^{\mathrm{m}}_3/\mathbf{T}^{\mathrm{m}}_3} = w^{\mathrm{s}}_{\mathbf{t}^{\mathrm{s,mod}}_3/\mathbf{T}^{\mathrm{m}}_3} \qquad (5.12)$$

with

$$w_{\mathbf{t}_i/\mathbf{T}^{\mathrm{m}}_j} = \left(\mathbf{t}_i - \mathbf{T}^{\mathrm{m}}_i\right)\cdot \mathbf{T}^{\mathrm{m}}_j \qquad (5.13)$$

All considered tip displacements $w_{\mathbf{t}_i/\mathbf{T}_j}$ are shown in Figure 5.10.

Since the triads of the initial configuration are not aligned in the general case and the rotation should be described by the tip displacements of the base vectors, one side has to be mapped in a unique way to the other in order to describe the displacement with respect to one local initial
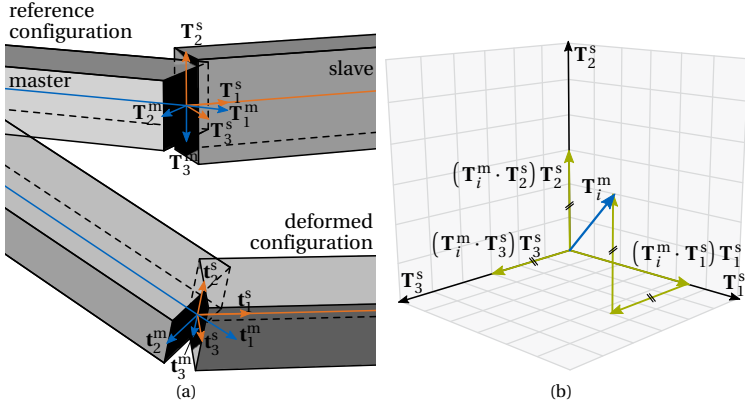
Figure 5.11: Mapping operation from slave to master side: (a) beam configuration in undeformed and deformed configuration and (b) splitting a base vector from the master side into the components of the slave triad (adapted from Bauer et al. [8]).

coordinate system. This can be done by using the projection rule of the initial coordinate systems also for the actual coordinate systems.

A mapping of a base vector $\mathbf{t}_i^s$ from the slave side to the master side $\mathbf{t}_i^{s,mod}$ can be computed by the following

$$\mathbf{t}_i^{s,mod} = \left(\mathbf{T}_i^m \cdot \mathbf{T}_1^s\right) \mathbf{t}_1^s + \left(\mathbf{T}_i^m \cdot \mathbf{T}_2^s\right) \mathbf{t}_2^s + \left(\mathbf{T}_i^m \cdot \mathbf{T}_3^s\right) \mathbf{t}_3^s \tag{5.14}$$

This mapping is unique for arbitrary configurations and preserves the initial relation, which is also illustrated in Figure 5.11.

Figure 5.12 shows an overview of all steps in the coupling formulation, which have to be conducted. The relation between the master and slave point in the reference configuration is used to transform the actual configuration of the slave point. These modified base vectors $\mathbf{t}_i^{s,mod}$ and the actual base vectors of the master point $\mathbf{t}_i^m$ are then used for the difference vector with the reference master base vectors $\mathbf{T}_i^m$. The difference vectors are projected into the reference master coordinate system. These projections $w_{\mathbf{t}_i^{m/s,mod}/\mathbf{T}_j^m}$ are used to evaluate the difference in rotation of both sides by comparison.
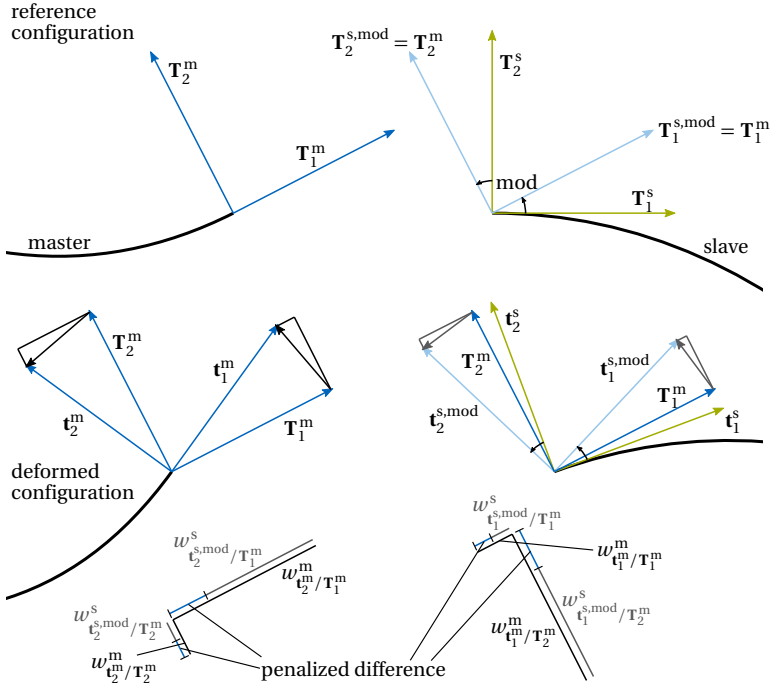
Figure 5.12: All mapping steps of the proposed coupling condition (adapted from Bauer et al. [8]).

Moreover, coupling conditions can be applied for only one base vector. This corresponds to a scissor joint which can also change its orientation in space during the deformation process (see Figure 5.13). The respective conditions for a pin in $\mathbf{t}_2^m$ direction would e.g. be:

$$u_x^m = u_x^s \qquad\qquad u_y^m = u_y^s \qquad\qquad u_z^m = u_z^s \qquad (5.15)$$

$$w_{\mathbf{t}_2^m/\mathbf{T}_1^m}^m = w_{\mathbf{t}_2^{s,mod}/\mathbf{T}_1^m}^s \qquad w_{\mathbf{t}_2^m/\mathbf{T}_2^m}^m = w_{\mathbf{t}_2^{s,mod}/\mathbf{T}_2^m}^s \qquad w_{\mathbf{t}_2^m/\mathbf{T}_3^m}^m = w_{\mathbf{t}_2^{s,mod}/\mathbf{T}_3^m}^s \qquad (5.16)$$

Note that these displacements could also be transformed into angles which would give a direct analogy to a rotational spring. However, this would
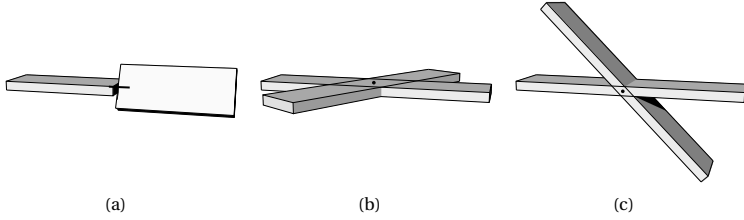
Figure 5.13: Scissor joints: (a) free torsion with $w_{\mathbf{t}_1/\mathbf{T}_i^{\mathrm{m}}}$, (b) free bending moment M_ν with $w_{\mathbf{t}_2/\mathbf{T}_i^{\mathrm{m}}}$ and (c) free bending moment M_n with $w_{\mathbf{t}_3/\mathbf{T}_i^{\mathrm{m}}}$ (adapted from Bauer et al. [8]).

result in a more complex computation of the derivatives and variations in the implementation.

Alternative Coupling Conditions

This section briefly shows how the components of the proposed coupling condition can be used in alternative approaches.

Displacements w.r.t. the local coordinate system

The displacements can also be expressed in the local coordinate system of the master. This is simple for the reference local system, which can be used for e.g. supports.

$$u_{\mathbf{T}_i^{\mathrm{m}}}^{\mathrm{m}} = \mathbf{u}^{\mathrm{m}} \cdot \mathbf{T}_i^{\mathrm{m}} = \mathbf{u}^{\mathrm{s}} \cdot \mathbf{T}_i^{\mathrm{m}} = u_{\mathbf{T}_i^{\mathrm{m}}}^{\mathrm{s}} \tag{5.17}$$

The same holds for the local coordinate system in the actual configuration. This is for example useful for the modeling of shear force hinges.

$$u_{\mathbf{t}_i^{\mathrm{m}}}^{\mathrm{m}} = \mathbf{u}^{\mathrm{m}} \cdot \mathbf{t}_i^{\mathrm{m}} = \mathbf{u}^{\mathrm{s}} \cdot \mathbf{t}_i^{\mathrm{m}} = u_{\mathbf{t}_i^{\mathrm{m}}}^{\mathrm{s}} \tag{5.18}$$

In contrast to the local reference frame, this is not directly compatible with the implementation of the originally proposed method as additional variations arise with the projection to $\mathbf{t}_i^{\mathrm{m}}$ since $\mathbf{t}_i^{\mathrm{m}}$ is dependent on the DOFs.

Rotations w.r.t. the global coordinate system

The rotation of $\mathbf{t}_i^m$ and $\mathbf{t}_i^{s,\text{mod}}$ could also be measured in the global coordinate system which results in a small change in the coupling conditions.

$$\mathbf{w}_{\mathbf{t}_i}^m = \left(\mathbf{t}_i^m - \mathbf{T}_i^m\right) \tag{5.19}$$

$$\mathbf{w}_{\mathbf{t}_i}^{s,\text{mod}} = \left(\mathbf{t}_i^{s,\text{mod}} - \mathbf{T}_i^{s,\text{mod}}\right) \tag{5.20}$$

$$\mathbf{w}_{\mathbf{t}_i}^m = \mathbf{w}_{\mathbf{t}_i}^{s,\text{mod}} \tag{5.21}$$

This modification is especially useful for boundary conditions, which are aligned to the global system, if the local coordinate system is not applicable. It implies only a minimal change in the implementation and both options can easily be provided.

Remark: Rotation of an arbitrary local axis

The same mapping that is used for the mapping of the slave to the master side, can also be used to generate an arbitrarily oriented pin joint between two structural elements (see Figure 5.14). Furthermore, it can be applied for restraining an arbitrary rotation in a support point.

Therefore, the rotation axis $\mathbf{J}$ is expressed by the reference base vectors of each side, which is equal to the mapping in Equation (5.14). The transformation rule is then applied to the actual base vectors of both sides.

$$\mathbf{t}_{\mathbf{J}}^{m,\text{mod}} = \left(\mathbf{J} \cdot \mathbf{T}_1^m\right) \mathbf{t}_1^m + \left(\mathbf{J} \cdot \mathbf{T}_2^m\right) \mathbf{t}_2^m + \left(\mathbf{J} \cdot \mathbf{T}_3^m\right) \mathbf{t}_3^m \tag{5.22}$$

$$\mathbf{t}_{\mathbf{J}}^{s,\text{mod}} = \left(\mathbf{J} \cdot \mathbf{T}_1^s\right) \mathbf{t}_1^s + \left(\mathbf{J} \cdot \mathbf{T}_2^s\right) \mathbf{t}_2^s + \left(\mathbf{J} \cdot \mathbf{T}_3^s\right) \mathbf{t}_3^s \tag{5.23}$$

Thereby, the globally defined rotation axis becomes a locally defined rotation axis and can rotate with the structure during the analysis. The displacement of the tip of the axis expressed by the transformed base vectors is then compared in the coupling condition. Note that the displacements are expressed in
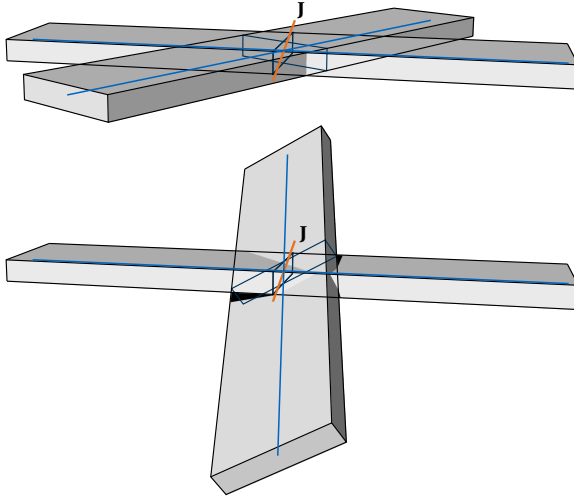
Figure 5.14: Coupling of two beams by an arbitrarily oriented pin joint: reference and deformed configuration.

the initial local coordinate system of the master side, which could also be replaced by another one.

$$w^{\mathrm{m}}_{\mathbf{t}^{\mathrm{m,mod}}_{\mathbf{J}}/\mathbf{T}^{\mathrm{m}}_1} = w^{\mathrm{s}}_{\mathbf{t}^{\mathrm{s,mod}}_{\mathbf{J}}/\mathbf{T}^{\mathrm{m}}_1} \tag{5.24}$$

$$w^{\mathrm{m}}_{\mathbf{t}^{\mathrm{m,mod}}_{\mathbf{J}}/\mathbf{T}^{\mathrm{m}}_2} = w^{\mathrm{s}}_{\mathbf{t}^{\mathrm{s,mod}}_{\mathbf{J}}/\mathbf{T}^{\mathrm{m}}_2} \tag{5.25}$$

$$w^{\mathrm{m}}_{\mathbf{t}^{\mathrm{m,mod}}_{\mathbf{J}}/\mathbf{T}^{\mathrm{m}}_3} = w^{\mathrm{s}}_{\mathbf{t}^{\mathrm{s,mod}}_{\mathbf{J}}/\mathbf{T}^{\mathrm{m}}_3} \tag{5.26}$$

Relative condition

The relative coupling condition of the displacements is directly convertible to the enforcing of the same displacements on both sides.

$$\begin{aligned}
\delta W^{\mathrm{coup}} &= -\alpha^{\mathrm{disp}} \cdot \left(\left(\mathbf{x}^{\mathrm{m}} - \mathbf{x}^{\mathrm{s}} \right) - \left(\mathbf{X}^{\mathrm{m}} - \mathbf{X}^{\mathrm{s}} \right) \right) \cdot \delta \left(\left(\mathbf{x}^{\mathrm{m}} - \mathbf{x}^{\mathrm{s}} \right) - \left(\mathbf{X}^{\mathrm{m}} - \mathbf{X}^{\mathrm{s}} \right) \right) \\
&= -\alpha^{\mathrm{disp}} \cdot \left(\left(\mathbf{x}^{\mathrm{m}} - \mathbf{X}^{\mathrm{m}} \right) - \left(\mathbf{x}^{\mathrm{s}} - \mathbf{X}^{\mathrm{s}} \right) \right) \cdot \delta \left(\left(\mathbf{x}^{\mathrm{m}} - \mathbf{X}^{\mathrm{m}} \right) - \left(\mathbf{x}^{\mathrm{s}} - \mathbf{X}^{\mathrm{s}} \right) \right) \\
&= -\alpha^{\mathrm{disp}} \cdot \left(\mathbf{u}^{\mathrm{m}} - \mathbf{u}^{\mathrm{s}} \right) \cdot \delta \left(\mathbf{u}^{\mathrm{m}} - \mathbf{u}^{\mathrm{s}} \right)
\end{aligned} \tag{5.27}$$

The proposed approach can also provide a relative condition for the rotations. Comparing the deformed base vectors $\mathbf{t}_i^{\mathrm{m}}$ and $\mathbf{t}_i^{\mathrm{s,mod}}$ would be for example a relative condition since the modified slave base vectors are computed such that they reproduce the initial relation between the two coupling partners.

$$\mathbf{t}_i^{\mathrm{m}} = \mathbf{t}_i^{\mathrm{s,mod}} \tag{5.28}$$

The relative angles between all base vectors could also explicitly be measured and be enforced to be constant.

Remark: Shell - beam coupling

The presented method can also be used to couple the rotations of a beam and a shell. The approach only has to be modified in the sense that the shell provides an orthonormal coordinate system at the coupling point. Such an orthonormal basis can be defined by e.g. $\mathbf{G}_1$ and the surface normal $\mathbf{G}_3$.

$$\mathbf{T}_1 = \frac{\mathbf{G}_1}{\|\mathbf{G}_1\|_2} \tag{5.29}$$

$$\mathbf{T}_3 = \frac{\mathbf{G}_1 \times \mathbf{G}_2}{\|\mathbf{G}_1 \times \mathbf{G}_2\|_2} = \mathbf{G}_3 \tag{5.30}$$

$$\mathbf{T}_2 = \mathbf{T}_3 \times \mathbf{T}_1 \tag{5.31}$$

All presented steps and alternative formulations can be used after replacing the respective base vectors on one side.

5.3.2 Examples

Several benchmarks will be performed in the following in order to prove the validity and generality of the proposed coupling formulation for an Euler-Bernoulli beam.

Cantilever

A straight cantilever modeled by two beams is shown as first benchmark (see Figure 5.15). The coupling point is in the middle of the total length of
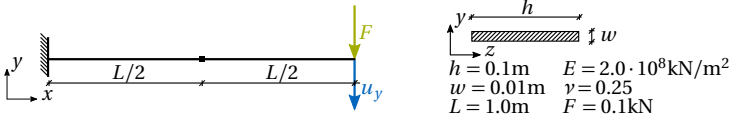
Figure 5.15: Setup of a cantilever with tip load consisting of two beams (adapted from Bauer et al. [8]).

the cantilever. It is loaded by a tip load. A linear analysis is performed in order to have analytic results to compare with.

Figure 5.16 shows the relative error of the displacement for a range of penalty factors for rotation coupling. The penalty factor of displacements is kept constant to $\alpha^{\text{disp}} = 10^{10}$ since it was observed that the result is only affected by the expected error which is introduced modeling the coupling condition with the penalty method, i.e. adding a virtual spring between the coupled points. The error of the tip displacement of the cantilever is dominated by the evolving gap $\Delta u = \frac{F}{\alpha^{\text{disp}}} = \frac{0.1}{10^{10}} = 10^{-11}$. Furthermore, the number of elements per beam and the polynomial degree is varied. The relative error of the tip displacement is computed with the analytic solution as reference as follows:

$$\varepsilon_{u_y} = \frac{u_y - u_y^{\text{ref}}}{u_y^{\text{ref}}} \quad \text{with} \quad u_y^{\text{ref}} = \frac{FL^3}{3EI_z} \tag{5.32}$$

It can be observed that the quality of the results improves in the beginning as expected for an increasing penalty factor. After a certain level, here $\alpha^{\text{rot}} = 10^9$, the quality of the result is corrupted by the conditioning of the equation system solved in the analysis.

A circular cross section is used as a second benchmark example in order to be able to check different relative orientations of the cross sections against the single beam solution (see Figure 5.17). Furthermore, a geometrically nonlinear analysis is conducted in order to check large displacements. The cantilever is bent by a single force at the tip. The first beam is fixed whereas the initial cross section orientation of the second beam is rotated around its axis by an angle ϕ. Each coupled beam is modeled by a B-Spline with polynomial degree $p = 5$ and 16 elements, which corresponds to 21 control points. The single beam is modeled by 32 elements with polynomial degree
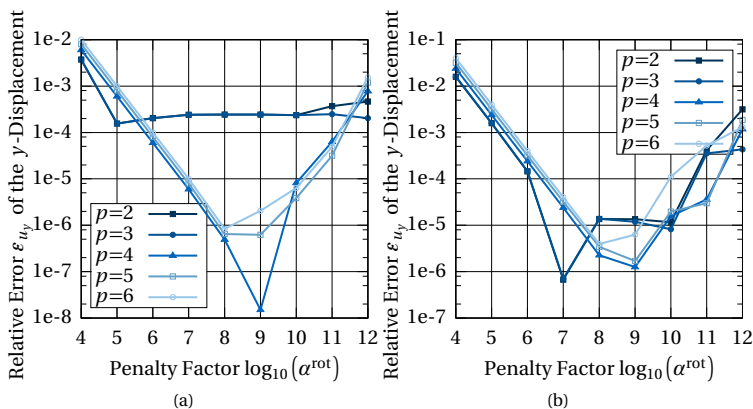
Figure 5.16: Relative error of the u_y-displacement of a cantilever under a tip load modeled by two coupled beams with different amount of elements: (a) 16 elements and (b) 64 elements (adapted from Bauer et al. [8]).

$p = 5$, which results in 37 control points. The penalty factors are $\alpha^{\mathrm{disp}} = 10^{12}$ and $\alpha^{\mathrm{rot}} = 10^9$.

One can observe that the evolving gap Δu between the two coupled ends correlates to the penalty factor which was chosen to be $\alpha^{\mathrm{disp}} = 10^{12}$ (see Figure 5.18(a)). The penalty factor acts like a spring with stiffness α^{disp} between the two beams. The gap opens only in the direction of the load and the length of the gap corresponds to the elongation of a spring under the respective load which is transferred in this joint.

$$\Delta u = \|\mathbf{u}^{\mathrm{m}} - \mathbf{u}^{\mathrm{s}}\|_2 = \Delta u_z = \frac{F}{\alpha^{\mathrm{disp}}} = \frac{25}{10^{12}} = 2.5 \cdot 10^{-11} \tag{5.33}$$

The relative angle between the two beams remains almost constant as can be seen in Figure 5.18(b).

$$\varepsilon_{\phi_i} = \arccos(\mathbf{t}_i^{\mathrm{m}} \cdot \mathbf{t}_i^{\mathrm{s}}) - \arccos(\mathbf{T}_i^{\mathrm{m}} \cdot \mathbf{T}_i^{\mathrm{s}}) \tag{5.34}$$

The relative error of the absolute displacement at the coupling point $\mathbf{u}^{\mathrm{mid}}$ and at the tip $\mathbf{u}^{\mathrm{tip}}$ is computed using the single patch solution as reference.
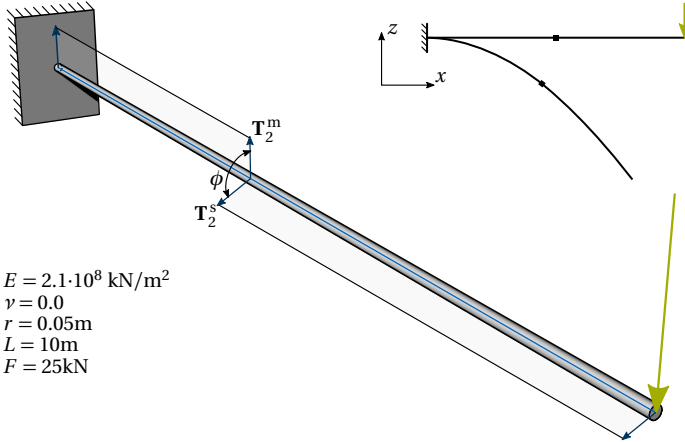
Figure 5.17: Setup of a cantilever with tip load consisting of two beams with circular cross section where the second beam is rotated around its axis (adapted from Bauer et al. [8]).

The results are depicted in Figure 5.18(c) and Figure 5.18(d).

$$\varepsilon_{u_i^{\text{mid}}} = \frac{u_{i,\text{coupled}}^{\text{mid}} - u_{i,\text{single}}^{\text{mid}}}{u_{i,\text{single}}^{\text{mid}}} \qquad\qquad \varepsilon_{u_i^{\text{tip}}} = \frac{u_{i,\text{coupled}}^{\text{tip}} - u_{i,\text{single}}^{\text{tip}}}{u_{i,\text{single}}^{\text{tip}}}$$

$$(5.35)$$

The coupled beams show very good accordance with the single beam solution, also for varying correlation between the base vectors of the cross section.

Circular Arch Cantilever

The next example will test the most complex loading on the coupling, i.e. bending torsion interaction. Therefore, a circular arch cantilever with a point load on the free end is chosen (see Figure 5.19). The beams are modeled with the same parametric discretization, but the polynomial degree and the number of elements are varied.
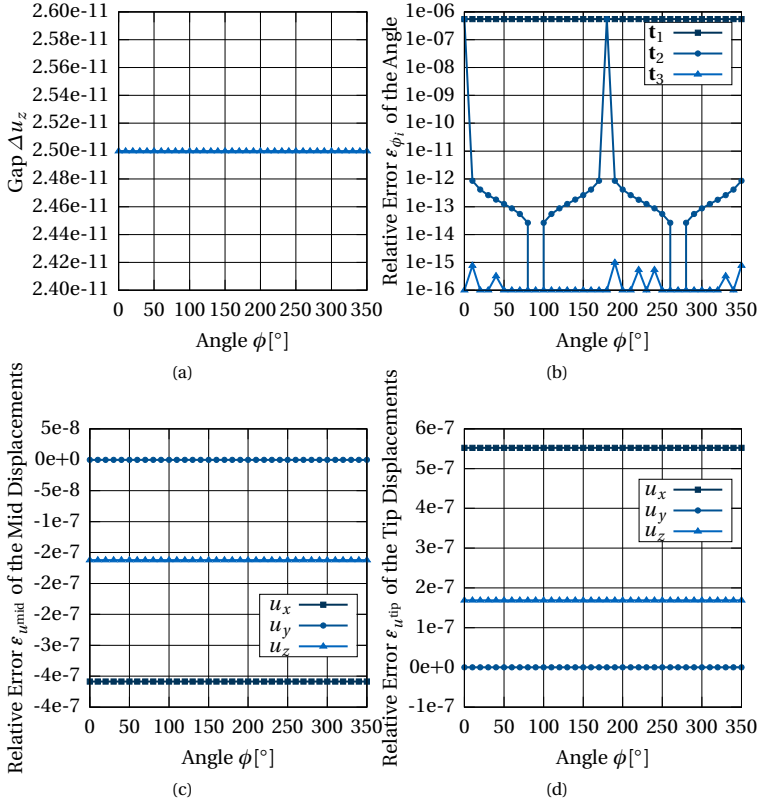
Figure 5.18: Results of the cantilever beam with rotating cross section: (a) evolving gap between the two beams, (b) error of the angle between the cross sectional base vector, (c) relative error of the displacements at the coupling point and (d) relative error of the displacements at the tip (adapted from Bauer et al. [8]).
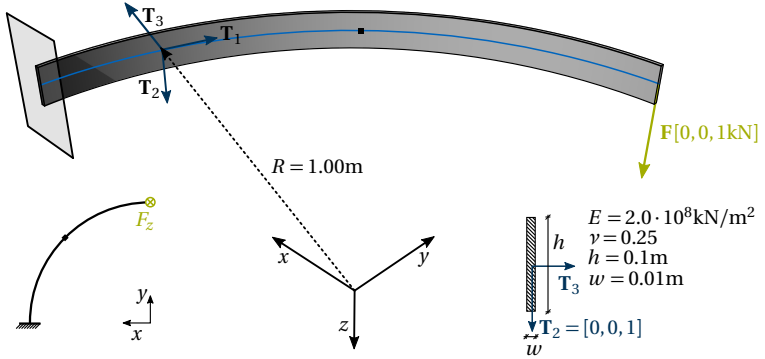
Figure 5.19: Setup of a quarter circle cantilever (adapted from Bauer et al. [10]) (adapted from Bauer et al. [8]).

The linear analytic results of the tip displacement and the support forces at the clamped end are computed as follows:

$$u_z^{\text{tip}} = \int_0^{\frac{\pi}{2}} \left(\frac{1}{EI_3}(-FR \cdot \cos\alpha)(-R \cdot \cos\alpha) \right.$$

$$\left. + \frac{1}{GI}\left(FR \cdot (1-\sin\alpha)\right)\left(R \cdot (1-\sin\alpha)\right) \right) R \, d\alpha \tag{5.36}$$

$$= \frac{FR^3\pi}{4EI_3} + \frac{FR^3}{GI}\left(\frac{3\pi}{4} - 2\right) = 0.138285322802514\text{m}, \tag{5.37}$$

$$\phi^{\text{tip}} = \int_0^{\frac{\pi}{2}} \left(\frac{1}{EI_3}(-FR \cdot \cos\alpha) \cdot \cos\alpha + \frac{1}{GI}\left(F \cdot (1-\sin\alpha)\right) \cdot \sin\alpha \right) R \, d\alpha$$

$$= -\frac{FR^2\pi}{4EI_3} + \frac{FR^2}{GI}\left(1 - \frac{\pi}{4}\right) = 0.0757632997455722\text{rad} \tag{5.38}$$

$$\tilde{M}_n = -F_z R = -1.0\text{kNm} \tag{5.39}$$

$$\tilde{M}_t = F_z R = 1.0\text{kNm} \tag{5.40}$$

The first evaluation of this example compares the relative error for different penalty factors α^{rot} and polynomial degrees p. The plots in Figure 5.20 show the relative error w.r.t. the single-beam-solution in order to separate
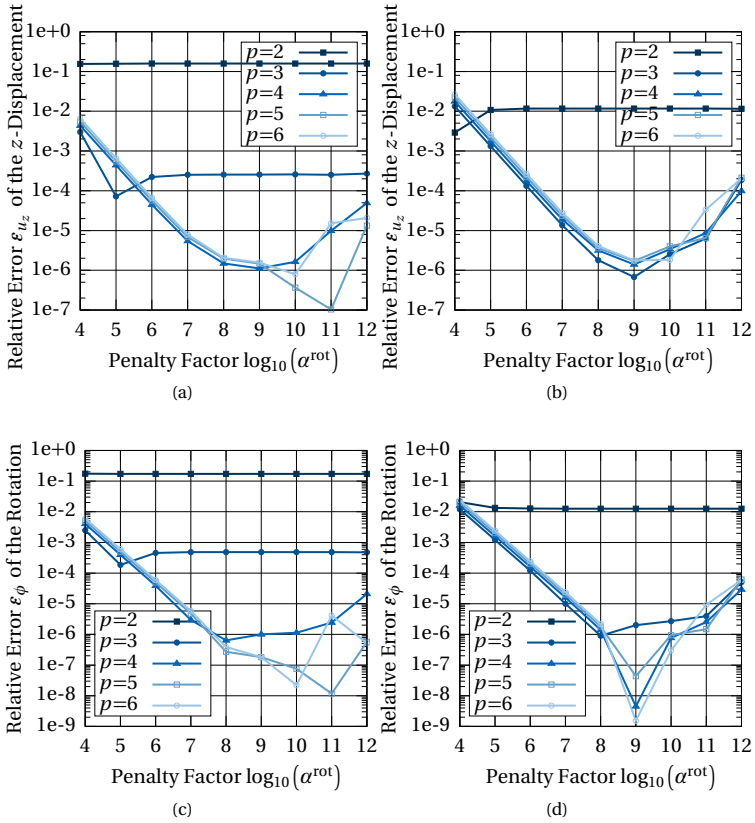
Figure 5.20: Relative error at the tip for: (a) u_z for 4 elements, (b) u_z for 16 elements, (c) ϕ for 4 elements, and (d) ϕ for 16 elements (adapted from Bauer et al. [8]).

discretization errors from the investigated coupling errors. The coupled model has 4 or 16 elements per beam, which corresponds to 8 or 32 elements in the single-patch model.

Figure 5.20 shows a different behavior for polynomial degree $p = 2, 3$ than for higher polynomial degrees. This convergence to a different result is linked to the still existing differences in the discretization. Figure 5.21
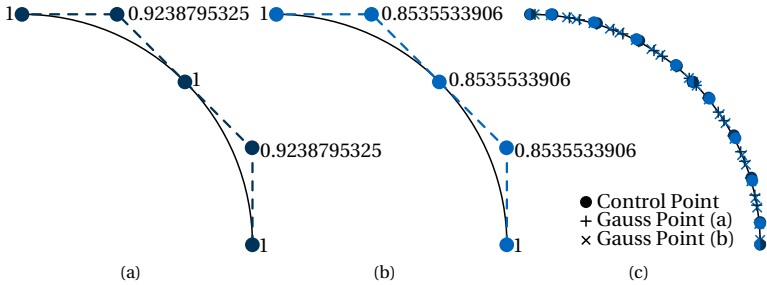
Figure 5.21: Different discretizations of the coupled circular arch: (a) control points with respective weights of the two curves, which are constructed by two 45° circular segments (dark blue), (b) control points with respective weights of the two curves, which are constructed by knot insertion into a 90° circular segment (lighter blue) and (c) refined control points and Gauss integration points for 4 nonzero knot spans and both discretizations (adapted from Bauer et al. [8]).

shows the control points and weights of two 45°-segments, constructed by two independent segments with CAD (see Figure 5.21(a)) and with knot insertion in the middle of a 90°-segment (see Figure 5.21(b)). One can observe in Figure 5.21(c) that the weights of the control points and the positioning of the Gauss points differ for these parametrizations, where each curve was refined to 4 nonzero knots spans, which in return influences the outcome of the result if the curves are not refined enough.

This is confirmed in Figure 5.22 where the discretization of Figure 5.21(b) is used which is closer to the parametrization of the single beam. Note that there is still a difference due to continuity in the middle of the knot span.

The polynomial degree has no influence on the quality of the result if there are many elements as can be seen in Figure 5.22(b) and Figure 5.22(d). The leveling-off of the error in Figure 5.22(a) and Figure 5.22(c) is therefore not related to the coupling scheme but the discretization. As observed above, the quality of the result reaches its optimum for a penalty factor $\alpha^{\text{rot}} = 10^9$.

Figure 5.23 shows the convergence behavior for different polynomial degrees p and numbers of elements per beam with penalty factor $\alpha^{\text{rot}} = 10^{10}$.
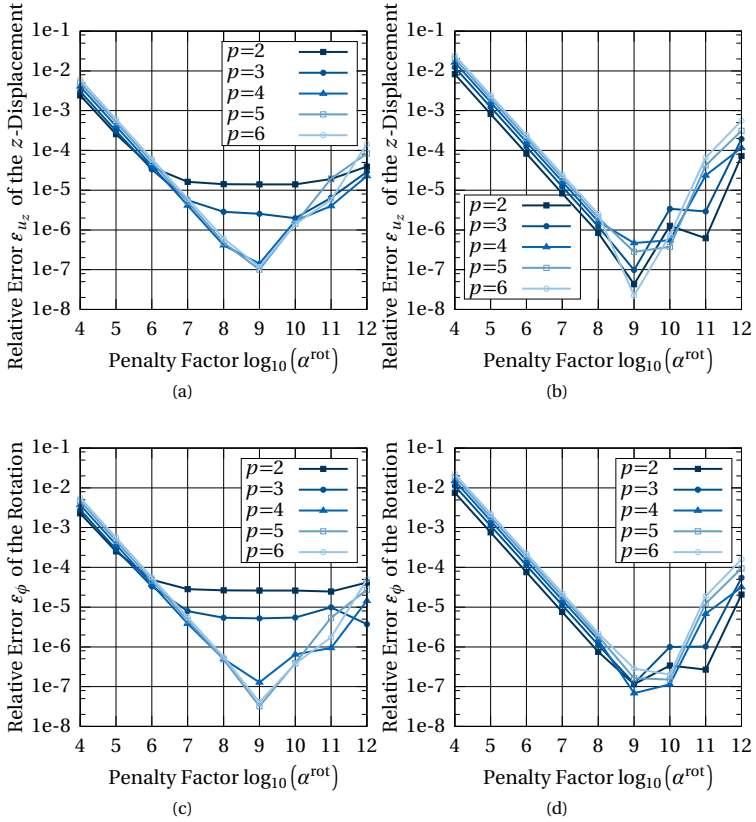
Figure 5.22: Relative error at the tip for: (a) u_z for 4 elements, (b) u_z for 16 elements, (c) ϕ for 4 elements, and (d) ϕ for 16 elements (adapted from Bauer et al. [8]).
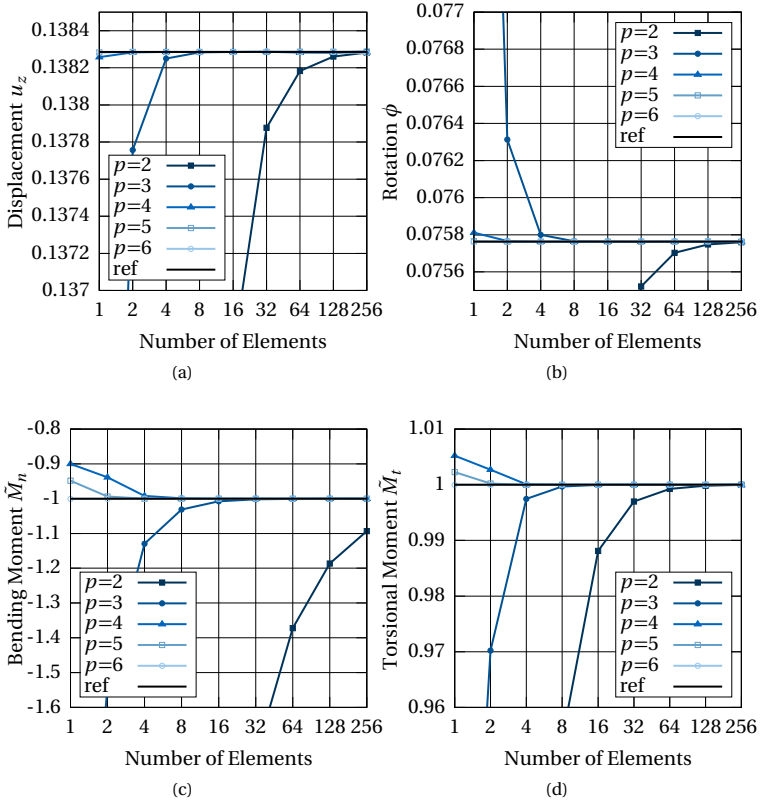
Figure 5.23: Numerical results for the quarter circle cantilever under tip load: (a) u_z at the tip, (b) ϕ at the tip, (c) $\tilde{M}_n$ at the support, and (d) $\tilde{M}_t$ at the support (adapted from Bauer et al. [8]).
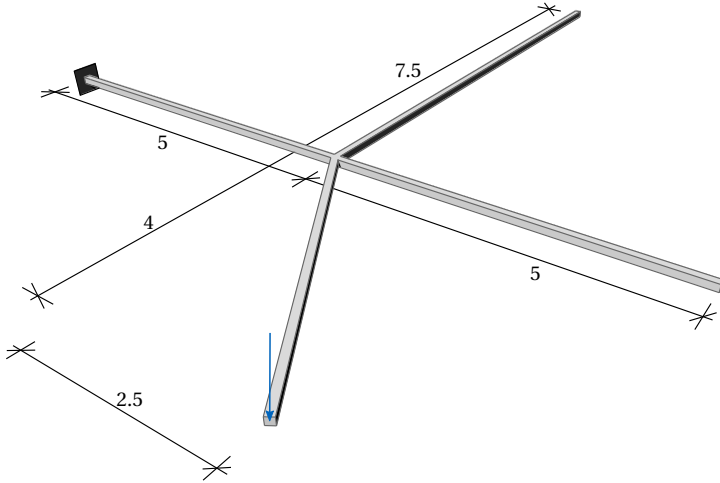
Figure 5.24: Cantilevering skew cross modeled by four coupled beams (adapted from Bauer et al. [8]).

Note that the discretization of Figure 5.21(a) was used for Figure 5.23 since this parametrization is the outcome of the ''real'' modeling in common CAD systems.

Cross Junction

The next example should check if several beams can be coupled to one point and if the forces are transferred correctly. Non-matching tangents are a further property of this example to be verified. Therefore, four beams assembled as a cross with one angular beam are modeled as shown in Figure 5.24. Note that the coupling is not restricted to orthogonal configurations. One beam is clamped on the end and the skew one has a tip load. The clamped beam is the master beam for all three coupling conditions. The beams without boundary conditions should ideally remain straight and only be translated and rotated without internal forces.

As can be observed in the deformation plot with respective internal forces, the results match the expected behavior. The unbounded beams remain
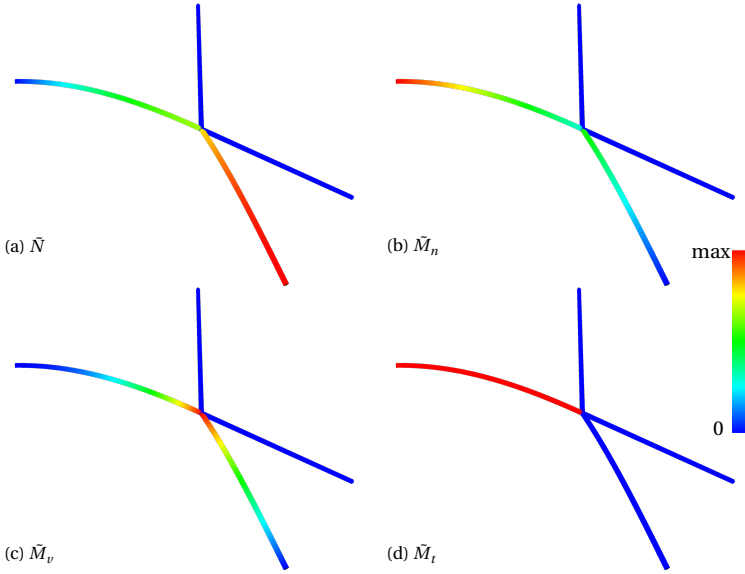
Figure 5.25: Inner force of the cantilevering cross: (a) normal force $\tilde{N}$, (b) bending moment $\tilde{M}_n$, (c) bending moment $\tilde{M}_v$, and (d) torsional moment $\tilde{M}_t$ (adapted from Bauer et al. [8]).

straight and no internal forces evolve. The internal forces of the other two beams are in equilibrium with the load and the support forces respectively.

The largest difference $\Delta\phi_{ij}$ measured as angle between two base vectors $\mathbf{t}_i^m$ and $\mathbf{t}_j^s$ at the coupling point is 6.66e-8rad, which is sufficiently small.

$$\Delta\phi_{ij} = \arccos(\mathbf{t}_i^m \cdot \mathbf{t}_j^s) - \arccos(\mathbf{T}_i^m \cdot \mathbf{T}_j^s) \tag{5.41}$$

Mainspring

The mainspring benchmark example was chosen in order to test the capability to undergo large rotations. A cantilever with the length $L = 20\pi$ is again modeled by two beams with flat rectangular cross sections. Every center line is modeled by a B-Spline curve with $p = 6$ and 10 nonzero knot spans. A moment $M = \frac{2\pi}{L}EI$ at the tip is needed to bend the straight

beam into a circle. The load factor k is incrementally increased from 0 to 2, which ideally should result in a double circle with radius $R = \frac{EI}{k \cdot M} = \frac{L}{4\pi} = 5$. Note that the moment cannot be applied directly to the system since the element formulation of the beam is displacement-based and the nodal forces are changing during the simulation. Yet, it can be incorporated by the external work which generates additional terms in the stiffness matrix. The penalty factors for displacement and rotation are both set to $\alpha = 10^7$. The setup and the corresponding deformation is shown in Figure 5.26(a). The analytic solution of the tip displacement is

$$u_{\text{ref}} = L - \sin(k \cdot 2\pi) \cdot \frac{L}{k \cdot 2\pi}, \qquad v_{\text{ref}} = \left(1 - \cos(k \cdot 2\pi)\right) \cdot \frac{L}{k \cdot 2\pi}. \quad (5.42)$$

The comparison of the tip displacements to the analytic reference solution in Figure 5.26(b) shows an agreement over the whole load path.

Gridshell

A lattice gridshell is a perfect application example for advanced coupling conditions. Three by three beams are laid over each other and connected at the intersection points. In this case, the formulation for scissor joints is applied, i.e. only $\mathbf{t}_2$ is coupled. All ends are supported in z-direction. All beams are loaded with a line dead load in order to bend them into space as shown in Figure 5.27(a).

Figure 5.27(b) shows the close-up of one outer joint. It can be observed that the base vectors $\mathbf{t}_2$ at the joint are matching within the tolerance introduced by the penalty approach. The angle between them, which corresponds to the error of the result, is $\phi_{\mathbf{t}_2^m \mathbf{t}_2^s} = 0.00198$. The initial angle of $\phi_{\mathbf{T}_1^m \mathbf{T}_1^s} = \frac{\pi}{2}$ between the tangents of the beam changed to $\phi_{\mathbf{t}_1^m \mathbf{t}_1^s} = 1.384$. This behavior is perfectly in accordance with the modeling of a scissor joint, which can change its orientation during the analysis and stays local on the beam. Also the internal moments as shown in Figure 5.28(a) and Figure 5.28(b) are matching the expected result. The laths are bent around their weak axis and torsion occurs only in the outer four laths. Evaluating the normal forces is more demanding. The continuous basis functions are not able to represent discontinuities as introduced by the point coupling. In order to represent the correct behavior, the length of the tangent would have to change suddenly at the coupling, which is not possible. High oscillations
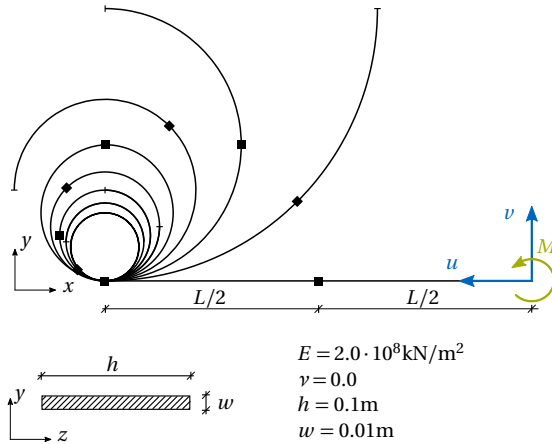
(a)
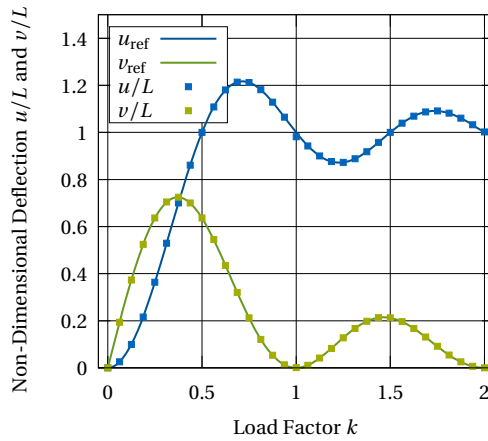
(b)

Figure 5.26: Mainspring modeled by two coupled beams: (a) setup and several deformed states and (b) comparison of the tip displacement with the reference solution (adapted from Bauer et al. [8]).
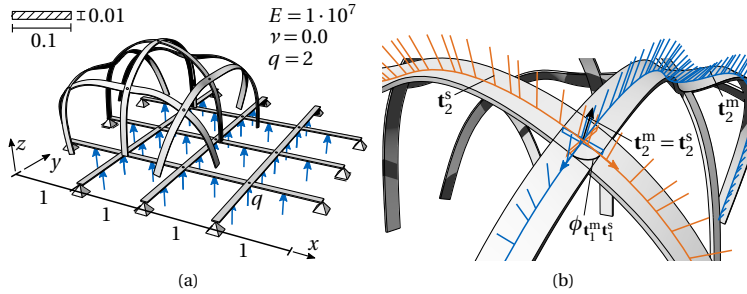
Figure 5.27: Gridshell with three by three laths connected by scissor joints: (a) setup with supports and loads and respective deformed structure and (b) close-up on one joint with base vectors $\mathbf{t}_2$ at every Gauss point of each beam and respective cross sections (adapted from Bauer et al. [8]).

are the result (cf. Figure 5.28(c)). This phenomenon can also be observed with other higher-order basis functions. In order to restrain the propagation of these oscillations, local refinement, i.e. knot insertion around the discontinuity points, can be applied to the curves, which leads to a proper representation of the normal force as can be seen in Figure 5.28(d). However, the displacement of the two different refinements differs only by 0.299%, which implies that the not locally refined curve can be used for the evaluation of the overall structural behavior.

5.4 Embedded Isogeometric Elements

Coupling of overlapping elements as illustrated in Figure 5.29 can also be described in an implicit way. The requirement is that one element has to completely lie inside another one. The smaller entity can be a point, a curve or a surface and even a volume if volumetric NURBS are considered. The relation can be expressed by redefining the geometry description. For this reason, the smaller one is projected into the parameter space of the larger one, which is similar to the description of trimming curves. Consequently, the projected NURBS patch is expressed by the master NURBS patch and its NURBS description in the parameter space of the master patch. The
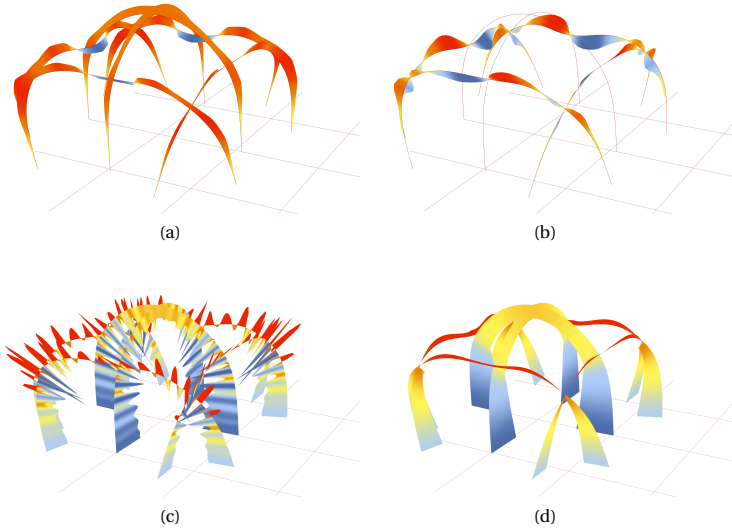
Figure 5.28: Inner forces of the gridshell: (a) bending moment $\tilde{M}_n$, (b) torsional moment $\tilde{M}_t$, (c) normal forces $\tilde{N}$ and (d) normal forces $\tilde{N}$ with locally refined curves (adapted from Bauer et al. [8]).

technique of expressing one entity by another one is also called embedding.

A more detailed explanation of this concept will be given in the following for a curve, which is embedded into a NURBS surface. The description is adopted from Section 2.2 and 2.3 of Bauer et al. [9].

The control points $\overline{\mathbf{P}}_i$ of the embedded curve have the coordinates of the parameter space (θ^1, θ^2) of the surface. The computation of the NURBS curve in the parameter space is performed analogously to Equation (3.4).

$$\overline{\mathbf{C}}(\bar{\theta}^1) = \begin{pmatrix} \theta^1(\bar{\theta}^1) \\ \theta^2(\bar{\theta}^1) \end{pmatrix} = \sum_{\tilde{\imath}=1}^{\tilde{n}} R_{\tilde{\imath},\tilde{p}}(\bar{\theta}^1)\overline{\mathbf{P}}_{\tilde{\imath}} \tag{5.43}$$

This kind of description is directly available from CAD, when constructed by intersection of a surface and a curve or other surface (see Figure 5.30).

97
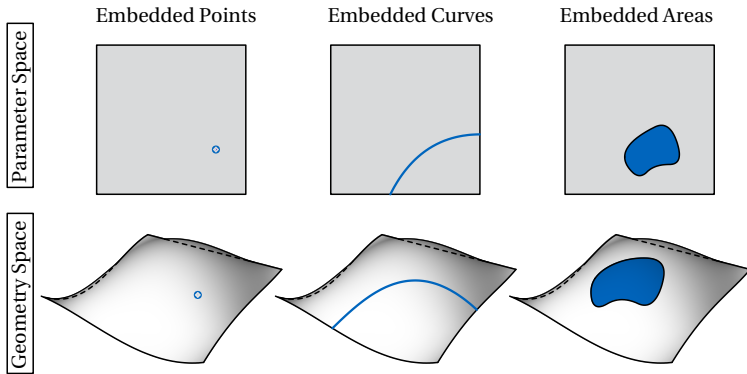
Figure 5.29: Geometry and parameter space of a surface with different types of embedded entities.

The curve description with knot vector and control points in the parameter space results from a surface-to-surface intersection (SSI) problem, see Choi [34], Krishnan et al. [79], Patrikalakis [103], and Sederberg et al. [119]. In general, it is not possible to describe the resulting curve by the same knot vector nor to exactly represent the original (intersecting) curve. The precision is dependent on the tolerances of the CAD system respectively the SSI-algorithm. Note that the position of those control points within the parameter space of the master element does not change during the analysis. The deformation of the curve is only implied by the deformation of the surface (cf. Figure 5.31).

The curve in the geometric space can then be expressed as follows (see Figure 5.32):

$$
\begin{aligned}
\mathbf{C}(\bar{\theta}^1) &= \sum_{i=1}^{n}\sum_{j=1}^{m} R_{ij,pq}\left(\bar{\theta}^1\right)\mathbf{P}_{ij} = \sum_{i=1}^{n}\sum_{j=1}^{m} R_{ij,pq}\left(\theta^1\left(\bar{\theta}^1\right),\theta^2\left(\bar{\theta}^1\right)\right)\mathbf{P}_{ij} \\
&= \sum_{i=1}^{n}\sum_{j=1}^{m} R_{ij,pq}\left(\sum_{\bar{i}=1}^{\bar{n}} R_{\bar{i},\bar{p}}\left(\bar{\theta}^1\right)\overline{\mathbf{P}}_{\bar{i}}\right)\mathbf{P}_{ij}
\end{aligned} \tag{5.44}
$$

Table 5.1 gives an overview of all aforementioned curve definitions and their mapping space.

control point net with $\mathbf{P}_{ij}$ of the surface $\mathbf{S}(\xi, \eta)$

control point net with $\mathbf{P}_i$ of the initial geometry curve $\mathbf{C}_0(\xi_c)$

Geometry Space

η

ξ

initial geometry curve $\mathbf{C}_0(\xi_c)$

SSI

Parameter Space

control point net with $\overline{\mathbf{P}}_{\bar{i}}$ of the projected curve in the parameter space of the surface

projected curve in the parameter space of the surface $\overline{\mathbf{C}}(\bar{\xi})$

η

ξ

Geometry Space

projected curve in the geometry space $\mathbf{C}(\bar{\xi})$

η

ξ

Figure 5.30: NURBS surface and curve defined in the geometry space (CAD) (adapted from Bauer et al. [9]).
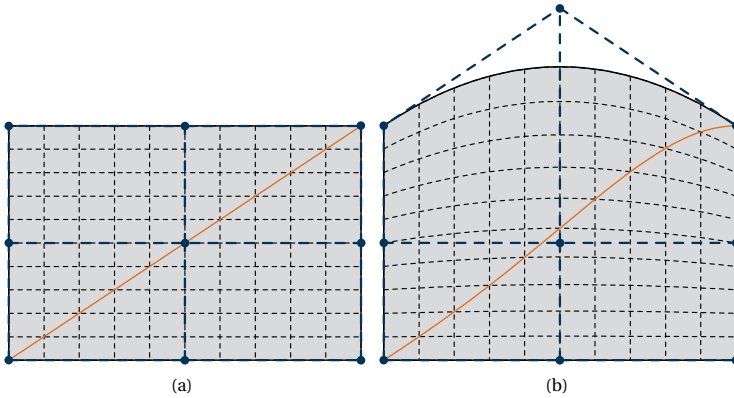
Figure 5.31: Embedded curve in the (a) undeformed surface and (b) in the deformed surface. The surface knot vector is $\Xi_s = H_s = [0, 0, 0, 1, 1, 1]$ and the curve knot vector is equal to $\Xi_c = [0, 0, 1, 1]$ for a linear curve. The control points of the curve are located at $\overline{\mathbf{P}}_1 = [0, 0]^T$ and $\overline{\mathbf{P}}_2 = [1, 1]^T$. Note that the curve in the deformed configuration is still represented by a linear curve in the parameter space (adapted from Bauer et al. [9]).

general curve description in geometry space	$\mathbf{C} : \theta_c^1 \rightarrow \mathbb{R}^3$
embedded curve description in parameter space	$\overline{\mathbf{C}} : \bar{\theta}^1 \rightarrow \mathbb{R}^2$
embedded curve description in geometry space	$\mathbf{C} : \bar{\theta}^1 \rightarrow \mathbb{R}^3$

Table 5.1: Overview of curve definitions with respective mapping space.

Additionally, a local coordinate system $\mathbf{B}_i$ is introduced in order to describe a local 3D continuum. The base vectors $\mathbf{B}_i$ are defined as unit vectors and orthogonal respectively tangential to the curve (see also Figure 5.32).

$$\mathbf{B}_i = \frac{\widehat{\mathbf{B}}_i}{\|\widehat{\mathbf{B}}_i\|_2} \tag{5.45}$$

$\widehat{\mathbf{B}}_i$ denotes the not normalized base vectors. These base vectors of the curve can be derived from the base vectors of the surface $\mathbf{A}_i$. The first base vector is aligned to the tangent of the curve, the second corresponds to the
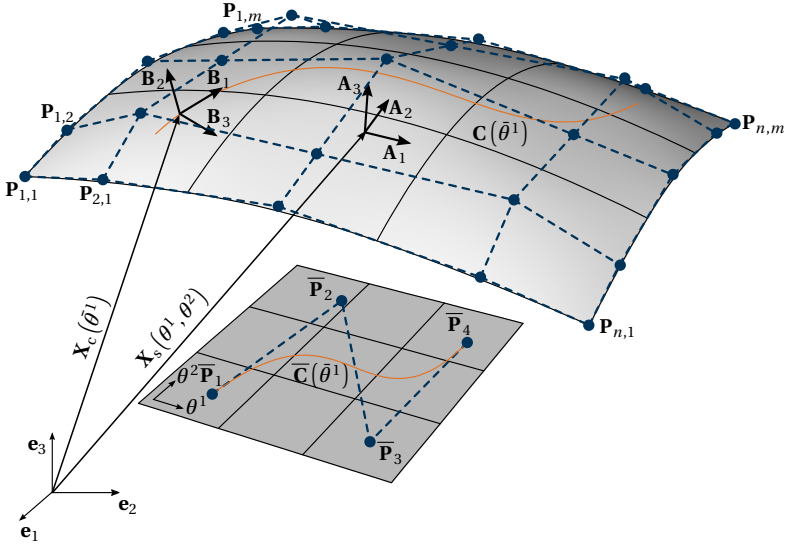
Figure 5.32: Surface with embedded curve and the underlying parameter space with the defining NURBS curve: definition of the base vectors of the embedded curve $\mathbf{B}_i$ and of the base vectors of the underlying surface $\mathbf{A}_i$ (adapted from Bauer et al. [9]).

surface normal $\mathbf{A}_3$ and the third is perpendicular to the others.

$$\widehat{\mathbf{B}}_1 = \frac{\partial \mathbf{X}_s}{\partial \bar{\theta}^1} = \mathbf{A}_1 \frac{\partial \theta^1}{\partial \bar{\theta}^1} + \mathbf{A}_2 \frac{\partial \theta^2}{\partial \bar{\theta}^1} \tag{5.46}$$

$$\widehat{\mathbf{B}}_2 = \mathbf{A}_3 = \mathbf{A}_1 \times \mathbf{A}_2 \tag{5.47}$$

$$\widehat{\mathbf{B}}_3 = \widehat{\mathbf{B}}_1 \times \widehat{\mathbf{B}}_2 \tag{5.48}$$

The base vector $\widehat{\mathbf{B}}_3$ can be rewritten with the help of a pseudo parameter $\bar{\theta}^2$ and the triple product expansion, see Breitenberger et al. [28]:

$$\widehat{\mathbf{B}}_3 = \mathbf{A}_1 \frac{\partial \theta^1}{\partial \bar{\theta}^2} + \mathbf{A}_2 \frac{\partial \theta^2}{\partial \bar{\theta}^2} \qquad \text{with } \frac{\partial \theta^1}{\partial \bar{\theta}^2} = \widehat{\mathbf{B}}_1 \cdot \mathbf{A}_2 \text{ and } \frac{\partial \theta^2}{\partial \bar{\theta}^2} = -\widehat{\mathbf{B}}_1 \cdot \mathbf{A}_1 \tag{5.49}$$

NURBS-based Embedded Finite Elements

Variations with respect to a discrete global vector of degrees of freedom $\hat{\mathbf{u}}$ of the geometric quantities are usually required for the formulation of a finite element. In the following, discrete nodal values will be denoted by $(\hat{\bullet})$. Each node has the degrees of freedom of the element formulation of the surface element. These are e.g. three displacement DOFs u, v, w. Optionally, additional DOFs for the embedded element, like a rotation around the center line ϕ, can be applied. Note that these additional DOFs are also attributed to the surface control points even though they do not influence the surface element itself.

$$\hat{\mathbf{u}} = \begin{bmatrix} \hat{u}^{1,1} & \hat{v}^{1,1} & \hat{z}^{1,1} & (\hat{\phi}^{1,1}) & | & \dots \\ & | & \hat{u}^{n,m} & \hat{v}^{n,m} & \hat{w}^{n,m} & (\hat{\phi}^{n,m}) \end{bmatrix} \tag{5.50}$$

The center line $\mathbf{x}_c$ of the deformed configuration can be described as a function of the initial coordinates of the surface control points and their respective displacements.

$$\mathbf{x}_c(\bar{\theta}^1) = \sum_{i=1}^{n}\sum_{j=1}^{m} R_{ij,pq}\left(\theta^1(\bar{\theta}^1), \theta^2(\bar{\theta}^1)\right)\hat{\mathbf{x}}^{ij}$$

$$= \sum_{i=1}^{n}\sum_{j=1}^{m} R_{ij,pq}\left(\sum_{\bar{l}=1}^{\bar{n}} R_{\bar{l},\bar{p}}(\bar{\theta}^1)\overline{\mathbf{P}}_{\bar{l}}\right)\cdot\left(\hat{\mathbf{X}}^{ij} + \hat{\mathbf{u}}^{ij}\right) \tag{5.51}$$

Since all parameters of the undeformed geometry are invariant to the variation, the variation $\mathbf{x}_{c,r}$ of the position vector with respect to the variation parameter r (the r-th component of $\hat{\mathbf{u}}$ as defined in Equation (5.50)) can be written as:

$$\mathbf{x}_{c,r} = \sum_i\sum_j R_{ij,pq}\left(\hat{\mathbf{X}}^{ij} + \hat{\mathbf{u}}^{ij}\right)_{,r} = \sum_i\sum_j R_{ij,pq}\hat{\mathbf{u}}^{ij}_{,r} \tag{5.52}$$

The description of the center line also influences the variation of the base vectors $\mathbf{b}_i$:

$$\widehat{\mathbf{b}}_{1,r} = \mathbf{x}_{\text{c},\bar{1},r} = \sum_i \sum_j R_{(ij,pq),\bar{1}} \hat{\mathbf{u}}^{ij}_{,r}$$

$$= \sum_i \sum_j \left(\frac{\partial R_{(ij,pq)}}{\partial \theta^1} \frac{\partial \theta^1}{\partial \bar{\theta}^1} + \frac{\partial R_{(ij,pq)}}{\partial \theta^2} \frac{\partial \theta^2}{\partial \bar{\theta}^1} \right) \hat{\mathbf{u}}^{ij}_{,r} \qquad (5.53)$$

$$\widehat{\mathbf{b}}_{2,r} = \left(\mathbf{x}_{,1} \times \mathbf{x}_{,2} \right)_{,r} = \sum_i \sum_j \left(\left(\frac{\partial R_{(ij,pq)}}{\partial \theta^1} \hat{\mathbf{u}}^{ij}_{,r} \right) \times \left(\frac{\partial R_{(ij,pq)}}{\partial \theta^2} \hat{\mathbf{u}}^{ij} \right) \right.$$

$$\left. + \left(\frac{\partial R_{(ij,pq)}}{\partial \theta^1} \hat{\mathbf{u}}^{ij} \right) \times \left(\frac{\partial R_{(ij,pq)}}{\partial \theta^2} \hat{\mathbf{u}}^{ij}_{,r} \right) \right) \quad (5.54)$$

The integration of the terms related to the curve element for FE analysis is required. As commonly applied, this is realized as a Gauss-quadrature. Note that the coordinates and weights of the Gauss points are derived from the elements of the curve in the parameter space of the surface. The minimal number of Gauss points is derived by the largest polynomial degree $p+1$ either of the parameter curve or the surface. The refinement of NURBS curves in the parameter space can be executed in the same manner as for space curves. This refinement does not alter the geometry. Only the number of control points in the parameter space is increased, but since no additional DOFS are introduced, it does not enrich the solution space. Nevertheless, a refinement of the curve in the range of the refinement of the surface is beneficial since they share the same DOFs. This can be realized by e.g. inserting knots at every crossing of the parameter curve over a knot line of the surface (see Figure 5.33). The size of the elements is then similar and the numerical error of the integration is in the same order as for the surface elements, see Breitenberger et al. [28].

5.4.1   Embedded Beam

The implicit geometry description is perfectly suited for the representation of a beam that is coupled to a surface, i.e. embedded into the surface. The description of the derivation of the element formulation is based on Section 3.2 of Bauer et al. [9].

(a)   (b)
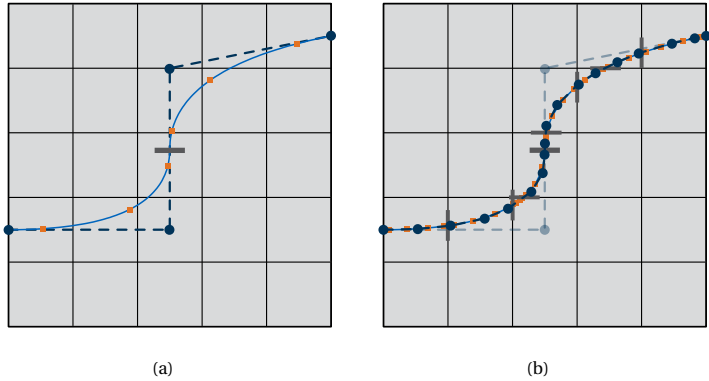
Figure 5.33: Embedded curve ($p_c = 2$) with Gauss points (orange squares) and respective knots (gray lines) for (a) unrefined curve and (b) refined curve with knot insertion at the intersections with the knot lines of the surface and order elevation corresponding to the polynomial degree of the the surface $p_s = 3$ (adapted from Bauer et al. [9]).

There are two convenient attachments for a beam to a surface, which is described in the parameter space: (i) rigidly attached and (ii) hinge-attached.

How to apply the nested parametrization concept to the element formulation of the nonlinear spatial isogeometric Bernoulli beam (BB) presented in Section 4.4 for those two cases is shown in the following.

Analogously to Section 4.4, $\mathbf{X}$ and $\mathbf{x}$ are the position vectors for the continuum of the beam and are defined as follows (see also Figure 5.34):

$$\mathbf{X}\left(\bar{\theta}^1, \bar{\theta}^2, \bar{\theta}^3\right) = \mathbf{X}_c\left(\bar{\theta}^1\right) + \bar{\theta}^2 \mathbf{B}_2^B\left(\bar{\theta}^1\right) + \bar{\theta}^3 \mathbf{B}_3^B\left(\bar{\theta}^1\right) \tag{5.55a}$$

$$\mathbf{x}\left(\bar{\theta}^1, \bar{\theta}^2, \bar{\theta}^3\right) = \mathbf{x}_c\left(\bar{\theta}^1\right) + \bar{\theta}^2 \mathbf{b}_2^B\left(\bar{\theta}^1\right) + \bar{\theta}^3 \mathbf{b}_3^B\left(\bar{\theta}^1\right) \tag{5.55b}$$

The center lines $\mathbf{X}_c$ and $\mathbf{x}_c$ are defined by the curve in the parameter space. The remaining input parameters, i.e. the base vectors $\mathbf{B}_i^B$ and $\mathbf{b}_i^B$ can be described by transferring the original element formulation to the nested curve properties. Note that the surface normal $\mathbf{A}_3$ provides a unique reference. Hence, the moving trihedral with the respective Λ-operator, which
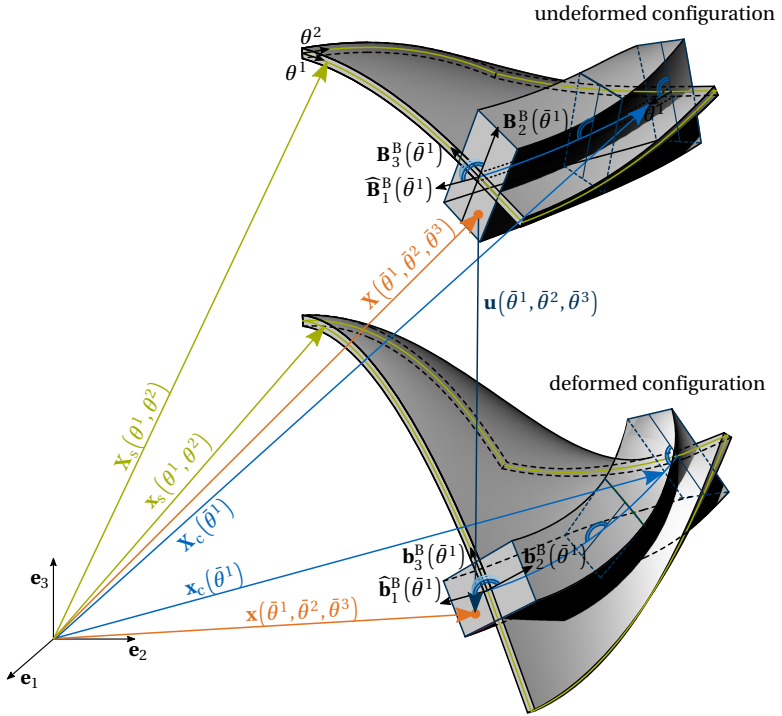
Figure 5.34: Definition of the position vectors $\mathbf{X}$ and $\mathbf{x}$, the surface vectors $\mathbf{X}_s$ and $\mathbf{x}_s$ and the center line vectors $\mathbf{X}_c$ and $\mathbf{x}_c$ for the undeformed and deformed configuration with a cross section defined by $\mathbf{B}_2^B$ and $\mathbf{B}_3^B$. Here illustrated for a rectangular cross section, which is aligned to the surface normal (adapted from Bauer et al. [9]).

has been introduced in Section 4.4 in order to create a reference trihedral for the description of the cross section, is not needed in the embedded formulation.

Rigidly Attached Beam Element

Rigidly attached means that the cross section of the beam is fully linked to the surface. In other words when the surface is twisted, also the beam is twisted. This corresponds e.g. to ribs on a shell structure.

Consequently, the local coordinate system $\mathbf{B}_i$, which is strictly derived from the surface, can be applied as the base vectors $\mathbf{B}_i^\mathrm{B}$ of the continuum of the beam (Figure 5.34). The not normalized base vector $\widehat{\mathbf{B}}_1$ is used in tangential direction in order to represent longitudinal changes. In contrast to the original element formulation from Section 4.4, the fourth DOF ψ for torsion is not applicable, since the twisting is tracked solely by the surface.

Hinge-attached Beam Element

An application for this formulation is e.g. a beam supported membrane. In this case, the orientation of the cross section of the beam is independent of the surface. Only the center line stays attached. The base vectors $\mathbf{B}_\alpha^\mathrm{B}$ and $\mathbf{b}_\alpha^\mathrm{B}$ with $\alpha \in \{2, 3\}$ are derived by modifying the reference base vectors from the surface $\mathbf{B}_\alpha$ and $\mathbf{b}_\alpha$, respectively . Therefore, a fourth, torsional DOF is activated. It measures the relative rotation around the curve tangent. The reference vectors are then rotated by a correction angle in the reference and/or the torsional DOF in the deformed configuration (cf. Figure 5.35).

$$\mathbf{B}_\alpha^\mathrm{B}\big(\bar{\theta}^1\big) = \overline{\mathbf{R}}_{\mathbf{B}_1}(\Psi)\,\mathbf{B}_\alpha\big(\bar{\theta}^1\big) \tag{5.56a}$$

$$\mathbf{b}_\alpha^\mathrm{B}\big(\bar{\theta}^1\big) = \overline{\mathbf{R}}_{\mathbf{b}_1}\big(\psi\big)\,\overline{\mathbf{R}}_{\mathbf{b}_1}(\Psi)\,\mathbf{b}_\alpha\big(\bar{\theta}^1\big) \tag{5.56b}$$

The angle is applied with an Euler-Rodrigues rotation matrix with $\mathbf{B}_1$ or $\mathbf{b}_1$ as axis of rotation. For more details within the context of beam elements, see Bauer et al. [10].

$$\overline{\mathbf{R}}_{\mathbf{b}_1}\big(\psi\big) = \mathbf{I}\cos\big(\psi\big) + \sin\big(\psi\big)\,\mathbf{b}_1 \times \mathbf{I} + \overbrace{\big(1 - \cos\big(\psi\big)\big)\mathbf{b}_1 \otimes \mathbf{b}_1}^{=0}$$

$$= \mathbf{I}\cos\big(\psi\big) + \sin\big(\psi\big)\,\mathbf{b}_1 \times \mathbf{I} \tag{5.57}$$

Nonlinear Kinematics

The kinematics are derived directly from the geometric description in combination with the laws of continuum mechanics. Strains and stresses are

(a)

(b)

(c)

(d)
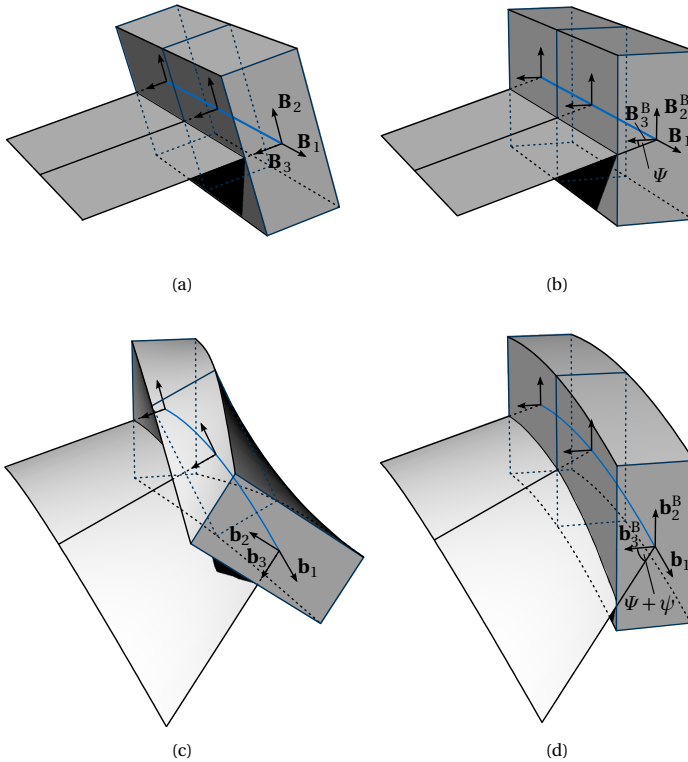
Figure 5.35: Modification of the twisting of the beam: (a) initial configuration of the reference base vectors **B** in the undeformed geometry, (b) application of the correction angle Ψ in order to obtain the reference configuration for the analysis, (c) initial configuration of the reference base vectors **b** in the deformed geometry, (d) application of the correction angle Ψ and torsional DOF ψ in order to obtain the resulting deformed configuration (adapted from Bauer et al. [9]).

determined by using the Green-Lagrange strain tensor and the energetically conjugated second Piola-Kirchhoff stress tensor.

The base vectors of the continuum of the curve element are defined as:

$$\mathbf{G}_i = \frac{\partial \mathbf{X}}{\partial \bar{\theta}^i} = \mathbf{X},_{\bar{i}}, \qquad \mathbf{g}_i = \frac{\partial \mathbf{x}}{\partial \bar{\theta}^i} = \mathbf{x},_{\bar{i}} \tag{5.58}$$

Then, the GL strain tensor can be computed according to Equation (2.25) as follows:

$$E_{ij} = \frac{1}{2}\left(g_{ij} - G_{ij}\right) \tag{5.59}$$

Following the derivation of the element formulation in Section 4.4, the following weak form of the equilibrium evolves for both attachments with $\mathbf{B}_\alpha^{\mathrm{B}}$ being principal axes of the cross section:

$$\delta W_{\mathrm{int}} = -\int_{\Omega_0} \mathbf{S} : \delta \mathbf{E}\, \mathrm{d}\Omega = -\int_L \frac{E}{B_{11}^2} \cdot \left(A\epsilon\, \delta\epsilon + I_{\mathbf{B}_3^{\mathrm{B}}} \kappa_{21}\, \delta\kappa_{21}\right.$$
$$\left. + I_{\mathbf{B}_2^{\mathrm{B}}} \kappa_{31}\, \delta\kappa_{31}\right) + \frac{G I_{\mathbf{B}_1^{\mathrm{B}}}}{B_{11}} \cdot \left(-\frac{1}{2}\kappa_{32}\, \delta\kappa_{32} + \frac{1}{2}\kappa_{23}\, \delta\kappa_{23}\right) \mathrm{d}L\,, \tag{5.60}$$

where A is the area of the cross section and $I_{\mathbf{B}_i^{\mathrm{B}}}$ the moments of inertia w.r.t. the base vectors.

Examples

The following examples will demonstrate the validity and potential of the proposed embedded approach for beams, which will be referred to as plug-on beam (POB) from here on. Moreover, variations in order to use the formulation for mass assignment and boundary conditions are shown.

Mainspring

The mainspring provides a good benchmark example for the embedded beam formulation. The problem is geometrically nonlinear and can be modeled with a rigidly attached beam. Therefore, a cantilevering shell strip with two embedded beams on the edges is generated (see Figure 5.36). The surface description consists of a trimmed patch with polynomial degree $p = q = 5$. The cutting curves are not aligned to knot lines. Thus, the
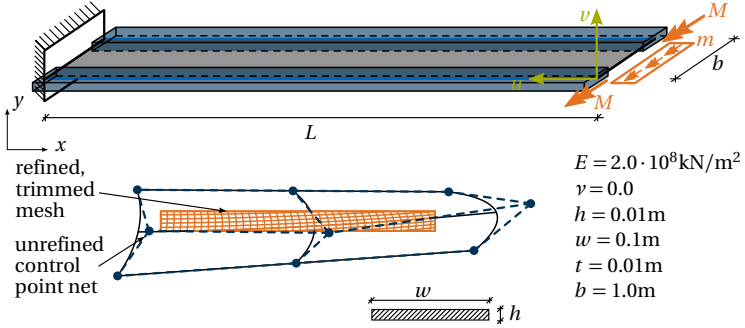
Figure 5.36: Initial geometry of the mainspring with input parameters and trimmed mesh with initial control point net. The virtual volume of the beam is depicted in blue (adapted from Bauer et al. [9]).

embedded beams run skew through the parameter space. There are no control points that can be used for a standard NURBS curve description at the edge. The beam orientation is connected to the surface normal. The shell element formulation is the same as the Kirchhoff-Love shell presented in Section 4.2. Bending moments are applied to each structural element on one end of the structure. In order to turn the strip by 2π, the moments $M = \frac{2\pi E h w^3}{12L}$ and $m = \frac{2\pi E t^3}{12L}$ are needed at the free edge for the beams and the shell, respectively.

Figure 5.37(a) shows different intermediate stages of the roll up process and Figure 5.37(b) compares the numerical tip displacements to the analytical result (see Equation (5.42)), which are in good agreement.

Bending-torsion interaction

The quarter circle example is used in this section in order to test the bending torsion interaction. Therefore, a circular shell strip is modeled and a beam is embedded onto the longest boundary edge as illustrated in Figure 5.38. The beam is not attached to the surface normal. The cantilever is supported on one side by fixing all displacements of the outer control points on this edge. Additionally, the second control point in the circular
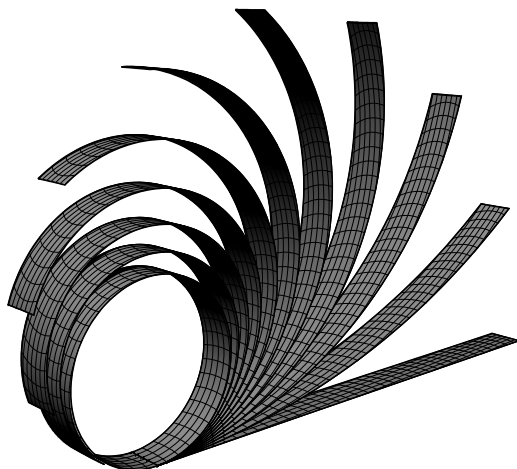
(a)
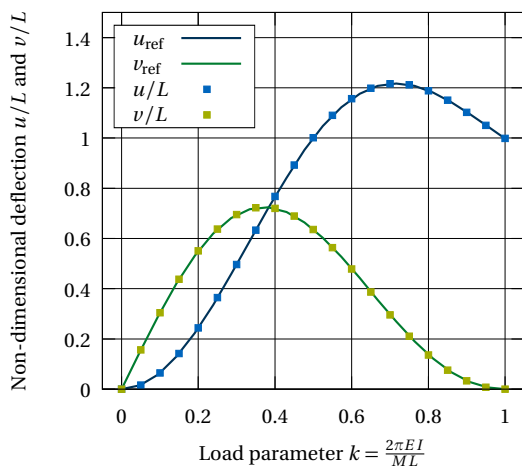
(b)

Figure 5.37: Computed results of the mainspring: (a) deformed geometry for ten load steps and (b) numerical results compared to the analytic solution (adapted from Bauer et al. [9]).

$E = 1.25 \cdot 10^7 \text{ kN/m}^2$ $h = 0.3\text{m}$
$\nu = 0.25$ $w = 0.1\text{m}$
$P_z = 15\text{kN}$ $t = 0.01\text{m}$
 $b = 0.5\text{m}$

$\alpha = 90°$ $R = 10.0\text{m}$

$\alpha_A = 45°$
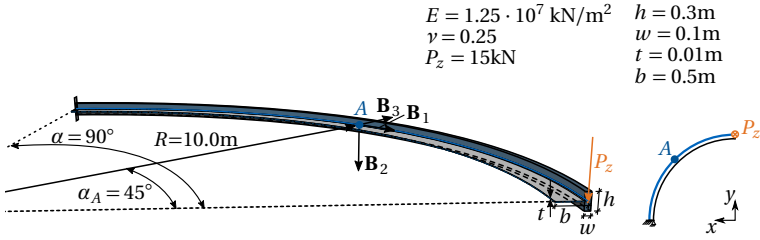
Figure 5.38: Cantilevering quarter circle with out-of-plane tip load: definition of the geometry, the cross sections and the loading scenario. The virtual volume of the beam is depicted in dark blue.

direction of the corner of the beam is fixed in order to clamp the beam. A point load is applied at the other end of the beam.

In order to evaluate the behavior of the element formulation, a convergence study for the refinement is done. The refinement of the surface in tangential direction is varied for different polynomial degrees whereas the second direction has a constant parametrization with $p = 2$ and three elements. The displacement is evaluated at the tip of the beam (see Figure 5.39) and the inner forces inside the beam at point A, which is is located in the middle of the beam (see Figure 5.40). All polynomial degrees converge to the same value for a sufficient number of elements.

This problem has no analytical solution that can be used for the assessment of accuracy. However, due to the parametrization, the embedded model can be compared to the independent Bernoulli beam (BB) formulation of Section 4.4. The beam lies on the edge of an untrimmed surface and the control points of the surface and an individually modeled curve coincide if the same parametrization is chosen. Since the cross section of the beam is not oriented along the surface normal, only a displacement coupling is necessary, which can be implied by sharing the same DOFs. Figure 5.41 shows the relative error ε, which is computed by Equation (5.61) for the displacement, plotted against the number of elements for different polynomial degrees. Note that the BB result has the same refinement as the POB one.

$$\varepsilon = \frac{\|(\bullet)_{\text{BB}} - (\bullet)_{\text{POB}}\|_2}{\|(\bullet)_{\text{BB}}\|_2} \tag{5.61}$$
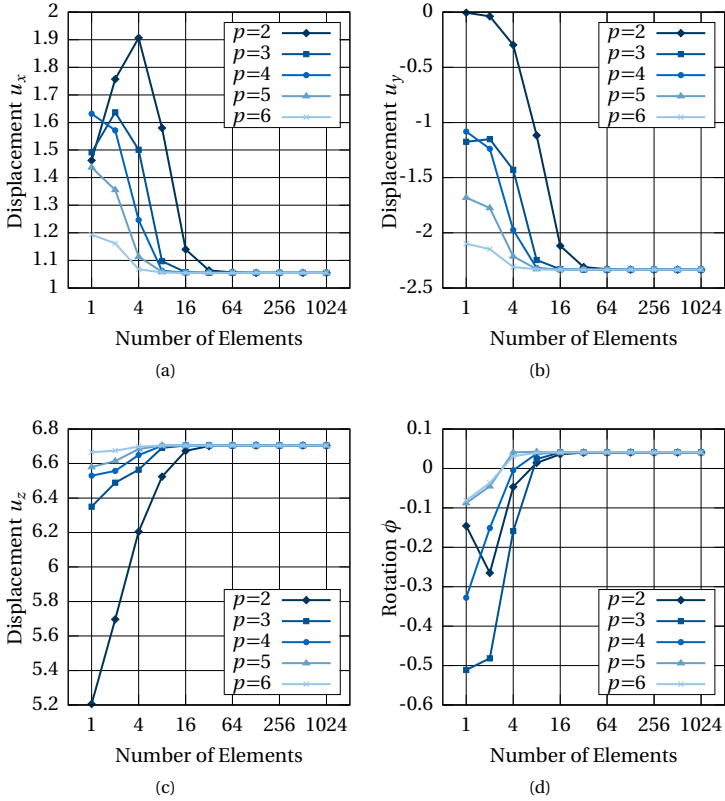
Figure 5.39: Convergence of the tip-displacements for the quadrant cantilever: (a) x-displacement u_x^{tip}, (b) y-displacement u_y^{tip}, (c) z-displacement u_z^{tip}, (d) rotation ϕ^{tip}
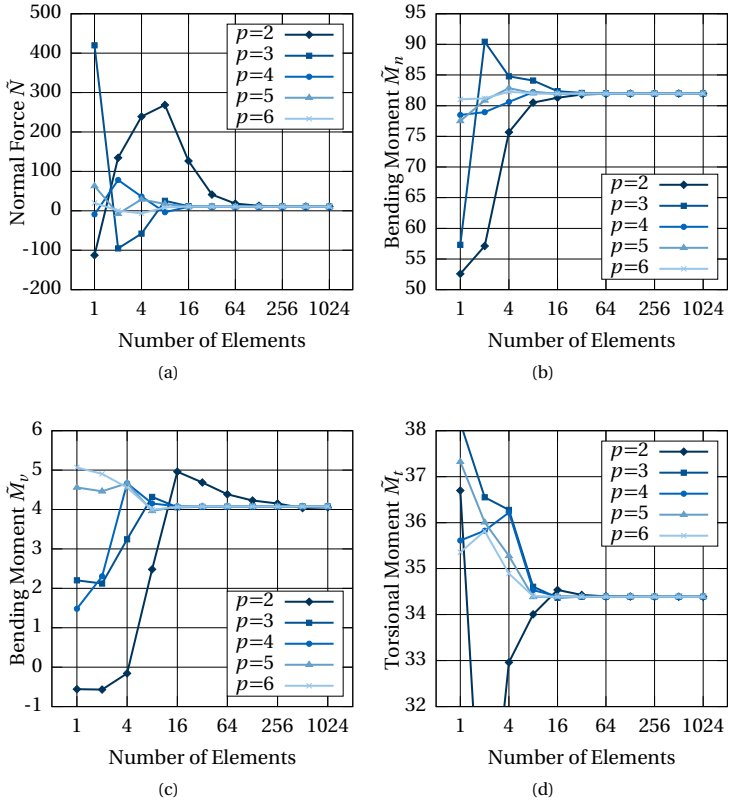
Figure 5.40: Convergence of inner forces for the quadrant cantilever at point A: (a) normal force $\tilde{N}$, (b) bending moment $\tilde{M}_n$, (c) bending moment $\tilde{M}_v$, (d) torsional moment $\tilde{M}_t$.
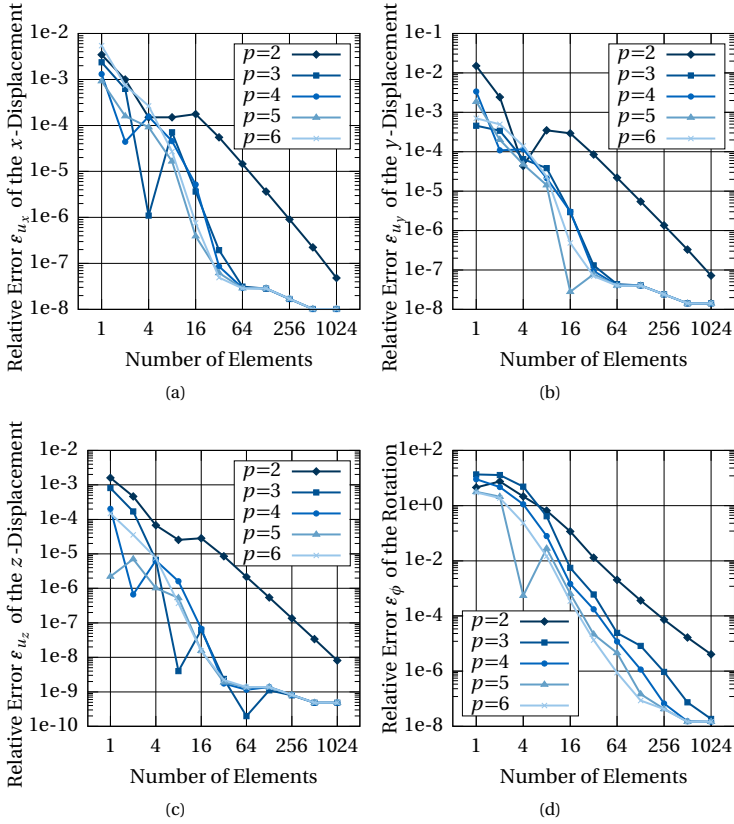
Figure 5.41: Comparison of the tip-displacements of the plug-on beam with the Bernoulli beam for the quadrant cantilever: (a) x-displacement u_x^{tip}, (b) y-displacement u_y^{tip}, (c) z-displacement u_z^{tip}, (d) rotation ϕ^{tip}

Beam: $\rho = \rho_{\text{beam}}\,[\text{kg/m}]$
$A = 1.0\,\text{m}^2$
$\bar{\rho} = \rho_{\text{beam}} \cdot A\,[\text{kg/m}]$
$EI = 0.0\,\text{kNm}^2$

Plate: $\rho = 1.0\,\text{kg/m}^3$
$t = 0.01\,\text{m}$
$\bar{\rho} = 0.01\,\text{kg/m}^2$
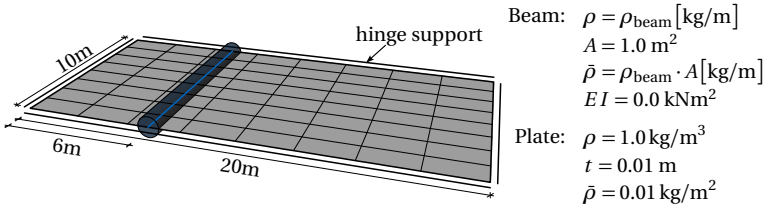
Figure 5.42: Setup of a mass manipulated, simply supported plate with mesh. The additional weight at the curve is varied by the respective density. No additional stiffness is applied. The blue volume only visualizes the additional mass (adapted from Bauer et al. [9]).

The rotational degree of freedom ϕ^{tip} is defined differently for the Bernoulli beam. Consequently, it is not suitable as a reference value. Instead, the rotation is compared to an extremely refined configuration with 2048 elements and a polynomial degree of $p = 9$ (POB2048).

$$\varepsilon_\phi = \frac{\|(\bullet)_{\text{POB2048}} - (\bullet)_{\text{POB}}\|_2}{\|(\bullet)_{\text{POB2048}}\|_2} \tag{5.62}$$

The implementation shows good convergence to the reference values and the hinge attached formulation with an additional rotational DOF can be considered as applicable.

Mass manipulation

The embedded formulation can also be used to add or remove mass to or from a system, which may be needed in an eigenvalue or dynamic analysis. The example with mass from Bauer et al. [9] consists of a flat, simply supported plate with an aspect ratio of $2:1$ (see Figure 5.42). A non-structural mass is added along an embedded line, which is independent of the knot lines. The plate is modeled with 50 elements in each direction and a polynomial degree of $p = q = 4$. No stiffness is added to the curve, i.e. $E = 0.0$, in order to separate the effects of mass and stiffness. The eigenfrequencies and -forms are investigated in an eigenvalue analysis for a varying mass on the embedded curve.

Figure 5.43(a) shows the eigenmodes of the plate without additional mass. The eigenfrequency decreases for an increased mass on the curve. The asymmetric configuration distorts the shape and sequence of the eigen-

$f = 0.2003984$ $f = 0.1687506$ $f = 0.1452303$

$f = 0.3206378$ $f = 0.2825097$ $f = 0.2712789$

$f = 0.5210538$ $f = 0.5144196$ $f = 0.4332633$

$f = 0.6813572$ $f = 0.5304918$ $f = 0.5120579$

(a) $\rho_{\text{beam}} = 0.00$ (b) $\rho_{\text{beam}} = 0.05$ (c) $\rho_{\text{beam}} = 0.10$
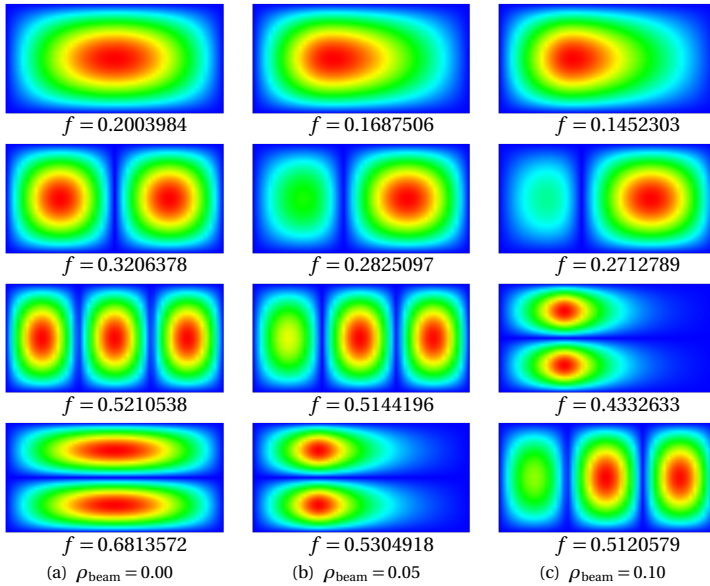
Figure 5.43: First four eigenforms of the mass manipulated plate (see Figure 5.42) with respective eigen angular frequency f for: (a) $\rho_{\text{beam}} = 0.00$, (b) $\rho_{\text{beam}} = 0.05$ and (c) $\rho_{\text{beam}} = 0.10$ (adapted from Bauer et al. [9]).

forms (see Figures 5.43(b) and (c)).

Edge-independent line loads and supports

On top of adding additional elements, the embedded description can also be directly used for the consideration of boundary conditions, which are independent of the parametrization. Typical applications are supports and loads. Figure 5.44(a) shows a plate, which is deformed by fixing certain lines on a shell by a support and applying a pressure load next to it in order to bend the plate around the support. The lower dark blue body in Figure 5.44 is only visualized for illustration purposes since the simulation resembles a simplified forming process. The stresses depicted in Figure 5.44(b) match the expected behavior. The von-Mises stresses are concentrated in the
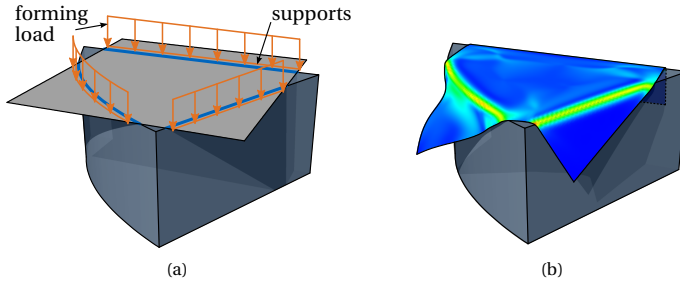
Figure 5.44: (a) Setup of the forming example with support and loads, (b) deformed shell with von-Mises stresses. The upper shell is computed, the lower body is only depicted for illustration purposes (adapted from Bauer et al. [9]).

bent area along the supports. The corner of the plate that is bent around the straight edge, stays flat and experiences no stress. Note that the edge is not aligned to the knot lines. The corner that is bent around the curved edge is undulating since it is not possible to fold the sheet around the edge without stresses.

5.4.2 Embedded Area

The same technique can not only be used for curves on surfaces but also for areas within a surface. Here, different boundary curves are applied to the same untrimmed NURBS patch. The integration of these areas is analogue to trimmed surfaces. The embedding for areas can be used for the support and load application but also to modify the properties of the surface element. An example for the weakening of a shell strip is given in Figure 5.45. The strip is clamped on one side and loaded on the other by a line load p_z. A small band, which is not oriented along the knot lines, is assigned with a lower Young's modulus. The strip can either be modeled by explicitly modeling the three areas or by considering the band as an embedded area with negative Young's modulus in a homogeneous strip. The displacement of the three parametrizations as illustrated in Figure 5.45(c) are compared in Figure 5.45(b). The embedded and the trimmed parametrization have the same underlying NURBS patch, but

(a)

(b)

(c)
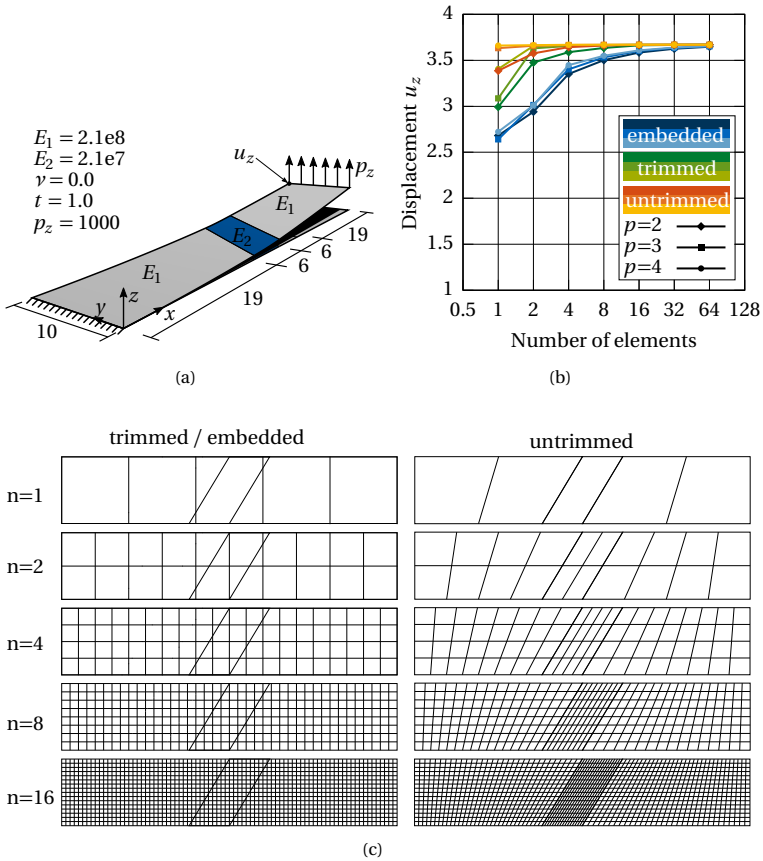
Figure 5.45: Weakening of a shell strip by an embedded area: (a) problem description with the weakened area (Young's modulus E_2) in blue, (b) convergence plot of the displacement u_z for the strip modeled by embedding, coupling of trimmed and untrimmed patches with several polynomial degrees and (c) discretization by knot lines for the untrimmed and trimmed/embedded case, respectively.

the trimmed case consists of three independent patches that are weakly coupled. The untrimmed parametrization models the band directly and the three patches with different parametrizations are coupled as well by a weak rotational coupling.

The untrimmed case shows the best convergence behavior. The solution can be represented by a coarse mesh. The trimmed coupled case performs slightly worse since the band is not aligned to the knot lines. Nevertheless, good results can be achieved for relatively coarse meshes. The embedded model avoids weak coupling. Weak and strong areas w.r.t. the bending resistance are represented by the same control points which is the reason for the slightly poorer convergence behavior.

5.4.3   Embedded Point

Points can be embedded in curves and surfaces. Usually, they are used for boundary conditions that cannot be applied in a strong form, i.e. by constraining the respective control points. The location of the embedded point is defined by a θ^1-coordinate for curves or (θ^1, θ^2)-coordinates for surfaces. The structural element or boundary condition is then added to the system by an additional term in the internal or external work. Since a point does not have a dimension, integration is not needed. The additional part in the internal work for a fixed support introduced by the penalty approach is constituted of the following:

$$\delta W_{\text{int}} = -\alpha \cdot \mathbf{u}(\theta^1, \theta^2) \cdot \delta \mathbf{u}(\theta^1, \theta^2) \tag{5.63}$$

5.5   Isogeometric Sliding Elements

Coupling including a sliding interface is a next step in the complexity of the coupling of two structural members. Note that this section is a revised version of Bauer et al. [13].

A structure sliding along another one still poses a challenge to finite element models since the topology information, i.e. which elements interact, is changing. Typically, this problem is overcome by either the derivation of an application specific element e.g. by Arya et al. [3], Aufaure [4], Chen et al. [33], Coulibaly et al. [41], Ghoussoub [53], Pargana et al. [101], and Zhou et al. [133] or by the introduction of a contact search. Each procedure
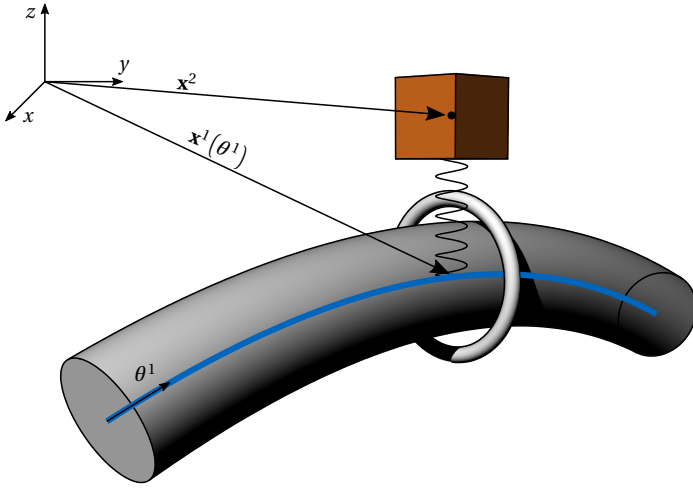
Figure 5.46: Description of the continuum with the position vectors $\mathbf{x}^1\left(\theta^1\right)$ and $\mathbf{x}^2$ (adapted from Bauer et al. [13]).

comprises a disadvantage. Special elements are not general enough and can only be used for one type of finite element whereas contact search is computationally expensive.

The proposed formulation for a sliding contact without friction makes use of the parameter space of a NURBS patch and is inherently free of the aforementioned problems. In contrast to classical finite elements, the parameter space of the geometry is not subdivided into smaller independent parameter spaces. The point of contact for sliding can be described with one curve (or surface) parameter over the whole sliding domain. The contact search becomes unnecessary since the point of contact is inherently described by the parameter. Further benefit can be seen in the smoothness of the NURBS. Sliding is not corrupted by kinks and conversion to an approximated curvature is avoided.

5.5.1 Element Formulation

The proposed new element formulation is a sliding contact formulation. It takes advantage of the parameter space of the NURBS discretization. The core idea is introducing a relative kinematic which is defined in the parameter space and thus providing slip along the curve. The point on the curve defined by the unfixed curve parameter θ^1 can be coupled to a spatial point by a weak coupling formulation as proposed by Bauer et al. [9, 12]. Therefore, an additional term δW^{sc} based on the penalty approach is added to the virtual work. The distance between the point $\mathbf{x}^1 = \mathbf{C}\left(\theta^1\right)$ on the NURBS curve $\mathbf{C}$, and the spatial point $\mathbf{x}^2$ is penalized with a penalty factor α.

$$\delta W^{\text{sc}} = -\alpha\left(\mathbf{x}^1\left(\theta^1\right) - \mathbf{x}^2\right)\cdot\left(\delta\mathbf{x}^1\left(\theta^1\right) - \delta\mathbf{x}^2\right) \tag{5.64}$$

The coupled points (cf. Figure 5.46) are described as follows

$$\mathbf{x}^1\left(\theta^1\right) = \sum_{i=0}^{n} R_{i,p}\left(\theta^1 + \bar{u}_{\theta^1}^1\right)\left(\mathbf{X}_i^1 + \mathbf{u}_i^1\right) \tag{5.65}$$

$$\mathbf{x}^2 = \mathbf{X}^2 + \mathbf{u}^2 \tag{5.66}$$

In contrast to common isogeometric elements, this formulation is including an additional degree of freedom $\bar{u}_{\theta^1}^1$, which is added to the parameter point, and thereby inherently providing sliding of the point along the curve. Consequently, the vector of the discrete degrees of freedom $\hat{\mathbf{u}}$ of the system consists of the following components.

$$\hat{\mathbf{u}} = \begin{bmatrix} \bar{u}_{\theta^1}^1 & | & u_x^1 & u_y^1 & u_z^1 & | & \dots \\ & | & u_{nx}^1 & u_{ny}^1 & u_{nz}^1 & | & u_x^2 & u_y^2 & u_z^2 \end{bmatrix} \tag{5.67}$$

The resulting residual force vector R_r^{sc} and tangential stiffness matrix K_{rs}^{sc} of the additional penalty term are computed by inserting Equation (5.64) in Equation (3.6) and Equation (3.7).

$$R_r^{\text{sc}} = \frac{W}{\partial \hat{u}_r} = \alpha\left(\mathbf{x}^1\left(\theta^1\right) - \mathbf{x}^2\right)\cdot\frac{\partial\left(\mathbf{x}^1\left(\theta^1\right) - \mathbf{x}^2\right)}{\partial \hat{u}_r} \tag{5.68}$$

$$K_{rs}^{sc} = \frac{\partial^2 W}{\partial \hat{u}_r \partial \hat{u}_s} = \alpha \frac{\partial \left(\mathbf{x}^1 \left(\theta^1 \right) - \mathbf{x}^2 \right)}{\partial \hat{u}_s} \cdot \frac{\partial \left(\mathbf{x}^1 \left(\theta^1 \right) - \mathbf{x}^2 \right)}{\partial \hat{u}_r}$$

$$+ \alpha \left(\mathbf{x}^1 \left(\theta^1 \right) - \mathbf{x}^2 \right) \cdot \frac{\partial^2 \left(\mathbf{x}^1 \left(\theta^1 \right) - \mathbf{x}^2 \right)}{\partial \hat{u}_r \partial \hat{u}_s} \tag{5.69}$$

The distinct influence on the positioning of the two coupled spatial points of the respective degrees of freedom is shown in Figure 5.47. Figure 5.47(a) shows the initial matching positions and all degrees of freedom of the system. Figure 5.47(b) depicts the evolving gap Δx for $u_y^2 = 1$, which results in a nonzero entry in R_r^{sc} and K_{rs}^{sc}. Furthermore, the degrees of freedom of the curve, e.g. $u_{1y}^1 = 1$, initialize a penalized gap as illustrated in Figure 5.47(c). The spatial point $\mathbf{x}^1$ on the curve is also moved by the new degree of freedom in the parameter space $\bar{u}_{\theta^1}^1 = 1$. It slides along the curve while moving the point in the parameter space as exemplified in Figure 5.47(d).

It should be noted that the proposed approach is independent of the structural element formulation of the curve, which in turn implies that every NURBS-based element derivation, e.g. cable or beam, can be used.

Remark: Sliding along a Multipatch Geometry

The sliding point on the curve is deliberately coupled to a point in space because this allows a flexible application, meaning that the sliding condition can be attached to arbitrary points, i.e. on structural elements or boundary conditions. In order to be able to slide, the degree of freedom in the parameter space is needed. Hence, the whole sliding domain has to be described by one parameter domain. In the case of cable elements, this is easily viable since the knot vectors of multiple curves can just be joined together. If the other side is always in contact with the sliding element, the spatial point can be fully attached to the element and the continuous domain is not necessary. It can thus be modeled by a multipatch (see Figure 5.48).
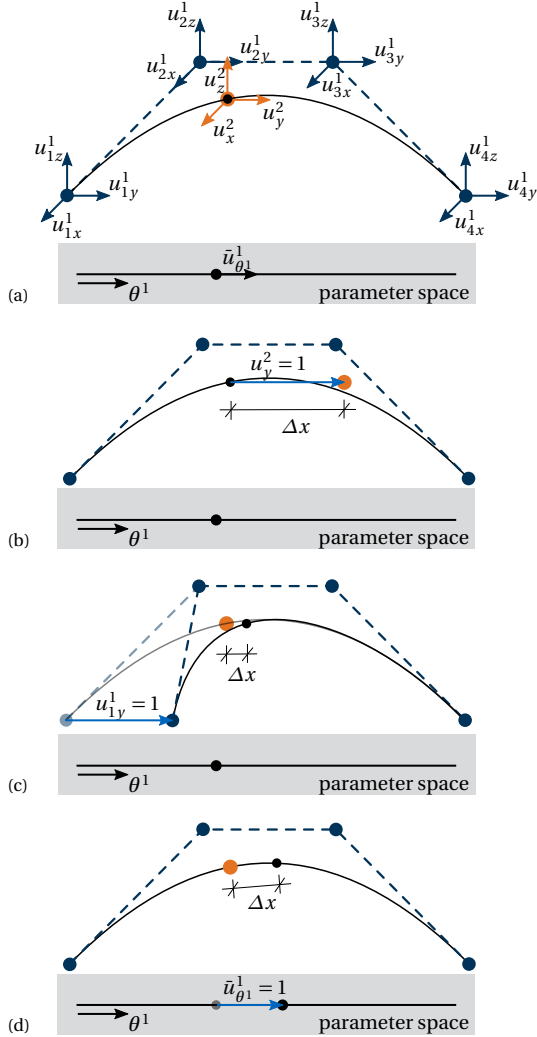
Figure 5.47: Detachment $\Delta x = \|\left(\mathbf{x}^1 - \mathbf{x}^2\right)\|_2$ of the spatial points for the variation w.r.t. different types of degrees of freedom. (a) undeformed system with coincident points and all degrees of freedom, (b) resulting Δx for DOF u_y^2, (c) Δx for DOF u_{1y}^1 and (d) Δx for DOF $\bar{u}_{\theta^1}^1$ (adapted from Bauer et al. [13]).
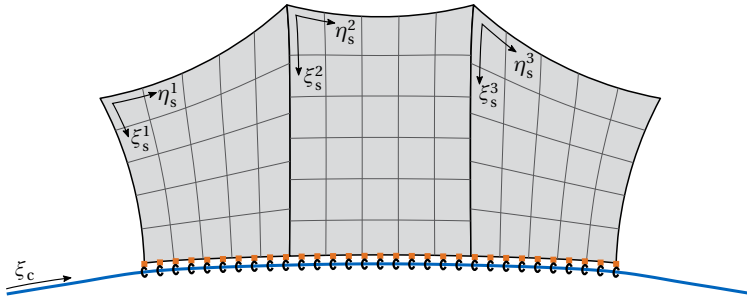
Figure 5.48: Coupling of a sliding cable to a multipatch surface.

5.5.2 Examples

The following examples will validate the concept of sliding using the parametric domain of NURBS.

Cable over a Pulley

A pulley as shown in Figure 5.49 is a good example for frictionless sliding of a cable. The initial cable is prestressed with $\sigma_0 = 1$. Both ends are moved by the same absolute length u_0. If the cable can slide on the pulley without restrictions, the inner force in the cable does not change. The contact area on the pulley is assumed to be constant and not moving. Therefore, it can be modeled by points approximating the sliding line. Here 50 points were chosen. The points are fixed in space, but the respective points in the parameter space of the curve are loose in order to make sliding possible.

In general, the normal force in the cable is constant and equal to the prestress. Small oscillations may occur in this example due to the abrupt change of curvature at the end of the pulley. This is induced by the smooth basis functions, here polynomial degree $p = 3$, which cannot exactly represent such a discontinuity.

Prestressing

The sliding cable can also be used to apply prestress into an initially unstressed membrane as shown in this benchmark example. A quarter of
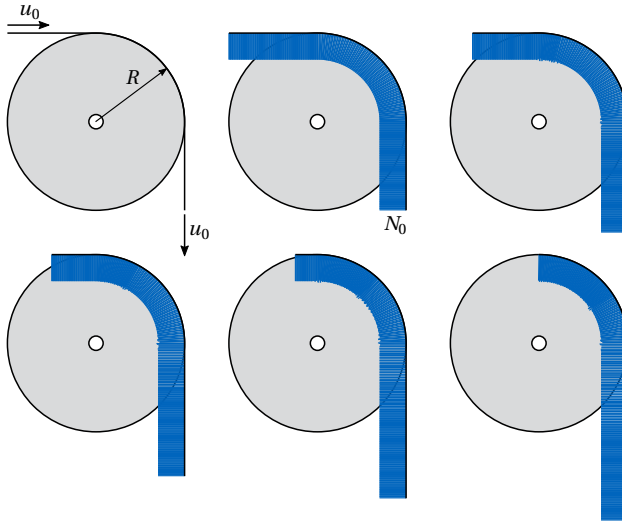
Figure 5.49: Pulley with conducted sliding cable and the respective normal forces for several displacement steps.

a membrane with a hole in the middle is modeled (see Figure 5.50). The inner ring is bounded by a sliding cable which is connected to the membrane by several sliding points. Therefore, the spatial point is coupled to the membrane, whereas the point can slide in the parameter space of the edge curve. This corresponds to a cable in a sleeve. Shortening the cable in the sleeve, i.e. pulling the cable out of the sleeve, introduces a normal force in the cable. This force has to be in equilibrium with the respective stresses in the membrane.

If the outer borders are far away from the inner ring, the ring keeps the form of a perfect circle but shrinks. The relation between the normal force of the cable and the respective principal normal stress of the membrane is given by the boiler formula. The displacement of the membrane is linearly increasing in radial direction from the domain towards the edge cable.
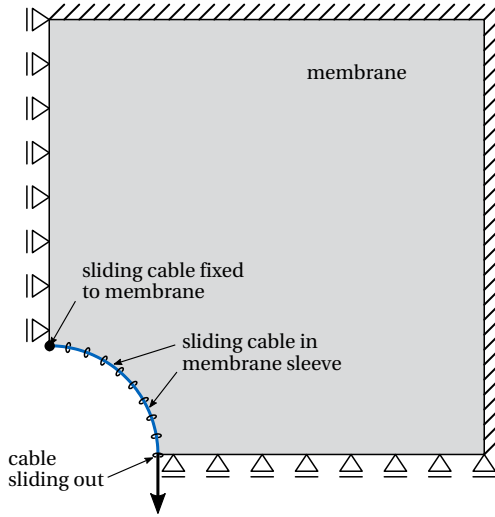
(a)
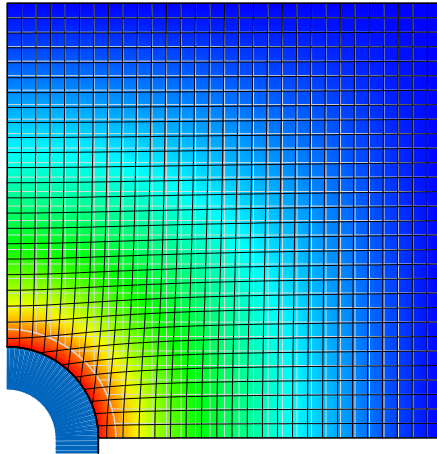
(b)

Figure 5.50: Prestressing of a membrane by the tightening of an inner ring. The cable is pulled out by a force. (a) Setup of the model and (b) resulting normal force in the cable and displacement plot with the deformed (black) and undeformed (gray) isolines of the trimmed NURBS surface (adapted from Bauer et al. [13]).

CAD-integrated Isogeometric Design Process

This chapter will concentrate on the peculiarities of an isogeometric design process. It will show all necessary steps for the establishment of a fully integrated, smooth process and feature the potentials in the design of lightweight structures.

In order to create a continuous workflow, an isogeometric design tool was developed in Rhinoceros, which is a common CAD program for the design of complex free form structures. TeDA[1] (Tool to enhance Design by Analysis) was initiated by Breitenberger et al. [28] with the focus on B-Rep surfaces. It is an interface in Rhinoceros, which can assign structural properties to surfaces, i.e. cross sections, loads and supports, and generate an input file for the solvers Carat++[2] and Kratos Multiphysics[3]. This research extended TeDA for the needs of a more comprehensive analysis

---

[1] https://www.bgu.tum.de/st/software2/forschung/teda/
[2] https://www.bgu.tum.de/st/software2/forschung/carat/
[3] https://github.com/KratosMultiphysics/Kratos

tool, including e.g. beams, multi-stage analysis and advanced loading path options.

Moreover, Rhinoceros provides a parametric environment, called Grasshopper, which is widely used by designers from all industries. The parametric setup of models has great potentials for the design processes since adaptions can easily be made for the whole model. Hence, an interface, named Kiwi!3d[4], was created in cooperation with str.ucture GmbH. It is built upon TeDA. Since the model has to adapt to every change in the input, automation of the generation of the analysis models was one of the biggest tasks, i.e. avoiding to manually remodel the whole analysis model by clicking when something is changed.

An overview of the main steps of a fully CAD-integrated design process is given in Figure 6.1. It includes pre-processing in CAD, parsing the analysis model to the solver, which is in this case Carat++, and post-processing in CAD. Note that the solving is not done in CAD but with an external solver. This has the advantage that the process becomes more flexible as the solver could be exchanged in order to solve other analysis tasks. Moreover, the user does not have to interact with the solver, i.e. it runs in the background, and no difference to a fully CAD-integrated solver will be noted. The different possibilities of where to set the point of transfer between CAD and FE solver in this process are described in detail in Teschemacher et al. [123]. TeDA/Kiwi!3d and Carat++ communicate with each other on patch level, which implies that the full geometry information is available at any time.

6.1 Pre-Processing

The first step in the design process is identifying the boundaries and goals of the planning task and developing an initial geometric model thereof. This model may later be refined and optimized in the design iterations. In order to enable analysis on the geometric model, the geometries, surfaces and curves, have to be attributed with the corresponding structural element type, e.g. shell or membrane, material and cross section properties. Furthermore, it is often necessary to add a refinement strategy to the patch, since initial geometries are often parametrized with few control points that do not allow for the necessary solution space. The boundary conditions

---

[4]   https://www.kiwi3d.com/

Pre-Processing		Simulation	Post-Processing
Geometry Model	**Analysis Model**	**Solver Carat++**	**Result Model**

Surfaces
Curves
Points
Topology
	Analysis
	  Accuracy
	    Result Types
	  Structural Elements
	    Material
	    Section
	    Refinement
	  Boundary Conditions
	    Supports
	    Loads
	    Coupling
		Integration Points
		Stiffness Matrices
		Force Vectors
		Solving
			Deformed Geometry
			Results on
			Integration Points

Figure 6.1: CAD-integrated workflow with the main tasks of the pre-processing, simulation and post-processing.

can either be applied on the existing geometries or a boundary-specific geometry can be derived. This means that the boundary conditions are only applied on parts of the structural element, e.g. in the corners.

The CAD-inherent topology information contains only B-Reps, i.e. the connection between surfaces. In order to be able to deal with curve-like structural elements, the topology between curves has to be added. The same holds for the interaction of curves and surfaces (see Figure 6.2). Therefore, the B-Rep methodology of describing coupling is extended. Each side of the coupling has its segment in the respective parameter space. In addition to having all topology information, it is necessary to define the type of coupling in between the elements. This implies simple interaction types like rigid or hinge-like connections but also more complex types.

Once the analysis model is complete, a text file is written in order to parse the model to the solver. The steps in the solver were already part of Section 3 to Section 5 and are not explained further in this chapter.
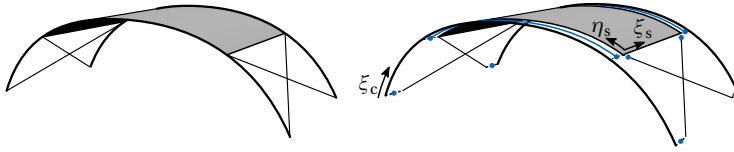
Figure 6.2: Necessary topology information (in blue) for a structural system consisting of curve-like and surface-like elements.

6.2 Post-Processing

Post-processing, i.e. visualization of results, is an important feature for the design of structures. The designer receives a visual feedback of the structural response w.r.t. different quantities, which are important for the design decisions. Typically, color plots visualize these results. The degrees of freedom are related to the control points for IGA, which are not related to a specific point on the patch and often lie outside of the geometry. Nevertheless, the CAD program can easily visualize these results by using the CAD-inherent rendering mesh or a custom visualization mesh. The respective ξ_v- and η_v-coordinates on the NURBS patch of the nodes of this visualization mesh are evaluated w.r.t. the respective degree of freedom on the NURBS patch (see also Herrema [66] and Hsu et al. [69]). Consequently, it is possible to extract the exact result value $V(\xi_v, \eta_v)$ for any point on the surface at any time with the basis functions $R_{i,p}$ and the discrete results V_i on the control points.

$$V(\xi_v, \eta_v) = \sum_{i=1}^{n} R_{i,p}(\xi_v, \eta_v) \cdot V_i \tag{6.1}$$

The CAD program uses the mesh in order to interpolate the values on the nodes and creates a smooth color plot.

Nonetheless, not every result of an isogeometric structural analysis is attributed to the control points. Those are secondary results, for example the stresses. Typically, stresses or the like are evaluated on the Gauss points and not on the FE nodes. Figure 6.3 summarizes the different locations of the results in geometry and parameter space and illustrates the relation to the visualization mesh.
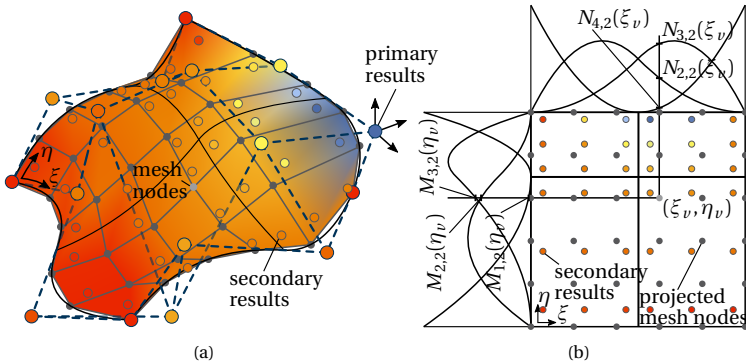
Figure 6.3: Visualization of results by a coarse visualization mesh: (a) geometry space with primary results (degrees of freedom) and secondary results (e.g. stresses) and (b) parameter space with projected nodes of the visualization mesh and secondary results.

Secondary results exist also in classical finite elements. However, these results may then be projected to the mesh nodes. The FE mesh nodes and the visualization mesh nodes usually coincide for classical elements. The nodes know their neighboring finite elements and one can thereof interpolate the result values of the respective Gauss points. In contrast, the visualization mesh of isogeometric elements is independent and the correlation is not defined a priori. A direct interpolation of all corresponding points for the visualization nodes is much more difficult and computationally expensive since it has to search for the respective Gauss points and a sophisticated interpolation scheme has to be used.

Bypassing this through first projecting the results from the Gauss points to the control points, e.g. by a least-square fit, and then evaluating the visualization mesh nodes as presented in Equation (6.1) is cumbersome and the results are getting smeared. The smearing is caused by two reasons. The basis functions are smooth and the results are represented by those basis function and secondly, the influence area of a control point, i.e. FE node, is typically much larger for isogeometric elements than for classical finite elements. Each element usually has $p + 1$ Gauss points and the node

(a)   (b)
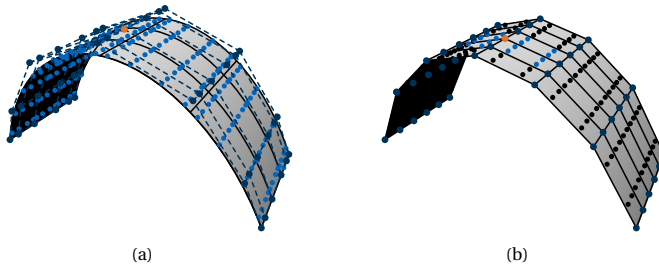
Figure 6.4:   FE node (orange) with corresponding influencing Gauss points (light blue): (a) isogeometric NURBS elements and (b) linear elements.

influences up to $p + 1$ neighboring elements in each direction. Figure 6.4 shows the corresponding Gauss points (light blue) of one FE node (orange) for NURBS and quad-elements. Note that the two parametrizations have the same amount of FE nodes. A further challenge is trimming since trimmed elements corrupt the equally distributed rectangular topology of the integration points.

If CAD is enhanced such that it can compute the necessary results from the degrees of freedom, e.g. the stresses from the displacement, the color plot could be generated similar to the control point entities. The post-processor can arbitrarily compute and retrieve the needed nodal values of the visualization mesh. However, this might be complex and requires an implementation of the FE code in the CAD software. Furthermore, the post-processing tool is then restricted to the implemented result types. Additionally, there are result types, which cannot be computed only from the degrees of freedom on the control points. This is for example the case for a structural analysis including damage since the points have to be tracked over the whole analysis and cannot just be evaluated at a certain time. Therefore, a more general approach using the Gauss point results directly is discussed in the following sections.

6.2.1   Scalar Results

As previously described, the given data for the post-processing are the refined NURBS patch information and a set of points on the NURBS patch,
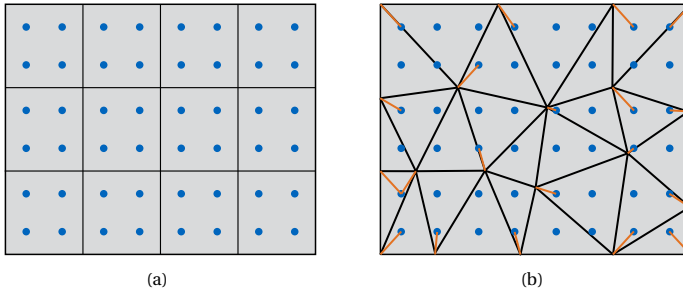
Figure 6.5: Visualization in the post-processing: (a) knot spans with Gauss points and (b) visualization mesh for color plot with nearest Gauss points.

which are described by ξ- and η-coordinates. These points, later also referred to as result points, are attributed with the respective result that has to be visualized. The task is to transfer the results from the initial set of points, often the Gauss points, to the nodes of the visualization mesh.

The interpolation of the result points is not challenging for curves, since the mapping of the result points is only in 1D and linear interpolation can easily be implemented, if necessary. Therefore, only the visualization of surface results will be explained in more detail.

Figure 6.5(a) depicts such a set of points, i.e. the Gauss points, for a simple rectangular plate. Note that the number of Gauss points was reduced to two per direction and knot span for illustration purposes. The corresponding visualization mesh is shown in Figure 6.5(b). A nearest-neighbor approach determines the values for the visualization nodes. The closest Gauss point in the parameter space is identified and its value is assigned to the visualization node. The distance in the parameter space is chosen. The search for the closest point has to be fast since it has to be computed for every visualization mesh. Moreover, by scaling the deformation of the structure other parts of the structure might come closer than the initially nearest Gauss point and the value suddenly jumps.

The quality of such a visualization approach is strongly dependent on the quality of the meshes. Therefore, the meshes in Figure 6.6 are investigated.
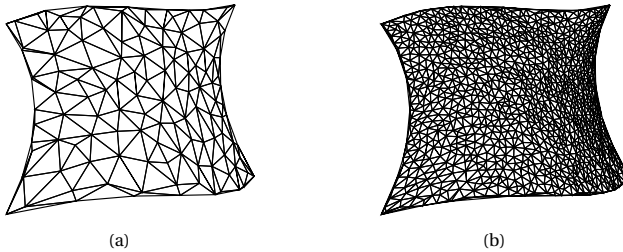
Figure 6.6: Visualization meshes: (a) coarse and (b) fine.

In addition to the visualization mesh, the density of the result points is crucial for the quality of the color plot. Figure 6.7 shows the result of the nearest neighbor search for different density levels. Squares depict the result points whereas circles illustrate the nodes of the visualization mesh. The color indicates the assigned result value.

Figure 6.8 shows the resulting color plot for the nearest neighbor search in Figure 6.7. It can be seen that a smooth color plot is the outcome in the case of many result points. The quality is then only depending on the quality of the visualization mesh, e.g. no distorted elements, since there is always a result point which is very close to the visualization node. The quality of the color plot is in general lower for a coarse result point set. Increasing the density of the visualization mesh only results in a separation of colors since many visualization points find the same result point as nearest neighbor and therefore generate an area with a constant result value. If the nodes of a coarse visual mesh are distributed equally to the result points, i.e. every result point is only nearest neighbor to one visualization point, also this combination can produce smooth color plots. Advanced shaders can also be used to further smoothen the result.

Other more sophisticated interpolation techniques could give better results in the case of unequally distributed points. Nevertheless, it was found that the nearest neighbor approach in this context generates sufficiently good results and is additionally very robust for any type of point configuration, which is one of the most important properties.

The previous example showed the visualization of a continuous result. Despite the continuous basis functions, the results may also be discontinuous

(a)

(b)

(c)

(d)
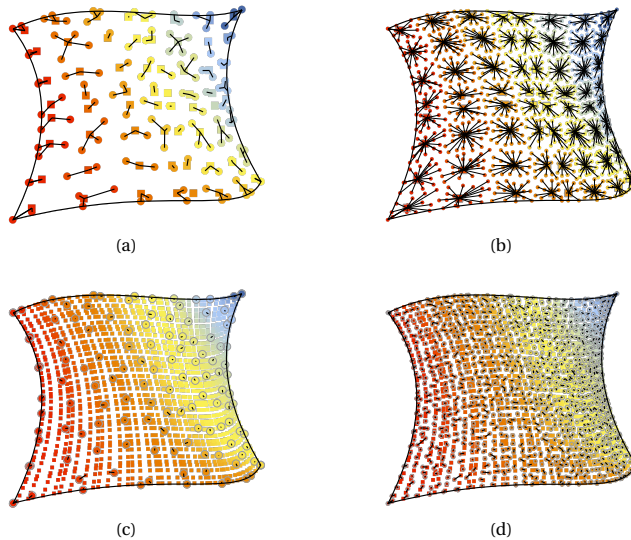
Figure 6.7: Nearest neighbor search for visualization mesh nodes (circles) to result points (squares): (a) coarse visualization mesh and few result points, (b) fine visualization mesh and few result points, (c) coarse visualization mesh and many result points, and (d) fine visualization mesh and many result points.

as e.g. in structural analysis including damage. Figure 6.9 contains a patch, where all result points inside the inner square have the value one whereas the outer ones have zero. The smearing of the results for the projection to the control points is shown on the left. The right side shows the color plot that was generated with the result points only. The visualization mesh is the same for both cases.

If the visualization mesh does not change, it would also be possible to pass the location of the mesh vertices in the parameter space of the structural elements to the solver. These points must not be considered in the analysis itself but have to be evaluated for the desired stresses and other entities. An interpolation or nearest neighbor search is then avoided. However, in general the visualization mesh is changing for the deformed structure. Computing the visualization mesh from the Gauss point would be another
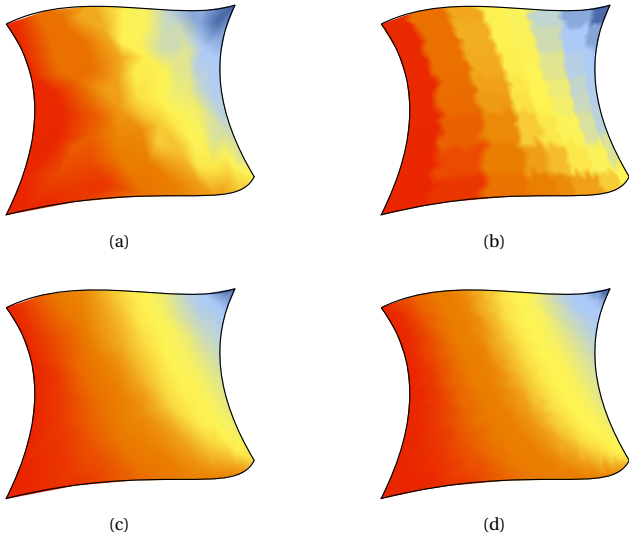
Figure 6.8: Color plot of results for: (a) a coarse visualization mesh and few result points, (b) a fine visualization mesh and few result points, (c) a coarse visualization mesh and many result points, and (d) a fine visualization mesh and many result points.
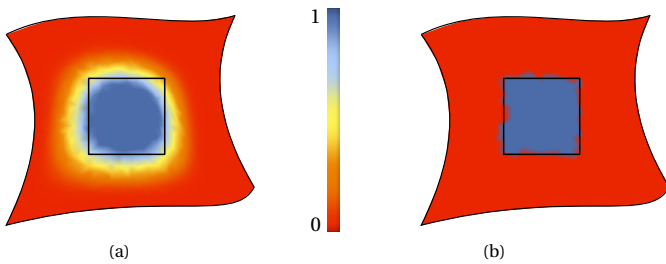
Figure 6.9: Discontinuous results: (a) visualization with backmapping of the results to the control points and (b) visualization by using the result points directly.
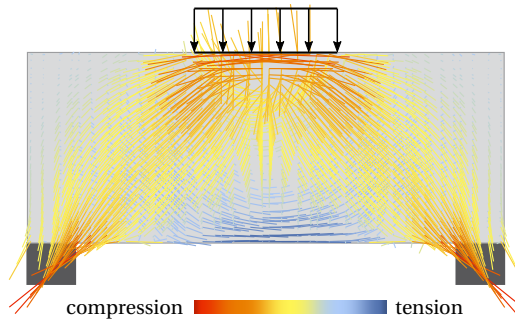
Figure 6.10:   Vector results for a plate under load.

approach to the problem. In this case, one has to ensure that additional evaluation points on the borders of the geometry are added in the beginning of the analysis.

6.2.2   Vector Results

The results may also contain vectors. Consequently, the ability of the post-processor of displaying vector results is needed. The directions are directly displayed on the result point. Additionally, if the length of the vector is a measure for the result, a coloring is meaningful (see Figure 6.10).

If the vector results are written with Cartesian coordinates by the FE solver, it is important to look at the results in the corresponding deformation state in order to avoid misinterpretation of results. Alternatively, the vector results could be expressed in relation to the base vectors of the NURBS patch in order to enable scaling.

6.3   Parametric Environment

Parametric modeling is widely spread in engineering and architecture. Proceeding from input parameters, combining and applying functions to the input set generates the necessary data. This is closely related to programming. The focus in the field of architecture is mainly on shape generation and appearance. Bringing structural analysis tools into common design

environments opens up a totally new range of possibilities. Engineering and architecture interlock much closer since both professions can work on the same model and tools from one area are accessible to the other. Architects obtain structural feedback whereas engineers can use the CAD functionalities to derive complex shapes and also e.g. load distributions.

This is possible for classical finite elements as well. Nevertheless, avoiding meshing in the sense of approximating the geometry with a polygonal mesh is a benefit of IGA, especially in the parametric environment. This affects not only the structural elements themselves but also their interaction. Meshing surfaces and curves, which are most common in the field of construction engineering, is rather robust compared to volumes. In spite of that, considering the interaction between several elements may be demanding and effort has to be made in order to generate matching parametrizations at the boundaries. This can be also seen in Figure 6.11. A curve should be coupled to a surface (see Figure 6.11(a)). Figure 6.11(b) shows the parametrization with NURBS in CAD. The meshed FE parametrizations for classical analysis are shown in Figure 6.11(c) for independent meshing and Figure 6.11(d) for meshing generating a matching interface. Automating the generation of the matching interface may be cumbersome but necessary in a parametric design workflow. The NURBS-based FE model in contrast can directly apply the parametrization of the design. The interface of the curve and surface are in general not matching, i.e. the control points, which are the FE nodes, do not coincide. Nevertheless, due to weak coupling formulations, this parametrization can be used. Note that the geometries themselves, i.e. curve and surface, still coincide within the CAD tolerances, whereas the independently meshed geometries often do not.

The parametric interface Kiwi!3d for isogeometric analysis is implemented in Grasshopper inside Rhinoceros. In this setup, Grasshopper provides visual programming. The ''components'' are basically functions depending on input parameters and return output data, e.g. a circle component that constructs a circle by a center point, a radius and a normal. These components are linked with ''wires'' on the ''canvas''. The wires transfer data from one component to another. Native Grasshopper components are mainly focused on geometry and data processing. Since the program structure is open and rather well documented, many third party plug-ins

(a)

(b)

(c)

(d)
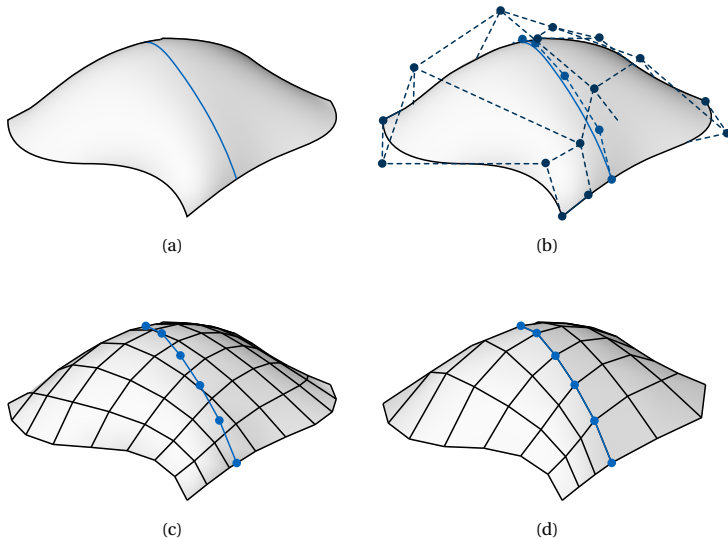
Figure 6.11: Coupling of a surface with a curve: (a) problem setup, (b) unrefined NURBS control polygons, which can be used for IGA, (c) meshing of the problem for classic finite elements without the consideration of the coupling and (d) meshing of the problem for classic finite elements considering the coupling.

have been developed. The plug-ins can also be combined to accomplish a project including different design tasks and evaluation methods.

Linking isogeometric analysis into the parametric CAD environment enables the construction of parametric models which contain geometric and structural parameters. Furthermore, it is possible to automate a whole design chain. This means that the results of analysis ''one'' can be used to setup analysis ''two''. Consequently, if one parameter is changed, the whole design chain updates. This is one of the main advantages of a parametric CAD-integrated design tool. Many variations of a design task can be evaluated with one model, including different types of parameters, without the need of reconstructing the whole model for every change. Parametric modeling related to IGA was also examined by Alic [1], Herrema [66], and Hsu et al. [69].
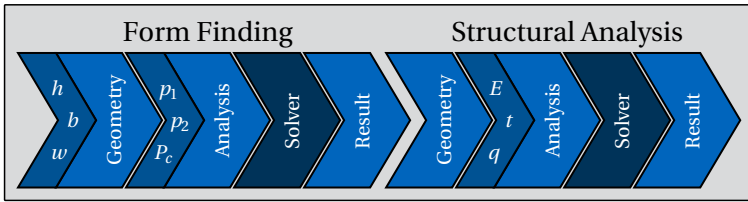
Figure 6.12: Parametric design of a four-point sail including form finding and structural analysis with the parameters h, w and b for the geometry of the form finding, p_1, p_2 and P_c for the form finding analysis model and E, t and q for the analysis model in structural analysis.

Figure 6.12 corresponds to the parametric design process of a four-point sail seen in Figure 6.13, which is form found and loaded. Therefore a form finding and a structural analysis are conducted. The dimensions h, w and b define the support points and the initial geometry of the sail. The prestress values p_1 and p_2 are assigned to the surface. The edge cables are derived from the boundaries of the surface and are prestress by the parameter P_c. Having the analysis model, one can solve the form finding analysis. The form found structure is given in the result model and the deformed geometry can directly be used as input for the consecutive structural analysis under a dead load q. Young's modulus E and thickness t can be assigned in this step for the analysis model since the form finding analysis is material-independent.

Figure 6.14 presents the result, i.e. the deformed sail under the load q, of the structural analysis originating from a simple parameter study with changing height h, prestress P_c in the cable and Young's modulus E of the membrane. If the height of the sail changes for example, the form finding and the structural analysis are updated automatically since the result of the form finding is used to build the analysis model for the structural analysis.

Further design studies using Kiwi!3d within the parametric CAD environment can be found in Bauer et al. [11], Goldbach et al. [54–56], Längst et al. [82, 83], and Oberbichler et al. [98].

Given that the creation of the design model is fully automated, the analysis can be used as a black box inside an automated optimization loop (see
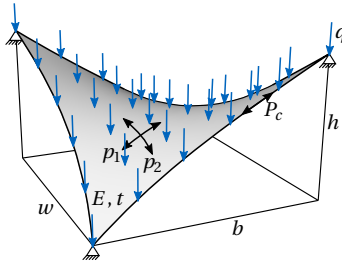
Figure 6.13: Parameters of a four-point sail: height h, widths w and b, membrane prestress p_1 and p_2, cable prestress P_c, Young's modulus E, thickness t and load q.

$h = 3.0$ $h = 5.0$ $h = 7.0$

$P_c = 10$ $P_c = 20$ $P_c = 40$

$E = 50000$ $E = 200000$ $E = 800000$
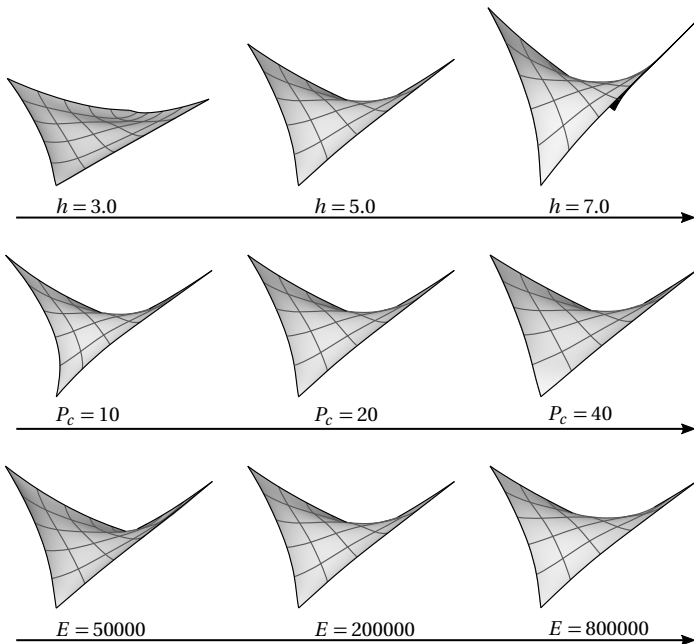
Figure 6.14: Deformed four-point sail under a vertical load q as a parameter study for three different parameters.
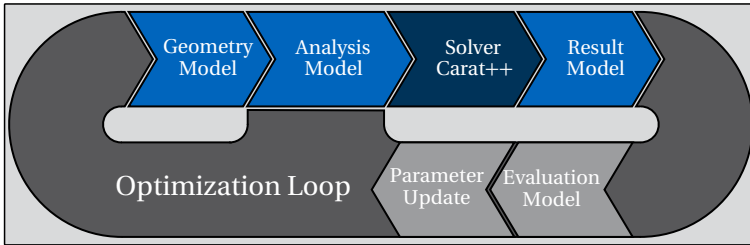
Figure 6.15: Schematic optimization loop inside the parametric domain with design object described by the isogeometric analysis chain, evaluation model and parameter update.

Figure 6.15). Starting from a given parameter set, which can include geometric as well as structural parameters, the analysis model can be built. The results are then evaluated with regard to one or several objectives. These objectives can be as simple as a maximal displacement but also complex including several operations as e.g. for the check of the ultimate limit state or additional analysis as e.g. a daylight analysis for the energy input. Furthermore, it is possible to check if constraints are violated. The CAD environment is especially useful if there are geometric constraints since CAD-internal functions can directly detect clashes between geometries.

The optimization algorithm provides an updated parameter set for the geometry and analysis model. Basically any optimization tool can incorporate this simulation inside the parametric domain. Zero-order algorithms are most suitable since only the value of the objective is given for evaluation. Derivatives of the objective are not directly given but can be computed by finite differences for first order algorithms in order to achieve a more goal-driven optimization loop. Those algorithms are especially powerful for few design variables.

An example of such an optimization was performed for a bending-active beam, which should be bent from flat pieces into a defined shape. Three additional layers as shown in Figure 6.16 generate unequally distributed stiffness in order to obtain an asymmetric shape in equilibrium between the two simple supports without external forces. The length of each layer is given in the parameter space of the underlying beam by f_i^s and f_i^e. The
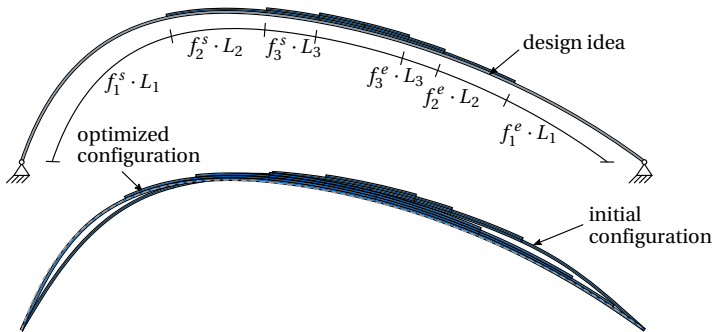
Figure 6.16: Optimizing the cross section of a bending-active beam by positioning layers in order to match the design idea: initial and optimized equilibrium shape.

underlying curve is trimmed and offset by the thickness. Galapagos[5], a built-in evolutionary optimization solver in Grasshopper, can directly be used to determine an optimized parameter set. The objective function is defined by a minimization of the gap between the intended shape, i.e. design idea, and the actual shape of the bending-active beam. Therefore, the distance of 30 points on the design shape to the actual shape is measured and summed up. This sum could be minimized from 9.01 to 1.05, with the length of the beam being 29.13. This corresponds to an improvement of 88.3%.

6.4 Analysis-enhanced Design Process of Lightweight Structures

Lightweight structures are characterized by their load carrying behavior. Form and force are directly related to each other, i.e. they are only in equilibrium for a distinct shape w.r.t. the boundary conditions. In return, this implies that the designer cannot create the form in an arbitrary way but has to follow certain rules, which can be evaluated by experiments and mock-ups such as those by Heinz Isler and Frei Otto or by simulations.

---

[5] by David Rutten: https://www.grasshopper3d.com/group/galapagos
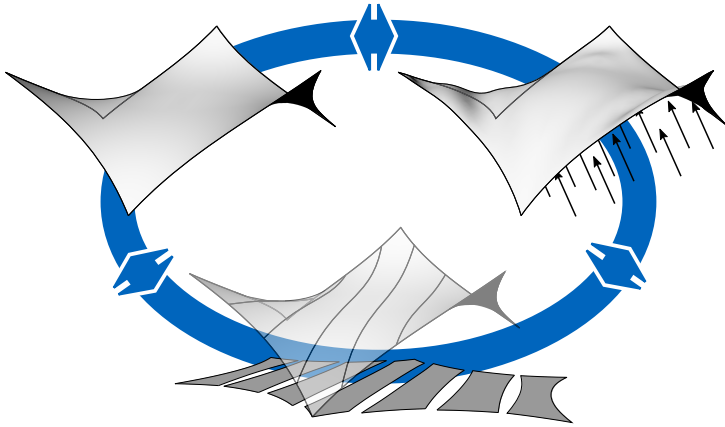
Figure 6.17: Design cycle of tensile structures: form finding, structural analysis and cutting pattern generation.

Popular examples are tensile and bending-active structures. As one can imagine, a tight interaction between the design software, i.e. CAD, and the simulation of the physical behavior, i.e. FE analysis, is beneficial for the design process.

6.4.1 Design Cycle of Membrane Structures

In the case of membrane structures, the continuous workflow is especially important since not only the form finding process has to be considered but also structural analysis and manufacturing (cf. Figure 6.17). Form finding is necessary to find a shape in equilibrium, whereas structural analysis ensures the safety and serviceability in the built state. Manufacturing is important since the typical anticlastic shapes of tensile membrane structures and the synclastic ones of pneus are non-developable surfaces and can thus not be manufactured by flat textiles or foils from rolls. The approximation using flat pieces of material, i.e. the cutting pattern, influences the appearance and behavior of the whole structure.

Form Finding Analysis

Form finding analysis has to be conducted in order to find a geometry in equilibrium. An overview of form finding strategies can be found in Veenendaal et al. [126]. The applied method for the form finding of tensile structures in this thesis, the Updated Reference Strategy (URS), was originally introduced by Bletzinger et al. [23] and applied with isogeometric analysis in Philipp et al. [105] and Philipp [106]. It can be seen as an extension of the force density method by Linkwitz [89] for membranes. The goal is a shape in equilibrium for a given stress state. A system is in equilibrium is found if the internal and external work are balanced in the current configuration.

$$\delta W^{\mathrm{cur}} = \delta W_{\mathrm{int}}^{\mathrm{cur}} + \delta W_{\mathrm{ext}}^{\mathrm{cur}} = -\int_{\Omega} (\boldsymbol{\sigma} : \delta \mathbf{e}) \, \mathrm{d}\Omega + \int_{\Omega} (\mathbf{p} : \delta \mathbf{u}) \, \mathrm{d}\Omega \qquad (6.2)$$

The resulting singular system can be solved by adding a stabilization term, which in this case is the linearly blended virtual work in the reference configuration. The reference geometry is updated after every computation step. An equilibrium is found if the stress in the reference configuration, i.e. the PK2 stress, matches the stress in the current configuration, i.e. the Cauchy stress. This is equivalent to the reference configuration matching the current one.

In the case of form finding of mechanically prestressed membrane structures, the external load can be neglected and thus the virtual work can be simplified to $\delta W = \delta W_{\mathrm{int}}$. This is legitimate since the dead weight of a membrane and thus the respective stresses are usually very small in comparison to the stresses due to prestressing.

Elastic members can also be considered in the form finding analysis as e.g. necessary for a membrane that is spanned between elastic beams. Since prestress is introduced into the membrane, the flexible beams deform which in return changes the boundaries of the membrane. The respective terms of the virtual work of the elastic members can be computed like for the standard structural analysis. In contrast to the form finding elements, the reference configuration is never updated for the elastic elements. Furthermore, the necessary geometry update of the form finding elements should only be executed when the total system has found an equilibrium within the set tolerances in order to ensure a stable simulation.

Structural Analysis

Structural analysis in the design cycle mainly has to be performed in order to check the ultimate (ULS) and serviceability (SLS) limit state. The ULS is principally characterized by the resistance to loading, whereas the SLS is more concerned about proper functioning and comfort. The analysis itself is a (geometrically) nonlinear analysis, which has already been described in Section 2 and Section 3.

$$\delta W = \delta W_{\text{int}} + \delta W_{\text{ext}} = - \int_{\Omega_0} (\mathbf{S} : \delta \mathbf{E}) \, \mathrm{d}\Omega + \int_{\Omega_0} \big(\mathbf{p} : \delta \mathbf{u}\big) \, \mathrm{d}\Omega \qquad (6.3)$$

Cutting Pattern Analysis

As mentioned before the surfaces of a membrane structure are usually not developable. However, the membrane has to be fabricated from originally flat material with a limited size. Therefore, the form found structure is divided into stripes, which are flattened. Knitting can avoid this problem because arbitrary curved shapes and sizes can theoretically be produced. Nevertheless, the second task of the cutting pattern analysis, namely the compensation, still has to be considered. The form found structure was defined by boundary conditions and prestresses in the structural members. These stresses are typically incorporated by stretching the membrane, i.e. the initial geometry is unequal to the form found geometry, even for developable surfaces. In order to retrieve an initial geometry for manufacturing, several methods have been proposed in literature, see e.g. Dieringer [43], Gee et al. [52], Govindjee et al. [57, 58], Gründig et al. [61], Haug et al. [65], Kim et al. [76], Linhard [86], Linkwitz et al. [87, 88], Maurin et al. [93], Mc-Cartney et al. [94, 95], Sheffer et al. [121], Topping et al. [124], Vaillant et al. [125], Wang et al. [127], and Widhammer [131]

Note that there are also form finding algorithms which already include the cutting pattern in the optimization of the shape (see e.g. Gade et al. [51]).

In this dissertation, the Variation of Reference Strategy (VaReS) by Widhammer [131], adapted to isogeometric analysis by Goldbach et al. [56], is applied. The concept of this approach to cutting pattern generation is minimization of the difference of the potentials of the given prestress state and the elastic potential. In order to determine the elastic potential, a (flat) reference geometry is used to compute the displacements, strains

and stresses in the current, i.e. target, configuration. The degrees of freedom are the coordinates of the reference configuration. The best possible cutting pattern is reached for the minimal total potential.

$$\min_{\mathbf{X} \in \Omega_0} \Pi_{\text{total}}(\mathbf{X}) = \min_{\mathbf{X} \in \Omega_0} \left(\Pi_\chi(\mathbf{X}) - \Pi_{\text{pre}} \right) \tag{6.4}$$

Mounting Analysis

The mounting analysis simulates the joining of the stripes of the cutting pattern and the edge cables. It can be performed in two different ways (see Figure 6.18). The first option is close to the strategy of the cutting pattern analysis, which computes the stresses out of an initial displacement. The other one is closer to the real mounting process as sewing and pulling into form is considered. The advantages and disadvantages will be discussed in the following.
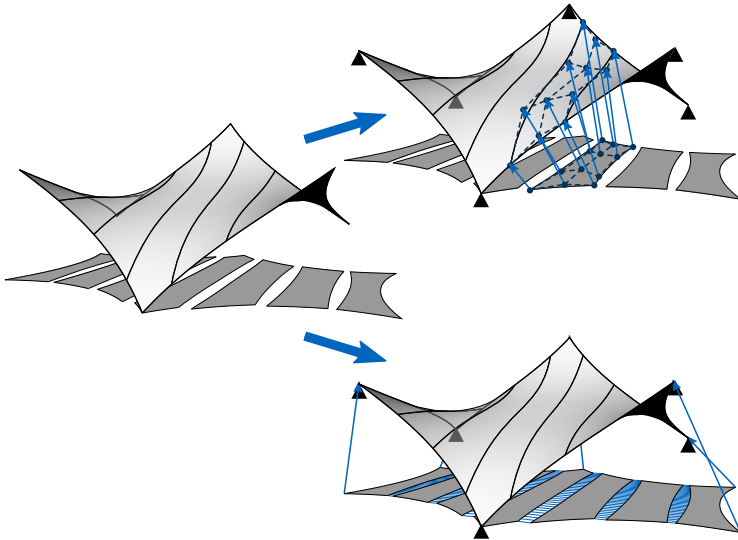
Figure 6.18: Mounting analysis strategies for membrane structures: assembly in the target configuration (top right) and in the initial configuration (bottom right)

Mounting by assembly in the target configuration

This approach utilizes the fact that the target geometry is known in the case of a membrane mounting. The form found structure is the optimal shape and the cutting pattern has the same initial parametrization. Refining the NURBS patches for the cutting pattern analysis does not change anything on the stress state, since NURBS refinement reproduces the exact same shape. Similar to the VaReS approach of the cutting pattern generation, the flat configuration is set as reference geometry of the form found structure. This is the starting point of standard geometrically nonlinear structural analysis including initial displacements. The equilibrium is found by proceeding from this initial deformation. The advantage of this approach is the easy modeling of the mounting. The relation between the cutting patterns are already defined in the target structure. They match within the tolerances in CAD and weak coupling is applied. The same holds for the cables. They can be attached to the membrane in the target geometry, both fixed and sliding. The prestress of the cables can either be applied as prestress or with a reference geometry. Note that the reference geometry has to be constructed by scaling the target geometry in order to generate constant prestress as assumed in the form finding analysis. It is not recommended to refer to a straight cable with respective length $L = f \cdot l$. More details are provided in Section 6.4.2. The scaling factor f for the cable reference geometry is computed as follows:

$$f = \sqrt{\left(\frac{2 \cdot S_{\mathrm{pre}}}{E} + 1 \right)^{-1}} \tag{6.5}$$

from

$$S_{\mathrm{pre}} \cdot A = \frac{a_{11} - A_{11}}{2 \cdot A_{11}} \cdot EA = \frac{\left(\|\mathbf{a}_1\|_2 \right)^2 - \left(\|\mathbf{A}_1\|_2 \right)^2}{2 \cdot \left(\|\mathbf{A}_1\|_2 \right)^2} \cdot EA$$

$$= \frac{\left(\|\mathbf{a}_1\|_2 \right)^2 - \left(f \cdot \|\mathbf{a}_1\|_2 \right)^2}{2 \cdot \left(f \cdot \|\mathbf{a}_1\|_2 \right)^2} \cdot EA = \frac{1 - f^2}{2 \cdot f^2} \cdot EA$$

It is feasible to use one scaling factor for the whole curve since there is a linear relation between the length of the basis vectors and the positions of the control points. The center of the scaling is free of choice as the supports are applied on the target shape.
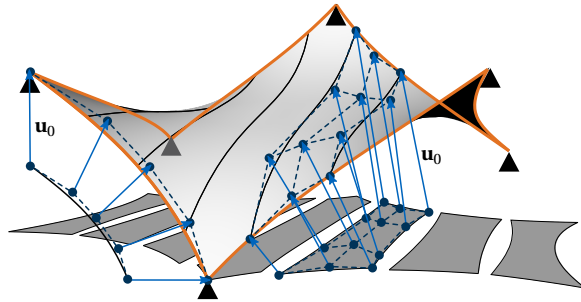
Figure 6.19: Mounting of the membrane by assembly in the target configuration with flat reference geometry, i.e. initial displacements. The edge cables are shown in orange.

Figure 6.19 shows the setup of mounting by assembly in the target configuration.

Mounting by assembly in the initial configuration

Assembling the membrane in the flat configuration comes closer the ''real'' assembly. Therefore, the boundary points of the membrane are pulled from the flat configuration towards the supports. The geometry curves of adjacent seam lines are subdivided and contracting cables or a connecting element formulation pulls the resulting points together. It is important that the seam lines of two neighboring stripes have the same length in order to avoid restraints similar to those in Section 5.2. How to enforce same seam lengths is described in e.g. Dieringer [43]. However, if the cutting pattern is manufactured with unequal seam lengths, such restraints can be considered. There are several methods to involve the edge cables in the simulation differing in their modeling complexity. The simplest option is to put the cables on the edges of the flat membrane, compare the total lengths in the flat and the target configuration and add the missing stress as prestress. It is assumed that the edge stretches almost uniformly since the goal is a constant stress in the membrane. Another approach is similar to the treatment of the edge cables in the assembly in the target configuration. The cable is already in the target configuration and stresses evolve from shrinking. The connection points with the membrane can
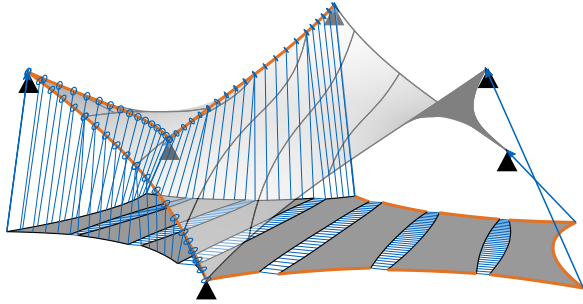
Figure 6.20: Mounting of the membrane by assembly in the initial flat configuration with contracting cables (blue). The edge cables are shown in orange.

easily be determined since the parametrization of the target and the flat configuration of the membrane are the same. Hence, ξ- and η-coordinates can be derived in one configuration and directly used on the other one. The respective points on the flat geometry can be pulled towards the edge cables. The points on the edge cables may slide on them in order to avoid restraints similar to the one between the membrane stripes. Both modeling approaches are illustrated in Figure 6.20. Furthermore, material nonlinearities can be considered in this assembling process since the history of strains and stresses is available.

This setup of the mounting can have problems with the stability of the simulation. If a member loses tension, it might not be solvable with the implicit FE solver. The prestresses for the contracting cables have to be chosen carefully. Also the patterns should be positioned as close as possible for a stable simulation and the support points should be approached in several steps.

Figure 6.21 compares the stresses of the two mounting methods. It can be observed that the stresses in the membrane as well as the edge cables are more equally distributed for the assembly in the target configuration. This lets conclude that the relation between the patch edges changes.

(a)

(b)
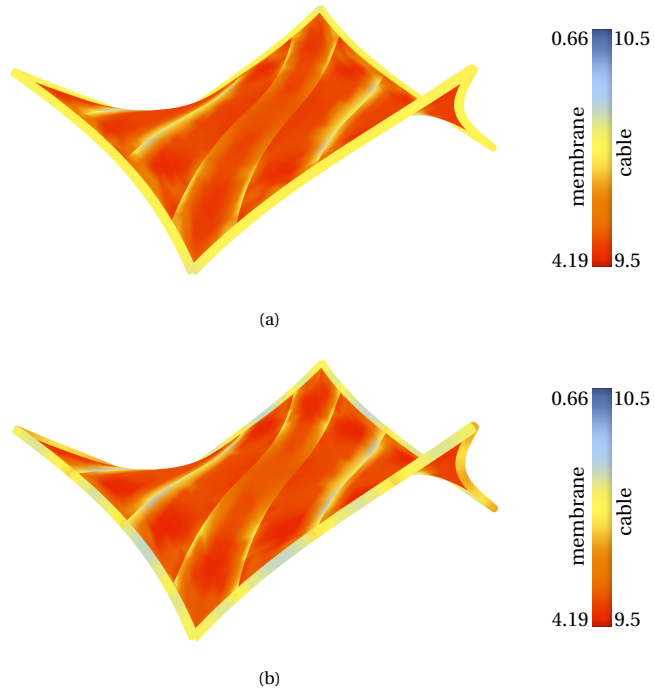
Figure 6.21: Principal normal force 1 in the mounted membrane and normal force in the edge cables: (a) assembly in the target configuration and (b) assembly in the flat configuration.

6.4.2 Form Finding of Bending-Active Structures

This section is a revised and shortened version of Bauer et al. [15]. The indented remarks are not part of the original contribution.

Bending-active structures are a subcategory of lightweight structures. Their design is especially difficult since the assembled structure has to consider the mounting process. This is usually done by laying out flat rods, lifting and pulling them with cables and forces into the desired shape. The final form can e.g. be influenced by changing the flat layout. However, determining this initial layout, which results in the closest possible shape to the design idea, can be difficult. It would be beneficial to be able to start the
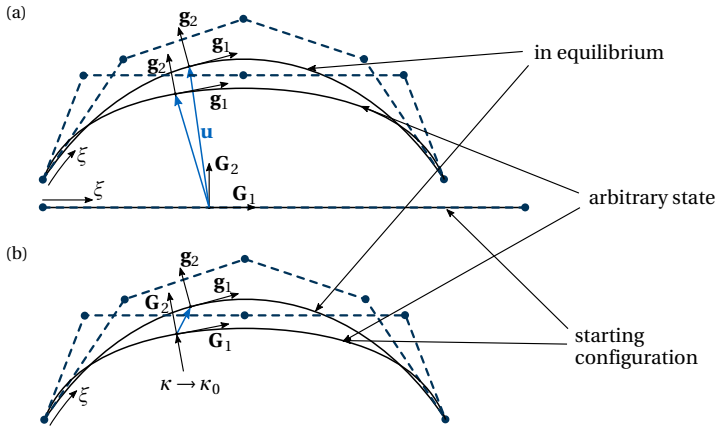
Figure 6.22: Geometry configuration with base vectors for: (a) standard approach and (b) inverse approach (adapted from Bauer et al. [15]).

computation with a configuration close to the intended design. Inverse methods are needed in order to retrieve correct stress-strain information from the already deformed state. This is possible with certain assumptions about the initial geometry. The stresses and strains can then be computed based on these assumptions. Similar approaches already exist in literature such as e.g. by Bellmann [19] and in other software such as e.g. in K2Engineering[6].

In order to incorporate these assumptions, the reference configuration of the isogeometric element formulations is modified. The modifications are of minor intrusion since the element formulations themselves are not changed. In the standard approach, the geometries of the current and reference configuration are compared at every material point. The corresponding Green-Lagrange strains $\mathbf{E}$ and the energetically conjugated 2nd Piola-Kirchhoff stresses $\mathbf{S}$ are computed from the metric.

---

[6]   by Cecilie Brandt-Olsen: https://github.com/CecilieBrandt/K2Engineering

$$E_{ij} = \frac{1}{2}\left(\mathbf{g}_i \cdot \mathbf{g}_j - \mathbf{G}_i \cdot \mathbf{G}_j\right) \tag{6.6}$$

where $\mathbf{G}_i$ and $\mathbf{G}_j$ are the local base vectors of the geometry. They correspond to a local fiber length and can also be used for measuring geometric properties such as curvature.

Strains and stresses can be computed for any arbitrary pair of geometry configurations (see Figure 6.22(a)). The parametric coordinates are used to link the corresponding material points. This even allows for geometry refining, i.e. adding degrees of freedom, and still being able to get the link between the reference and the actual configuration. When releasing the geometrical form apart from the intended Dirichlet boundary conditions, the system deforms towards its equilibrium state.

The proposed inverse approach distinguishes itself from the standard procedure by not starting the search for equilibrium in the initially unstressed state but in an arbitrary deformed state (see Figure 6.22(b)). The initial configuration is not modeled explicitly but considered by certain assumptions that will be described in the following sections. Similar to the *InitStress* method, the integration is then performed in the initial deformed configuration. This strategy is appropriate for a certain type of structures. One primary condition is that large in-plane strains are not expected or that the initial integration area can be derived from additional assumptions. A more complex cutting pattern analysis has to be conducted in order to consider such large in-plane strains correctly.

Inverse Bending

The term related to bending in the Principle of Virtual Work can be derived from the change in curvature $\boldsymbol{\kappa}$.

$$\delta W_{\text{int}}^{\text{bend}} = -\int_{A/L} \mathbf{m} : \delta\boldsymbol{\kappa} \, \mathrm{d}X \tag{6.7}$$
$$\text{with} \quad \mathbf{m} = I \cdot \mathbf{D} \cdot \boldsymbol{\kappa} \text{ and } \boldsymbol{\kappa} = \left(\boldsymbol{\kappa}_{\text{act}} - \boldsymbol{\kappa}_{\text{initial}}\right)$$

The reduced integration domain is denoted by A for surface elements and L for curve elements. Material matrix $\mathbf{D}$ and the respective moment of inertia I for the bending axis, which is a result of the pre-integration over
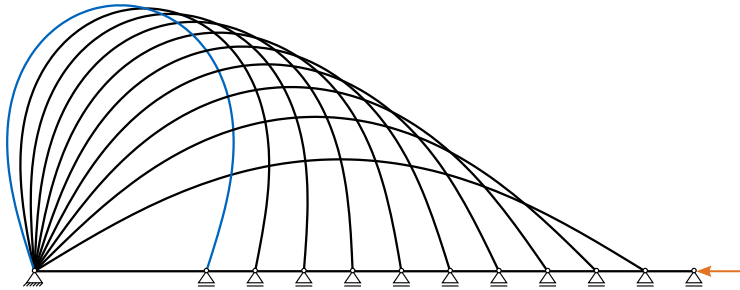
Figure 6.23: Straight beam bent to elastica shape by bringing its two ends together (adapted from Bauer et al. [15]).

the cross section, link the strain to the moments. The change of curvature is purely defined by the geometry and can thus be computed by the base vectors.

The curvature of an initially flat structure is zero and can therefore directly be used for computing the actual strains and stresses in a given geometry. One of the most simple and illustrative examples is the elastica. A single straight beam is bent by bringing its two ends together as shown in Figure 6.23.

The same result for the two final Dirichlet boundary conditions of the beam can be obtained by drawing an arbitrary initial shape as shown in Figure 6.24. Note that the length of this arbitrary curve has to match the length of the initial flat configuration. All three arbitrary shapes deform into the same relaxed state which matches the reference solution from bending the initially straight beam in shape and forces. If the refinement is sufficient, the relaxed shape is independent of how close the starting and the equilibrated geometry are.

Inverse Torsion

The method of the inverse approach can also be used for torsional forces. However, curve and surface elements have to be treated differently. The approach for beam elements is in general the same as for bending. The change of the twist is used for computing the torsional moment. If the reference twist is set to zero, as it is for an initially untwisted rod, one can
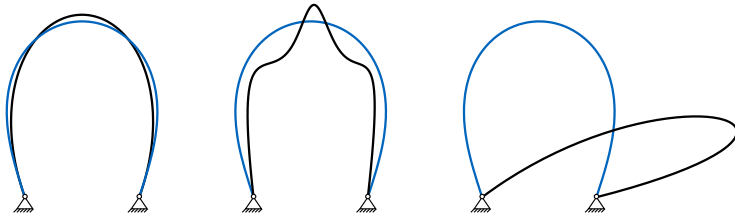
Figure 6.24: Inverse method for bending applied to three starting shapes (black) with the same boundary conditions as the elastica in Figure 6.23 and its equilibrated shape (blue) (adapted from Bauer et al. [15]).
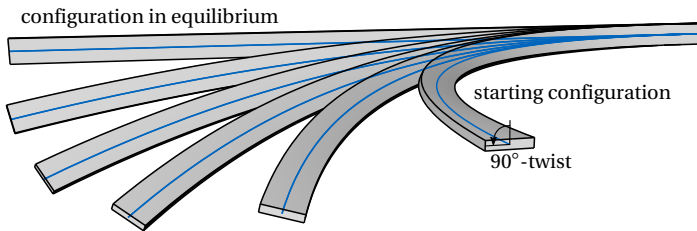
Figure 6.25: Application of inverse torsion and bending to a twisted and bent beam with all states from starting configuration to relaxed configuration (adapted from Bauer et al. [15]).

use the evolving torsional moments to obtain equilibrium. The main task for designers is to define the orientation of the cross section in the actual state.

A simple example, which contains bending and torsion, is a beam with the shape of a quarter circle. The cross section is twisted increasingly around the center line with a final twist of 90°. When releasing this state with the inverse method the beam deforms back into the assumed straight, untwisted state as shown in Figure 6.25.

In contrast to the beam, there is no specific term related to torsion in the Kirchhoff-Love shell element proposed by Kiendl et al. [74]. Figure 6.26 shows the same structural problem as Figure 6.25 but is modeled by a shell. Figure 6.26(a) takes only bending stresses into account. Consequently, a

(a)

(b)
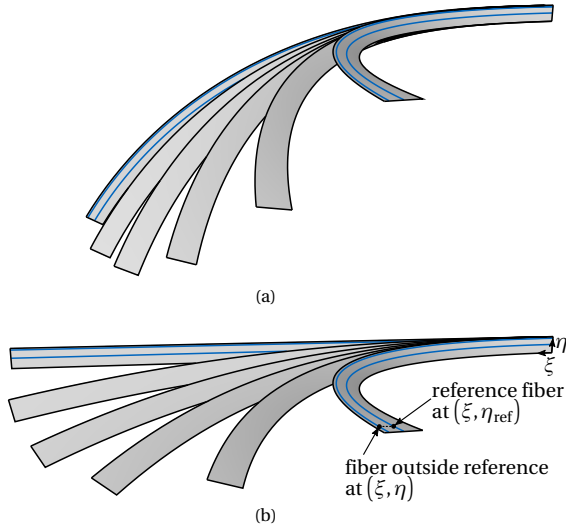
Figure 6.26: Twisted and bent shell as starting configuration with two respective fibers (blue): (a) application of inverse bending and (b) application of inverse torsion and bending (adapted from Bauer et al. [15]).

flattening happens. However, the result is not a straight strip but a curved one.

This is due to different lengths of the fibers in the starting configuration as indicated in Figure 6.26(a). If this varying length can be interpreted as result of torsion, one can also pursue a different approach. Twisting results in different elongations and therefore different strains and stresses in the fibers. Fibers close to the center line are less stretched than fibers on the outside if the length of the strip is maintained. This is called helix-torsion and is described in more detail by Lumpe et al. [90]. By defining one initial fiber length, which corresponds to the length of the base vector, for all fibers, as is the case for initially straight shells, one can also consider this twisting effect for shells. Note that the reference length is not necessarily constant along the longer dimension of the shell.

The reference fiber length can easily be defined when using NURBS for the FE model. The whole surface is described by one entity $\mathbf{S}(\xi, \eta)$ and is not

subdivided into several smaller elements as is usually the case for classical finite elements. The new metric G_{ij} is simply computed by

$$G_{11}(\xi,\eta) = \mathbf{G}_1(\xi,\eta_{\text{ref}}) \cdot \mathbf{G}_1(\xi,\eta_{\text{ref}}) \tag{6.8}$$

$$G_{22}(\xi,\eta) = \mathbf{G}_2(\xi,\eta) \cdot \mathbf{G}_2(\xi,\eta) \tag{6.9}$$

$$G_{12}(\xi,\eta) = G_{21}(\xi,\eta) = \big(\mathbf{G}_1(\xi,\eta) \cdot \mathbf{G}_2(\xi,\eta)\big) \cdot \frac{\|\mathbf{G}_1(\xi,\eta_{\text{ref}})\|_2}{\|\mathbf{G}_1(\xi,\eta)\|_2} \tag{6.10}$$

if the fiber length is pointing in $\mathbf{G}_1$-direction. The position of the reference fiber is described by η_{ref} on the surface. If $\mathbf{G}_2$ is the respective fiber direction, the indices as well as ξ and η have to be swapped.

Applying this modification to the bent and twisted quarter circle results in a relaxation as shown in Figure 6.26(b). The released strip finds its equilibrium in a flat and straight configuration. A more detailed evaluation and large scale application can be found in Schikore et al. [114].

Remark: Normal Forces

Similar to the phenomena described in Section 3.2.3, the solution space may influence the result. The presented relaxing models flatten in the correct way. However, the normal forces in the structures are heavily oscillating if the refinement level is not high enough. In order to obtain a deformation without normal forces, the length of the base vector must not change. An exact solution is not possible in the general case as can be shown by the simple example of a parabola, which is defined by three control points (see Figure 6.27). It should flatten in a bending relaxation. Only the second and third control point can move and they have to lie on the x-axis, i.e. all y-coordinates are zero, for the flat configuration.

When comparing the two definitions of the base vector lengths, it can be found that there is no solution, satisfying the condition for all points of the curve.
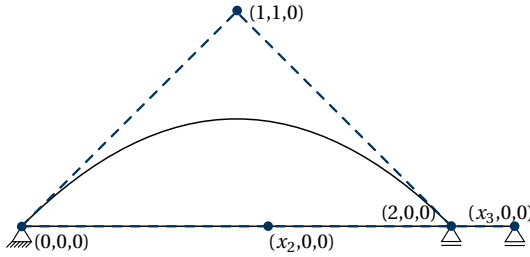
Figure 6.27: Setup of a flattening parabola.

$$\|\mathbf{G}_1\|_2 = \sqrt{\mathbf{G}_1 \cdot \mathbf{G}_1} = \sqrt{\left(\sum_{i=1}^{n} N'_{i,p} X_i\right)^2 + \left(\sum_{i=1}^{n} N'_{i,p} Y_i\right)^2}$$

$$= \sqrt{\left((4\xi+2)\cdot 1 + 2\xi \cdot 2\right)^2 + \left((4\xi+2)\cdot 1\right)^2}$$

$$= 2\sqrt{20\xi^2 + 12\xi + 2} \tag{6.11}$$

$$\|\mathbf{g}_1\|_2 = \sqrt{\mathbf{g}_1 \cdot \mathbf{g}_1} = \sqrt{\left((4\xi+2)\cdot x_2 + 2\xi \cdot x_3\right)^2} \tag{6.12}$$

$$\|\mathbf{G}_1\|_2 = \|\mathbf{g}_1\|_2 \tag{6.13}$$

$$\Rightarrow \text{no solution for } x_2 \text{ and } x_3$$

Nevertheless, since the problem is assumed to be bending-dominated, this inaccuracy is acceptable. When increasing the number of control points, the error decreases as well.

Remark: Fast Design Exploration

Even though the inverse approach is an approximation of the correct solution, it may be an approach for fast design explorations with relatively few degrees of freedom. For form finding problems of bending-active structures, it may even be more accurate than using artificial reference geometries. This is related to the normal forces which evolve from differences in
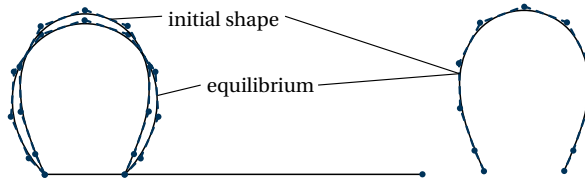
Figure 6.28: Relaxing of a curved initial shape, which already is very close to the physical equilibrium state with a reference configuration (left) and the inverse approach (right).

the distribution of the length of the base vectors as already explained in the previous remark. Applying the inverse approach on the example of Figure 3.10, where a geometry in equilibrium was rebuilt with fewer control points, results more or less in the correct equilibrium state whereas the one with an equally distributed NURBS patch with the same parametrization as reference configuration deforms into a non-physical state (see Figure 6.28).

Once a satisfying configuration of structural elements and boundary conditions is found, it is necessary to perform a thorough classical forward analysis including the mounting sequence in order to ensure that the normal forces only have a minor influence on the final result.

Example

An illustrative application example is a bending-active gridshell. The final shape should be close to a part of a sphere. Therefore, a regular grid is projected onto a sphere. The projected curves are then used as starting configuration for the structural analysis. The beams have a circular cross section in order to provide the same bending stiffness in every direction. Each end is fixed by a simple support and the beams are coupled with each other by hinges. The inverse method is used to derive the stress-strain state. The final structure in equilibrium varies slightly from the starting assembly as can be seen in Figure 6.29. By removing all horizontal supports beside the necessary ones for a statically determined support, the gridshell
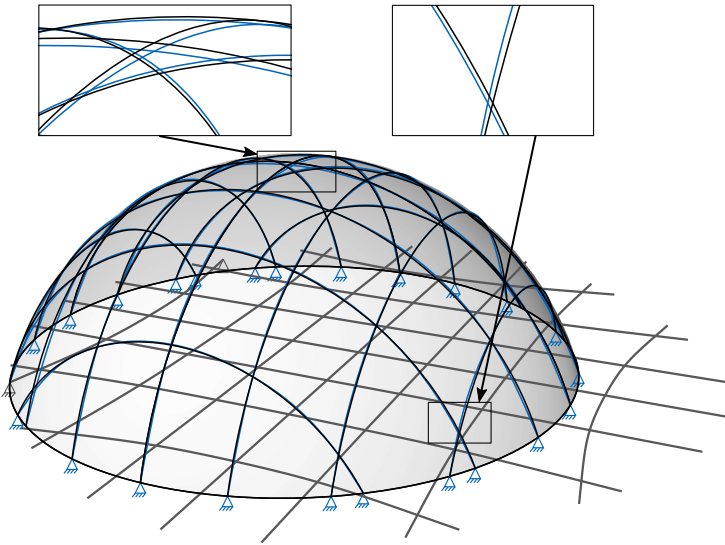
Figure 6.29: Spherical gridshell with starting assembly (black), relaxed configuration (blue) and flat, bent assembly pattern for the straight rods (gray) (adapted from Bauer et al. [15]].

finds a flat equilibrated state which can be used for a simplified initial assembly of the rods on the ground. Note that the flat configuration still has bending moments in the rods since they are curved. Torsion never occurs during the whole simulation due to the circular cross section and the simple hinges.

The results of the inverse method are verified by taking the flat assembly with remaining bending moments, remodeling it with a new discretization and pushing it into shape again. The maximum distance between the beams of the forward and backward analysis is 0.658mm where the diameter of the gridshell on the ground is 11.31m and the height is 3.95m. The maximum bending moment differs by 0.154%.

7

APPLICATION EXAMPLES

This chapter will highlight the potentials and applicability of the proposed CAD-integrated methods in complex application examples in the design of lightweight structures. The coupling formulation for beams will be verified with systems consisting of many coupled elements. Applications of the embedded approach and the sliding formulation are briefly presented. Potentials of the interactive workflow are exemplified. Academic examples as well as actually built systems will be shown.

7.1 Gridshells

Gridshells are highly complex structural systems. This section will present two examples verifying the beam coupling formulation presented in Section 5.3. In addition, the second example is a bending-active gridshell using the form finding approach of Section 6.4.2.

7.1.1 Torus

The torus-shaped grid structure shows the applicability of the rotational coupling formulation for beams in a complex scenario. Therefore, a hexagonal grid, where the nodes lie on a torus, is constructed. The shape is parametrized by the following parameters: the radius of the center line of the torus $r_c = 40$, the radius of the torus around the center line $r_i = 10$, the number of repeated basic modules $n_c = 28$ and the number of nodes per circle on the torus $n_i = 13$. All parameters are also illustrated in Figure 7.1(a). For the given parameters, 2184 curves evolve and 4368 coupling conditions become necessary. The linear curves are refined to a polynomial degree $p = 3$ and thus possess four control points. A circular cross section with $r = 0.1$ is assigned to the curves. A Young's modulus $E = 2.1 \cdot 10^5$ and a Poisson's ratio $v = 0.0$ are chosen. Four opposite points in the center plane are supported in z-direction. The load $F = 7.5$ towards the center of the torus, in this case the x-direction, is applied to one of those support points and the respective opposite point is held in all directions. The support point with the load is additionally supported in y-direction (see Figure 7.1(c)).

Figure 7.1(b) shows the load-displacement curve with a maximum displacement of $u = 23.956$ of the load application point. The example can prove that the application works for complex structures with many degrees of freedom and arbitrary orientation.

7.1.2 Moving Mechanism of a Bending-Active Gridshell with Scissor Joints

Coupling of only certain local rotations as e.g. for scissor joints can result in kinematic structures. Transformation mechanisms can use this degree of freedom. The grid shell as shown in Figure 7.2 is supported in z-direction at the bottom end of the beams. The horizontal displacement of two opposite points is controlled and moved towards the center of the structure. The beams are oriented such that the cross sections are aligned at the coupling points. The coupling points are also positioned inside the parameter domains and not only at the ends, where interpolating control points exist. By selecting an irregular pattern for the connection points, a double-curved shape can be generated.

The generation of such grid structures has been investigated in detail by e.g. Panetta et al. [100] and Soriano et al. [122]. In the present case study,

(a)

(b)

(c)
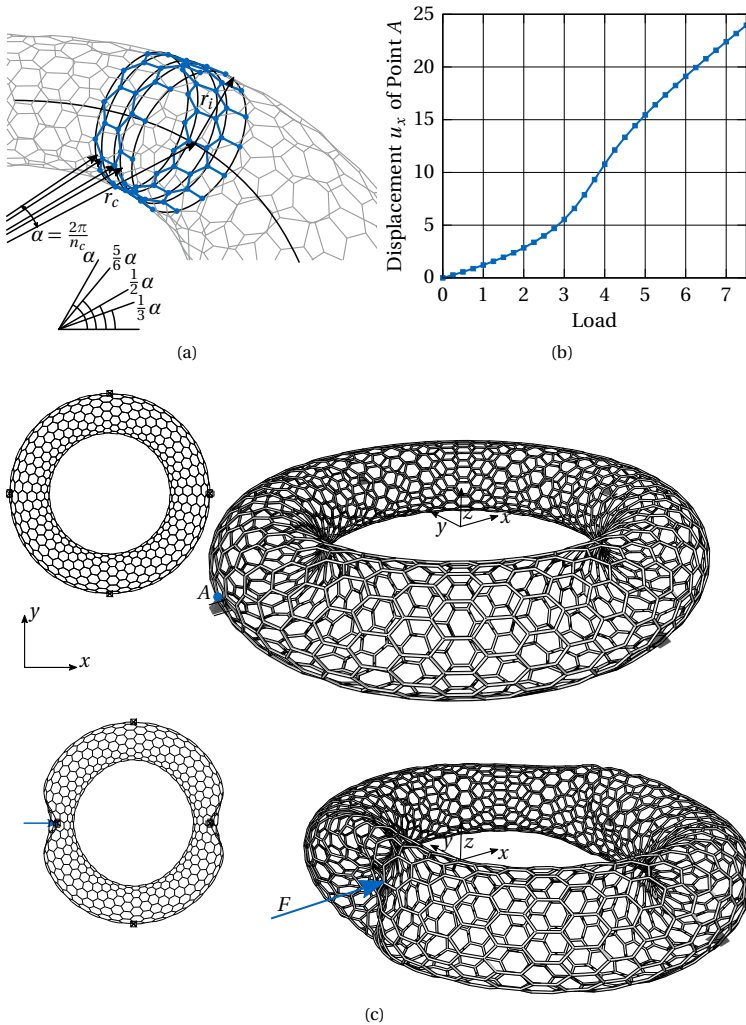
Figure 7.1: Torus with hexagonal beam grid: (a) parameters for
the initial geometry model, (b) load displacement curve and (c)
initial and deformed model (adapted from Bauer et al. [8]).
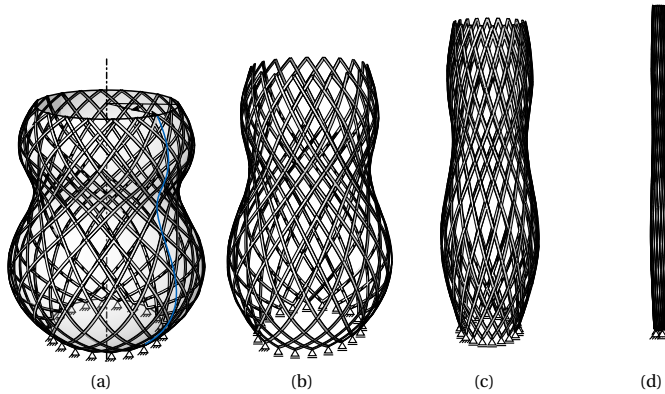
Figure 7.2: Gridshell with scissor joints: (a) initial shape defined by a surface of revolution, (b) relaxed gridshell, which is in equilibrium with the bottom supports, (c) intermediate state while closing by moving the two fixed bottom supports towards each other and (d) closed shape.

the form is generated by an arbitrary surface of revolution. Geodesic lines are computed with CAD functions on this surface (see Figure 7.2(a)). The respective beams are then relaxed by the method described in Section 6.4.2 (see Figure 7.2(b)). The transformation from an open to a closed state by a controlled movement of two opposite points at the bottom is shown in Figure 7.2(b)-(d).

7.2 Hyperbolic Paraboloid Shell

Hyperboloids are often used in lightweight shell design. The geometry of this example is inspired by Wilhelm J. Silberkuhl (see Figure 7.3(a)). The dimensions are taken from Scheffler [113]. The double-curvature of the hyperbolic paraboloid is used to span over a rather large distance $L = 18$m compared to the shell thickness $t = 5$cm. Each module is supported on its short sides and it is assumed that the single modules are coupled with each other. The structure is additionally stiffened by centrical tendons, which are embedded into the concrete. These tendons can be modeled

(a)

Displacement u_z

max

min

(b)

von-Mises stress

max

min

(c)
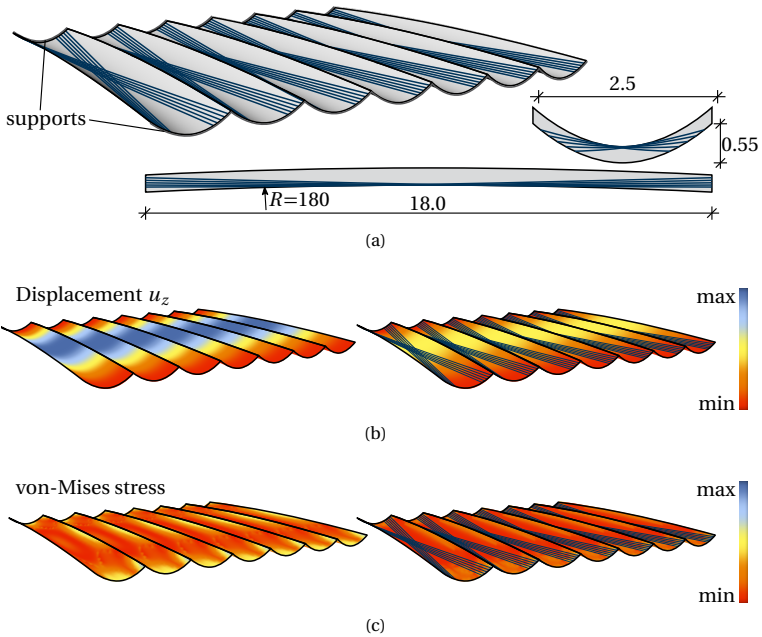
Figure 7.3: Lightweight concrete roof: (a) geometry setup, (b) comparison of the displacement u_z without and with tendons and (c) comparison of the von-Mises stresses without and with tendons.

perfectly with the embedded approach. They reduce the displacements as well as the stresses in the hyperbolic paraboloid shell under its self-weight (see Figures 7.3(b) and (c)).

7.3 Sliding Cables

This section will present two application examples for the sliding cable formulation (see also Bauer et al. [13]).

7.3.1 Membrane Roof

Sliding cables are often used in membrane structures due to the membrane being attached to the cables with pockets. The following example will not only show that it is possible to model the sliding, but also that there is a substantial difference in the structural response when the sliding is considered compared to when it is not.

The investigated structure is a six-point sail with edge and ridge cables as depicted in Figure 7.4. While form finding, it is not important whether the cables are fully attached to the membrane or not, since the form finding only searches for an optimal stress state. The structural analysis is then conducted either with sliding cables or fully attached ones. The color plot on the right in Figure 7.4 shows the displacement field of the membrane under a wind load for both cases. The displacement behavior is nearly the same, but the maximum displacement of the membrane with the sliding cables is larger. A clearer distinction can be seen in the normal forces of the cables (see Figure 7.5). Due to peaks in the corners, the maximum value is 2.76 times higher for the fixed cables than for the sliding ones, leading to different required cable dimensions. In consequence, a correct modeling of the cables is important. This was also found by e.g. Dinh et al. [44] and Pauletti et al. [104].

The sliding coupling formulation also works for discrete connections. The cable detaches from the membrane and straightens in the uncoupled segments as can be seen in Figure 7.6. Note that in this case, the refinement of the cables has to be very fine in order to represent such sharp kinks (cf. Section 3.3.1).

7.3.2 Membrane Wing

Lightweight design with membranes has also potential applications outside of construction engineering. It has been rediscovered for the design of turbine blades based on the construction of the wings of early airplanes. The wing profile is shaped using ribs and the surface is generated by a tautened membrane in-between. This example considers a simplified module of such a blade (see Figure 7.7). The profile of the wing is defined by a fixed border and the leading edge is modeled by a stiff shell. The membrane is placed on the wing area. A sliding cable is added to the trailing edge to restrain the membrane. The sliding cable can also be used to adapt
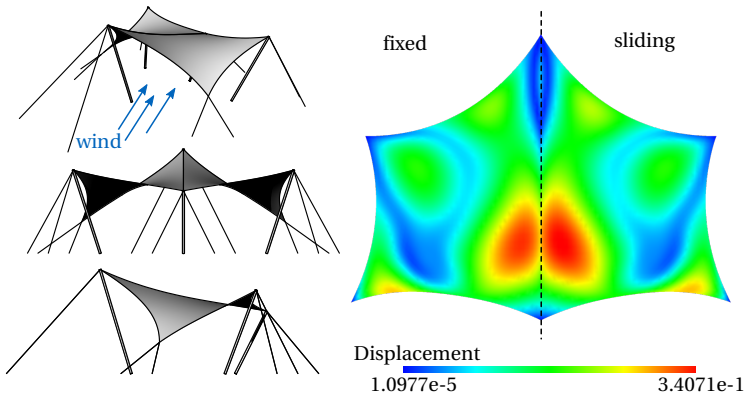
Figure 7.4: Membrane roof under wind load. Different views of the form found structure on the left hand side. The displacement field of the membrane for fixed and sliding cables on the right hand side (adapted from Bauer et al. [13]).
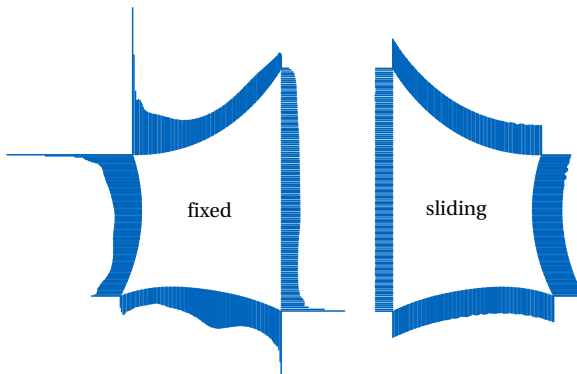
Figure 7.5: Normal forces in the edge cable of the membrane roof under wind load, which are highly concentrated in the corners for the fixed cable (adapted from Bauer et al. [13]).
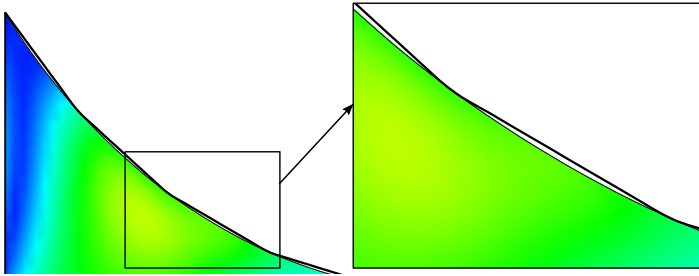
Figure 7.6: Straightening and detaching of the cable by using few sliding points for connecting cable and membrane (adapted from Bauer et al. [13]).

the structure, i.e. apply different tensioning to the membrane in order to control the structural behavior. A form finding analysis is needed here as well. The difference between full coupling and sliding appears in the structural analysis with a wind load. Note that the loads on the membrane surfaces are simplified to constant pressure loads and that they are not coupled by the volume inside the module. The displacements are almost the same while the normal forces differ. The sliding cable has a constant distribution whereas the normal forces in the fixed cable increase towards the ends (see Figure 7.7).

7.4 Bending-Active Façade

The next example is inspired by the adaptive façade of the *One Ocean* Pavilion in Seoul by SOMA and Knippers Helbig, see Knippers et al. [78]. The façade is clad on one side with several lamellas made of glass fiber reinforced polymers (GFRP). The peculiarity of this system is that it can be transformed by introducing elastic deformation in the lamellas and thus opening up the façade. The mechanism of this adaptive façade fixates one corner on the top and bottom while the other corner is moved in the position for the respective translucence (see Figure 7.8). In order to model such a system, displacement control features considering a defined load path are necessary.
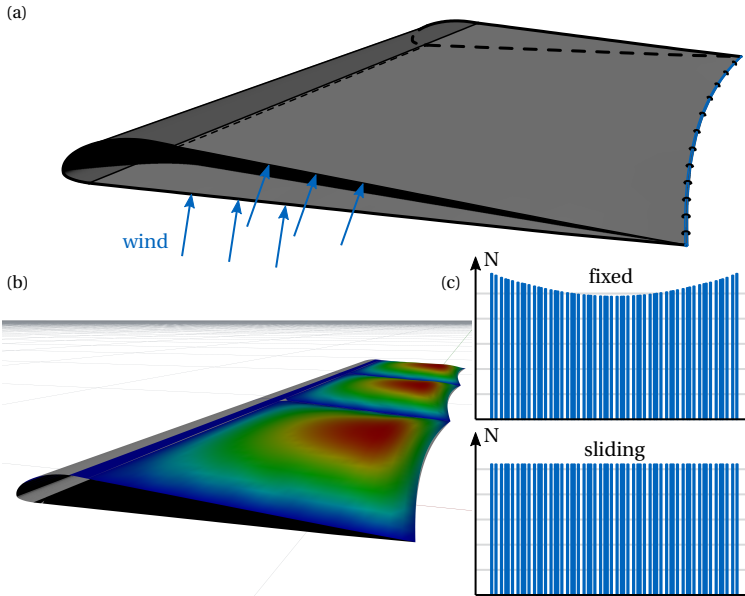
Figure 7.7: Form found module of a membrane wing under wind load with edge cable at the trailing edge. (a) Setup for the nonlinear structural analysis, (b) displacement field for several modules scaled by 5 for the sliding cable visualized in Rhinoceros and (c) normal forces in the fixed and the sliding edge cable at the trailing edge (adapted from Bauer et al. [13]).

The states of a fully opened and closed façade are shown in Figure 7.9. Intermediate states are possible as well as different opening states for the single lamellas with a respective control system.

In the design of façades, properties like translucence, shading or energy input are key features besides resistance to external forces. With the integration of the analysis in CAD, evaluation tools for those properties are directly available for every opening state, which is dependent on the deformation. Since the elements are not meshed, the tools can directly work with the smooth NURBS representation.

(a)   (b)
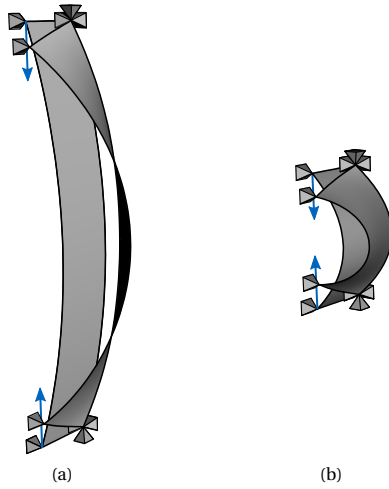
Figure 7.8:   Bending-active opening mechanism for (a) a long and (b) a short lamella of the façade of the *One Ocean* pavilion in Seoul.

(a)

(b)
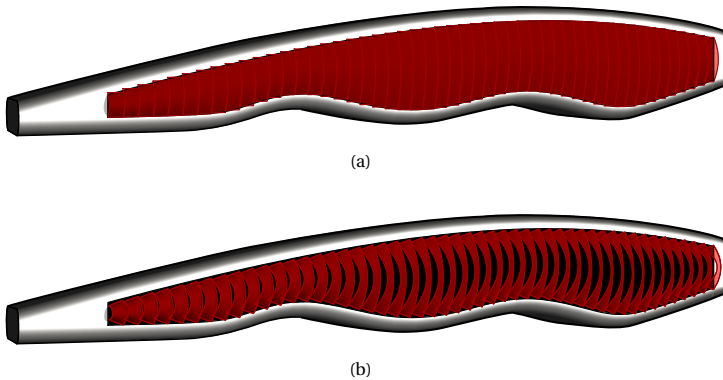
Figure 7.9:   Façade of the *One Ocean* pavilion in Seoul in (a) closed and (b) open state.

7.5   Design Process Including Multi-Stage Analysis

The following application examples will show the evaluation of the structural behavior during an assembly process with several stages and will provide insight into the design chain of such complex structures.

7.5.1   Beach Bar

The beach bar is a rather simple example, which nevertheless combines most of the aspects presented before. It is a hybrid structure consisting of actively bent beams and a form found membrane including the cutting pattern and structural wind analysis. The construction and design process is illustrated in Figure 7.10. The whole structural model is set up depending on several parameters. The parameters allow a modification of the final shape in a convenient way since the whole assembly process is considered. Two initially straight beams with lengths L_1 and L_2 are bent towards the fixed support points, which are defined by L_0 and W. By connecting two points, which are defined by C_1 and C_2, the rods are lifted in space and provide a frame for the membrane. The initial shape of the membrane and the edge cables for the form finding is derived from the assembled shape of the beams. Start and end point are defined by M_1 and M_2. This geometry is derived automatically by CAD from the previous results. Due to the weak coupling, the connection points do not have to be considered in the previous analyses, i.e. no node at the coupling points is needed. The beams serve as elastic supports in the form finding analysis. Further inputs for the analysis are the respective prestresses for the membrane p_1 and p_2 and the cable P_c. The form found shape depends on both geometric and structural parameters. In addition, the structural behavior of the form found structure can be evaluated under e.g. a wind load. The cutting pattern can be generated in order to obtain a manufacturable membrane.

7.5.2   Pringle

The *Pringle* is also a bending-active hybrid structure. It is the outcome of a students workshop for the M1 project by Lienhard [85]. The design process is shown in Figure 7.11. A beam is bent into a circle. The meeting ends are fixed. Contracting cables are used to force the beam into the a pringle-like
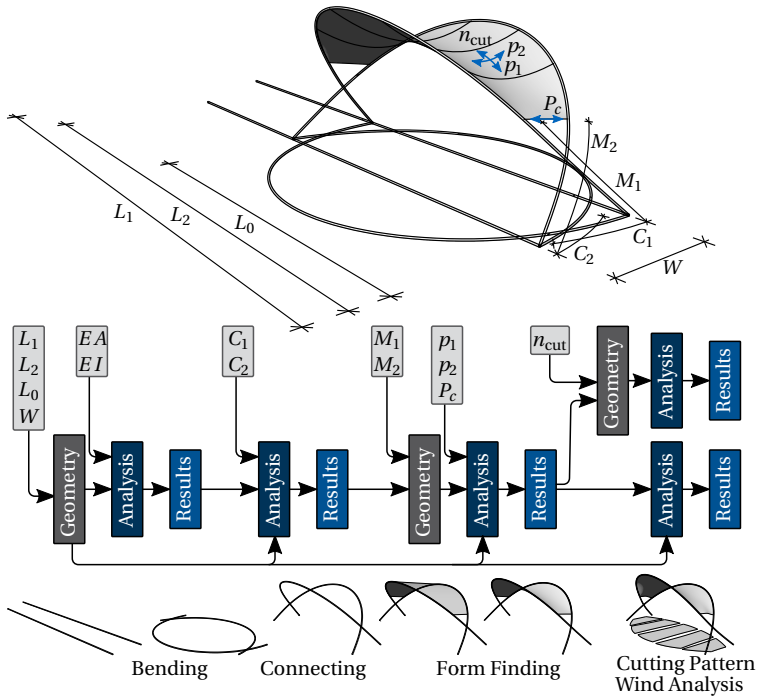
Figure 7.10: Geometric and structural parameters in the
simulation of the beach bar with all steps in the design process
(adapted from Goldbach et al. [55]).

shape. A membrane is added for form finding with elastic supports. This
complex structure perfectly illustrates the need for CAD-integration.

Furthermore, a study on the importance of tracking the strains and stresses
of the assembly process has been conducted. Figure 7.12 and Figure 7.13
clearly show that the structural behavior is different if the previous analysis
is ignored and the geometry is just updated.

(a)

(b)

(c)

(d)

(e)

© J. Lienhard
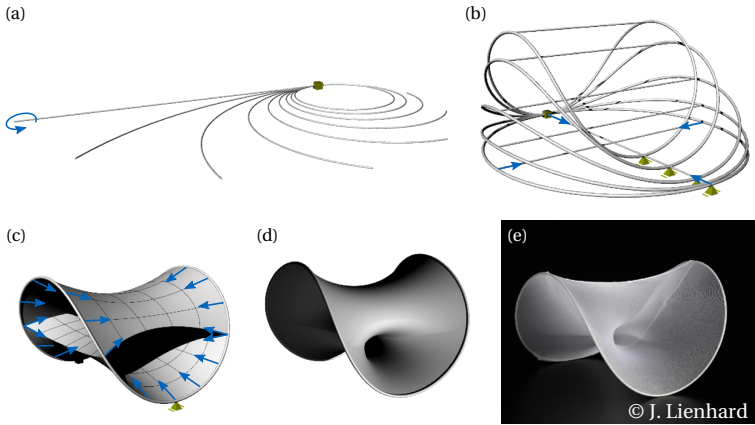
Figure 7.11: Design process of the *Pringle*: (a) bending of a straight beam to a circle, (b) bending the circle to a pringle-shape with cables, (c) generating the initial shape for the form finding, (d) form found *Pringle* and (e) physical mock-up (adapted from Bauer et al. [12]).
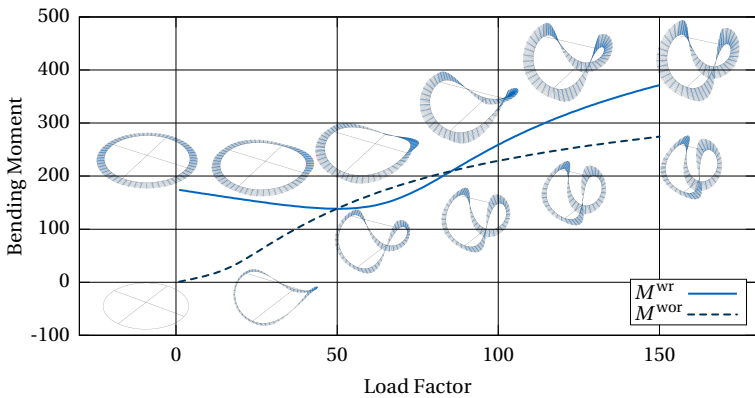
Figure 7.12: Total bending moment while bending the beam from the circle to the pringle shape with a straight reference configuration (wr) and without (wor) (adapted from Bauer et al. [12]).
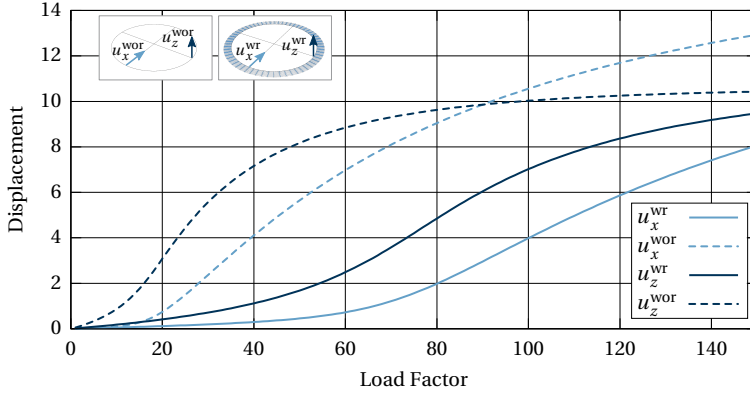
Figure 7.13: Displacement of the beam at the cable connectors while bending from the circle to the pringle shape with a straight reference configuration (wr) and without (wor) (adapted from Bauer et al. [12]).

7.6 Shape Generation

The application of isogeometric analysis in the design process is not only restricted to tracking stress states and computing deformations. It can also be used to generate shapes. This can be related directly to the structures which have to be form found as described in Section 6.4.1 for membranes and Section 6.4.2 for bending-active structures. But it is also possible to use these techniques as an intermediate step.

7.6.1 Centre Pompidou Metz

Motivated by the *Centre Pompidou Metz* of 2010 by Shigeru Ban and Jean de Gastines, a gridshell that has an appealing natural shape was found. This gridshell, which is covered by a membrane, should surround the museum. Minimal surfaces are an obvious approach to this design task. The surface can be form found from several boundary curves. The boundary curves consider the form of the museum which consists of two cantilevers connecting to the outside through the holes in the surface. The initial shape can be constructed by multiple flat surfaces defining the topology of
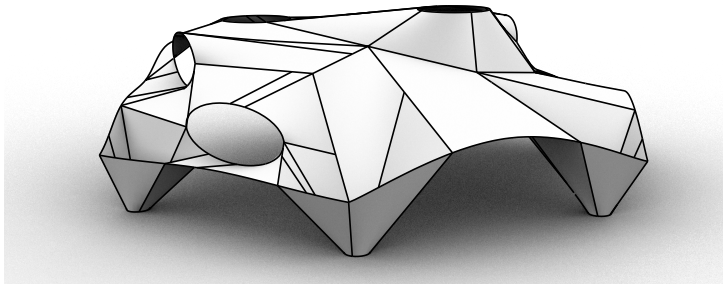
(a)
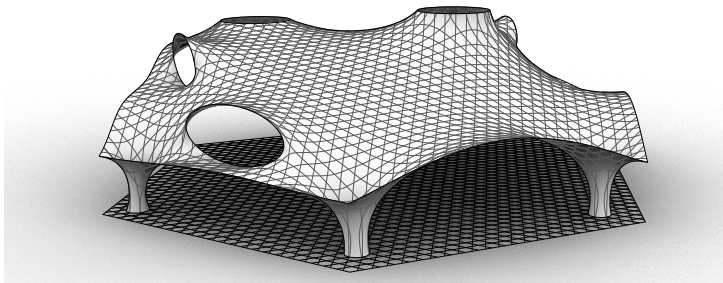
(b)

Figure 7.14:   Form finding of the lattice gridshell of the Centre
Pompidou Metz: (a) initial shape for the form finding and (b) form
found shape with projected hexagonal grid (adapted from Bauer
et al. [11]).

the final shape (see Figure 7.14(a)). After form finding, the smooth shape
is available and can be used to project a regular hexagonal grid from the
ground to the surface (see Figure 7.14(b)). Note that in this case, the beams
will be manufactured as curved beams and the shape is therefore directly
in equilibrium if self-weight is neglected. The boundary curves as well as
the grid layout can be modified until a satisfactory spatial grid is reached.

Figure 7.15 shows the scaled deformation of the form found gridshell under
a dead load. The structure is supported at the base of the columns and the
top holes. The result indicates that stiff edge beams are necessary as well
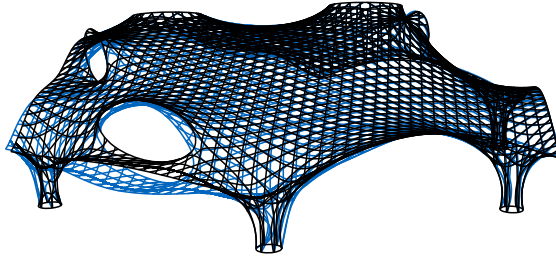
Figure 7.15: Gridshell of the Centre Pompidou Metz under load: undeformed and deformed structure (adapted from Bauer et al. [11]).

some additional supports, which were also realized for the original *Centre Pompidou Metz*.

7.6.2 Hotel Canopy

The hotel canopy is a project realized by Eike Schling and Jonas Schikore (see Figure 7.16). The structural system is based on asymptotic lines on an anticlastic surface. It is the first commercially built structure of this type. A large-scale prototype, the *INSIDE/OUT* pavilion (see Schling et al. [117]), was built before at the inner court of the Technical University of Munich. The grid is chosen such that the lines follow a path that experiences no so-called normal curvature w.r.t. the surface (see Schling [116]). This makes it possible to use straight lamellas and bend them into the grid such that they have their larger cross section dimension perpendicular to the surface. In contrast, conventional bending-active gridshells like the *Multihalle Mannheim* of 1972 by Frei Otto have the smaller dimension aligned to the surface normal. By orientating the stiff axis perpendicular to the surface, a higher stiffness for out-of-plane loading is achieved. More details on the structural principle can be found in Schling [116].

The initial surface for the design of an asymptotic gridshell can be created with an isogeometric form finding analysis. The asymptotic lines can be computed starting from so-called seed points. If the surface is minimal, the grid intersects by 90°. It is beneficial that the surface has not been meshed because meshing would subdivide the whole surface in many independent

(a)   (b)

Figure 7.16:   Canopy at the hotel Intergroup near Ingolstadt.

faces. The lines can be computed in the NURBS patch having the precise curvature information without kinks at every point of the surface.

Lamellas can be produced by an offset of the found lines. One major problem in the analysis of such a structure is that the designed structure is already assembled and has internal forces from bending and twisting. Due to the rather large height of the lamellas, helix-torsion becomes an issue and has to be considered in the dimensioning. The inverse approach for shells as presented in Section 6.4.2 provides a perfect strategy to simplify the structural analysis of such a complex design task.

The production process, as documented in Figure 7.17, includes straight lamellas which are assembled flat on the ground. This assembly is then pulled up on one side. Note that the grid automatically results in the design shape since this is the local minimum of the elastic energy for the given boundary conditions. The lifting can also be simulated with isogeometric analysis as presented in Figure 7.18. The force needed to lift one side basically corresponds to the dead weight of the structure in the simulation

Figure 7.17:   Mounting process of the canopy grid in the workshop: (a) flat assembly on the ground and (b) intermediate state during the mounting.
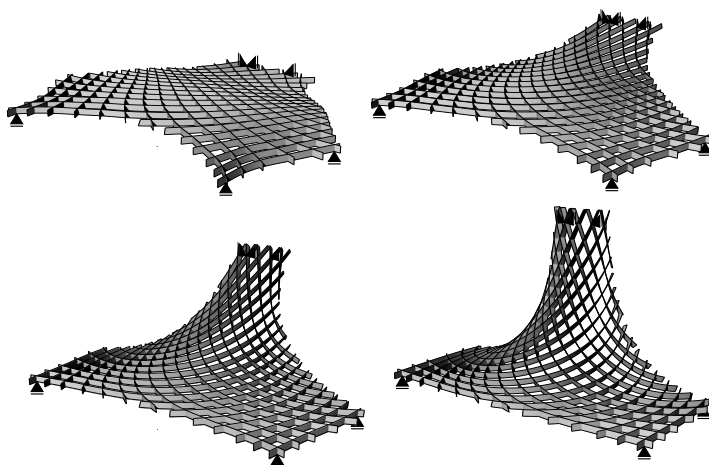
Figure 7.18:   Simulation of the mounting process.

as well as in the real manufacturing (see Schikore et al. [114]). The final form of the module is then fixated by adding a stiff frame to the borders.

8

SUMMARY AND CONCLUSIONS

Lightweight structures are an interesting field of application for isogeo-metric analysis. Large deflections of smooth structures can be represented in an elegant way. Applying CAD-integrated IGA can significantly facilitate their design process.

This thesis presents the basic types of nonlinearity in structural analysis. Differential geometry is outlined for the fundamentals of structural me-chanics, where the focus is set on geometric nonlinearity. Furthermore, the correct linking between consecutive analyses is investigated.

This is followed by an introduction to isogeometric analysis. The geometry description of NURBS and Boundary-Representation models are briefly summarized and the main aspects of finite element analysis with NURBS are presented. Furthermore, aspects that have to be taken into account while modeling analysis suitable NURBS, are illustrated as final considera-tions in this chapter.

An overview of the applied isogeometric structural element formulations is given in the consecutive chapters. After an overview of the fundamen-tals of coupling and connecting, three different coupling procedures are

proposed. The first one provides a coupling formulation for the rotation of beams. Emphasis was laid on the generality of the formulation in order to be able to represent different coupling types. The second coupling procedure is an implicit one. It avoids explicit coupling formulations by adapting the geometry description and expressing one entity within the parameter space of another. This approach is explained in detail for an embedded beam and briefly for the embedding of surfaces and points. The last variant implies coupling with a sliding interface. Adding a degree of freedom to the parametric coordinates of the coupling partners elegantly incorporates the complex sliding boundary condition. The proposed formulation is compatible with every NURBS-based structural element. Computationally expensive contact search and custom structural element formulations, e.g. cables with pulleys, become obsolete.

An important feature in the realization and adoption of the proposed methods in practice is the possibility to conveniently apply them. Therefore, key aspects of the integration of isogeometric analysis in the CAD environment are emphasized. Once a continuous workflow is realized, the process can be integrated in a parametric environment that significantly enriches the design process. Design with structural feedback, where optimization criteria may be provided, is enabled and may lead to an improved design. The design-through-analysis chain is explained for the design cycle of membrane structures, where several structural aspects interact in the shape generation. Different modeling techniques are discussed for the final mounting analysis. Furthermore, an approach for the fast design exploration of bending-active structures, including beams and shells, is proposed. The correct, but potentially computationally expensive mounting and assembly process can be omitted in the proposed approach: The structure is modeled in the assembled state and the structural behavior is approximated by assuming certain properties for a fictitious reference configuration. A standard geometrically nonlinear structural analysis is used to compute the equilibrium state.

The potential of the proposed methods and procedures is demonstrated with selected examples. Moreover, the advantages of a fully CAD-integrated workflow are illustrated through the simulation of the assembly of hybrid structures. The importance of considering the sequence of analysis steps is a further subject of those examples. The isogeometric analysis can also be used to generate shapes. The last example considers a built bending-active

project and shows how isogeometric analysis is applied in manifold ways at different steps of the design process.

Parametric design is a key feature in the design of structures. This is especially true for lightweight structures characterized by a tight interaction between form and force. The designer depends on structural feedback in order to verify the equilibrium state and needs to have methods in order to generate equilibrium shapes. Moreover, the closed NURBS-based design cycle provides huge potential in the design since the disciplines - design, engineering, manufacturing - can be combined.

The following goals have been reached within the present thesis. Missing element formulations were developed and implemented into the Chair's research FE code Carat++ in order to enable a general isogeometric analysis workflow inside CAD for the field of construction engineering. The main attention is given to one-dimensional structural elements and their interaction with each other and other elements. A lack of methods was identified this area. The result is e.g. a rotational coupling formulation that allows for both rigid and scissor joint coupling.

Furthermore, novel insights on the geometric modeling with NURBS were gained. Activating the parameter space, which was virtually ignored before, has a large potential in the modeling of structural systems. The parameter space of NURBS is very large in contrast to classical polynomial elements and can be used for the modeling of embedded entities. Furthermore, additional degrees of freedom can be added to this embedded description, which allow for a sliding interface or adaptable properties. The embedded geometry description was adapted for optimization by Hirschler et al. [68].

The applicability of the new element formulations is demonstrated for various examples. The proposed element formulations in combination with the existing ones enable the analysis, evaluation and optimization of a huge variety of structures in the field of construction engineering. A special focus was set on the realm of structures with large displacements. Form finding methods for lightweight structures including tensile and bending-active structures are integrated in the design workflow.

Kiwi!3d is the resulting interface between the FE kernel Carat++ and the CAD environment Rhino with Grasshopper. The software is published online and is available for everyone. Several workshops have been conducted at conferences and Kiwi!3d is used in teaching at the Chair of Structural
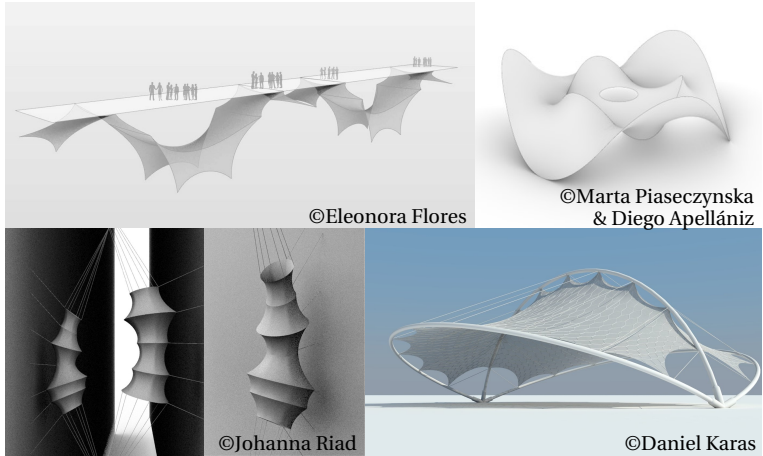
Figure 8.1: Several workshop results of the participants at the *Advances in Architectural Geometry 2018* in Gothenburg and the *Design Modeling Symposium 2019* in Berlin.

Analysis at TUM as well as in other departments and universities. The users are able to apply isogeometric analysis in an intuitive way, which leads to the design of complex structures. Some results of the participants of the *Structural NURBS* workshop at the *Advances in Architectural Geometry* (AAG 2018) in Gothenburg and the *Design Modeling Symposium Berlin* in 2019 are shown in Figure 8.1.

The accomplished examples including built structures lead to the conclusion that the realization of a holistic design tool using IGA was successful.

Integrating the analysis into CAD by IGA is a step towards a unified digital model of the design object. Many attempts were made to bring analysis into the life cycle management, which is also referred to as building information modeling (BIM) in the field of construction or digital twin. Applying isogeometric analysis in this context would imply that no separate meshed model for classical FEM is needed. However, other challenges persist. One of them is the derivation of the dimensionally reduced models from the volumetric model. Discussions with the industry show that necessary modifications in the process chain would only result in a small overhead, which

could be compensated by the benefits of a unified model in the future. It is already often the case that the volumes are constructed from surfaces and curves. Keeping those inside the model and giving the draftsman some guidelines for analysis-suitable models would directly allow the use of IGA.

Further encouragement towards such a digital model could be generated by modified isogeometric elements that are not represented by the center line or surface. These eccentric elements can use the same structural formulation with an updated geometry description. These are either updated integration boundaries or additional control point values describing the eccentricity.

Such eccentricities can also be useful for the simulation of more complex cross sections. T-beams or prestressed cables that have a varying position in the cross section in order to provide better bending resistance are for example an application for this. Both examples are ideally suited for embedding. Currently, it is possible to place prestressed cables with and without bond inside the surface description of the master element by using embedding, fixed or sliding coupling. Restraining the degree of freedom in the parameter space after the initial deformation would represent subsequent bond.

Another way to combine sliding with the proposed methods is sliding with aligned base vectors. This may be useful for the simulation of e.g. grid shells or weaves. By adding a prescribed distance (in the direction of the base vector), one can consider the thickness of the single structural elements. This is also interesting without sliding. Also other types of complex joints, especially between beams, are imaginable. The advantages and applicability of higher quality methods, like Lagrange multipliers and Nitsche method, in this context have still to be investigated.

The modularity due to the tight relation to the geometry makes it possible to combine the proposed methods in countless ways, as outlined here, and solutions for further complex modeling tasks of structural elements and their interaction can be found in order to provide even more flexible and general analysis methods for the CAD-integrated design.

This thesis constitutes a step towards an interactive responsive design process capable of supporting future concepts in the design of structures.

LIST OF FIGURES

List of Figures

BIBLIOGRAPHY

[1] V. Alic. "Computational Methods in Conceptual Structural Design." Dissertation. Lund: Lund University, 2018.

[2] A. Apostolatos, R. Schmidt, R. Wüchner, and K.-U. Bletzinger. "A Nitsche-type formulation and comparison of the most common domain decomposition methods in isogeometric analysis." In: *International Journal for Numerical Methods in Engineering* 97.7 (2014), pp. 473–504. DOI: `10.1002/nme.4568`.

[3] M. Arya, N. Lee, and S. Pellegrino. "Crease-free biaxial packaging of thick membranes with slipping folds." In: *International Journal of Solids and Structures* 108 (2017), pp. 24–39. DOI: `10.1016/j.ijsolstr.2016.08.013`.

[4] M. Aufaure. "A finite element of cable passing through a pulley." In: *Computers & Structures* 46.5 (1993), pp. 807–812. DOI: `10.1016/0045-7949(93)90143-2`.

[5] F. Auricchio, F. Calabrò, T. J. R. Hughes, A. Reali, and G. Sangalli. "A simple algorithm for obtaining nearly optimal quadrature rules for NURBS-based isogeometric analysis." In: *Computer Methods in Applied Mechanics and Engineering* 249-252 (2012), pp. 15–27. DOI: `10.1016/j.cma.2012.04.014`.

[6] Y. Başar and W. B. Krätzig. *Mechanik der Flächentragwerke. Theorie, Berechnungsmethoden, Anwendungsbeispiele.* Braunschweig: Vieweg, 1985. ISBN: 3-528-08685-8.

[7] A. M. Bauer. "Nonlinear isogeometric spatial Bernoulli beam." Master's Thesis. München: Technische Universität München, 2015.

[8]   A. M. Bauer, R. Wüchner, and K.-U. Bletzinger. "Weak coupling of nonlinear isogeometric spatial Bernoulli beams." In: *Computer Methods in Applied Mechanics and Engineering* 361 (2020), p. 112747. DOI: 10.1016/j.cma.2019.112747.

[9]   A. M. Bauer, M. Breitenberger, B. Philipp, R. Wüchner, and K.-U. Bletzinger. "Embedded structural entities in NURBS-based isogeometric analysis." In: *Computer Methods in Applied Mechanics and Engineering* 325 (2017), pp. 198–218. DOI: 10.1016/j.cma.2017.07.010.

[10] A. M. Bauer, M. Breitenberger, B. Philipp, R. Wüchner, and K.-U. Bletzinger. "Nonlinear isogeometric spatial Bernoulli beam." In: *Computer Methods in Applied Mechanics and Engineering* 303 (2016), pp. 101–127. DOI: 10.1016/j.cma.2015.12.027.

[11] A. M. Bauer, A.-K. Goldbach, and K.-U. Bletzinger. "Mechanically enhanced parametric design of structures by isogeometric analysis." In: *Advanced Building Skins*. Ed. by Advanced Building Skins GmbH. 2019, pp. 613–619. ISBN: 978-3-9524883-0-0.

[12] A. M. Bauer, P. Längst, R. Wüchner, and K.-U. Bletzinger. "Isogeometric analysis for modeling and simulation of building processes." In: *Proceedings of the IASS Annual Symposium 2017*. Ed. by A. Bögle and M. Grohmann. 2017.

[13] A. M. Bauer, R. Wüchner, and K.-U. Bletzinger. "Innovative CAD-integrated isogeometric simulation of sliding edge cables in lightweight structures." In: *Journal of the International Association for Shell and Spatial Structures* 59.4 (2018), pp. 251–258. DOI: 10.20898/j.iass.2018.198.039.

[14] A. M. Bauer, R. Wüchner, and K.-U. Bletzinger. "Isogeometric analysis for staged construction within lightweight design." In: *Structural Membranes 2017*. Ed. by K.-U. Bletzinger, E. Oñate, and B. Kröplin. Barcelona, Spain: International Center for Numerical Methods in Engineering (CIMNE), 2017, pp. 311–322. ISBN: 978-84-946909-9-0.

[15] A. M. Bauer, R. Wüchner, and K.-U. Bletzinger. "Isogeometric analysis in the design process of lightweight structures." In: *Proceedings of the IASS Annual Symposium 2019 - Structural*

Membranes 2019. Ed. by C. Lázaro, K.-U. Bletzinger, and E. Oñate. 2019, pp. 780–787. ISBN: 978-84-121101-0-4.

[16]   Y. Bazilevs, V. M. Calo, J. A. Cottrell, J. Evans, T. J. R. Hughes, S. Lipton, M. A. Scott, and T. W. Sederberg. "Isogeometric analysis using T-splines." In: *Computer Methods in Applied Mechanics and Engineering* 199.5-8 (2010), pp. 229–263. DOI: `10.1016/j.cma.2009.02.036`.

[17]   L. Beirão da Veiga, A. Buffa, C. Lovadina, M. Martinelli, and G. Sangalli. "An isogeometric method for the Reissner-Mindlin plate bending problem." In: *Computer Methods in Applied Mechanics and Engineering* 209-212 (2012), pp. 45–53. DOI: `10.1016/j.cma.2011.10.009`.

[18]   L. Beirão da Veiga, A. Buffa, G. Sangalli, and R. Vázquez. "Analysis-suitable T-Splines of arbitrary degree: Definition, linear independence and approximation properties." In: *Mathematical Models and Methods in Applied Sciences* 23.11 (2013), pp. 1979–2003. DOI: `10.1142/S0218202513500231`.

[19]   J. Bellmann. "Active bending starting on curved architectural shape." In: *Structural Membranes 2017*. Ed. by K.-U. Bletzinger, E. Oñate, and B. Kröplin. Barcelona, Spain: International Center for Numerical Methods in Engineering (CIMNE), 2017, pp. 265–274. ISBN: 978-84-946909-9-0.

[20]   D. J. Benson, Y. Bazilevs, M.-C. Hsu, and T. J. R. Hughes. "Isogeometric shell analysis: The Reissner-Mindlin shell." In: *Computer Methods in Applied Mechanics and Engineering* 199.5-8 (2010), pp. 276–289. DOI: `10.1016/j.cma.2009.05.011`.

[21]   D. J. Benson, S. Hartmann, Y. Bazilevs, M.-C. Hsu, and T. J. R. Hughes. "Blended isogeometric shells." In: *Computer Methods in Applied Mechanics and Engineering* 255 (2013), pp. 133–146. DOI: `10.1016/j.cma.2012.11.020`.

[22]   R. L. Bishop. "There is more than one way to frame a curve." In: *The American Mathematical Monthly* 82.3 (1975), pp. 246–251. DOI: `10.2307/2319846`.

[23]   K.-U. Bletzinger and E. Ramm. "A general finite element approach to the form finding of tensile structures by the Updated Reference Strategy." In: *International Journal of Space Structures* 14.2 (1999), pp. 131–145. DOI: `10.1260/0266351991494759`.

[24]   W. Boehm. "Inserting new knots into B-spline curves." In: *Computer-Aided Design* 12.4 (1980), pp. 199–201. DOI: `10.1016/0010-4485(80)90154-2`.

[25]   C. de Boor. *A practical guide to splines: With 32 figures*. Rev. ed. Vol. 27. Applied mathematical sciences. New York: Springer, 2001. ISBN: 0-387-95366-3.

[26]   C. Bracco, A. Buffa, C. Giannelli, and R. Vázquez. "Adaptive isogeometric methods with hierarchical splines: An overview." In: *Discrete & Continuous Dynamical Systems - A* 39.1 (2019), pp. 241–261. DOI: `10.3934/dcds.2019010`.

[27]   M. Breitenberger. "CAD-integrated design and analysis of shell structures." Dissertation. München: Technische Universität München, 2016.

[28]   M. Breitenberger, A. Apostolatos, B. Philipp, R. Wüchner, and K.-U. Bletzinger. "Analysis in computer aided design: Nonlinear isogeometric B-Rep analysis of shell structures." In: *Computer Methods in Applied Mechanics and Engineering* 284 (2015), pp. 401–457. DOI: `10.1016/j.cma.2014.09.033`.

[29]   E. Brivadis, A. Buffa, B. Wohlmuth, and L. Wunderlich. "Isogeometric mortar methods." In: *Computer Methods in Applied Mechanics and Engineering* 284 (2015), pp. 292–319. DOI: `10.1016/j.cma.2014.09.012`.

[30]   A. Buffa and C. Giannelli. "Adaptive isogeometric methods with hierarchical splines: Error estimator and convergence." In: *Mathematical Models and Methods in Applied Sciences* 26.01 (2015), pp. 1–25. DOI: `10.1142/S0218202516500019`.

[31]   H. Casquero, L. Liu, Y. Zhang, A. Reali, and H. Gomez. "Isogeometric collocation using analysis-suitable T-splines of arbitrary degree." In: *Computer Methods in Applied Mechanics and Engineering* 301 (2016), pp. 164–186. DOI: `10.1016/j.cma.2015.12.014`.

[32]   H. Casquero, L. Liu, Y. Zhang, A. Reali, J. Kiendl, and H. Gomez. "Arbitrary-degree T-splines for isogeometric analysis of fully nonlinear Kirchhoff-Love shells." In: *Computer-Aided Design* 82 (2017), pp. 140–153. DOI: `10.1016/j.cad.2016.08.009`.

[33]   Z. H. Chen, Y. J. Wu, Y. Yin, and C. Shan. "Formulation and application of multi-node sliding cable element for the analysis of Suspen-Dome structures." In: *Finite Elements in Analysis and Design* 46.9 (2010), pp. 743–750. DOI: `10.1016/j.finel.2010.04.003`.

[34]   B. K. Choi. *Surface modeling for CAD/CAM*. Vol. 11. Advances in industrial engineering. Amsterdam, New York: Elsevier, 1991. ISBN: 0444884823.

[35]   F. Cirak and M. Ortiz. "Fully C^1-conforming subdivision elements for finite deformation thin-shell analysis." In: *International Journal for Numerical Methods in Engineering* 51 (2001), pp. 813–833. DOI: `10.1002/nme.182`.

[36]   F. Cirak, M. Ortiz, and P. Schröder. "Subdivision surfaces: a new paradigm for thin-shell finite-element analysis." In: *International Journal for Numerical Methods in Engineering* 47.12 (2000), pp. 2039–2072. DOI: `10.1002/(SICI)1097-0207(20000430)47:12<2039::AID-NME872>3.0.CO;2-1`.

[37]   F. Cirak, M. J. Scott, E. K. Antonsson, M. Ortiz, and P. Schröder. "Integrated modeling, finite-element analysis, and engineering design for thin-shell structures using subdivision." In: *Computer-Aided Design* 34.2 (2002), pp. 137–148. DOI: `10.1016/S0010-4485(01)00061-6`.

[38]   E. Cohen, T. Lyche, and R. Riesenfeld. "Discrete B-splines and subdivision techniques in computer-aided geometric design and computer graphics." In: *Computer Graphics and Image Processing* 14.2 (1980), pp. 87–111. DOI: `10.1016/0146-664X(80)90040-4`.

[39]   E. Cohen, R. F. Riesenfeld, and G. Elber. *Geometric modeling with splines: An introduction*. Natick and Mass: AK Peters, 2001. ISBN: 978-1568811376.

[40] J. A. Cottrell, T. J. R. Hughes, and Y. Bazilevs. *Isogeometric Analysis: Toward Integration of CAD and FEA*. Chichester, UK: John Wiley & Sons, Ltd, 2009. ISBN: 9780470748737. DOI: 10.1002/9780470749081.

[41] J. B. Coulibaly, M.-A. Chanut, S. Lambert, and F. Nicot. "Sliding cable modeling: An attempt at a unified formulation." In: *International Journal of Solids and Structures* 130-131 (2018), pp. 1–10. DOI: 10.1016/j.ijsolstr.2017.10.025.

[42] F. Dieringer, B. Philipp, R. Wüchner, and K.-U. Bletzinger. "Numerical Methods for the Design and Analysis of Hybrid Structures." In: *International Journal of Space Structures* 28.3 (2013), pp. 149–160. DOI: 10.1260/0266-3511.28.3-4.149.

[43] F. H. Dieringer. "Numerical methods for the design and analysis of tensile structures." Dissertation. München: Technische Universität München, 2014.

[44] T. D. Dinh, A. Rezaei, W. Punurai, L. de Laet, M. Mollaert, D. van Hemelrijck, and W. van Paepegem. "A shape optimization approach to integrated design and nonlinear analysis of tensioned fabric membrane structures with boundary cables." In: *International Journal of Solids and Structures* 83 (2016), pp. 114–125. DOI: 10.1016/j.ijsolstr.2016.01.004.

[45] W. Dornisch, S. Klinkel, and B. Simeon. "Isogeometric Reissner-Mindlin shell analysis with exactly calculated director vectors." In: *Computer Methods in Applied Mechanics and Engineering* 253 (2013), pp. 491–504. DOI: 10.1016/j.cma.2012.09.010.

[46] W. Dornisch, R. Müller, and S. Klinkel. "An efficient and robust rotational formulation for isogeometric Reissner-Mindlin shell elements." In: *Computer Methods in Applied Mechanics and Engineering* 303 (2016), pp. 1–34. DOI: 10.1016/j.cma.2016.01.018.

[47] W. Dornisch, J. Stöckler, and R. Müller. "Dual and approximate dual basis functions for B-splines and NURBS - Comparison and application for an efficient coupling of patches with the isogeometric mortar method." In: *Computer Methods in Applied*

Mechanics and Engineering 316 (2017), pp. 449–496. DOI: 10.1016/j.cma.2016.07.038.

[48]   W. Dornisch, G. Vitucci, and S. Klinkel. "The weak substitution method - an application of the mortar method for patch coupling in NURBS-based isogeometric analysis." In: *International Journal for Numerical Methods in Engineering* 103.3 (2015), pp. 205–234. DOI: 10.1002/nme.4918.

[49]   X. Du, G. Zhao, and W. Wang. "Nitsche method for isogeometric analysis of Reissner-Mindlin plate with non-conforming multi-patches." In: *Computer Aided Geometric Design* 35-36 (2015), pp. 121–136. DOI: 10.1016/j.cagd.2015.03.005.

[50]   R. Echter, B. Oesterle, and M. Bischoff. "A hierarchic family of isogeometric shell finite elements." In: *Computer Methods in Applied Mechanics and Engineering* 254 (2013), pp. 170–180. DOI: 10.1016/j.cma.2012.10.018.

[51]   J. Gade, M. Bischoff, and R. Kemmler. "Advanced approaches for analysis and form finding of membrane structures with finite elements." In: *Structural Membranes 2017*. Ed. by K.-U. Bletzinger, E. Oñate, and B. Kröplin. Barcelona, Spain: International Center for Numerical Methods in Engineering (CIMNE), 2017, pp. 275–293. ISBN: 978-84-946909-9-0.

[52]   M. W. Gee, C. Reeps, H. H. Eckstein, and W. A. Wall. "Prestressing in finite deformation abdominal aortic aneurysm simulation." In: *Journal of Biomechanics* 42.11 (2009), pp. 1732–1739. DOI: 10.1016/j.jbiomech.2009.04.016.

[53]   L. Ghoussoub. "Analyse de quelques éléments du comportement des écrans de filets pare-blocs." Dissertation. Paris: Université Paris Est, 2015.

[54]   A.-K. Goldbach, A. M. Bauer, and K.-U. Bletzinger. "Advantages of a CAD-integrated approach for the design cycle of structural membranes." In: *Advanced Building Skins*. Ed. by Advanced Building Skins GmbH. 2019, pp. 391–396. ISBN: 978-3-9524883-0-0.

[55]   A.-K. Goldbach, A. M. Bauer, R. Wüchner, and K.-U. Bletzinger. "CAD-integrated parametric lightweight design with isogeometric B-Rep analysis." In: *Frontiers in Built Environment* 6 (2020), p. 44. DOI: 10.3389/fbuil.2020.00044.

[56] A.-K. Goldbach and K.-U. Bletzinger. "CAD-integrated parametric design cycle for structural membranes." In: *Proceedings of the IASS Annual Symposium 2019 - Structural Membranes 2019*. Ed. by C. Lázaro, K.-U. Bletzinger, and E. Oñate. 2019. ISBN: 978-84-121101-0-4.

[57] S. Govindjee and P. A. Mihalic. "Computational methods for inverse deformations in quasi-incompressible finite elasticity." In: *International Journal for Numerical Methods in Engineering* 43.5 (1998), pp. 821–838. DOI: 10.1002/(SICI)1097-0207(19981115)43:5<821::AID-NME453>3.0.CO;2-C.

[58] S. Govindjee and P. A. Mihalic. "Computational methods for inverse finite elastostatics." In: *Computer Methods in Applied Mechanics and Engineering* 136.1-2 (1996), pp. 47–57. DOI: 10.1016/0045-7825(96)01045-6.

[59] L. Greco and M. Cuomo. "An implicit G^1 multi patch B-spline interpolation for Kirchhoff-Love space rod." In: *Computer Methods in Applied Mechanics and Engineering* 269 (2014), pp. 173–197. DOI: 10.1016/j.cma.2013.09.018.

[60] L. Greco and M. Cuomo. "B-Spline interpolation of Kirchhoff-Love space rods." In: *Computer Methods in Applied Mechanics and Engineering* 256 (2013), pp. 251–269. DOI: 10.1016/j.cma.2012.11.017.

[61] L. Gründig, E. Moncrieff, P. Singer, and D. Ströbel. "High-performance cutting pattern generation of architectural textile structures." In: *IASS-IACM 2000: Fourth International Colloquium on Computation of Shell & Spatial Structures*. Ed. by M. Papadrakakis, A. Samartin, and E. Oñate. National technical University of Athens, 2000.

[62] Y. Guo, J. Heller, T. J. Hughes, M. Ruess, and D. Schillinger. "Variationally consistent isogeometric analysis of trimmed thin shells at finite deformations, based on the STEP exchange format." In: *Computer Methods in Applied Mechanics and Engineering* 336 (2018), pp. 39–79. DOI: 10.1016/j.cma.2018.02.027.

[63] Y. Guo and M. Ruess. "Nitsche's method for a coupling of isogeometric thin shells and blended shell structures." In: *Computer Methods in Applied Mechanics and Engineering* 284 (2015), pp. 881–905. DOI: 10.1016/j.cma.2014.11.014.

[64] Y. Guo, M. Ruess, and D. Schillinger. "A parameter-free variational coupling approach for trimmed isogeometric thin shells." In: *Computational Mechanics* 59.4 (2017), pp. 693–715. DOI: 10.1007/s00466-016-1368-x.

[65] E. Haug, P. de Kermel, B. Gawenat, and A. Michalski. "Industrial design and analysis of structural membranes." In: *International Journal of Space Structures* 24.4 (2009), pp. 191–204. DOI: 10.1260/026635109789968227.

[66] A. J. Herrema. "A framework for isogeometric-analysis-based design and optimization of wind turbine blades." Dissertation. Ames, Iowa: Iowa State University, 2018.

[67] A. J. Herrema, E. L. Johnson, D. Proserpio, M. C. Wu, J. Kiendl, and M.-C. Hsu. "Penalty coupling of non-matching isogeometric Kirchhoff-Love shell patches with application to composite wind turbine blades." In: *Computer Methods in Applied Mechanics and Engineering* 346 (2019), pp. 810–840. DOI: 10.1016/j.cma.2018.08.038.

[68] T. Hirschler, R. Bouclier, A. Duval, T. Elguedj, and J. Morlier. "The embedded isogeometric Kirchhoff-Love shell: From design to shape optimization of non-conforming stiffened multipatch structures." In: *Computer Methods in Applied Mechanics and Engineering* 349 (2019), pp. 774–797. DOI: 10.1016/j.cma.2019.02.042.

[69] M.-C. Hsu, C. Wang, A. J. Herrema, D. Schillinger, A. Ghoshal, and Y. Bazilevs. "An interactive geometry modeling and parametric design platform for isogeometric analysis." In: *Computers & Mathematics with Applications* 70.7 (2015), pp. 1481–1500. DOI: 10.1016/j.camwa.2015.04.002.

[70] T. J. R. Hughes, J. A. Cottrell, and Y. Bazilevs. "Isogeometric analysis: CAD, finite elements, NURBS, exact geometry and mesh refinement." In: *Computer Methods in Applied Mechanics and*

Engineering 194.39-41 (2005), pp. 4135–4195. DOI:
`10.1016/j.cma.2004.10.008`.

[71]   T. J. R. Hughes, A. Reali, and G. Sangalli. "Efficient quadrature for NURBS-based isogeometric analysis." In: *Computer Methods in Applied Mechanics and Engineering* 199.5-8 (2010), pp. 301–313. DOI: `10.1016/j.cma.2008.12.004`.

[72]   P. Kang and S.-K. Youn. "Isogeometric shape optimization of trimmed shell structures." In: *Structural and Multidisciplinary Optimization* 53.4 (2016), pp. 825–845. DOI: `10.1007/s00158-015-1361-6`.

[73]   J. M. Kiendl, Y. Bazilevs, M.-C. Hsu, R. Wüchner, and K.-U. Bletzinger. "The bending strip method for isogeometric analysis of Kirchhoff-Love shell structures comprised of multiple patches." In: *Computer Methods in Applied Mechanics and Engineering* 199.37-40 (2010), pp. 2403–2416. DOI: `10.1016/j.cma.2010.03.029`.

[74]   J. M. Kiendl, K.-U. Bletzinger, J. Linhard, and R. Wüchner. "Isogeometric shell analysis with Kirchhoff-Love elements." In: *Computer Methods in Applied Mechanics and Engineering* 198.49-52 (2009), pp. 3902–3914. DOI: `10.1016/j.cma.2009.08.013`.

[75]   H.-J. Kim, Y.-D. Seo, and S.-K. Youn. "Isogeometric analysis with trimming technique for problems of arbitrary complex topology." In: *Computer Methods in Applied Mechanics and Engineering* 199.45-48 (2010), pp. 2796–2812. DOI: `10.1016/j.cma.2010.04.015`.

[76]   J.-Y. Kim and J.-B. Lee. "A new technique for optimum cutting pattern generation of membrane structures." In: *Engineering Structures* 24.6 (2002), pp. 745–756. DOI: `10.1016/S0141-0296(02)00003-2`.

[77]   E. Klingbeil. *Tensorrechnung für Ingenieure*. unveränd. Nachdr. Vol. 197. BI-Hochschultaschenbücher. Mannheim and Wien u.a.: Bibliogr. Inst, 1985. ISBN: 3411001976.

[78] J. Knippers, H. Jungjohann, F. Scheible, and M. Oppe. "Bio-inspirierte kinetische Fassade für den Themenpavillon ''One Ocean'' EXPO 2012 in Yeosu, Korea." In: *Bautechnik* 90.6 (2013), pp. 341–347. DOI: `10.1002/bate.201300034`.

[79] S. Krishnan and D. Manocha. "An efficient surface intersection algorithm based on lower-dimensional formulation." In: *ACM Transactions on Graphics* 16.1 (1997), pp. 74–106. DOI: `10.1145/237748.237751`.

[80] L. Kudela, N. Zander, T. Bog, S. Kollmannsberger, and E. Rank. "Efficient and accurate numerical quadrature for immersed boundary methods." In: *Advanced Modeling and Simulation in Engineering Sciences* 2.1 (2015), p. 763. DOI: `10.1186/s40323-015-0031-y`.

[81] L. Kudela, N. Zander, S. Kollmannsberger, and E. Rank. "Smart octrees: Accurately integrating discontinuous functions in 3D." In: *Computer Methods in Applied Mechanics and Engineering* 306 (2016), pp. 406–426. DOI: `10.1016/j.cma.2016.04.006`.

[82] P. Längst, A. M. Bauer, R. La Magna, and J. Lienhard. "Isogeometric methods at the interface of architecture and engineering." In: *Creativity in Structural Design*. Ed. by C. Mueller and S. Adriaenssens. DS Graphic, 2018.

[83] P. Längst, A. M. Bauer, A. Michalski, and J. Lienhard. "The potentials of isogeometric analysis methods in integrated design processes." In: *Proceedings of the IASS Annual Symposium 2017*. Ed. by A. Bögle and M. Grohmann. 2017.

[84] Z. Lei, F. Gillot, and L. Jezequel. "A C^1/G^1 multiple patches connection method in isogeometric analysis." In: *Applied Mathematical Modelling* 39.15 (2015), pp. 4405–4420. DOI: `10.1016/j.apm.2014.12.055`.

[85] J. Lienhard. *Bending-active structures: form-finding strategies using elastic deformation in static and kinetic systems and the structural potentials therein*. Forschungsberichte aus dem Institut für Tragkonstruktionen und Konstruktives Entwerfen, Universität Stuttgart. Stuttgart: ITKE, 2014. ISBN: 9783922302360.

[86]   J. Linhard. "Numerisch-mechanische Betrachtung des Entwurfsprozesses von Membrantragwerken." Dissertation. München: Technische Universität München, 2009.

[87]   K. Linkwitz and H.-J. Schek. "Einige Bemerkungen zur Berechnung von vorgespannten Seilnetzkonstruktionen." In: *Ingenieur-archiv* 40.3 (1971), pp. 145–158. DOI: 10.1007/BF00532146.

[88]   K. Linkwitz, H.-J. Schek, and L. Gründig. "Die Gleichgewichtsberechnung von Seilnetzen unter Zusatzbedingungen." In: *Ingenieur-archiv* 43.4 (1974), pp. 183–192. DOI: 10.1007/BF00534000.

[89]   K. Linkwitz. "Formfinding by the ''Direct Approach'' and Pertinent Strategies for the Conceptual Design of Prestressed and Hanging Structures." In: *International Journal of Space Structures* 14.2 (1999), pp. 73–87. DOI: 10.1260/0266351991494713.

[90]   G. Lumpe and V. Gensichen. *Evaluierung der linearen und nichtlinearen Stabstatik in Theorie und Software: Prüfbeispiele, Fehlerursachen, genaue Theorie*. Bauingenieur-Praxis. Berlin: Ernst W. + Sohn Verlag, 2014. ISBN: 978-3-433-03053-0.

[91]   E. Marino, J. Kiendl, and L. de Lorenzis. "Explicit isogeometric collocation for the dynamics of three-dimensional beams undergoing finite motions." In: *Computer Methods in Applied Mechanics and Engineering* 343 (2019), pp. 530–549. DOI: 10.1016/j.cma.2018.09.005.

[92]   B. Marussig and T. J. R. Hughes. "A review of trimming in isogeometric analysis: Challenges, data exchange and simulation aspects." In: *Archives of Computational Methods in Engineering* 30.8 (2017), p. 657. DOI: 10.1007/s11831-017-9220-9.

[93]   B. Maurin and R. Motro. "Cutting pattern of fabric membranes with the stress composition method." In: *International Journal of Space Structures* 14.2 (1999), pp. 121–129. DOI: 10.1260/0266351991494740.

[94]   J. McCartney, B. K. Hinds, and K. W. Chong. "Pattern flattening for orthotropic materials." In: *Computer-Aided Design* 37.6 (2005), pp. 631–644. DOI: 10.1016/j.cad.2004.09.006.

[95]   J. McCartney, B. Hinds, and B. Seow. "The flattening of triangulated surfaces incorporating darts and gussets." In: *Computer-Aided Design* 31.4 (1999), pp. 249–260. DOI: 10.1016/S0010-4485(99)00025-1.

[96]   A. P. Nagy and D. J. Benson. "On the numerical integration of trimmed isogeometric elements." In: *Computer Methods in Applied Mechanics and Engineering* 284 (2015), pp. 165–185. DOI: 10.1016/j.cma.2014.08.002.

[97]   V. P. Nguyen, P. Kerfriden, M. Brino, S. P. A. Bordas, and E. Bonisoli. "Nitsche's method for two and three dimensional NURBS patch coupling." In: *Computational Mechanics* 53.6 (2014), pp. 1163–1182. DOI: 10.1007/s00466-013-0955-3.

[98]   T. Oberbichler, A. M. Bauer, A.-K. Goldbach, R. Wüchner, and K.-U. Bletzinger. "CAD-integrierte Analyse im Entwurfsprozess." In: *Bautechnik* 96.5 (2019), pp. 400–408. DOI: 10.1002/bate.201800105.

[99]   B. Oesterle, R. Sachse, E. Ramm, and M. Bischoff. "Hierarchic isogeometric large rotation shell elements including linearized transverse shear parametrization." In: *Computer Methods in Applied Mechanics and Engineering* 321 (2017), pp. 383–405. DOI: 10.1016/j.cma.2017.03.031.

[100] J. Panetta, M. Konaković-Luković, F. Isvoranu, E. Bouleau, and M. Pauly. "X-Shells." In: *ACM Transactions on Graphics* 38.4 (2019), pp. 1–15. DOI: 10.1145/3306346.3323040.

[101] J. B. Pargana, D. Lloyd-Smith, and B. A. Izzuddin. "Fully integrated design and analysis of Tensioned Fabric Structures: Finite elements and case studies." In: *Engineering Structures* 32.4 (2010), pp. 1054–1068. DOI: 10.1016/j.engstruct.2009.12.032.

[102] J. Parvizian, A. Düster, and E. Rank. "Finite cell method." In: *Computational Mechanics* 41.1 (2007), pp. 121–133. DOI: 10.1007/s00466-007-0173-y.

[103] N. M. Patrikalakis. "Surface-to-surface intersections." In: *IEEE Computer Graphics and Applications* 13.1 (1993), pp. 89–95. DOI: 10.1109/38.180122.

[104]   R. M. Pauletti and C. B. Martins. "Modeling the slippage between membrane and border cables." In: *Evolution and Trends in Design, Analysis and Construction of Shell and Spatial Structures*. Ed. by A. Domingo Cabo and C. Lázaro. 2009, pp. 2059–2070.

[105]   B. Philipp, M. Breitenberger, I. D'Auria, R. Wüchner, and K.-U. Bletzinger. "Integrated design and analysis of structural membranes using the Isogeometric B-Rep Analysis." In: *Computer Methods in Applied Mechanics and Engineering* 303 (2016), pp. 312–340. DOI: 10.1016/j.cma.2016.02.003.

[106]   B. F. Philipp. "Methodological treatment of non-linear structural behavior in the design, analysis and verification of lightweight structures." Dissertation. München: Technische Universität München, 2017.

[107]   L. Piegl and W. Tiller. *The NURBS Book*. Second Edition. Monographs in Visual Communication. Berlin and Heidelberg: Springer, 1997. ISBN: 978-3-642-59223-2. DOI: 10.1007/978-3-642-59223-2.

[108]   H. Pottmann. *Architectural geometry*. 1st ed. Exton, PA: Bentley Institute Press, 2007. ISBN: 9781934493045.

[109]   S. B. Raknes, X. Deng, Y. Bazilevs, D. J. Benson, K. M. Mathisen, and T. Kvamsdal. "Isogeometric rotation-free bending-stabilized cables: Statics, dynamics, bending strips and coupling with shells." In: *Computer Methods in Applied Mechanics and Engineering* 263 (2013), pp. 127–143. DOI: 10.1016/j.cma.2013.05.005.

[110]   E. Rank, M. Ruess, S. Kollmannsberger, D. Schillinger, and A. Düster. "Geometric modeling, isogeometric analysis and the finite cell method." In: *Computer Methods in Applied Mechanics and Engineering* 249-252 (2012), pp. 104–115. DOI: 10.1016/j.cma.2012.05.022.

[111]   M. Ruess, D. Schillinger, Y. Bazilevs, V. Varduhn, and E. Rank. "Weakly enforced essential boundary conditions for NURBS-embedded and trimmed NURBS geometries on the basis of the finite cell method." In: *International Journal for Numerical Methods in Engineering* 95.10 (2013), pp. 811–846. DOI: 10.1002/nme.4522.

[112]   M. Ruess, D. Schillinger, A. I. Özcan, and E. Rank. "Weak coupling for isogeometric analysis of non-matching and trimmed multi-patch geometries." In: *Computer Methods in Applied Mechanics and Engineering* 269 (2014), pp. 46–71. DOI: `10.1016/j.cma.2013.10.009`.

[113]   T. Scheffler. "Development and application of precast hyperboloid shells in East and West Germany from the 1950s to the 1980s." In: *Proceedings of the IASS Annual Symposium 2017*. Ed. by A. Bögle and M. Grohmann. 2017.

[114]   J. Schikore, A. M. Bauer, R. Barthel, and K.-U. Bletzinger. "Large torsion on elastic lamella grid structures." In: *Proceedings of the IASS Annual Symposium 2019 - Structural Membranes 2019*. Ed. by C. Lázaro, K.-U. Bletzinger, and E. Oñate. 2019, pp. 788–795. ISBN: 978-84-121101-0-4.

[115]   D. Schillinger, J. A. Evans, A. Reali, M. A. Scott, and T. J. R. Hughes. "Isogeometric collocation: Cost comparison with Galerkin methods and extension to adaptive hierarchical NURBS discretizations." In: *Computer Methods in Applied Mechanics and Engineering* 267 (2013), pp. 170–232. DOI: `10.1016/j.cma.2013.07.017`.

[116]   E. Schling. "Repetitive structures: Design and construction of curved support structures with repetitive parameters." Dissertation. München: Technische Universität München, 2018. DOI: `10.14459/2018md1449869`.

[117]   E. Schling, M. Kilian, H. Wang, J. Schikore, and H. Pottmann. "Design and construction of curved support structures with repetitive parameters." In: *AAG 2018 - advances in architectural geometry 2018*. Ed. by L. Hesselgren, A. Kilian, S. Malek, K.-G. Olsson, O. Sorkine-Hornung, and C. Williams. 2018, pp. 140–165. ISBN: 978-3-903015-13-5.

[118]   S. Schuß, M. Dittmann, B. Wohlmuth, S. Klinkel, and C. Hesch. "Multi-patch isogeometric analysis for Kirchhoff-Love shell elements." In: *Computer Methods in Applied Mechanics and Engineering* 349 (2019), pp. 91–116. DOI: `10.1016/j.cma.2019.02.015`.

[119] T. W. Sederberg and R. J. Meyers. "Loop detection in surface patch intersections." In: *Computer Aided Geometric Design* 5.2 (1988), pp. 161–171. DOI: 10.1016/0167-8396(88)90029-5.

[120] Y.-D. Seo, H.-J. Kim, and S.-K. Youn. "Isogeometric topology optimization using trimmed spline surfaces." In: *Computer Methods in Applied Mechanics and Engineering* 199.49-52 (2010), pp. 3270–3296. DOI: 10.1016/j.cma.2010.06.033.

[121] A. Sheffer and E. de Sturler. "Parameterization of faceted surfaces for meshing using angle-based flattening." In: *Engineering with Computers* 17.3 (2001), pp. 326–337. DOI: 10.1007/PL00013391.

[122] E. Soriano, R. Sastre, and D. Boixader. "G-shells: Flat collapsible geodesic mechanisms for gridshells." In: *Proceedings of the IASS Annual Symposium 2019 - Structural Membranes 2019*. Ed. by C. Lázaro, K.-U. Bletzinger, and E. Oñate. 2019, pp. 1894–1901. ISBN: 978-84-121101-0-4.

[123] T. Teschemacher, A. M. Bauer, T. Oberbichler, M. Breitenberger, R. Rossi, R. Wüchner, and K.-U. Bletzinger. "Realization of CAD-integrated shell simulation based on isogeometric B-Rep analysis." In: *Advanced Modeling and Simulation in Engineering Sciences* 5.1 (2018), p. 19. DOI: 10.1186/s40323-018-0109-4.

[124] B. H. V. Topping and P. Iványi. *Computer aided design of cable membrane structures*. Saxe-Coburg publications on computational engineering. Kippen: Saxe-Coburg Publ, 2007. ISBN: 978-1874672111.

[125] M. Vaillant and Glaunès J. "Surface matching via currents." In: *Information processing in medical imaging*. Ed. by G. E. Christensen and M. Sonka. Lecture Notes in Computer Science. Berlin: Springer, 2005, pp. 381–392. ISBN: 978-3-540-26545-0. DOI: 10.1007/11505730_32.

[126] D. Veenendaal and P. Block. "An overview and comparison of structural form finding methods for general networks." In: *International Journal of Solids and Structures* 49.26 (2012), pp. 3741–3753. DOI: 10.1016/j.ijsolstr.2012.08.008.

[127] C. C. Wang, S. S.-F. Smith, and M. M. Yuen. "Surface flattening based on energy model." In: *Computer-Aided Design* 34.11 (2002), pp. 823–833. DOI: 10.1016/S0010-4485(01)00150-6.

[128]   Y.-W. Wang, Z.-D. Huang, Y. Zheng, and S.-G. Zhang.
         "Isogeometric analysis for compound B-spline surfaces." In:
         Computer Methods in Applied Mechanics and Engineering 261-262
         (2013), pp. 1–15. DOI: `10.1016/j.cma.2013.04.001`.

[129]   O. Weeger, S.-K. Yeung, and M. L. Dunn. "Fully isogeometric
         modeling and analysis of nonlinear 3D beams with spatially
         varying geometric and material parameters." In: *Computer
         Methods in Applied Mechanics and Engineering* 342 (2018),
         pp. 95–115. DOI: `10.1016/j.cma.2018.07.033`.

[130]   O. Weeger, S.-K. Yeung, and M. L. Dunn. "Isogeometric collocation
         methods for Cosserat rods and rod structures." In: *Computer
         Methods in Applied Mechanics and Engineering* 316 (2017),
         pp. 100–122. DOI: `10.1016/j.cma.2016.05.009`.

[131]   A. M. Widhammer. "Variation of Reference Strategy: Generation of
         optimized cutting patterns for textile fabrics." Dissertation.
         München: Technische Universität München, 2015.

[132]   W. Wunderlich and W. D. Pilkey. *Mechanics of structures:
         Variational and computational methods.* 2nd ed. Boca Raton, FL:
         CRC Press, 2003. ISBN: 978-0849307003.

[133]   B. Zhou, M. L. Accorsi, and J. W. Leonard. "Finite element
         formulation for modeling sliding cable elements." In: *Computers &
         Structures* 82.2-3 (2004), pp. 271–280. DOI:
         `10.1016/j.compstruc.2003.08.006`.

Bisherige Titel der Schriftenreihe

Band   Titel

1   Frank Koschnick, *Geometrische Lockingeffekte bei Finiten Elementen und ein allgemeines Konzept zu ihrer Vermeidung*, 2004.

2   Natalia Camprubi, *Design and Analysis in Shape Optimization of Shells*, 2004.

3   Bernhard Thomée, *Physikalisch nichtlineare Berechnung von Stahlfaserbetonkonstruktionen*, 2005.

4   Fernaß Daoud, *Formoptimierung von Freiformschalen - Mathematische Algorithmen und Filtertechniken*, 2005.

5   Manfred Bischoff, *Models and Finite Elements for Thin-walled Structures*, 2005.

6   Alexander Hörmann, *Ermittlung optimierter Stabwerkmodelle auf Basis des Kraftflusses als Anwendung plattformunabhängiger Prozesskopplung*, 2006.

7   Roland Wüchner, *Mechanik und Numerik der Formfindung und Fluid-Struktur-Interaktion von Membrantragwerken*, 2006.

8   Florian Jurecka, *Robust Design Optimization Based on Metamodeling Techniques*, 2007.

9   Johannes Linhard, *Numerisch-mechanische Betrachtung des Entwurfsprozesses von Membrantragwerken*, 2009.

10   Alexander Kupzok, *Modeling the Interaction of Wind and Membrane Structures by Numerical Simulation*, 2009.

11   Bin Yang, *Modified Particle Swarm Optimizers and their Application to Robust Design and Structural Optimization*, 2009.

Band	Titel
25	Majid Hojjat, *Node-based parametrization for shape optimal design*, 2015.
26	Ute Israel, *Optimierung in der Fluid-Struktur-Interaktion - Sensitivitätsanalyse für die Formoptimierung auf Grundlage des partitionierten Verfahrens*, 2015.
27	Electra Stavropoulou, *Sensitivity analysis and regularization for shape optimization of coupled problems*, 2015.
28	Daniel Markus, *Numerical and Experimental Modeling for Shape Optimization of Offshore Structures*, 2015.
29	Pablo Suárez, *Design Process for the Shape Optimization of Pressurized Bulkheads as Components of Aircraft Structures*, 2015.
30	Armin Widhammer, *Variation of Reference Strategy - Generation of Optimized Cutting Patterns for Textile Fabrics*, 2015.
31	Helmut Masching, *Parameter Free Optimization of Shape Adaptive Shell Structures*, 2016.
32	Hao Zhang, *A General Approach for Solving Inverse Problems in Geophysical Systems by Applying Finite Element Method and Metamodel Techniques*, 2016.
33	Tianyang Wang, *Development of Co-Simulation Environment and Mapping Algorithms*, 2016.
34	Michael Breitenberger, *CAD-integrated Design and Analysis of Shell Structures*, 2016.
35	Önay Can, *Functional Adaptation with Hyperkinematics using Natural Element Method: Application for Articular Cartilage*, 2016.
36	Benedikt Philipp, *Methodological Treatment of Non-linear Structural Behavior in the Design, Analysis and Verification of Lightweight Structures*, 2017.
37	Michael Andre, *Aeroelastic Modeling and Simulation for the Assessment of Wind Effects on a Parabolic Trough Solar Collector*, 2018.